Laser-Control of Molecular Dynamics

Dissertation

zur Erlangung des
naturwissenschaftlichen Doktorgrades
der Bayerischen Julius-Maximilians-Universität Würzburg

vorgelegt von

Stefanie Gräfe

aus

Düsseldorf

Würzburg 2005

Eingereicht am: ....

bei der Fakultät für Chemie und Pharmazie

1. Gutachter: ....

2. Gutachter: ....

der Dissertation

1. Prüfer: ....

2. Prüfer: ....

3. Prüfer: ....

des Öffentlichen Promotionskolloquiums

Tag des Öffentlichen Promotionskolloquiums: ....

Doktorurkunde ausgehändigt am: ....

Contents

Introduction **1**

1 Theory **7**

1.1 Dynamical Equations 7

1.1.1 Classical Dynamics 7

1.1.2 Quantum Dynamics 9

1.1.3 Born-Oppenheimer Approximation 12

1.2 Design of Electro-Magnetic Fields 15

1.3 Time-Dependent Perturbation Theory 19

1.3.1 Fermi's Golden Rule 21

1.4 Strong Field: Rabi Oscillations 23

2 Numerical Methods **25**

2.1 Classical Trajectories 25

2.2 Quantum Propagation 26

2.3 Eigenstates 28

3 Control Theories **30**

3.1 Genetic Algorithms 31

3.2 Optimal Control Theory (OCT) 33

3.3 Restricted Optimal Control Theory 35

3.4 Instantaneous Dynamics 37

3.4.1 Classical Picture 38

3.4.2 Energy Condition 41

3.4.3 Momentum Condition 42

3.4.4 Population Transfer 42

4 Dynamics in Double Well Potentials **46**

4.1 One-Dimensional Cases 46

4.1.1 Classical Trajectories 47

4.1.2 Quantum Dynamical Picture 50

4.1.3 Asymmetric Double-Well Potential 52

4.2 Two-Dimensional Case 56

5 Selective Bond Breaking: The HOD Molecule **62**

5.1 The HOD Model System 63

5.2 Dissociation 65

5.2.1 Momentum Condition 66

5.2.2 Energy Condition 67

6 Resonant vs. Non-resonant Transitions 70

6.1 Description of the 3-Level Model System 72

6.2 Control of Photodissociation Dynamics 75

6.2.1 Genetic Algorithm 76

6.2.2 Optimal Control Theory (OCT) 80

6.2.3 Restricted OCT 84

6.2.4 Instantaneous Dynamics 86

6.2.5 Restricted Instantaneous Dynamics 89

6.3 Alternative Coupling scheme 90

6.4 Extended Model System: 4 electronic potentials 95

6.4.1 Instantaneous Dynamics 97

6.4.2 Optimal Control Theory 103

6.4.3 Genetic Algorithm 104

7 The Sodium Dimer 108

7.1 The Model System 108

7.2 Time-Frequency Analysis 110

7.3 Instantaneous Dynamics 111

7.3.1 $|A\rangle$ State Population Transfer 112

7.3.2 $|\Pi\rangle$ State Population Transfer 117

7.3.3 Orientational Effects 121

7.4 Wave Packet Imaging 125

7.4.1 Pump/Probe Ionization Signals 125

7.4.2 Photoelectron Spectra 126

7.4.3 Transient Ion Yields 129

7.4.4 Transient Fragment Distributions 130

7.4.5 Numerical Results 133

7.5 Monitoring Control Processes 138

8 Iodine Dimer 143

8.1 Model System 144

8.2 Adiabatic Limit - STIRAP 147

8.3 CARS-Signals 153

8.4 Numerical Results 157

8.4.1 Pump/ Stokes Resonant Excitation 157

8.4.2 Pump/Stokes Off-Resonant Excitation 162

8.4.3 Intensity Effects 168

Summary 176

Zusammenfassung 181

Dank 198

Lebenslauf 201

Introduction

With increasing knowledge about the structure and dynamics of molecules, the goal to not only observe, but to actively control chemical processes has been approached in the last decades. The development of pulse shapers [1] makes it possible to phase- and amplitude-modulate electromagnetic fields to be employed to influence atoms, molecules and solid state systems in a desired way. Theoretical, as well as experimental efforts along these directions are summarized in two recent monographs [2,3] and numerous review articles [4–8].

Several activities originated from research groups in Würzburg (supported within the Sonderforschungsbereich 347) where organometallics like $Fe(CO)_5$ [9], and also organic polymers [10,11] were selectively dissociated or excited, respectively. A generic control scheme is visualized in fig. 1.

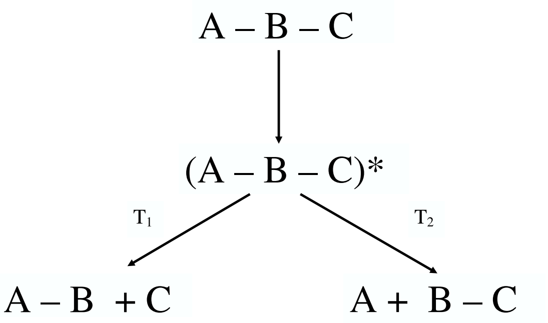

Figure 1: *General scheme for a controlled dissociation of a molecule A – B – C. After an excitation process one bond, either the A – B or the B – C bond, is broken selectively.*

For a molecule A – B – C with two different bonds, the objective of control is to selectively excite or break one of these bonds. Various control theories have been developed to achieve this “selective bond-breaking”. The intuitive Tannor–Rice–Kosloff scheme employs the explicit time-dependence of wave packets prepared by ultrashort laser pulses [12, 13]. Starting from an initial state ψ_0, a first pulse excites the molecule. The branching ratio between competing reaction channels of the system can be controlled by timing a second laser pulse correctly. Figure 2 illustrates the excitation scheme. After the excitation, dynamical processes take place in the excited state ($\psi^*(t)$). Depending on the system's properties, a second laser excitation taking place at different times T_1, T_2 is able to produce alternatively products of type (1) or (2).

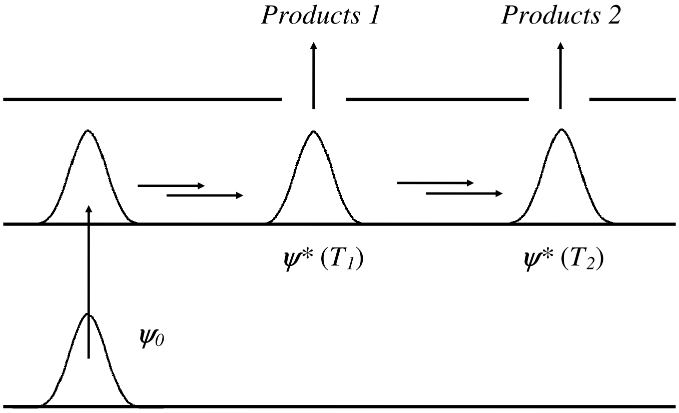

Figure 2: *Tannor – Rice – Kosloff scheme: After a first excitation, a second laser pulse fired at different times populates one or the other reaction channel.*

Within the STIRAP (acronym for “stimulated Raman adiabtic passage”) method a population transfer is performed employing time-delayed pulses in a counter-intuitive sequence [14]. Thereby, the population in the excited state $|2\rangle$ in the so-called Λ- configuration (see fig. 3) is negligible for all times. In a physical picture, this strong-field phenomenon is explained with a strong perturbation induced by the first pulse, the Stokes pulse, inducing the formation of new “field-

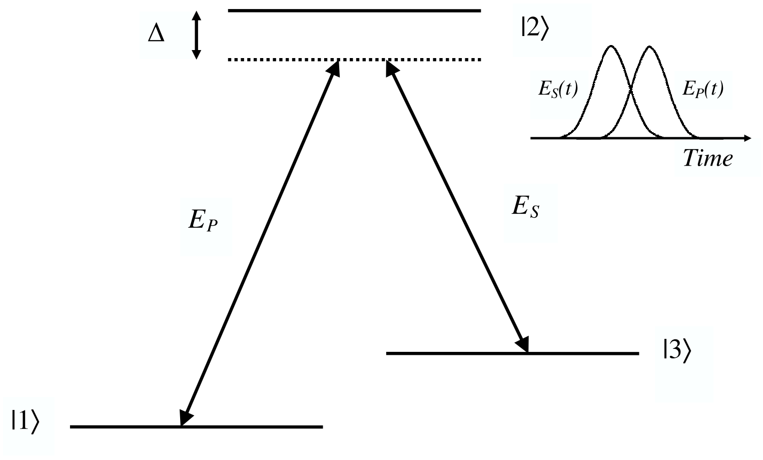

Figure 3: *Population transfer for a three-level system in the so-called* Λ*-configuration. Two pulses in a counter-intuitive pulse sequence, pump- (*$E_P(t)$*) and Stokes-pulse* $E_S(t)$ *couple the three levels, as indicated. Within the STIRAP-process the excited state* $|2\rangle$ *which may be not resonantly accessible because of an energy detuning* Δ *is not populated remarkably at all times.*

dressed" states. The second pulse, the pump-pulse, then transfers population along one of these states, avoiding the excited state $|2\rangle$.

Brumer and Shapiro developed a method to control reaction yields via interference effects of phase-varied laser pulses [15, 16]. Competing multiphoton pathways to access a final state are marked with a phase difference which then leads to an interference – very much like in Young's double-slit experiment.

Variationally derived control fields relying on an overlap of a system's wavefunction with a target state being maximized, are iteratively determined within optimal control theory [17, 18]. Therefore, the system's initial state is forward propagated while, with the backward propagated target state the time-dependent overlap of the states is used to construct the electric field.

In a combination of pulse-shaping techniques and feedback from a (measured or calculated) signal, control fields can be obtained adapting genetic algorithms [19]. Starting from a random distribution, the driving field is determined by random modification of parameters in terms of the biological evolution in a parallel search.

In most of the above described techniques, the derived control fields are difficult to interpret in terms of the system's properties. In order to gain insight into the entanglement of the applied perturbation and the molecular dynamics, an algorithm is developed within this work which determines the control fields from the instantaneous response of the system. This extents early work of Tannor and others [20–23].

The principle can be visualized in regarding a classical particle moving along a trajectory in an anharmonic potential. An increase of the particle's energy as a function of time is achieved if an external field is constructed propotional to the instantaneous momentum of the particle. In contrary, the particle's energy decreases in choosing the external field to be phase shifted to the momentum. Figure 4 illustrates the case where a heating of a particle moving in a Morse potential occurs. The particle's energy increases in a Morse potential (panel (a)) and the trajectory (panel (b)), as well as the field, driving the system in resonance is shown (panel (c)).

The such established "principle of instantaneous control" is applied to various molecular processes in this work [24–26]. Therefore, different objectives are defined as the energy transfer in double well potentials, the excitation and dissociation of selective vibrational modes, and also the population transfer between molecular electronic states.

This work is organized as follows: The first three chapters summarize the employed theoretical (chapter 1) and numerical methods (chapter 2), as well as several control theories (chapter 3).

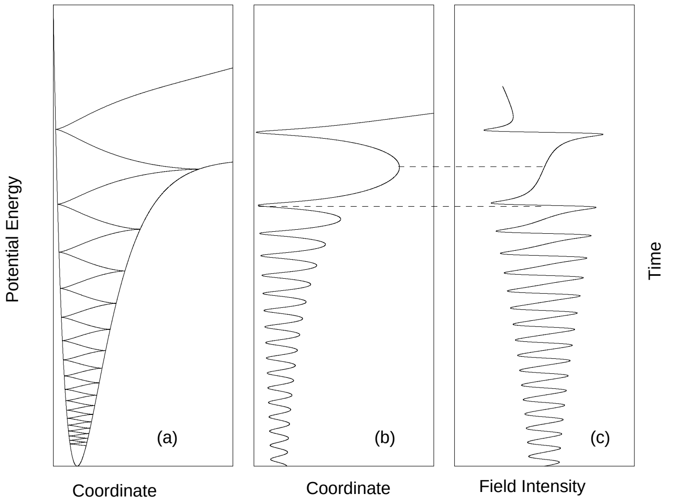

Figure 4: *Panel (a): A classical particle's trajectory in a Morse potential; panel (b) displays the trajectory depending on time, driven by a control field in panel (c). The dashed lines indicate times where the trajectory is at a classical turning point, and the electric field is zero.*

The application of the instantaneous response algorithm to energy transfer problems is presented in chapter 4. Relating the control fields to the vibrational dynamics, it is shown that taylored IR-fields are able to effectively heat or cool molecules.

Selective mode excitation leading to dissociation is studied for the HOD-molecule in chapter 5. Here, control fields are constructed to break one or the other bond within the electronic ground state.

The population transfer via non-resonant excitation into excited electronic states is investigated in chapter 6. Here, the control fields derived from optimal control theory, genetic algorithms and the instantaneous response are compared for a model system representing methyl iodide.

Chapter 7 investigates selective population transfer in the sodium dimer. The structure of the control fields is related to the vibrational and electronic dynamics of the molecule. Orientational as well as field–strength effects are examined and time–resolved pump/probe spectroscopy is shown to yield information about the efficiency of control processes [27].

In cooperation with experimental investigations on molecular iodine, a STIRAP-like technique is transferred into the femtosecond–regime. It is shown that field dressed states and an adiabatic description are proper tools in characterizing population transfer into highly excited vibrational eigenstates without populating an excited electronic state remarkably. The motivation is to initiate a ground state dynamics on a time scale much faster than those of decoherence processes.

Chapter 1

Theory

1.1 Dynamical Equations

The dynamical properties of a system can be described within two different formalisms, the latter being classical mechanics and quantum mechanics. For macroscopic systems the methods of classical mechanics are appropiate, while these approaches are likely to fail for atoms and molecules because of their quantum mechanical attributes. In this section the classical and quantum dynamical equations of motion and their solutions will be reviewed. The equations are generally given for vectors if not denoted differently.

1.1.1 Classical Dynamics

Molecular dynamics (MD) methods employ the equations of classical mechanics to determine the properties of a system. Considering a particle with mass m and generalized coordinate x, the Lagrangian function $\mathcal{L}$, defined as the difference between the kinetic T and the potential energy V reads [28, 29]

$$\mathcal{L} = \frac{m}{2}\dot{x}^2 - V(x), \tag{1.1}$$

where $\dot{x}$ is the time derivative of x. The resulting (Lagrangian) equation of motion then is

$$\frac{d}{dt}\left(\frac{\partial \mathcal{L}}{\partial \dot{x}}\right) - \frac{\partial \mathcal{L}}{\partial x} = 0. \tag{1.2}$$

To ease the transition to quantum mechanics, Hamiltons formulation is adopted in defining the momenta p

$$p = \frac{\partial \mathcal{L}}{\partial \dot{x}}. \tag{1.3}$$

The Hamilton function $\mathcal{H}$, the sum of kinetic and potential energy ($\mathcal{H} = T + V$), is related to $\mathcal{L}$ via a Legendre transformation:

$$\mathcal{H} = \mathcal{H}(x, \dot{x}, p) = p\dot{x} - \mathcal{L}(x, \dot{x}, t). \tag{1.4}$$

The canonical or Hamilton's equations of motion read:

$$\frac{\partial \mathcal{H}}{\partial p} = \dot{x}; \quad \frac{\partial \mathcal{H}}{\partial x} = -\dot{p}. \tag{1.5}$$

The Hamilton function describes the system's energy. For $\dot{\mathcal{H}} = 0$, energy conservation law applies. In the case of a time-dependent external potential, e.g. a classical laser field acting on the system, the equations of motion are, in general, solved numerically (see chapter 2). For an ensemble of particles a trajectory ensemble $\{x_i\}$ can be propagated and statistically weighted with a probability P_i to construct a classical density $\rho(t)$. Depicting the classical density, each x_i is smoothed by a (Gaussian) distribution around this particular point

$$\rho(x,t) = \sum_i e^{-\beta(x-x_i)^2} P_i. \tag{1.6}$$

The classical density's motion is expressed by the classical Liouville equation

$$\frac{d\rho}{dt} \quad = \quad \frac{\partial \rho}{\partial t} + \left[\frac{\partial \rho}{\partial x_i}\dot{x}_i + \frac{\partial \rho}{\partial p_i}\dot{p}_i\right]$$

$$= \quad \frac{\partial \rho}{\partial t} + \left[\frac{\partial \rho}{\partial x_i} \frac{\partial \mathcal{H}}{\partial p_i} - \frac{\partial \rho}{\partial p_i} \frac{\partial \mathcal{H}}{\partial x_i} \right] = 0. \tag{1.7}$$

As the density ρ does not change along a trajectory, the total time derivative of the density vanishes. Therefore, the equation of motion can be re-written using poisson brackets

$$\frac{\partial}{\partial t} \rho = - \{\rho, \mathcal{H}\} \tag{1.8}$$

For a density describable by a δ-function, eq. (1.8) transforms to Newton's equations of motion [30].

1.1.2 Quantum Dynamics

The Hamiltonian formulation of classical dynamics can be transferred to quantum dynamics by some modifications [31]. A similar picture as the classical density can be regarded for a quantum mechanical description if assigning the classical variables to corresponding quantum mechanical operators (principle of correspondence). Operators representing physical observables have to be Hermitian. The vectors $x_i(t)$ are assigned to the complex linear vectors $|\psi(x,t)_i\rangle$ describing a state in Hilbert space (Born's proposal) [32]. The corresponding equation of motion for the state vectors describing a quantum mechanical system is the time-dependent Schrödinger equation

$$i\hbar \frac{\partial}{\partial t} |\psi(t)\rangle = (T + V)\; |\psi(t)\rangle = \mathcal{H}\, |\psi(t)\rangle, \tag{1.9}$$

where $\mathcal{H}$ is the quantum mechanical Hamiltonian. Its precise form (within the Born-Oppenheimer approximation) will be described in the next subsection, since for molecules in a quantum mechanical picture, as treated here, it is in general difficult to examine the dynamics of nuclei and electrons simultaneously.

In order to describe a quantity in analogy to the classical picture, a density operator ρ is defined

$$\rho(t) \equiv |\psi(t)\rangle\langle\psi(t)|. \tag{1.10}$$

Therefore, the quantum mechanical analogon of the classical density, the density matrix, can be written as

$$\rho(x,t) = \sum_i P_i \, \langle x|\psi_i(t)\rangle \, \langle\psi_i(t)|x\rangle, \tag{1.11}$$

with the probability distribution P_i. Integration over a volume V yields

$$\int_V \frac{\partial}{\partial t}\rho \, dx = \frac{d}{dt}\int_V \rho \, dx = 0, \tag{1.12}$$

where the divergence theorem was used. Eq. (1.12) describes the global conservation property, meaning that the integral of $|\psi|^2$ is independent of time - or rescaling for $V \rightarrow R^3$ (Hilbert space)

$$\int_{R^3} |\psi|^2 dx = 1. \tag{1.13}$$

The corresponding equation of motion (Liouville – Von Neumann equation) for the density matrix is

$$\frac{\partial}{\partial t}\rho = -\frac{i}{\hbar} \, [\mathcal{H}, \rho] \, . \tag{1.14}$$

Thereby, $i/\hbar$ times the commutator is used in analogy to the poisson brackets of classical mechanics. In the case of a pure state ($P_i = \delta_{i1}$ in eq. (1.11), $|\psi_1\rangle$) the system is uniquely described (within non-relativistic quantum mechanics) by the time-dependent Schrödinger equation. The solutions of eq. (1.9) can be represented in the complete and orthonormal basis set consisting of eigenvectors $|\phi_n\rangle$

of $\mathcal{H}$ having energies E_n defined by the time-independent Schrödinger equation

$$\mathcal{H}|\phi_n\rangle = E_n|\phi_n\rangle. \tag{1.15}$$

Thus one obtains:

$$|\psi(t)\rangle = \sum_n |\phi_n\rangle\langle\phi_n|\psi(t)\rangle. \tag{1.16}$$

The time evolution can be expressed by a time evolution operator $U(t, t_0)$

$$U(t, t_0) = \sum_n |\phi_n\rangle e^{-i/\hbar E_n(t-t_0)}\langle\phi_n|. \tag{1.17}$$

Expanding an arbitrary function $f(\mathcal{H})$ into a Taylor series one obtains

$$\begin{aligned} f(\mathcal{H}) &= \sum_{i=0}^{\infty} \frac{f^{(i)}(0)}{i!}\mathcal{H}^i \\ f(\mathcal{H})|\phi_j\rangle &= \sum_{i=0}^{\infty} \frac{f^{i}(0)}{i!}\mathcal{H}_j^i|\phi_j\rangle \equiv f(E_j)|\phi_j\rangle \\ \Rightarrow U(t, t_0) &= e^{-i/\hbar\mathcal{H}(t-t_0)}. \end{aligned} \tag{1.18}$$

The above specified propagator is only valid for time-independent Hamiltonians. Including a classical external radiation field the Hamiltonian becomes time-dependent and the propagator is of a different form. Employing a classical approximation (see next section) for the field-matter coupling term $W(t)$ yields

$$\mathcal{H}(t) = \mathcal{H}_0 + W(t). \tag{1.19}$$

A differential equation for the propagator can be derived when inserting the time evolution $|\psi(t)\rangle = U(t, t_0)\,|\psi(t_0)\rangle$ into the time-dependent Schrödinger equation

$$\frac{\partial}{\partial t}U(t, t_0)\,|\psi(t_0)\rangle = -\frac{i}{\hbar}\,\mathcal{H}(t)\,U(t, t_0)\,|\psi(t_0)\rangle. \tag{1.20}$$

As this equation is valid for any $|\psi(t_0)\rangle$ the propagator must also satisfy

$$\frac{\partial}{\partial t} U(t,t_0) = -\frac{i}{\hbar}\, \mathcal{H}(t)\, U(t,t_0). \tag{1.21}$$

Integrating the differential equation from time t_0 to t together with the initial condition $U(t_0,t_0) = 1$ results in the integral equation

$$U(t,t_0) = 1 - \frac{i}{\hbar} \int_{t_0}^{t} d\tau\, \mathcal{H}(\tau)\, U(\tau,t_0) \tag{1.22}$$

which can be solved iteratively leading to the Dyson-series

$$U(t,t_0) = 1 + \sum_{n=1}^{\infty} \left(-\frac{i}{\hbar}\right)^n \int_{t_0}^{t} d\tau_n \int_{t_0}^{\tau_n} d\tau_{n-1} \cdots \int_{t_0}^{\tau_2} d\tau_1 \mathcal{H}(\tau_n)\mathcal{H}(\tau_{n-1}) \cdots \mathcal{H}(\tau_1). \tag{1.23}$$

Here the time variables are fully ordered $t \geq \tau_n \geq \cdots \geq \tau_1 \geq t_0$ (for commutating Hamiltonians the time-ordering would be of no relevance) and the positive time-ordered exponential can equivalently be denoted as

$$U(t,t_0) = \exp_+ \left[-\frac{i}{\hbar} \int_{t_0}^{t} d\tau\, \mathcal{H}(\tau) \right]. \tag{1.24}$$

1.1.3 Born-Oppenheimer Approximation

The Hamiltonian describing a molecular system (neglecting spin-orbit interactions) is given as [33]

$$\mathcal{H} = T_{\mathrm{e}}(x) + T_{\mathrm{n}}(R) + V(x,R), \tag{1.25}$$

where x, R denote the electronic and nuclear coordinates, respectively. The kinetic energy operators of electrons $T_e(x)$ and nuclei $T_n(R)$, and the potential energy operator $V(x,R)$ for a Coulomb system without external forces can be identified as follows

$$\begin{aligned}
T_{\mathrm{e}}(x) &= -\frac{\hbar^2}{2m_e}\sum_i \nabla_i^2 \\
T_{\mathrm{n}}(R) &= -\sum_\alpha \frac{\hbar^2}{2M_\alpha}\nabla_\alpha^2 \\
V(x,R) &= \sum_i\sum_{j>i}\frac{e^2}{4\pi\varepsilon_0\,|x_i-x_j|}+\sum_\alpha\sum_{\beta>\alpha}\frac{e^2 Z_\alpha Z_\beta}{4\pi\varepsilon_0\,|R_\alpha-R_\beta|} \\
&- \sum_i\sum_\alpha\frac{e^2 Z_\alpha}{4\pi\varepsilon_0\,|x_i-R_\alpha|}.
\end{aligned} \tag{1.26}$$

The equations above contain m_e, M_α, the electron's and nuclei' masses, the gradients $\nabla_i = \partial/\partial x$, $\nabla_\alpha = \partial/\partial R$, and the indices $(i,j),(\alpha,\beta)$ numbering electrons and nuclei, respectively. Expanding the complete wave function $\psi(x,R)$ into a basis of electronic wave functions $\varphi_i(x,R)$ yields

$$\psi_{\mathrm{tot}}(x,R) = \sum_i \varphi_i(x,R)\,\chi_i(R), \tag{1.27}$$

with the expansion coefficients $\chi_i(R)$ representing functions of the nuclear coordinates. The electronic wave functions are solutions of the electronic Schrödinger equation

$$\mathcal{H}_{\mathrm{e}}(x,R)\,\varphi_i(x,R) = \epsilon_i(R)\,\varphi_i(x,R). \tag{1.28}$$

Here, i is the electronic quantum number of the electronic state. The $\epsilon_i(R)$ are the potential curves parameterically depending on the nuclear coordinates, and $H_e(x,R)$ denotes the electronic Hamiltonian

$$\mathcal{H}_{\mathrm{e}}(x,R) = T_{\mathrm{e}}(x) + V(x,R), \tag{1.29}$$

so that

$$\mathcal{H}_{\mathrm{tot}} = T_{\mathrm{n}}(R) + \mathcal{H}_{\mathrm{e}}. \tag{1.30}$$

Inserting the basis set expansion into the Schrödinger equation yields

$$\sum_i (T_{\mathrm{n}} + \mathcal{H}_{\mathrm{e}})\ \varphi_i(x,R)\,\chi_i(R) = E_{tot} \sum_i \varphi_i(x,R)\,\chi_i(R). \tag{1.31}$$

As the kinetic energy operator is a differential operator it transforms the coupled equations

$$\begin{aligned}
\sum_i \left(\sum_\alpha \frac{-\hbar^2}{2M_\alpha} \nabla_\alpha^2 + \mathcal{H}_{\mathrm{e}} \right) \varphi_i\,\chi_i &= E_{\mathrm{tot}} \sum_i \varphi_i\,\chi_i \\
\sum_i \left\{ \sum_\alpha \frac{-\hbar^2}{2M_\alpha} \nabla_\alpha^2 \,(\varphi_i\,\chi_i) + \mathcal{H}_{\mathrm{e}}\,\varphi_i\,\chi_i \right\} &= E_{\mathrm{tot}} \sum_i \varphi_i\,\chi_i \\
\sum_i \left\{ \sum_\alpha \frac{-\hbar^2}{2M_\alpha} \nabla_\alpha \left[(\varphi_i \nabla_\alpha\,\chi_i) + (\chi_i \nabla_\alpha\,\varphi_i) \right] + \chi_i \mathcal{H}_{\mathrm{e}}\,\varphi_i \right\} &= E_{\mathrm{tot}} \sum_i \varphi_i\,\chi_i \qquad (1.32) \\
\sum_i \left\{ \sum_\alpha \frac{-\hbar^2}{2M_\alpha} \varphi_i \left(\nabla_\alpha^2\,\chi_i \right) + \sum_\alpha \frac{-\hbar^2}{M_\alpha} \left(\nabla_\alpha\,\varphi_i \right) \left(\nabla_\alpha\,\chi_i \right) \right. & \\
\left. + \sum_\alpha \frac{-\hbar^2}{2M_\alpha} \chi_i \left(\nabla_\alpha^2\,\varphi_i \right) + \chi_i\,\epsilon_i\,\varphi_i \right\} &= E_{\mathrm{tot}} \sum_i \varphi_i\,\chi_i
\end{aligned}$$

Projection on the basis vector $\langle \varphi_j |$ results in the coupled set of equations:

$$\begin{aligned}
\sum_\alpha \frac{-\hbar^2}{2M_\alpha} \nabla_\alpha^2\,\chi_j + \epsilon_j\,\chi_j + \sum_i \left\{ \sum_\alpha \frac{-\hbar^2}{M_\alpha} \langle \varphi_j\,| \nabla_\alpha |\,\varphi_i \rangle \,(\nabla_\alpha \chi_i) \right. & \\
\left. + \sum_\alpha \frac{-\hbar^2}{2M_\alpha} \langle \varphi_j \left| \nabla_\alpha^2 \right| \varphi_i \rangle\,\chi_i \right\} &= E_{\mathrm{tot}}\,\chi_j. \qquad (1.33)
\end{aligned}$$

In equation (1.33), the electronic wave functions are comprised in the terms inside of the curly brackets, kinetically coupling different electronic states. Within the adiabatic approximation off-diagonal kinetic coupling terms (first and second order non-adiabatic coupling elements) are neglected, leading to a separation of electronic and nuclear degrees of freedom. For the electronic eigenstates being real functions, the diagonal non-adiabatic coupling elements ($\langle \varphi_j | \nabla_\alpha | \varphi_j \rangle$) are likewise zero using the orthonormality condition. Equation (1.33) then reads as

$$\begin{aligned}\left(\sum_\alpha \frac{-\hbar^2}{2M_\alpha}\nabla_\alpha^2 + \epsilon_j + \sum_\alpha \frac{-\hbar^2}{2M_\alpha}\langle\varphi_j\left|\nabla_\alpha^2\right|\varphi_j\rangle\right)\chi_j = E_{\text{tot}}\chi_j \\ \left(T_n + \epsilon_j + \sum_\alpha \frac{-\hbar^2}{2M_\alpha}\langle\varphi_j\left|\nabla_\alpha^2\right|\varphi_j\rangle\right)\chi_j = E_{\text{tot}}\chi_j,\end{aligned} \tag{1.34}$$

where in the second equation the kinetic energy operator was re-introduced. The matrix elements $\frac{-\hbar^2}{2M_\alpha}\langle\varphi_j|\nabla_\alpha^2|\varphi_j\rangle$ are known as the diagonal correction, being smaller than ϵ_j because the masses of the nuclei enter into the denominator. In the Born-Oppenheimer approximation [34] these slowly in R varying functions are neglected and the energy surface is solely determined by ϵ_j. Thus the Schrödinger equation for the nuclear motion in state j reads:

$$\left[T_{\text{n}} + \epsilon_j(R)\right]\chi_j(R) = E_{\text{tot}}\chi_j(R), \tag{1.35}$$

where the electronic energy ϵ_j represents the potential energy surface in the electronic state j.

1.2 Design of Electro-Magnetic Fields

The exact form of the Hamiltonian in eq. (1.19) can be derived from field quantization in quantum electrodynamics. Regarding the field-matter interaction of a particle with mass m and charge q in an electromagnetic field given by [35, 36]

$$E = -\frac{1}{c}\frac{\partial A}{\partial t} - \nabla\Phi \qquad ; \qquad B = \nabla \times A \tag{1.36}$$

where E is the electric field with vector potential A and scalar potential Φ, and B represents the magnetic field, results in a Hamiltonian

$$\mathcal{H} = \frac{1}{2m}\left(p - \frac{q}{c}A(x,t)\right)^2 + q\,\Phi(x,t). \tag{1.37}$$

The canonical momentum p is replaced by the kinetical momentum operators $m\dot{x} = p - q/cA$ whose commutators satisfy slightly different conditions ($[x_i, m\dot{x}_j] = i\hbar\delta_{ij}$, $[m\dot{x}_i, m\dot{x}_j] = i\hbar q\epsilon_{ijk}B_k$). In the limit of large photon numbers the electric field can be treated classically and described as

$$E(x,t) = E_0\,f(t)\left[e^{ikx-i\omega t} + e^{-ikx+i\omega t}\right]. \tag{1.38}$$

with the pulse envelope $f(t)$, and E_0 is half of the field strength. The first term in eq. (1.38) corresponds to light absorption and the second to light emission. Since usually molecules are much smaller than the optical wavelength of an external field, the dipole approximation can be adopted which amounts to a neglection of the position dependency, i.e.:

$$E(t) = E_0 f(t)\left[e^{-i\omega t} + e^{+i\omega t}\right]. \tag{1.39}$$

Therefore, the form of the external coupling $W(t)$ introduced in the last section can be denoted as the projection of the electric field vector $E(t)$ onto the system's dipole moment μ,

$$W(x,t) = -\mu\,E(t). \tag{1.40}$$

The laser fields used and calculated in this work are often composed of different frequencies (shaped) or are modulated in frequency- or time domain. Electric fields in time $E(t)$ and frequency domain $E(\omega)$ are connected by the Fourier relation [37]

$$
\begin{aligned}
E(t) &= \frac{1}{\sqrt{2\pi}} \int_{-\infty}^{\infty} \tilde{E}(\omega)\, e^{i\omega t} d\omega \\
\tilde{E}(\omega) &= \frac{1}{\sqrt{2\pi}} \int_{-\infty}^{\infty} E(t)\, e^{-i\omega t} dt
\end{aligned}
\tag{1.41}
$$

Since $E(t)$ is always a real quantity the relation in frequency domain is symmetric $\tilde{E}(-\omega) = \tilde{E}^*(\omega)$. For a full characterization of the electric field it is sufficient to regard positive frequencies. The related (complex) temporal fields can be written for positive and negative ω

$$
\begin{aligned}
E^+(t) &= \frac{1}{\sqrt{2\pi}} \int_{0}^{\infty} \tilde{E}(\omega)\, e^{i\omega t} d\omega \\
E^-(t) &= \frac{1}{\sqrt{2\pi}} \int_{-\infty}^{0} E(\omega)\, e^{-i\omega t} d\omega.
\end{aligned}
\tag{1.42}
$$

Therefore, $E^-(t) = [E^+(t)]^*$, and $E(t) = E^+(t) + E^-(t) = 2\Re\left(E^+(t)\right)$. For further calculations it is advantageous to regard the $E^+(\omega)$, as only $\omega \geq 0$ is physically meaningful. These fields can be described by an envelope function $f(t)\,(g(\omega))$ and a phase $\varphi(t)\,(\phi(\omega))$. Mathematically a phase modulation is implemented by expanding the time-dependent phase $\varphi(t)$ into a Taylor series:

$$
\varphi(t) = \omega(t_0) + \left.\frac{\partial\varphi(t)}{\partial t}\right|_{t_0} (t - t_0) + \frac{1}{2}\left.\frac{\partial^2\varphi(t)}{\partial t^2}\right|_{t_0} (t - t_0)^2 + \cdots,
\tag{1.43}
$$

where the first term is the constant phase of the field, the second indicates the carrier frequency, and the third one is a linear chirp in time domain. Higher order terms in general are called (n-1) order chirps. Pulses with temporally increasing frequency, exhibiting a positive linear chirp are called up-chirped pulses; the opposite behaviour is called down-chirped, accordingly. Introducing a time-domain chirp changes the spectral distribution of the pulse, not corresponding to the experimental setup where the spectral width remains constant and chirping is performed in frequency domain (e.g. routing the pulse through dispersive media or grating dispersion). Expanding the frequency dependent phase into a Taylor series leads to [38, 39]:

$$\phi(\omega) = \phi(\omega_0) + \alpha_1 \left.\frac{\partial \phi(\omega)}{\partial \omega}\right|_{\omega_0} (\omega - \omega_0) + \alpha_2 \left.\frac{\partial^2 \phi(\omega)}{\partial \omega^2}\right|_{\omega_0} (\omega - \omega_0)^2 + \cdots . \tag{1.44}$$

Analogously, the constant term determines the position in time domain, the second term indicates a temporal displacement and the third one displays a linear chirp in frequency domain. A linear dependency (i.e. only the first and second term contribute) is again called unchirped in frequency domain. The appearence of pulses in the particular domain after a Fourier transform is not easy to derive. Nevertheless, from symmetry it can be said that a pulse possessing an asymmetric distribution in one domain cannot be unchirped in the other. An important case is a Gaussian laser pulse

$$\begin{aligned} E^+(t) &= \frac{E_0}{2}\, e^{-2\ln 2 \cdot t^2/\tau^2} \cdot e^{i\omega_0 t} && (1.45)\\ \tilde{E}^+(\omega) &= E_0\, \tau \sqrt{\frac{\pi}{4\ln 2}}\, e^{-\tau^2(\omega-\omega_0)^2/(8\ln 2)}, && (1.46) \end{aligned}$$

where τ is the pulse duration, the width at half maximum of the intensity-envelope function $I(t) = \epsilon_0 E(t)^2$, and ω_0 is the carrier frequency. A special feature of Gaussian pulses is that, applying a linar chirp in frequency domain $1/2\, \phi''(\omega_0) \cdot (\omega - \omega_0)$, also implies a linear chirp in time domain. The resulting fields have the analytical form

$$\begin{aligned} E^+(t) &= \frac{E_0}{2\gamma^{1/4}}\, e^{-t^2/4\beta\gamma} \cdot e^{i(\delta t^2 - \epsilon)} \cdot e^{i\omega_0 t} && (1.47)\\ \tilde{E}^+(\omega) &= E_0 \tau \sqrt{\frac{\pi}{4\ln 2}}\, e^{-\tau^2(\omega-\omega_0)^2/(8\ln 2)} \cdot e^{i(\omega-\omega_0)^2 \phi''/2}, && (1.48) \end{aligned}$$

with

$$\beta = \frac{\tau^2}{8\ln 2}, \qquad \gamma = 1 + \frac{\phi''^2}{4\beta^2}, \qquad \delta = \frac{\phi''}{8\beta^2\gamma} \qquad \epsilon = 1/2\arctan(\frac{\phi''}{2\beta}). \tag{1.49}$$

The temporal broadening as a result of the linear chirp in frequency domain is expressed in

$$\frac{\tau_2}{\tau_1} = \sqrt{1 + \left(\frac{\phi'' 4\ln 2}{\tau_1^2}\right)^2}. \tag{1.50}$$

It can be seen that the pulse duration for a chirped pulse (τ_2) depends on one hand on the chirp ϕ'' and on the other, on the pulse duration of the unchirped pulse (τ_1). The resulting broadening has been calculated for Gaussian pulses before and can be taken from tables in the literature [38].

1.3 Weak Field Regime: Time-Dependent Perturbation Theory

Perturbation theory is appropriate for the description of systems with a weak time-dependent interaction $\epsilon\, V(t)$ in the Hamiltonian of eq. (1.19), with ϵ being a small dimensionless parameter [31]. For times $t < t_0$, the perturbation $V(t) = 0$ and the system is in an initial state $|\psi(t_0)\rangle$ satisfying the Schrödinger equation

$$i\hbar\frac{\partial}{\partial t}|\psi(t_0)\rangle = \mathcal{H}_0\, |\psi(t_0)\rangle. \tag{1.51}$$

When the perturbation sets in, a new state $|\psi(t)\rangle$ develops fulfilling the new Schrödinger equation

$$i\hbar\frac{\partial}{\partial t}|\psi(t)\rangle = [\mathcal{H}_0 + \epsilon V(t)]\, |\psi(t)\rangle, \tag{1.52}$$

with the initial condition $|\psi(t)\rangle = |\psi(t_0)\rangle$ for $t \leq t_0$. The temporal development of the wave function can be described with the afore defined propagator in eq. (1.18)

$$|\psi(t)\rangle = U(t,t_0)\,|\psi(t_0)\rangle, \tag{1.53}$$

where $U(t,t_0)$ satisfies eq. (1.21). For $\epsilon V(t)$ is assumed to be a small perturbation, the propagator U can be expressed differing only by a small amount from the unperturbed propagator U_0. One then writes

$$U = U_0\,W, \tag{1.54}$$

where W is an unitary operator implicating the interaction effects. Inserting the form of U from eq. (1.54) into the Schrödinger equation eq. (1.21) yields

$$i\hbar\frac{\partial}{\partial t}W(t,t_0) = \epsilon\,U_0^\dagger(t-t_0)\,V(t)\,U_0(t-t_0)W(t,t_0). \tag{1.55}$$

Combining

$$U_0^\dagger(t-t_0)\,V(t)\,U_0(t-t_0) \equiv V_{int}(t,t_0), \tag{1.56}$$

the solutions of $W(t,t_0)$ can be expanded into a series

$$W(t,t_0) \sim \sum_{n=0}^{\infty} \epsilon^n\,W_n(t,t_0). \tag{1.57}$$

Time integration of the resulting recursive set of differential equations for $n \geq 0$:

$$i\hbar\frac{\partial}{\partial t}W_{n+1}(t,t_0) = V_{int}(t,t_0)W_n(t,t_0), \tag{1.58}$$

and the intial condition $W(t_0,t_0) = 1$ yields terms of n^{th} order, each form given by the previous equation

$$W_1(t,t_0) \;=\; \frac{1}{i\hbar}\int_{t_0}^{t} V_{int}(\tau,t_0)\,d\tau \tag{1.59}$$

$$\begin{aligned} W_2(t,t_0) &= \frac{1}{i\hbar}\int_{t_0}^{t} V_{int}(\tau,t_0)\,W_1(\tau,t_0)\,d\tau \\ &\vdots \\ W_{n+1}(t,t_0) &= \frac{1}{i\hbar}\int_{t_0}^{t} V_{int}(\tau,t_0)\,W_n(\tau,t_0)\,d\tau. \end{aligned}$$

The integral equation results in the Dyson series; its solutions can be obtained via iterative insertion of term n into $n+1$. Later, we will refer to cases where the series can be truncated after the first term, describing first-order transitions.

1.3.1 Fermi's Golden Rule

The probability amplitude of a transition under the action of a weak external potential $\epsilon V(t)$ starting from a system in an eigenstate $|i(t_0)\rangle$, whose temporal development can be expressed according to eq. (1.17), into a final state $|f(t)\rangle$ is given by [31]

$$\begin{aligned} A_{i\to f}(t,t_0) &= \langle f|U(t,t_0)|i\rangle \\ &= e^{-i/\hbar E_f(t-t_0)}\langle f|W(t,t_0)|i\rangle. \end{aligned} \tag{1.60}$$

The last integral term can be calculated within first-order perturbation theory:

$$\begin{aligned} \langle f|W(t,t_0)|i\rangle &= \langle i|f\rangle + \frac{\epsilon}{i\hbar}\int_{t_0}^{t}\langle f|V_{int}(\tau,t_0)|i\rangle\,d\tau + O(\epsilon^2) \\ &= \delta_{if} + \frac{\epsilon}{i\hbar}\int_{t_0}^{t} e^{i/\hbar(E_f-E_i)(\tau-t_0)}\langle f|\mu V(\tau)|i\rangle\,d\tau + O(\epsilon^2). \end{aligned} \tag{1.61}$$

Because the transition probability is the absolute square of the transition amplitude and defining the transition frequency $\omega_{fi} = (E_f - E_i)/\hbar$, the expression reads as

$$|A(t)|^2 = \frac{\epsilon^2}{\hbar^2}\left|\int_{t_0}^{t} e^{i\omega_{fi}(\tau-t_0)}\langle f|V(\tau)|i\rangle d\tau\right|^2. \tag{1.62}$$

Considering an absorption process with $V(t) \approx \mu \exp(-i\omega t)$ and real eigenstates $|i\rangle, |f\rangle$ the transition probability can be expressed as

$$|A(t)|^2 = \frac{\epsilon^2}{\hbar^2} \left[\frac{\sin[(\omega - \omega_{fi})t/2]}{(\omega - \omega_{fi})/2} \right]^2 |\langle f|\mu|i\rangle|^2 . \tag{1.63}$$

The expression in the squared brackets is related to the δ function via

$$\lim_{T\to\infty} \frac{\sin^2 \alpha T}{\alpha^2 T} = \pi\delta(\alpha), \tag{1.64}$$

so for long times the transition probability is given by

$$\lim_{T\to\infty} |A_{i\to f}(T)|^2 = t\frac{2\pi}{\hbar}\delta(\hbar\omega + E_f - E_i) \, |\langle f|\mu|\epsilon i\rangle|^2 . \tag{1.65}$$

Therefore, the transition rate Γ_{if} (transition probability per time) can evaluated:

$$\Gamma_{if} \equiv \frac{2\pi}{\hbar}\delta(\hbar\omega + E_f - E_i) \, |\langle f|\mu|\epsilon i\rangle|^2 . \tag{1.66}$$

For a transition from a discrete initial to a final state in a continuous spectrum the above equation has to be integrated taking into account the density of states $\varrho(E_f)$. The number of eigenstates in the interval dE_f is calculated from the density of states for $\varrho(E_f)dE_f$ and the transition rate is

$$\sum_f \Gamma_{if} \sim \int dE_f \varrho(E_f)\Gamma_{if} = \varrho(E_i)\frac{2\pi}{\hbar} \, |\langle f|\mu|i\rangle|^2 . \tag{1.67}$$

Eq.(1.67) is the expression for Fermis golden rule.

1.4 Strong Field: Rabi Oscillations

The strong coupling of a two-level system with the eigenstates $|\varphi_a\rangle, |\varphi_b\rangle$ with an external radiation field cannot be described by perturbation theory. The state vector $|\psi(t)\rangle$ of this system is [36, 40]

$$|\psi(t)\rangle = C_a(t)|\varphi_a\rangle + C_b|\varphi_b\rangle. \tag{1.68}$$

The coefficients C_a, C_b describe the probability amplitudes of finding the system in the particular state. The time-dependent Schrödinger equation (eq.(1.9)) describes the temporal development of $|\psi(t)\rangle$ containing a total Hamiltonian $\mathcal{H}$

$$\mathcal{H} = \mathcal{H}_0 + W(t), \tag{1.69}$$

where $\mathcal{H}_0$ is the unperturbed part with the eigenstates $|\varphi_a\rangle, |\varphi_b\rangle$ and the eigenenergies $\varepsilon_a, \varepsilon_b$. The interaction part can be written as [36]

$$W(t) = -\mu_{ab} E(t). \tag{1.70}$$

Here, μ_{ab} denotes the matrix element of the electric dipole moment $e\langle\varphi_a|x|\varphi_b\rangle$ and the electric field, linearly polarized along the molecule's (x-) axis can be written, within the dipole approximation, as

$$E(t) = E_0 \cos \omega t \tag{1.71}$$

with the amplitude E_0 and the frequency ω. The equations of motion for C_a, C_b are obtained as

$$\dot{C}_a = -i/\hbar\, \varepsilon_a C_a + i\Omega_R \cos \omega t\, C_b \tag{1.72}$$

$$\dot{C}_b = -i/\hbar\, \varepsilon_b C_b + i\Omega_R \cos \omega t\, C_a. \tag{1.73}$$

In above equation, Ω_R is the Rabi frequency, defined as

$$\Omega_R \equiv \frac{|\mu_{ab}|E_0}{\hbar}. \tag{1.74}$$

The solutions of eq. (1.72) can be obtained by solving the equations for the slowly varying amplitudes c_a, c_b first

$$\begin{aligned} c_a &= C_a\, e^{i\varepsilon_a t/\hbar} \\ c_b &= C_b\, e^{i\varepsilon_b t/\hbar}. \end{aligned} \tag{1.75}$$

Inserting into eq. (1.72) yields

$$\dot{c}_a = i/2\, \Omega_R\, c_b\, e^{i(\Delta\epsilon-\omega)t/\hbar} \tag{1.76}$$

$$\dot{c}_b = i/2\, \Omega_R\, c_a\, e^{i(\Delta\epsilon-\omega)t/\hbar}. \tag{1.77}$$

For the solution the counter-rotating terms with $\exp(i(\Delta\epsilon+\omega)t/\hbar)$, where $\Delta\epsilon = \epsilon_a - \epsilon_b$ is the transition frequency, have been neglected. This is the so-called rotating wave approximation (RWA). With the initial condition φ_a, $c_a(t_0) = 1, c_b(t_0) = 0$, the probability $P(t)$ of finding the system in φ_b can be calculated

$$P_b(t) = |c_b(t)|^2 = \frac{\Omega_R^2}{\Omega^2} \sin^2\left(\frac{1}{2\hbar}\Omega t\right), \tag{1.78}$$

setting $\Omega = \sqrt{\Omega_R^2 + (\Delta\epsilon-\omega)^2}$. With the Rabi formula in eq. (1.78) periodic oscillations (Rabi oscillations) to find the system in $|\varphi_b\rangle$ are described. In the special case, when the carrier frequency of the field ω is in resonance with the energy difference of the two eigenstates $\Delta\varepsilon$ we get $\Omega = \Omega_R$ and for the probability

$$P_b(t) = \sin^2(\frac{1}{2\hbar}\Omega_R t). \tag{1.79}$$

Chapter 2

Numerical Methods

In this chapter the numerical methods applied to solve the equations introduced in chapter 1 are presented.

2.1 Classical Trajectories

To calculate a particle's position at time t starting from an initial condition $x(t_0), \dot{x}(t_0)$ (initial value problem), the time interval $[t_0, t]$ is divided into N time steps Δt. A Taylor-expansion around time t as

$$f(t) = \sum_{n=1}^{n=\infty} \frac{1}{n!} \frac{d^{(n)} f}{dt^n}(t) \Delta t^n, \tag{2.1}$$

yields, for the particle's position at time $t + \Delta t$,

$$x(t + \Delta t) = x(t) + \dot{x}(t)\Delta t + \frac{1}{2}\ddot{x}(t)\Delta t^2 + \cdots . \tag{2.2}$$

Truncation of the Taylor-series after the second term leads to an error of second-order in Δt (first-order Euler method). In the present work, trajectories $x_i(t)$ were calculated with a propagation method of a second-order error, the standard second-order Runge-Kutta algorithm. There, the following equations, employing intermediate points $x_{12}, \dot{x}_{12}$ at $t + \Delta t/2$ are employed successively to calculate points $x_1, \dot{x}_1$ at full time step $t + \Delta t$ [41]:

$$\begin{aligned} x_{12} &= x_0 + \frac{1}{2}\dot{x}_0 \Delta t \\ \dot{x}_{12} &= \dot{x}_0 + \frac{1}{2}\Delta t \left(-\frac{\partial V}{\partial x}(x_0)/m \right) \\ x_1 &= x_0 + \dot{x}_{12}\Delta t \\ \dot{x}_1 &= \dot{x}_0 + \Delta t \left(-\frac{\partial V}{\partial x}(x_{12})/m \right). \end{aligned} \tag{2.3}$$

2.2 Quantum Propagation

Propagating the wave function by applying the time-evolution operator (propagator) for N infinitesimal time steps Δt can be achieved numerically by using the Fast Fourier Transform (FFT) split operator method [42]. It is assumed that the (time-independent) Hamiltonian is composed out of terms depending on either the momentum p or coordinate x operator. Therefore, the propagator can be written as

$$e^{-i/\hbar (T(p)+V(x))\Delta t} = \prod_{j=1}^{a} e^{-i/\hbar b_j T(p)\Delta t}\, e^{-i/\hbar c_j V(x)\Delta t} + O\left((\Delta t/\hbar)^{N+1} \right). \tag{2.4}$$

The error arises from the neglection of higher-order commutators $\Delta t^N/\hbar^N$ $[T(p), V(x)]$. A symmetric splitting for $a = 2$ gives the short-time propagator of third order error used throughout this work. The particular exponential operators act on the wavefunction in momentum ($\tilde{\psi}(p)$) or coordinate space ($\psi(x)$) being connected via a Fourier transform

$$\tilde{\psi}(p) = \frac{1}{\sqrt{2\pi\hbar}} \int e^{-ipx/\hbar}\, \psi(x)\, dx. \tag{2.5}$$

A slightly different picture arises when the Hamiltonian is not time-independent. The form of the time ordered exponential (1.24) is approximated in the split operator method as

$$\begin{aligned}\exp_+\left[-\frac{i}{\hbar}\int_{t_0}^{t_1} d\tau H(\tau)\right] &\approx \exp\left(-\frac{i}{2\hbar}T(p)\Delta t\right)\cdot \\ \exp\left(-\frac{i}{\hbar}V(x)\Delta t\right) &\cdot \exp\left(-\frac{i}{\hbar}W(t)\Delta t\right)\cdot\exp\left(-\frac{i}{2\hbar}T(p)\Delta t\right), \quad (2.6)\end{aligned}$$

where $\Delta t = t_1 - t_0$, and the time-dependent term $W(t)$ displays the influence of an external potential, e.g. electromagnetic interaction with a laser field. As a function of a diagonal matrix remains in a diagonal form, the exponential terms containing T, V are also diagonal. The kinetic operators T are diagonal in momentum space and the potential energy operators V are diagonal in configuration space. An advantage of this unitary split-operator method (conservation of norm) is that the exponential operators simply affect the wave functions in the particular space by their multiplication with a complex number at each value of the discretized grid of $\{x_i, p_j\}$. Therefore the functions are represented on a spatial grid. Since the time-dependent term exhibits off-diagonal terms for a field coupling different electronic states, the operator has to be diagonalized first. For simple cases the matrix can be digonalized analytically, calculating the eigenvalues λ_i and the corresponding (normalized and orthogonal) eigenvectors arranged in a matrix A. Because of

$$A\,D(\lambda_i)\,A^T = W, \tag{2.7}$$

where the diagonal matrix D contains the eigenvalues λ_i and A^T denotes the transposed matrix of A, the original matrix W can be replaced by the expression on the left hand side of the equation (2.7). Again, applying the proposition that a function of a diagonal matrix remains in a diagonal form leads to the propagation scheme

$$\exp\left(-\frac{i}{\hbar}W(t)\,\Delta t\right) = A\,\exp\left(-\frac{i}{\hbar}D\,\Delta t\right)A^T. \tag{2.8}$$

The distances of grid points in coordinate $x_i \in [x_{min}, x_{max}]$ and momentum space $p_i \in [p_{min}, p_{max}]$ are related via

$$-p = -\frac{\hbar\pi}{\Delta x} \qquad \text{and} \qquad p = \frac{\hbar\pi}{\Delta x} \qquad \text{with} \qquad \Delta p = \frac{2\hbar\pi}{N\Delta x}. \tag{2.9}$$

The spatial resolution is such chosen ensuring a good description in momentum space, likewise (with respect to the computational effort, as each Fourier transform scales with $N\,log(N)$). In this work the very efficient Fast Fourier Transform library FFTW by Frigo and Johnson was used [43].

2.3 Eigenstates

The eigenstates of the stationary Schrödinger equation in eq. (1.15) can be obtained numerically. As an application of the afore described split-operator method the relaxation method by Kosloff [44] is starting from an arbitrary function $\varphi(x)$, propagating it with a complex time $\tau = -it$ (imaginary time-propagation). Its time-evolution ("eigenfunction expansion") reads as

$$\varphi(x, \tau + \Delta\tau) = \sum_n \langle\phi_n(x)|\varphi(x,\tau)\rangle\, e^{-\Delta\tau/\hbar E_n}\, |\phi_n(x)\rangle. \tag{2.10}$$

This non-unitary propagator diminishes the norm with increasing τ such that a re-normalization in each propagation step is required. For an eigenstate being less damped the initially guessed wavefunction φ converges in the limit $t \to \infty$

towards $|\phi_0\rangle$ (assuming a positive eigenvalue spectrum, $E_n > 0$). The eigenenergy is calculated as

$$E_n = -\frac{1}{2\Delta\tau} \ln\left(\frac{\langle\varphi_{i+1}|\varphi_{i+1}\rangle}{\langle\varphi_i|\varphi_i\rangle}\right), \tag{2.11}$$

where the $\varphi_i(\varphi_{i+1})$ is the propagated wave function at times $\tau_i(\tau_{i+1})$. Obtaining higher eigenstates is possible by projecting out already determined lower states in each time step.

Chapter 3

Control Theories

Several theoretical approaches have been developed concerning the control of the dynamics of molecules using external laser fields. An intuitive method arises from controlling a delay time between two pulses guiding the generated wavepacket into a defined reaction channel. Besides this Tannor-Rice-Kosloff scheme [12, 13, 18] a mathematical access, called optimal control theory is often applied [45, 46]. Within optimal control theory the overlap of a forward propagated initial state and a backward propagated, final state is maximized. In another theory, the coherent control theory by Brumer and Shapiro, dynamics is controlled by interferences of competing multi-photon transitions [8, 47]. Another possibility of quantum dynamical control determined by feedback from a signal using genetic algorithms has been proposed by Judson and Rabitz [17] and experimentally realized by several groups [9, 48–50]. Compared to these approaches a theory controlling a system's dynamics instantaneously gives more physical insight into the processes influencing and shaping the form of the derived electric field. This theory was first proposed by Tannor [20], Kosloff [51] and Rabitz [23] and later extended by us [24]. In this chapter some of the above mentioned theories are introduced.

3.1 Genetic Algorithms

Genetic algorithms are global optimization methods, combining elements of parallel and stochastic search. Terms and concepts of the applied operations are associated with biological evolution. A physical problem, e.g. maximizing a population in a selected electronic state $|k\rangle$, can be encoded in an optimization-procedure of a fitness-function. Therefore, information is stored in "genes“ x_i, which are a bit string of length N

$$x_i = (a_1, a_2, \cdots a_N), \tag{3.1}$$

where N is the number of parameters. As a result of the stochastic search a parameter set with size N_{pop} is chosen. In this work the parameter set contains pulse parameters α_1, $\alpha_2, ...$ of a laser field $E(\omega)$ with a non-linear chirp in frequency domain (see chapter 1)

$$\begin{aligned} E(\omega) &= E_0\, e^{-\frac{(\omega-\omega_0)^2}{2\gamma^2}} e^{-i/\hbar[\alpha_1(\omega-\omega_0)^2+\alpha_2(\omega-\omega_0)^3+\cdots]}; \qquad (3.2) \\ x_i &= (\alpha_{1,i}, \alpha_{2,i}, ...\alpha_{N,i}), \qquad i = 1, N_{pop}. \qquad (3.3) \end{aligned}$$

E_0 is the field strength (and can also be chosen as a parameter to be modified by the algorithm), the first exponential is a Gaussian shape function centered around the central frequency ω_0 having a width of γ. The term indicating temporal displacment $\alpha'(\omega - \omega_0)$ (compare with eq. (1.44)) is not included as it does not cause a chirped pulse. In order to constrain the spectral width we choose the Taylor-expansion of the laser field in frequency domain. An initial parameter set (a population) of pulse-parameters x_i is generated randomly. With each x_i a complete propagation of the quantum mechanical system is performed and the population A in state $|k\rangle$ is calculated. Each individual's fitness is determined via the definition of the fitness-function J. Possible definitions must be discriminative, which means the value of J selects the quality of an individual. For dissociative systems it may be helpful defining the fitness function via the dissociated part – as the amount of the wave-packet $|\psi_i^k(t)\rangle$ in state $|k\rangle$ on a dissociative potential surface which has passed a value R

$$J = \int_R^\infty dR' \left|\psi_i^k(R')\right|^2 . \tag{3.4}$$

Now each vector x_i is randomly perturbed with a certain, pre-defined probability. These modifications are called – according to evolutionary syntax – mutation and cross-over. Mutation means replacing a parameter with a random number

$$\begin{aligned} x_i &= (\alpha_1, \alpha_2, \alpha_3, \ldots \alpha_N) \\ \downarrow & \qquad Mutation \\ x_i' &= (\alpha_1, \beta_2, \alpha_3, \ldots \alpha_N). \end{aligned} \tag{3.5}$$

A cross-over causes an exchange of two parameter's positions, the child-gene is a mixture of two parental's genes

$$\begin{array}{ccc} x_i = (\alpha_1, \alpha_2, \alpha_3, \ldots \alpha_N) & & x_i' = (\alpha_1, \alpha_2, \beta_3, \ldots \alpha_N) \\ & Cross - Over & \\ & \longrightarrow & \\ x_j = (\beta_1, \beta_2, \beta_3, \ldots \beta_N) & & x_j' = (\beta_1, \beta_2, \alpha_3, \ldots \beta_N). \end{array} \tag{3.6}$$

The next metaphor is the principle ”survival of the fittest“: after applying these modification-operators the value of the fitness-function is re-calculated for the next (the modified) generation and selection is enforced. Within the here employed differential evolution algorithm [52] those modified individuals, which lead to a smaller value of the fitness-function, survive and replace their (non-modified) parents. This new set of parameters, i.e. the new generation, is again modified until the value of the fitness-function falls below a convergence criterion.

3.2 Optimal Control Theory (OCT)

Optimal control theory describes a mathematical way of maximizing a functional J. In the connection with quantum mechanical systems the latter is mostly defined as an overlap of a propagated state vector $|\psi\rangle$ starting in a defined initial state $|\varphi_0\rangle$ with a desired target state $|\varphi_f\rangle$ at time t_f. By forward-propagating a wave packet deriving from $|\varphi_0\rangle$ and backward-propagating a wave packet starting from $|\varphi_f\rangle$ the "optimal" electric field $E(t)$ is calculated as the time-dependent overlap of the wave packets. The precise form of the functional $J(E)$ depends on the method used. Here, the object functional is delimitated by an energy conservation condition via Lagrange multiplier λ, constraining the intensity of the form

$$\lambda = \frac{1}{\epsilon} \int_{t_0}^{t_f} E^2(t)\, dt, \tag{3.7}$$

using a skaling factor ϵ, and the fact that $|\psi\rangle$ has to satisfy the Schrödinger equation in introducing Lagrange multiplier χ

$$\langle \chi(t) | i\hbar \frac{\partial}{\partial t} - \mathcal{H} | \psi(t) \rangle = 0. \tag{3.8}$$

The target wave function is assumed to have a complex Gaussian shape

$$\varphi_f(x;t_f) = e^{-\beta(x-x_c)^2+i/\hbar\cdot p_0(x-x_c)}, \tag{3.9}$$

where the first term determines the position centered around x_c in configuration space and the second term characterizes the momentum space distribution. For dissociative systems the momentum p_0 is chosen corresponding to the kinetic energy of the kinetic energy of the fragments of the desired channel. Including the constraints via Lagrange multipliers $\chi(t), \lambda$ the functional can be written as

$$J = \langle\psi(t_f)|\varphi_f\rangle + \frac{i}{\hbar}\int_{t_0}^{t_f}(\langle\chi|i\hbar\frac{\partial}{\partial t} - \mathcal{H}|\psi\rangle - c.c.)dt + \frac{\lambda}{\hbar}[\int_{t_0}^{t_f} E^2(t)dt - \epsilon], \tag{3.10}$$

where *c.c.* means the complex conjugate. For a maxmimum value of the object functional the first derivative δJ with respect to the variations δE and $\delta\psi$ has to be calculated

$$\begin{aligned}\delta J &= \langle\delta\psi(t_f)|\varphi_f\rangle - \langle\varphi_f|\delta\psi(t_f)\rangle + \frac{i}{\hbar}\int_{t_0}^{t_f}(\langle\delta\psi|i\hbar\frac{\partial}{\partial t} - \mathcal{H}|\chi\rangle - c.c.)dt \\ &+\frac{i}{\hbar}\int_{t_0}^{t_f} -(\langle\chi|\frac{\partial\mathcal{H}}{\partial E}|\psi\rangle + \langle\psi|\frac{\partial\mathcal{H}}{\partial E}|\chi\rangle - 2\lambda i E(t))\,\delta E\,dt. \end{aligned} \tag{3.11}$$

Since $\partial\mathcal{H}/\partial E = \mu$ the last integral term is converted leading to

$$\begin{aligned}\delta J &= \langle\delta\psi(t_f)|\varphi_f\rangle - \langle\varphi_f|\delta\psi(t_f)\rangle + \frac{i}{\hbar}\int_{t_0}^{t_f}(\langle\delta\psi|i\hbar\frac{\partial}{\partial t} - \mathcal{H}|\chi\rangle - c.c.)dt \\ &+\frac{i}{\hbar}\int_{t_0}^{t_f} -(\langle\psi|\mu|\chi\rangle + c.c. - 2\lambda i E(t))\,\delta E\,dt. \end{aligned} \tag{3.12}$$

The overlap function $O(t) = \langle\psi(t)|\mu|\chi(t)\rangle$ linked to the electric field $E(t)$ by $E(t) = -O(t)/\lambda$ can be calculated from the dipole matrix in the last integral term. The exact form depends on the chosen system and will be given in chapter 4. We used the iteration algorithm given in the work of Rice et. al. [53]:

1. Setting an initial field $\bar{E}(t)$
2. Solving the Schrödinger equation for $\psi(t)$ with $\psi(t_0) = \varphi_0$ (FWD)
3. Projecting $\psi(t_f)$ onto the target function φ_f leading to a wave function $\chi(t_f)$
4. Backward propagation of the projected function $\chi(t_f)$ (BCKWD)
5. Renormalization of the wavefunction
6. Determining the overlap $O(t) = \Im\langle\psi(t)|\mu|\chi(t)\rangle$
7. Calculating a new field $E(t)$ with

$$E(t) = -\frac{O(t)}{\lambda} = -O(t)\left(\frac{1}{\epsilon}\int_{t_0}^{t_f} dt\,|O(t)|^2\right)^{-1/2} \tag{3.13}$$

After this last step the iteration restarts at step (2) till convergence is achieved. It is also possible to insert a Gaussian shape-function into the calculation guaranteing a moderate in- and decrease of the calculated field [54, 55].

3.3 Restricted Optimal Control Theory

Within the optimal control theory described in the last section there is only small influence on the derived electric field. There are some attempts in the literature to influence the parameters of e.g. a Tannor-Rice pump-dump scheme [53]. Here we constrain the electric field, rewriting it as a function of frequency ω and n

(time-independent) chirp parameters α_i according to eq. (3.2)

$$E(\omega) = E(\omega, \alpha_1, \alpha_2, ...\alpha_N). \tag{3.14}$$

For δE we get

$$\delta E = \sum_{i=1}^{N} \left(\frac{\partial E}{\partial \alpha_i} \delta \alpha_i \right). \tag{3.15}$$

Inserting eq. (3.15) into eq. (3.12) and adding the further condition that $\delta J = 0$ for all $\delta\alpha_i$ we get N equations to determine the set of chirp parameters

$$-\frac{i}{\hbar} \int_{t0}^{t_f} \left(\langle\psi| \frac{\partial \mathcal{H}}{\partial E} |\chi\rangle - c.c. - 2i\lambda E(t) \right) \frac{\partial E}{\partial \alpha_i} dt. \tag{3.16}$$

These coupled integral equations are solved via an anlytical expression for the first and second order derivatives of the functional concerning the chirp parameters. Therefore we compose two vectors F, A containing the first ($F(\alpha_i) = \delta J/\delta\alpha_i$) and second derivatives ($A(\alpha_i) = \delta F/\delta\alpha_i = \delta^2 J/\delta\alpha_i^2$), respectively. For small changes in the α_i the new set of parameters can be calculated by expansion into a Taylor series

$$F(\alpha_i + \delta\alpha_i) \approx F(\alpha_i) + A\,\delta\alpha_i \tag{3.17}$$

At extrema of the functional (i.e. if $\delta J \approx 0$) or close to extrema $F \rightarrow 0$ we get

$$\begin{aligned} 0 &\approx F + A\,\delta\alpha_i \\ \delta\alpha_i &\approx -A^{-1}F \end{aligned} \tag{3.18}$$

The iteration scheme now differs from the one described in the last section following the last step (calculation of the field). In more detail, the following, additional operations are necessary:

1. Setting up the partial derivatives of the electric field for the different chirp

parameters

2. Assigning λ according to eq.(3.7):

$$\lambda = -(\frac{1}{\epsilon}\int_{t_0}^{t_f} O^2(t)\,dt)^{1/2} \tag{3.19}$$

3. Calculation of the integrals eq. (3.16) obtaining F, A

4. Generation of a new set of parameters using eq. (3.18)

Inserting this new set of pulse parameters into eq. (3.2) a new field is constructed. This field is then Fourier-transformed into the time-domain and re-introduced into the iteration scheme of section 3.2.

3.4 Instantaneous Dynamics

The principle of control from instantaneous dynamics is best illustrated in regarding a classically forced harmonic oscillator in one-dimension. One can think of a physical process pumping energy into the system (heating) or taking energy away (cooling). A particle moving inside the harmonic potential is accelerated if an external field is applied acting in the same direction as its momentum. In contrary, a deacceleration is achieved by an laser acting in the opposite direction of the momentum. Furthermore, when the particle reaches a classical turning point and then changes its direction, the sign of the field has to be changed instantaneously to further drive the system. The frequency of the field therefore is in resonance with the oscillator. Obviously, the amplitude of the field would increase when the system's energy grows. In this section it is examined whether this picture can be used for directing (or controlling) a quantum mechanical wave packet. Therfore, the mathematical conditions are shortly introduced.

3.4.1 Classical Picture

A forced harmonic oscillator with coordinate x driven by an external, time-dependent force $F(t)$ is executing a forced vibration. The Lagrange function $\mathcal{L}$ for a particle with mass m is

$$\mathcal{L} = \frac{1}{2}m\dot{x}^2 - \frac{1}{2}kx^2 + xF(t). \tag{3.20}$$

As the Lagrangian is time-dependent, the energy conservation condition is not valid. The equation of motion for such a forced (driven) oscillator:

$$F(t) = m\ddot{x} + m\omega_0 x, \tag{3.21}$$

where $\omega_0 = \sqrt{k/m}$, has to be integrated. Possible solutions are of the form

$$x(t) = x_p(t) + x_{harm}(t). \tag{3.22}$$

The $x_{harm}(t)$ is an arbitrary solution of the homogenous equation of the free oscillator (without a driving force) and $x_p(t)$ any particular solution of eq. (3.21). If the force is a periodic function being harmonic at a frequency Ω

$$F(t) = F_0 \cos \Omega t \tag{3.23}$$

the linear oscillator will respond at that frequency. Inserting eq. (3.23) into eq. (3.21) gives a new equation of motion

$$F_0 \cos \Omega t = m\ddot{x} + m\omega_0 x. \tag{3.24}$$

A solution of $x_p(t) = C\cos(\Omega t + \gamma)$ for $\gamma = 0$ results in a condition for C

$$C = \frac{F_0}{m(\omega_0^2 - \Omega^2)}. \tag{3.25}$$

For $\Omega \neq \omega_0$ the general solution of eq. (3.24) can be expressed as

$$x(t) = A\sin(\omega_0 t + \delta) + \frac{F_0 \cos \Omega t}{m(\omega_0^2 - \Omega^2)}, \tag{3.26}$$

with A, δ as integration constants depending on the initial conditions. Eq. (3.26) represents a solution oscillating at two frequencies, ω_0 and Ω. The numerator is in phase with the driving force but the sign of the denominator depends on the relation between ω_0 and Ω. For $\Omega < \omega_0$ the Ω term is in phase with the driving force and is out of phase for $\Omega > \omega_0$ by π. The solution is not valid for $\Omega = \omega_0$. The correct solution for this resonant case is given by

$$x(t) = A\sin(\omega_0 t + \delta) + \frac{F_0 t \sin \omega t}{2m\omega_0}. \tag{3.27}$$

The amplitude of this vibration increases linearly with time t, resulting in the same picture as in the heating process described afore. Regarding the energy of the system, the sum of kinetic and potential energy terms

$$E = \frac{1}{2}m\dot{x}^2 + \frac{1}{2}m\omega_0^2 x^2, \tag{3.28}$$

the temporal change of energy for a resonant driven oscillator can be calculated:

$$\dot{E} = F\dot{x}. \tag{3.29}$$

With the initial conditions $x(0) = 0, \dot{x}(0) = 0$ parameters A and δ in eq. (3.27) are [29]:

$$\begin{aligned} x(0) &= A\sin(\omega_0 \cdot 0 + \delta) + \frac{F_0 \cdot 0 \sin\omega_0 \cdot 0}{2m\omega_0} = 0 \\ x(0) &= A\sin(\delta). \end{aligned} \tag{3.30}$$

Analogously, regarding the derivative $\dot{x}(t)$, given by

$$\dot{x}(t) = A\omega_0\cos(\omega_0 t + \delta) - \frac{F_0\omega_0 t\cos\omega_0 t}{2m\omega_0} + \frac{F_0\sin\omega_0 t}{2m\omega_0} \tag{3.31}$$

for $t = 0$ yields, together with eq. (3.30), that both parameters A, δ equal zero. The new equations for $x(t), \dot{x}(t)$ are

$$\begin{aligned} x(t) &= \frac{F_0 t}{2m\omega_0}\sin\omega_0 t \\ \dot{x}(t) &= \frac{F_0}{2m}\left(\frac{1}{\omega_0}\sin\omega_0 t + t\cos\omega_0 t\right). \end{aligned} \tag{3.32}$$

Inserting above equations into eq. (3.28) and eq. (3.29), respectively, the energy and energy rate can be expressed as

$$\begin{aligned} E &= \frac{F_0^2}{8}\left(t^2 + \frac{1}{\omega_0^2}\sin^2\omega_0 t + \frac{2t}{\omega_0}\sin\omega_0 t\cos\omega_0 t\right) \\ \dot{E} &= \frac{F_0^2}{2}\left(\frac{1}{\omega_0}\sin\omega_0 t + t\cos\omega_0 t\right)\cos\omega_0 t. \end{aligned} \tag{3.33}$$

Regarding the energy rate, it can be seen that for times $t \to \infty$ the energy increases.

3.4.2 Energy Condition

Consider, for simplicity, a quantum mechanical system in two dimensions (x, y), with a Hamiltonian

$$\mathcal{H} = \frac{p_x^2}{2m_x} + \frac{p_y^2}{2m_y} + V_0(x, y) + W(x, y, t) = \mathcal{H}_0 + W(x, y, t). \tag{3.34}$$

Here, p_x, p_y denote the momentum operators in directions x, y and m_x and m_y are the masses. The potential energy is given by $V_0(x, y)$ and an external potential $W(x, y, t)$ is added. The rate of energy change is given by

$$\begin{aligned} \frac{d\langle\mathcal{H}_0\rangle}{dt} &= \frac{i}{\hbar}\langle[\mathcal{H}_0, \mathcal{H}]\rangle \\ &= -\frac{i}{\hbar}E(t)\langle[\mu(x), T(p)]\rangle. \end{aligned} \tag{3.35}$$

Choosing a linear dipole moment, so that:

$$W(x, y, t) = -(\mu_x x + \mu_y y)E(t), \tag{3.36}$$

where the μ_x and μ_y are coefficients, one finds

$$\frac{d\langle\mathcal{H}_0\rangle}{dt} = \left(\frac{\langle p_x\rangle}{m_x}\mu_x + \frac{\langle p_y\rangle}{m_y}\mu_y\right)E(t). \tag{3.37}$$

This equation reveals that a proper choice of the external field $E(t)$ allows to heat $(d\langle\mathcal{H}_0\rangle/dt > 0)$ or cool $(d\langle\mathcal{H}_0\rangle/dt < 0)$ the system. Equation (3.37) is the quantum mechanical and two-dimensional version of the classical result obtained for the forced harmonic oscillator. The actual choice of $E(t)$ depends on the expectation value of the commutator between the dipole- and kinetic energy operator, which in turn is influenced by the external field.

3.4.3 Momentum Condition

Another possibility of driving a system is to minimize the temporal change of the momentum in one coordinate x. We can write

$$\begin{aligned}\frac{d}{dt}\langle\psi|p_x|\psi\rangle &= \langle\dot{\psi}|p_x|\psi\rangle + \langle\psi|p_x|\dot{\psi}\rangle \\ &= \frac{1}{i\hbar}\langle\psi|[p_x,\mathcal{H}]|\psi\rangle. \qquad (3.38)\end{aligned}$$

The commutator in eq. (3.38) can be evaluated as

$$\begin{aligned}[p_x,\mathcal{H}] &= [p_x, V+W(t)] = [p_x,V] + [p_x,W(t)] \qquad (3.39)\\ [p_x,W(t)] &= -\mu_x E(t)[p_x,x] = -E(t)\frac{\hbar}{i}\mu_x \\ [p_x,V] &= \frac{\hbar}{i}\frac{\partial V}{\partial x}.\end{aligned}$$

Inserting these into eq. (3.38) we get an expression for minimizing the integral via minimizing the expectation value of the force $\partial V/\partial x$:

$$\frac{d}{dt}\langle\psi|p_x|\psi\rangle = -\langle\psi|\frac{\partial V}{\partial x}|\psi\rangle + E(t)\mu_x. \qquad (3.40)$$

In order to $d/dt\langle p_x\rangle = 0$ the force of the molecule must be compensated by the electric field.

3.4.4 Population Transfer

The principle of population transfer employing the instantanous dynamics was first proposed by Tannor et al. [20] and extended by us [25, 26]. The temporal change of an observable A (here the population in state $|k\rangle$; $A = |k\rangle\langle k|$) can be expressed in terms of two commutators,

$$\frac{dA(t)}{dt} = \frac{i}{\hbar}\langle\psi|[\mathcal{H}, A]|\psi\rangle = \frac{i}{\hbar}\langle\psi|[\mathcal{H}_0, A]|\psi\rangle + \frac{i}{\hbar}\langle\psi|[W, A]|\psi\rangle. \tag{3.41}$$

The Hamiltonian of the unperturbed system, $\mathcal{H}_0$ commutes with A:

$$\mathcal{H}_0 = \sum_n |n\rangle\mathcal{H}_n \langle n| \tag{3.42}$$

$$[\mathcal{H}_0, A] = \sum_n |n\rangle\mathcal{H}_n \langle n|\, |k\rangle\langle k| - |k\rangle\langle k| \sum_n |n\rangle\mathcal{H}_n \langle n| = 0 \tag{3.43}$$

The temporal change of population $A(t)$ can be obained from the last term in eq. (3.41), if the interaction W and A do not commute. For

$$|\psi(t)\rangle = \sum_n \psi_n(t)\, |n\rangle, \tag{3.44}$$

$$W = -E(t)\sum_n\sum_m |n\rangle\mu_{nm} \langle m|, \tag{3.45}$$

the commutator can be derived for a population $S_k(t)$ in state $|k\rangle$ employing the projector $A = |k\rangle\langle k|$, so that

$$S_k(t) = \langle\psi(t)|A|\psi(t)\rangle \tag{3.46}$$

$$\begin{aligned}\frac{dS_k(t)}{dt} &= -E(t)\frac{i}{\hbar}\sum_m\{\langle\psi_m(t)|\mu_{mk}|\psi_k(t)\rangle - \langle\psi_k(t)|\mu_{km}|\psi_m(t)\rangle\} \\ &= -E(t)\frac{2}{\hbar}\sum_m \Im(\langle\psi_k(t)|\mu_{km}|\psi_m(t)\rangle),\end{aligned} \tag{3.47}$$

where $\Im$ denotes the imaginary part. The condition that the population $S_k(t)$ increases at all times can be fulfilled by a proper choice of the (real) electric field $E(t)$. From eq. (3.47) it is clear, that if one wants to control the flux into state $|k\rangle$, a (small) initial population in the target state is required. This is usually achieved by a seed-pulse, an arbitrary laser pulse that precedes the control pulse which transfers a small amount of population into the target state.

To understand the physical meaning of eq. (3.47), a two-level system interacting with a weak electric field $E(t) = \cos(\omega t)$ is treated. Employing first-order perturbation theory and imposing the initial condition $c_0(0) = 1$, the time-dependence of the state vector

$$|\psi(t)\rangle = c_0(t)|0\rangle + c_1(t)|1\rangle \tag{3.48}$$

is given by

$$\begin{aligned} c_0(t) &= e^{-iE_0 t/\hbar}, \\ c_1(t) &= \frac{i}{\hbar}\int_0^t dt' e^{-iE_1(t-t')/\hbar}\, \cos(\omega t')\, \mu_{10}\, e^{-iE_0 t/\hbar}. \end{aligned} \tag{3.49}$$

Here, the dipole matrix-element is $\mu_{10} = \langle 1|\mu|0\rangle$ and E_n is the eigenenergy of state $|n\rangle$. The matrix element appearing in eq. (3.47) is evaluated (for $k = 1$) as

$$\langle\psi_1(t)|\mu_{10}|\psi_0(t)\rangle = \frac{i}{\hbar}|\mu_{10}|^2 \int_0^t dt' \cos(\omega t')\, e^{-i\Delta(t'-t)}, \tag{3.50}$$

where $\Delta = (E_1 - E_0)/\hbar$ is assumed to be positive, in what follows. The rate then takes the form

$$\frac{dS_1(t)}{dt} = \frac{2}{\hbar^2}|\mu_{10}|^2 \int_0^t dt' \cos(\omega t)\, \cos(\omega t')\, \cos(\Delta(t'-t)). \tag{3.51}$$

The product of the cosine-functions can be rewritten as

$$\begin{aligned} \cos(\Delta(t'-t))\, \cos(\omega t)\, \cos(\omega t') &= \frac{1}{4}\{\cos[(\Delta-\omega)(t'-t)] + \cos[(\Delta+\omega)(t'-t)] \\ + \cos[(\Delta-\omega)t' - (\Delta+\omega)t] &+ \cos[(\Delta+\omega)t' - (\Delta-\omega)t]\}. \end{aligned} \tag{3.52}$$

If the fast oscillating terms containing $\Delta + \omega$ in the argument of the cos-function are neglected (rotating wave approximation (RWA)), one obtains

$$\frac{dS_1(t)}{dt} = \frac{|\mu_{10}|^2}{2\hbar^2} \int\limits_0^t dt' \, \cos[(\Delta - \omega)(t' - t)]. \tag{3.53}$$

Depending on time t, the integral assumes positive and negative values. The simplest choice for the parameter ω assuring that the rate of population change is always positive, is to force the integrand to be positive at each time t'. This is readily fulfilled by the choice $\omega = \Delta$, which is the resonance condition obtained from Fermi's Golden rule expression and ensures that the rate increases linearly with time [56]. That means, if the field oscillations ω are adjusted to match the system's dynamics, characterized by $(E_1 - E_0)/\hbar$, an efficient population transfer is induced. To conclude, the condition that, upon excitation, the population in a final state increases monotonically, leads (employing the usual approximation) directly to Fermi's Golden rule expression for the transition rate.

Chapter 4

Dynamics in Double Well Potentials

Double well potentials serve as model systems describing isomerizations [57] or proton [58–60] and electron transfer reactions [61–63], respectively. The objective is to influence such reactions, thereby using the system's dynamics as a guide. Within this chapter the algorithm is applied to classical and quantum mechanical one-dimensional oscillators. Afterwards, an extension to two-dimensional systems is presented.

4.1 One-Dimensional Cases

Let us first regard a symmetric double-minimum potential $V(x)$ of the form (in atomic units)

$$V(x) = (0.2x^4 - 8x^2 - 80) \cdot 10^{-4}, \tag{4.1}$$

which is displayed in fig. 4.1. This potential form describes, e.g. the ammonia umbrella motion giving rise to the NH_3 maser transitions [64]. Also, it often serves as a model to characterize proton transfer processes taking place along a reaction coordinate x [57, 65–67]. Regarding, e.g. a particle localized in the well at positive values of x, the objective is to move it over the potential barrier and stabilize it in the inner well, at least for times which are smaller than the time-scale where tunneling occurs. Therefore a heating field $E_h(t)$ is employed as long as the particle's coordinate is smaller than the position of the potential barrier. As soon as it has reached negative values of x the field is to be phase-shifted and exhibits the form of a cooling field $E_c(t)$.

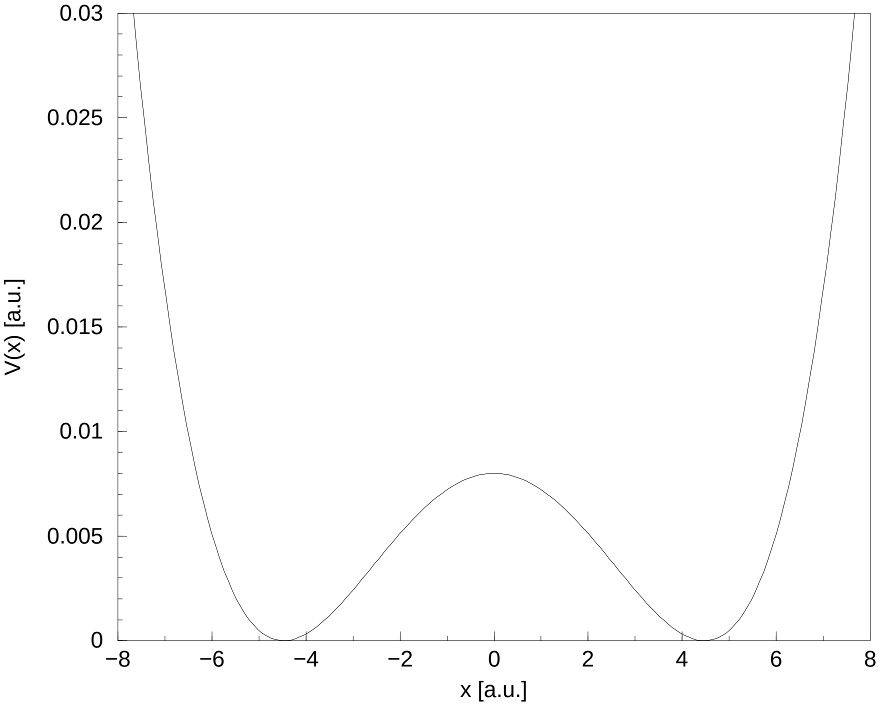

Figure 4.1: *Potential energy surface of the generic double minimum potential.*

4.1.1 Classical Trajectories

In the classical picture a trajectory, starting at point $x_0 = 5.1$ a.u. with an initial velocity $\dot{x} = 0$, was propagated using the Runge-Kutta algorithm. For a particle with proton mass m and a linear dipole moment $\mu(x) = 0.2x + 1$ a.u. the field was determined as

$$E(t) = E_0 \frac{\dot{x}(t)}{m} \{\Theta[-x(t)] - \Theta[x(t)]\} \tag{4.2}$$

where Θ denotes the Heaviside step function. This means that, if the particle's position is inside the starting well a heating occurs, whereas, if it exceeds the barrier, a cooling sets in. To facilitate a comparison to a quantum dynamical calculation an ensemble of 50 trajectories was propagated, weighted with a Gaussian distribution P_i of the form

$$P_i(x) = e^{-6\cdot(x_i - x_c)^2}, \tag{4.3}$$

where i counts the trajectories. In order to compare classical dynamics with the quantum dynamics the Gaussian was chosen to exhibit the same extent as a quantum mechanical wave function. The classical density is then constructed from the ensemble each at a point x_i, weighted with the Gaussian distribution P_i for the particular trajectory i

$$\rho = \sum_i P_i x_i. \tag{4.4}$$

The x_i were chosen to be centered around a value $x_c = 5.1$ a.u. according to the position where the quantum machanical wave packet is centered. Applying the Runge-Kutta algorithm

$$\begin{aligned} \rho^{12}(t) &= \rho^0 + \Delta t\, \dot{x}_i^0 \\ \rho^1(t) &= \rho^{12}(t) + \Delta t\, \dot{x}_i^{12} \end{aligned} \tag{4.5}$$

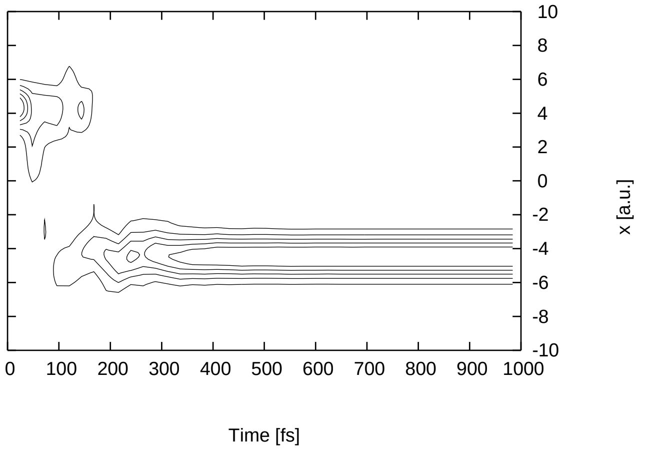

Figure 4.2: *Dynamics of the classical density in the double minimum potential. The initially localized trajectory ensemble in the outer potential well is transferred over the barrier and stabilized in the inner well.*

where the velocities $\dot{x}_i$ were weighted with the quantum mechanical momentum distribution $P_{i,mom}$, likewise assumed to be of Gaussian form

$$P_{i,mom}(\dot{x}) = e^{-0.3\cdot(\dot{x}_i - p_0)^2} \tag{4.6}$$

$$\dot{x}_i = \dot{x}_i P_{i,mom}. \tag{4.7}$$

The momentum distribution is centered around $p_0 = 0$, meaning that the most probable momentum is zero. The field resulting from eq. (4.2) driving the dynamics (fig. 4.2) is presented in fig. 4.3 where we used a value of $E_0 = 8 \cdot 10^{-4}$ a.u.. It can be seen that the transition is possible during the second vibrational period. Afterwards the cooling sets in and stabilizes the trajectory ensemble. The constructed electric field shows the temporal behaviour as described in chapter 3.

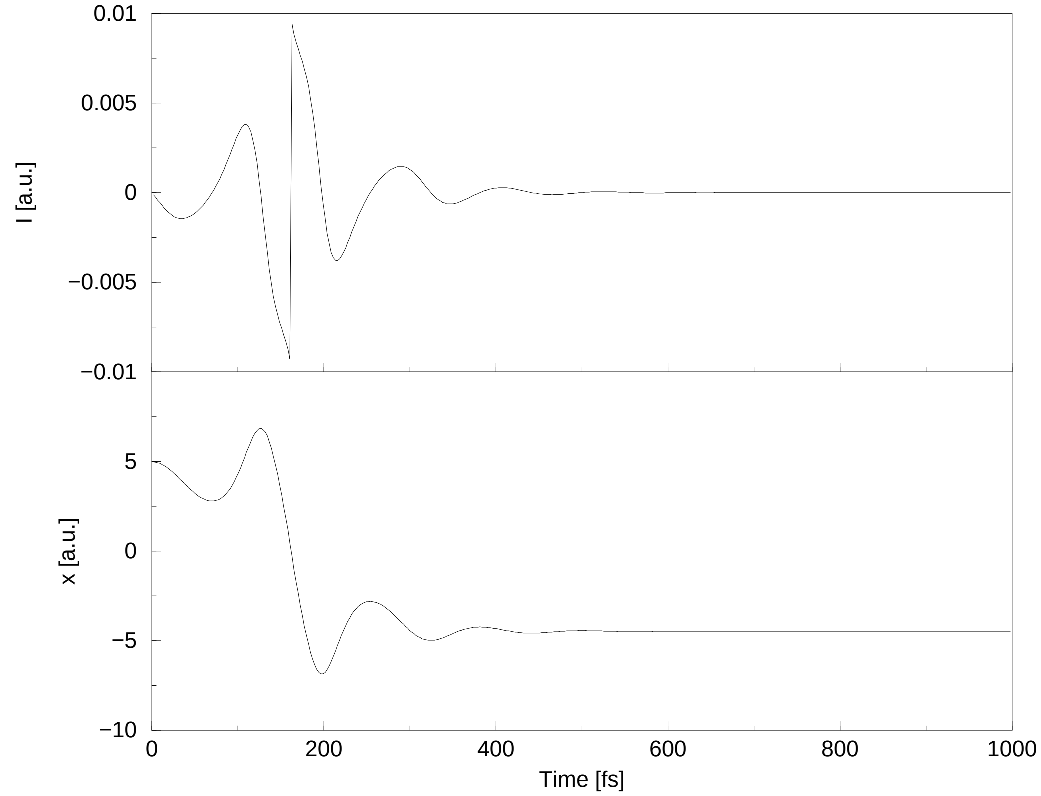

Figure 4.3: *Upper panel: Electric field constructed from the momentum changes in the classical system. The phase jump results from the Heaviside step function, occuring at the time where the ensemble average value $\langle x \rangle$ of the trajectory ensemble displayed in the lower panel equals zero.*

4.1.2 Quantum Dynamical Picture

Applying the algorithm of instantaneous control to the quantum dynamics, a field can be constructed in analogy to the classical procedure by replacing in eq. (4.2) the classical ensemble average value by the quantum mechanical expectation value. Therefore an initial Gaussian wave function centered around $x_c = 5.1$ a.u. with a width of 2 a.u. was employed and the dipole moment was chosen as in the classical treatment. A comparable dynamics was procured with a value of $E_0 = 1 \cdot 10^{-5}$. The wave packet dynamics and the corresponding field are shown in fig. 4.4, 4.5.

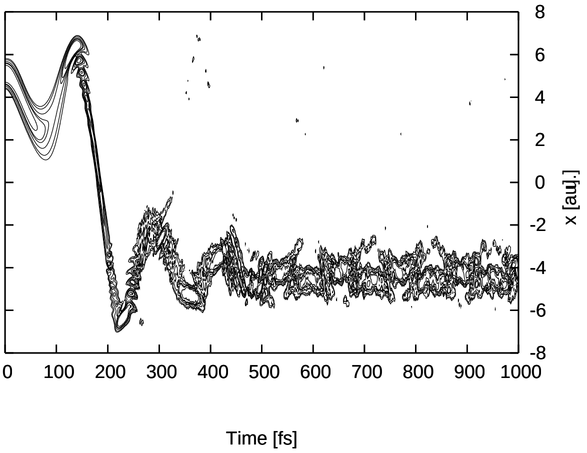

Figure 4.4: *Wave packet dynamics in the double minimum potential. The initially localized wave packet in the outer potential well is transferred over the barrier and stabilized in the inner well.*

The fields derived from the classical and the quantum mechanical description are similar. We tried to insert the classical field into the quantum dynamical calculations in order to examine the conduct of the quantized system. The result is pictured in fig. 4.6. It can bee seen that the population transfer is not complete, a part of the wave packet has too much energy and re-crosses the barrier. At the time when the cooling process sets in, two parts are cooled down in the particular well. The quantum dynamical behaviour can not be expressed completely in terms of classical mechanics.

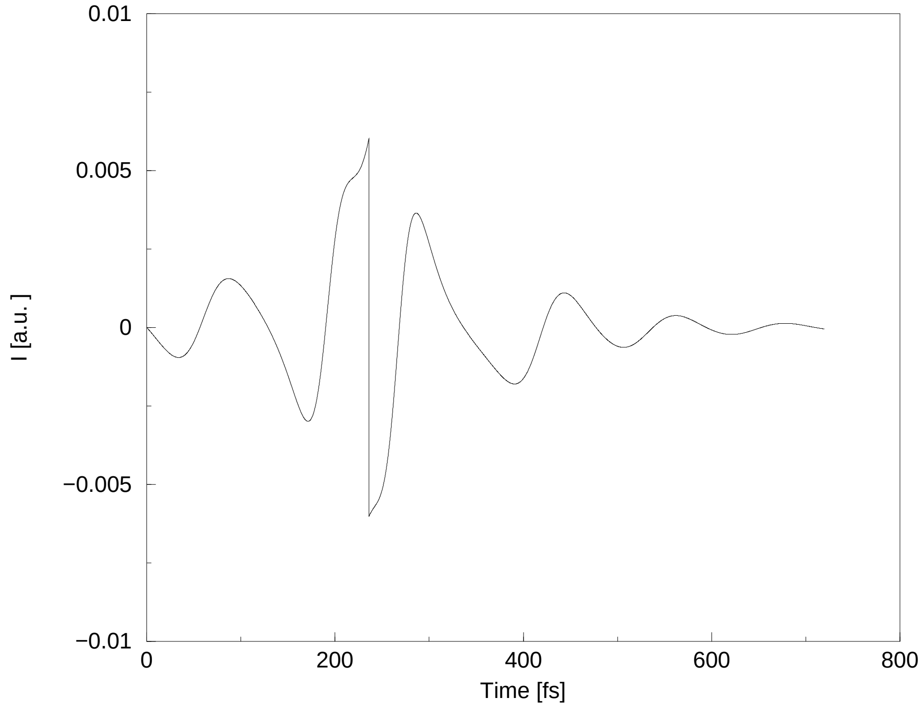

Figure 4.5: *Electric field constructed from the momentum changes in the system. The phase jump results from the Heaviside step function, occuring at the time where the bond-length expectation value $\langle x \rangle$ of the wave packet equals zero.*

4.1.3 Asymmetric Double-Well Potential

In what follows, the over-the-barrier dynamics in an asymmetric double-well potential is examined. Its analytical form is given as (in atomic units)

$$V(x) = (0.5x^4 - 1 \cdot 10^{-5}x^3 - 15x^2 - 12.02x + 160.2) \cdot 5 \cdot 10^{-4}. \tag{4.8}$$

The potential, together with the ground-state wave function, located in the outer potential well, is displayed in fig.(4.7) . As before, the objective is to transfer the wave function from its original position to the other potential well. In order to do so, energy has to be pumped into the system until the average energy exceeds the height of the potential barrier. If the then prepared wave packet passes the barrier to the left, it is to be stabilized in the other well by a cooling process.

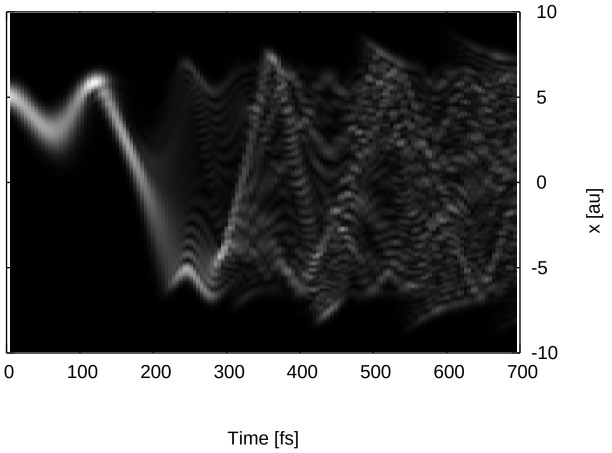

Figure 4.6: *Wave packet dynamics in the double minimum potential if applying the field due to the classical calculations into the quantum dynamical system.*

To achieve the transfer process the electric field was determined from Eq.(3.37) using the form

$$E(t) = E_0\, \mu_1\, \langle P(t) \rangle\, \{\Theta[\langle x(t) \rangle] - \Theta[-\langle x(t) \rangle]\}, \tag{4.9}$$

where $\langle x(t) \rangle$ ($\langle P(t) \rangle$) denotes the coordinate (momentum) expectation value. As in section 4.1.2 the dipole moment is taken to be a linear function: $\mu = \mu_1 x$, with μ_1=1 a.u. The parametrization of the field ensures that, as long as the average position of the wave packet is positive, the field is in phase with the particle momentum so that energy is absorbed. On the other hand, the field has the opposite sign as the momentum for negative values of $\langle x(t) \rangle$ which amounts to an effective cooling. As the initial wave function is an eigenstate of H_0, the expectation value of the momentum equals zero so that eq. (4.9) yields $E(t) = 0$. Therefore, initially a small constant field is applied which induces a small non-zero

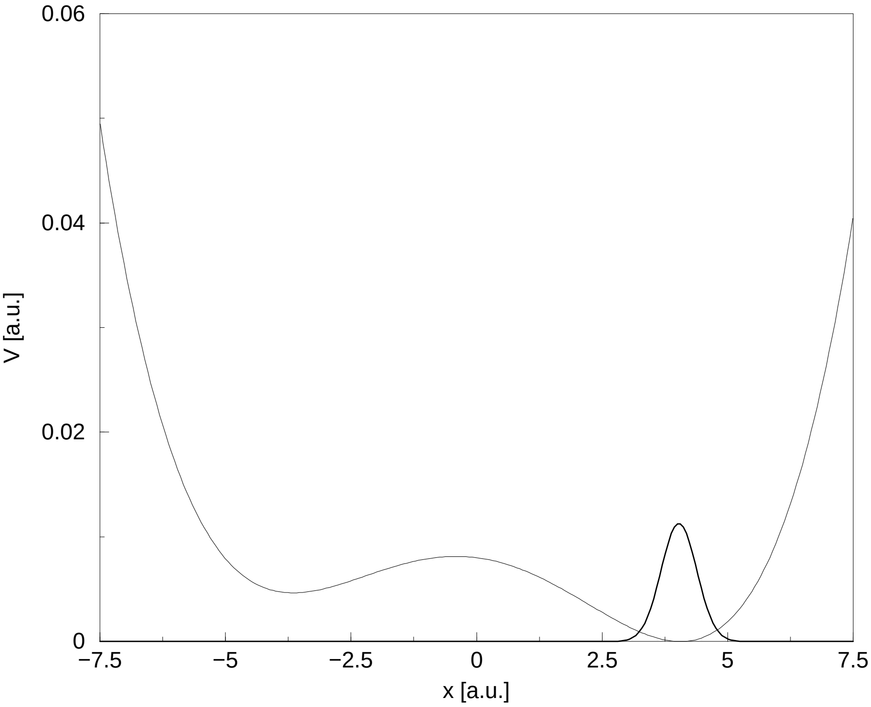

Figure 4.7: *Potential energy surface of the asymmetric double minimum potential.*

average momentum.

In our example for the transfer dynamics, a particle mass of 1823 a.u. and a strength parameter of $E_0 = 3 \cdot 10^{-6}$ a.u. is used. Figure 4.8 shows the coordinate expectation value (panel (a)) and the derived control field (panel (b)). It is seen that the field follows the vibrational dynamics of the system. Its maximal field amplitude corresponds to an intensity of $1.9 \cdot 10^9\, W/cm^2$, so that the field is not superintense. As the expectation value $\langle x(t) \rangle$ becomes negative, the field exhibits a phase jump so that energy is taken away from the system. This yields a wave packet localized - for the times regarded here - in the inner potential well. The wave-packet motion is illustrated in fig. 4.9. Starting from a stationary state, it takes some time until a vibrational motion with increasing amplitude sets in. This leads to a crossing of the barrier at about 280 fs. Afterwards, the wave

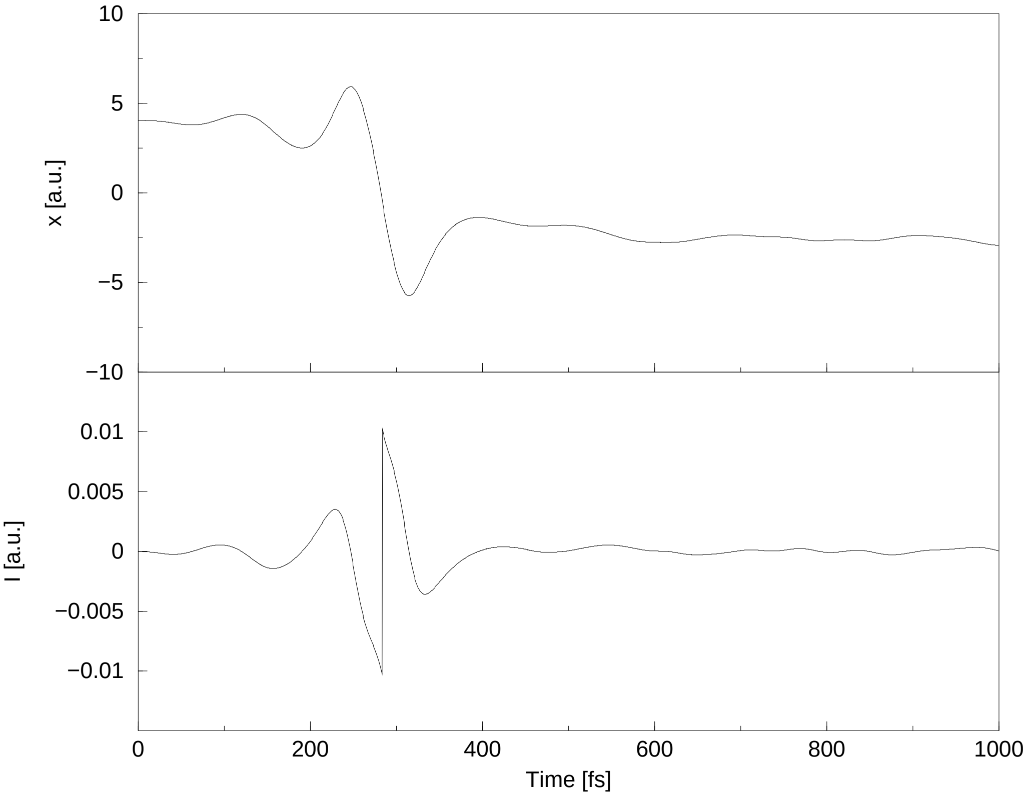

Figure 4.8: *Panel (a) Coordinate expectation value; panel (b) electric field constructed from the momentum changes in the system. The phase jump results from the Heaviside step function, occuring at the time where the bond-lenght expectation value $\langle x\rangle$ of the wave packet equals zero.*

packet is stabilized in the inner potential well, exhibiting vibrational dynamics.

Comparing results obtained from calculations performed with different field strengths E_0, it is found that the time required for the barrier crossing is inverse proportional to the field strength. However, if the field is too weak the dispersion of the wave packet becomes substantial (not for classical dynamics), and the momentum expectation value approaches zero so that eq. (4.9) is no longer suited as a condition to determine the control field.

In fig.(4.11) the mass-dependence of the driving dynamics is shown. The intuitive impression that a heavier particle requires lower field intensities because

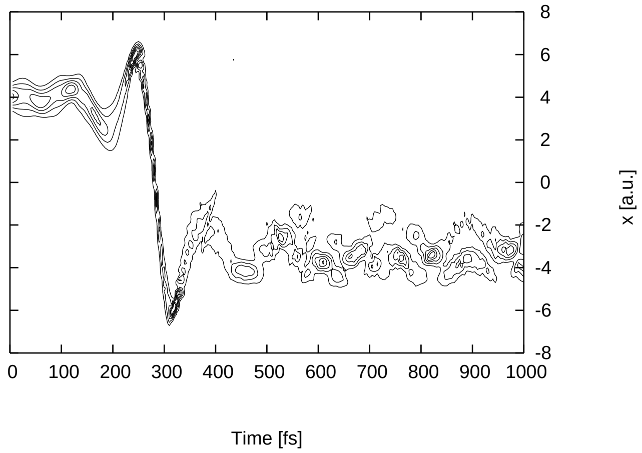

Figure 4.9: *Wave packet dynamics in the asymmetric double minimum potential. The ground-state wavefunction is transferred over the barrier and stabilized in the inner potential well.*

of close-lying energy levels to drive the system is confirmed. The simple form of the constructed field reflects directly the properties of the underlying quantum mechanical motion. One has to keep in mind that, if the motion is comparably slow, it might not be possible to experimentally realize such a field (up to date).

4.2 Two-Dimensional Case

To illustrate the influence of a motion in more than a single degree of freedom on the control fields, a two-dimensional problem is regarded. The model system is characterized by a Hamiltonian

$$H = \frac{p_x^2}{2m_x} + \frac{p_y^2}{2m_y} + V_0(x,y) + W(x,y,t) = H_0 + W(x,y,t), \tag{4.10}$$

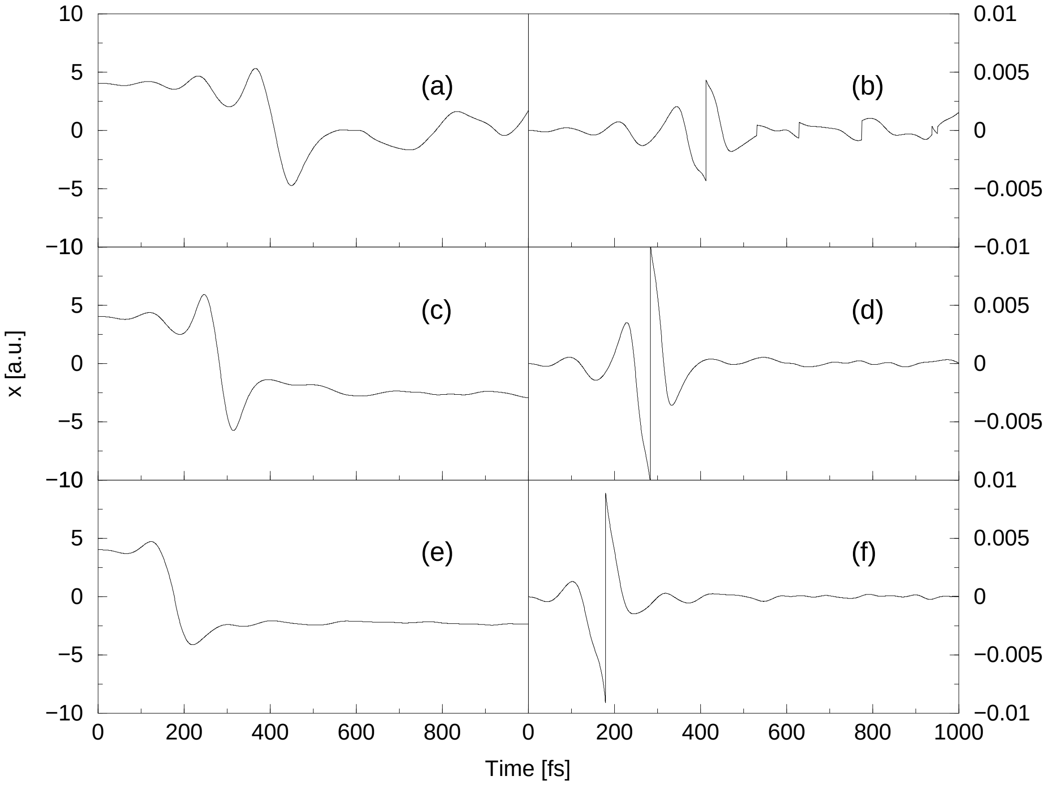

Figure 4.10: *Left hand side: Coordinate expectation values for different field strengths. Right hand side: appertaining fields. In going from (a) – (c) ((b) – (f))* E_0 *is increasing:* $2 \cdot 10^{-6}, 3 \cdot 10^{-6}, 4 \cdot 10^{-6}$.

with a potential energy $V(x, y)$ of the form (in atomic units)

$$V(x, y) = (0.2x^4 - 8x^2 + 8y^2 + \gamma xy) \cdot 10^{-4}. \tag{4.11}$$

The latter is displayed in fig. 4.12. The parameter γ controlls the coupling between the two degrees of freedom. For a value of $\gamma = 0$, the separable potential is a double minimum potential along the x direction, and a harmonic potential in the y coordinate. In analogy to the one-dimensional case, a linear dipole moment is assumed ($\mu(x, y) = \mu_1 x + \mu_2 y$, $\mu_1 = \mu_2 = 1$ a.u.). The expression for the field

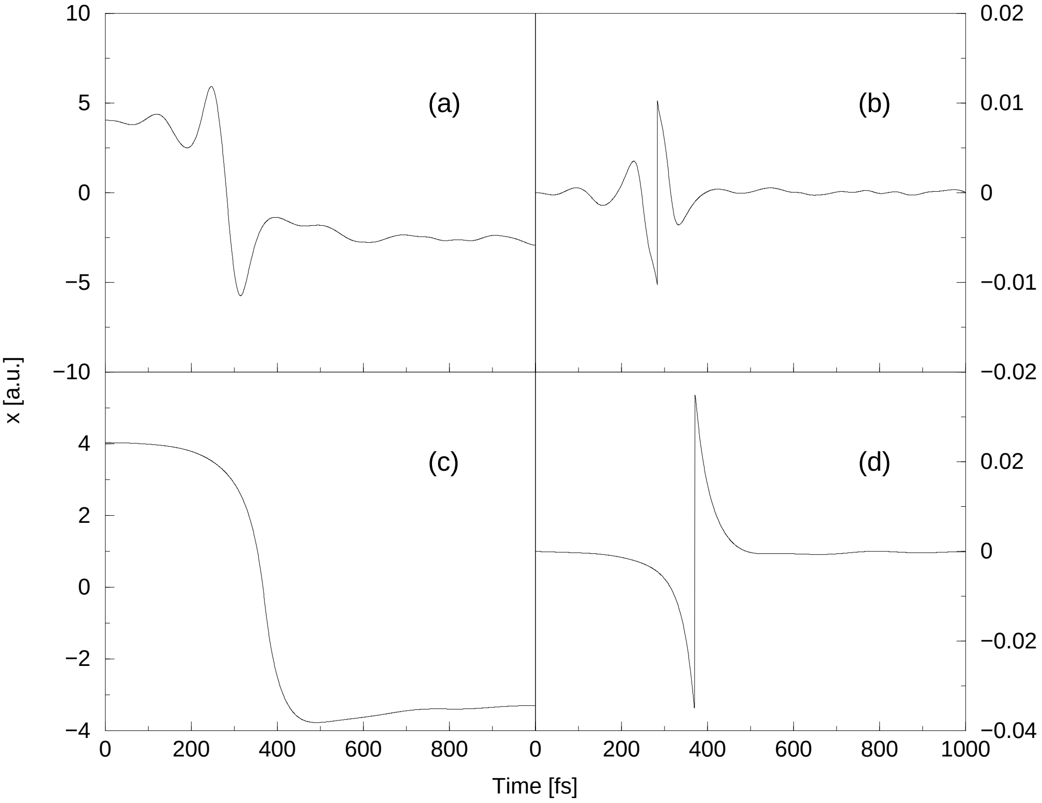

Figure 4.11: *Mass-dependence of the dynamics. Left hand side: Coordinate expectation values for different masses. Right hand side: appertaining fields. The lower panel shows the dynamics of a mass of 18229 a.u. and* E_0 *of* $3 \cdot 10^{-6}$ *vs. upper panel: mass = 1823 a.u. with same* E_0.

reads

$$E(t) = E_0 \, \{\mu_1 \langle P_1(t) \rangle + \mu_2 \langle P_2(t) \rangle\} \, \{\Theta[\langle x(t) \rangle] - \Theta[-\langle y(t) \rangle]\}. \qquad (4.12)$$

Here, the field is constructed from the motion in both degrees of freedom. Energy is transferred to the system if the expectation value of x is larger than zero and the cooling is effective if it is negative. In the calculation, the masses are fixed to the hydrogen mass and the coupling parameter is chosen as $\gamma = 1$ a.u. .

In fig. 4.13 the time-dependent expectation values of the two coordinates (middle panel) are compared with the control field (lower panel). For the em-

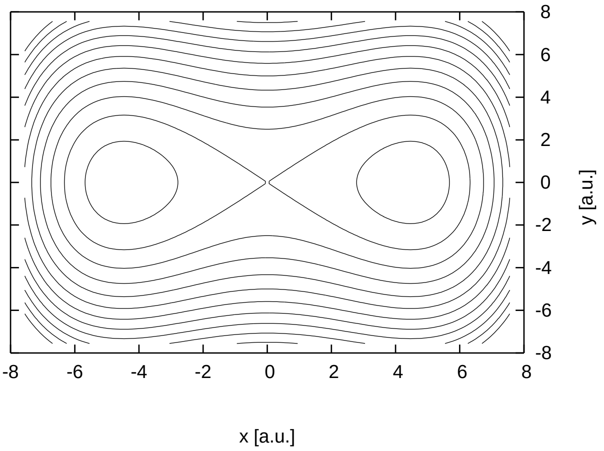

Figure 4.12: *Potential energy surface of a two-dimensional double minimum potential. Contours are shown as a function of the two coordinates x, y The contours start at an energy of* 0 *and increase in increments of* $5 \cdot 10^{-3} a.u.$.

ployed strength parameter ($E_0 = 6 \cdot 10^{-5} a.u.$), it takes about 150 fs to overcome the barrier, whereas it takes another 300 fs to cool the system and confine the wave packet to the other potential minimum. The electric field exhibits the same phase jump as in the one-dimensional case but now its time dependence is influenced by the motion in both degrees of freedom. An inspection of the wave function shows that it is not completely transferred from one potential well to the other. There is about 10 % of the probability amplitude which remains at positive values of the coordinate x.

It is instructive, to modify the procedure to construct the field, and exclusively determine it from the dynamics in the reaction coordinate x. This can formally be obtained in setting μ_2 in eq.(3.37) equal to zero. An example for the outcome of this construction scheme is presented in Fig. 4.14 ($E_0 = 5 \cdot 10^{-5}$a.u.). The

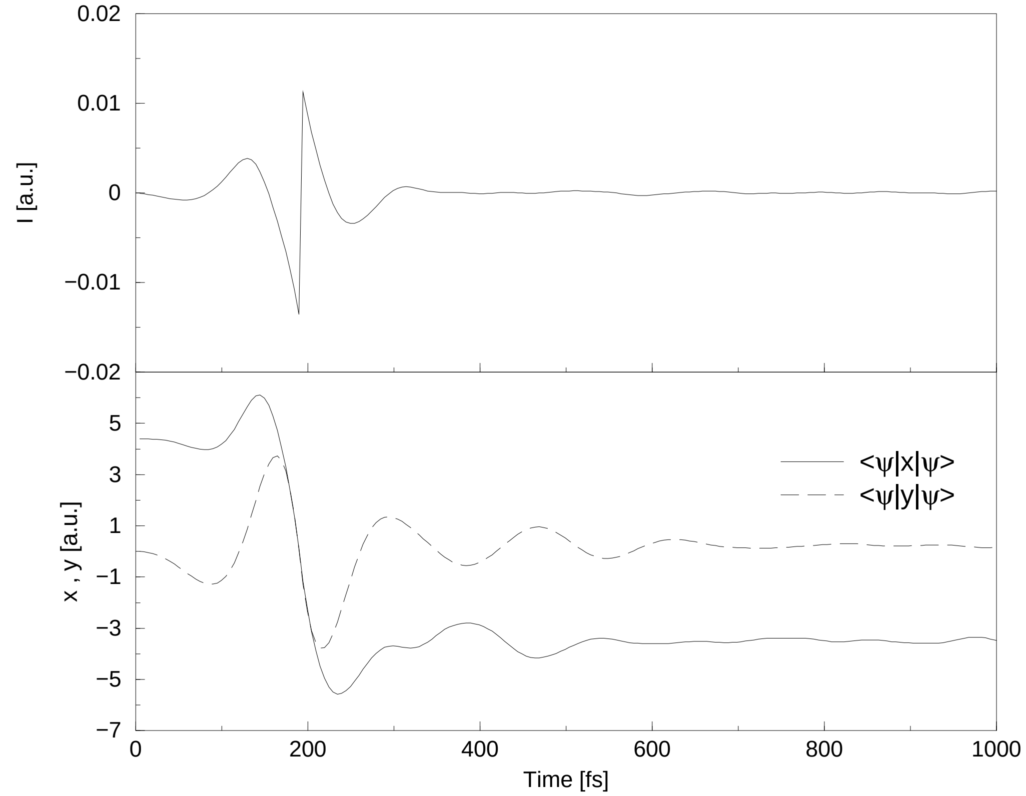

Figure 4.13: *Panel (a) Electric field constructed from the momentum changes in the system. The phase jump results from the Heaviside step function, occuring at the time where the bond-lenght expectation value $\langle x \rangle$ of the wave packet equals zero. Panel (b): Coordinate expectation values.*

expection value $\langle x(t) \rangle$ clearly shows that the wave-packet transfer takes place as found in the case discussed above. Nevertheless, here the cooling is only effective in the x-degree of freedom and the motion in the other coordinate, for the time interval displayed, exhibits a periodic motion showing a substantial amount of vibrational excitation. Comparing the above described possibilities of deriving a field for a two-dimensional system there are some conclusions. First, regarding the case where the field is derived from both coordinates, the absolute intensity of the constructed field is higher as both momenta contribute to the field. On the other hand, the vibrational motion is therefore cooled more effectively in both coordinates on a faster time scale. This can be explained since driving

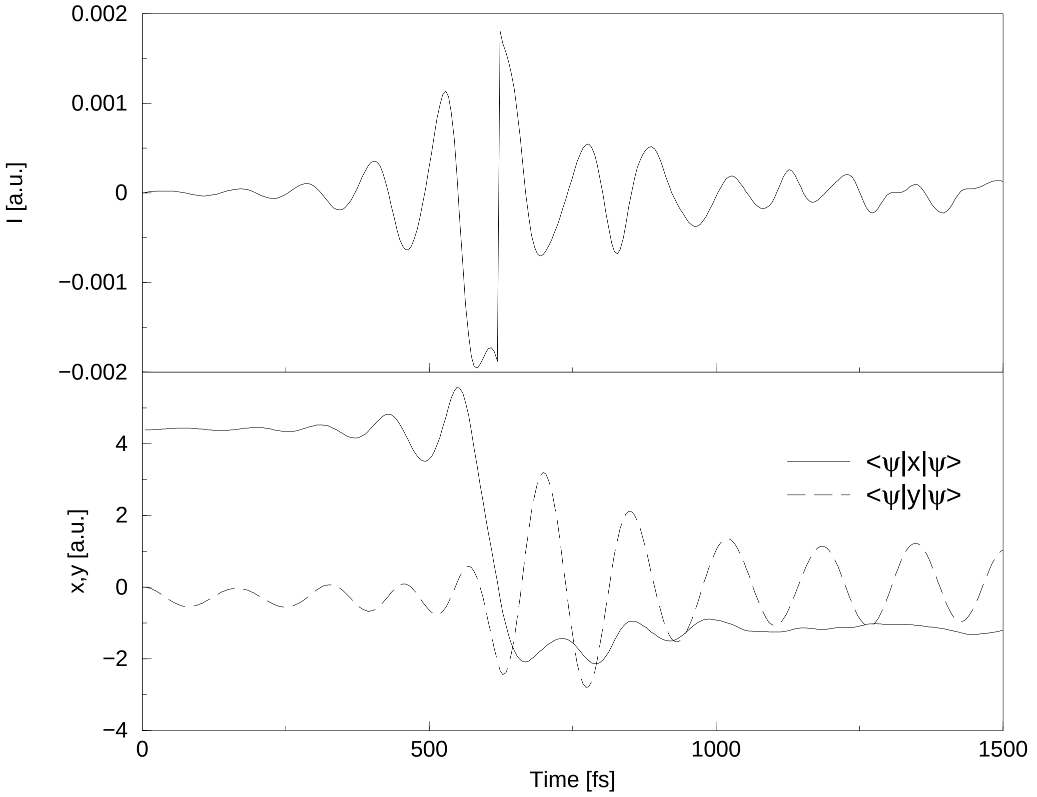

Figure 4.14: *Same as fig.(4.13), here only x coordinate contributes to the field.*

only one coordinate (x) resonantly the other coordinate is forced to follow the x-coordinate's dynamics. Considering the intensity, the second case suffices a lower intensity as only one coordinate is controlled – the other coordinate's dynamics is adapted.

Chapter 5

Selective Bond Breaking: The HOD Molecule

Much attention has been paid to the bond-selective dissociation of molecules. A well studied system is the HOD molecule [68–70]. The photo-dissociation into the two possible decomposition channels $H + OD$ and $D + OH$ has been investigated applying several theoretical approaches and experiments [71]. One possibility for a system initially in the electronic ground state $\tilde{X}^1A_1$ is to apply an intense IR-pulse and then excite via an UV-pulse into the dissociative $\tilde{B}^1A_1$-state. Controlling dissociation ratios by involving the excited dissociative state was realized by pump/dump control [68], fractional revivals [69], few-cycle pulses [70], coherent radiative control [72], and non-adiabatic tunneling [73]. Within the latter a stationary laser field is proposed by utilizing the phenomenon of complete reflection.

Another possibility to control branching ratios proceeds within one single electronic state leading to a bond breaking by selectively exciting one vibrational mode. This was accomplished by ladder-climbing via local or non-local modes [74,75], by applying optimal control theory [76] or few-cycle Gaussian-pulses [77].

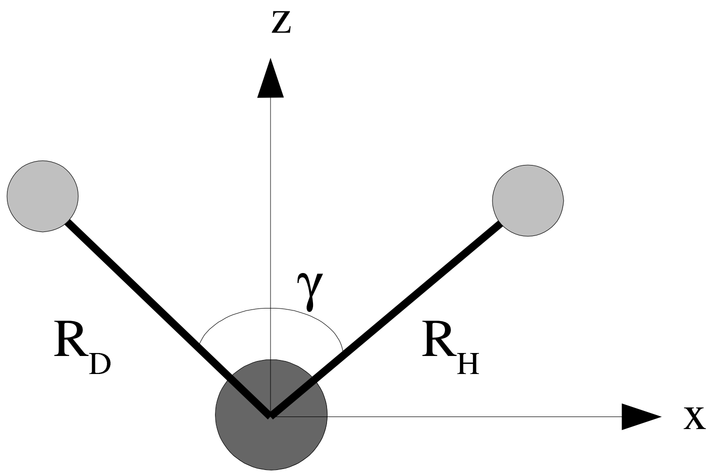

Figure 5.1: *Schematic representation of HOD. The molecule is lying in the xz-plane with a fixed bonding angle of $\gamma = 104°$ bisected by the z-axis. R_H and R_D denote the coordinates of H and D, respectively.*

In this chapter the model system is shortly introduced and the instantaneous dynamics approach is applied in order to control the ratio of products in the two fragmentation channels in the electronic ground state.

5.1 The HOD Model System

Treating the case of total angular momentum $J = 0$, freezing the bonding-angle γ, and separation of the rotation and translational motion of the molecule, the nine degrees of freedom of HOD are reduced to two independent vibrational modes: For the large mass difference of oxygen, and hydrogen and deuterium atom, respectively, the center-of-mass is set to the oxygen's position and the motions of the other atoms are described by coordinates according to fig. 5.1.

The bonding angle of HOD is fixed to its equilibrium value of 104°. The form of the potential energy surface (see fig. 5.2) is approximated by two coupled

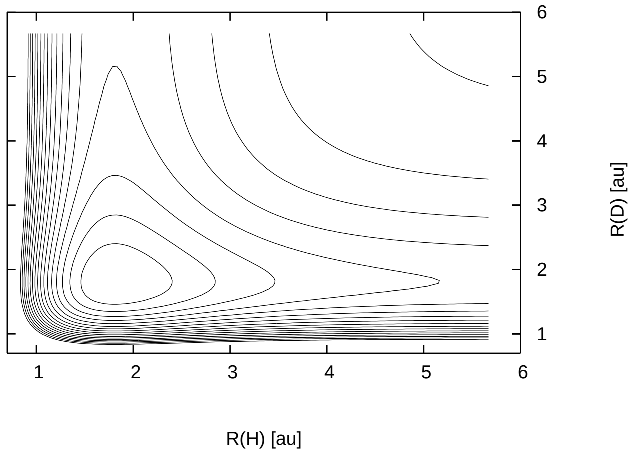

Figure 5.2: *Potential energy surface of the water molecule for fixed bending angle (104°). The contours start at zero energy and increase incrementally with 0.05 a.u..*

Morse-potentials as

$$V(r_H, r_D) = D(1 - e^{-\beta(R_H - r_0)})^2 + D(1 - e^{-\beta(R_D - r_0)})^2 - \frac{A(R_H - r_0)(R_D - r_0)}{1 + e^{(R_H - r_0)(R_D - r_0)}}. \tag{5.1}$$

The potential is taken from Ref. [78], with parameters $D = 0.2092$ a.u., $\beta = 1.1327$ a.u., $r_0 = 1.81$ a.u and $A = 0.00676$ a.u.. The kinetic energy operator is given as

$$T = -\frac{1}{2m_H}\frac{\partial}{\partial R_H^2} - \frac{1}{2m_D}\frac{\partial}{\partial R_D^2}, \tag{5.2}$$

where m_H is the mass of the hydrogen atom and m_D of the deuterium atom. The dipole moment was taken from Ref. [79] describing a bond-dipole moment as

$$\mu(R_H) = \mu_0 R_H \cdot e^{-(R_H/r_0)}, \tag{5.3}$$

where $\mu_0 = 1.63$ a.u. and $r_0 = 1.14$ a.u. The dipole moment is equal for both coordinates. Assuming, the HOD molecule is fixed in the xz plane (compare to fig. 5.1), the total dipole moment is given by $\mu(R_H, R_D) = \mu(R_H) + \mu(R_D)$ for a z-polarized electric field. A x-polarized electric field can be described by using a dipole moment of the form $\mu(R_H, R_D) = \mu(R_H) - \mu(R_D)$. To calculate the term $\mu \cdot E(t)$ the angluar dependency has to be included. That means the field is calculated by

$$\begin{aligned} E(t) &= E_c(t) \cdot \mu(R_H, R_D) \cos(52^\circ), \qquad \text{(for } z\text{-polarization)} \qquad (5.4) \\ E(t) &= E_c(t) \cdot \mu(R_H, R_D) \sin(38^\circ) \qquad \text{(for } x\text{-polarization).} \qquad (5.5) \end{aligned}$$

5.2 Dissociation

The branching ratio between the two fragment configurations is determined employing two different approaches within instantaneous control. The fragmentation ratio is calculated by applying a mask function $cof(R)$ which collects the part of a wave packet passing over a defined bondlength value

$$cof(R) = \begin{cases} 1 & : \; R < 5\,\text{a.u.} \\ cos^2(0.5\pi(5\,\text{a.u.} - R)) & : \; R \geq 5\,\text{a.u.} \end{cases} \qquad (5.6)$$

The wave packet is multiplied by the mask function in both coordinates. The result is collected as it displays the dissociated part of the wave packet. In a first example the electric field is derived from the condition that the temporal change of one coordinate's momentum is zero (comp. chapter 3). Another subsection describes the fields constructed by a heating process. Furthermore, the role of the polarization of the irradiating field is compared. It is mentioned explicitly that in this work both coordinates couple equally to the strong electric field.

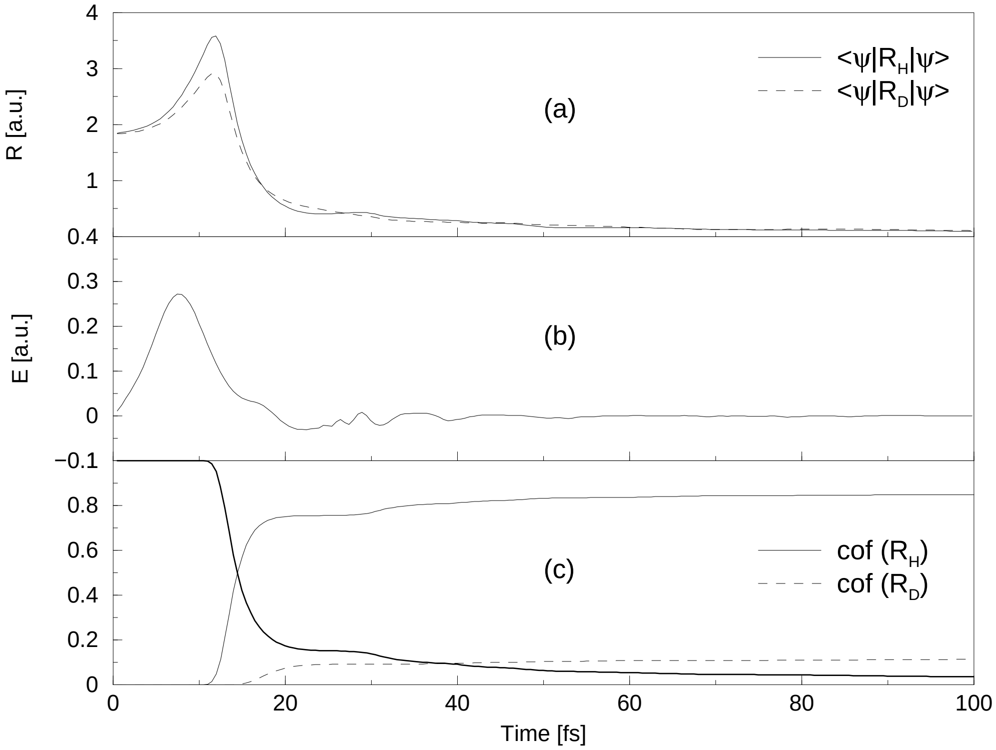

Figure 5.3: *HOD dynamics for a field derived with the momentum condition. Panel (a): expectation values of bondlengths. Panel (b): constructed electric field driving the instantaneous dynamics. Panel (c): temporal development of the norm (solid line) and the dissociated parts of the system, as indicated.*

5.2.1 Momentum Condition

As a first method the field is determined by the condition of the minimal temporal momentum change $d\langle p_H\rangle/dt = 0$. The field was constructed by the commutator

$$E(t) = \frac{E_0}{\hbar}\langle\psi(t)|[p(H),\mathcal{H}]|\psi(t)\rangle \tag{5.7}$$

$$E(t) = \frac{E_0}{\hbar}\left\langle\psi(t)\left|\frac{\partial V(R_H,R_D)}{\partial R_h}\right|\psi(t)\right\rangle \tag{5.8}$$

assuming a linear dipole moment $\mu(R_H,R_D) = \mu_1 R_H + \mu_2 R_D$, where $\mu_1,\mu_2 = 1$. In fig. 5.3 the dynamical behaviour is shown. The constructed electric field with $E_0 = 1.5$ a.u. has a relatively high field strength of 0.3 a.u., proceeding a dissociation process within one vibrational motion. This can be seen regarding the bond length expectation values in panel (a) compared with the dissociated part in panel (c). The dissociation process occurs at very short times, at longer times no fundamental change of the dynamical behaviour can be observed. Concerning the ratio of the exit channels the DO + H dissociation is executed with a 7 times higher probability. The strong field and the fast procedure feature the disadvantages of this method. Better results can be obtained imposing the heating condition as presented in the next subsection.

5.2.2 Energy Condition

The second possibility to selectively dissociate the molecule is to apply a heating process. Again, the H+OD channel ought to be populated. Therefore, the field is exclusively determined from the momentum in the R_H direction (compare to the two-dimensional double well dynamics in chapter 4):

$$E(t) = \frac{E_0}{\hbar} \langle \psi(t) \, | [\mu(R_H, R_D), T(P_H)] | \, \psi(t) \rangle. \tag{5.9}$$

The dipole moment now is non-linear, exhibiting the mathematical form according to eq. 5.3. The commutator yields a different condition, then. Neglecting second-order derivatives of the dipole-moment μ with respect to R the field is calculated by

$$E(t) = E_0 \cdot (\mu_H + \mu_D) \cdot \left\langle \psi(t) \left| \frac{\partial \mu(R_H, R_D)}{\partial R_h} \right| \psi(t) \right\rangle . \tag{5.10}$$

Fig. 5.4 shows a such constructed field. Panel (a) contains the expectation values of the two bondlengths, as indicated. The H-motion proceeds with a larger amplitude than the D-motion. The field (panel (b)) follows the vibrations in the

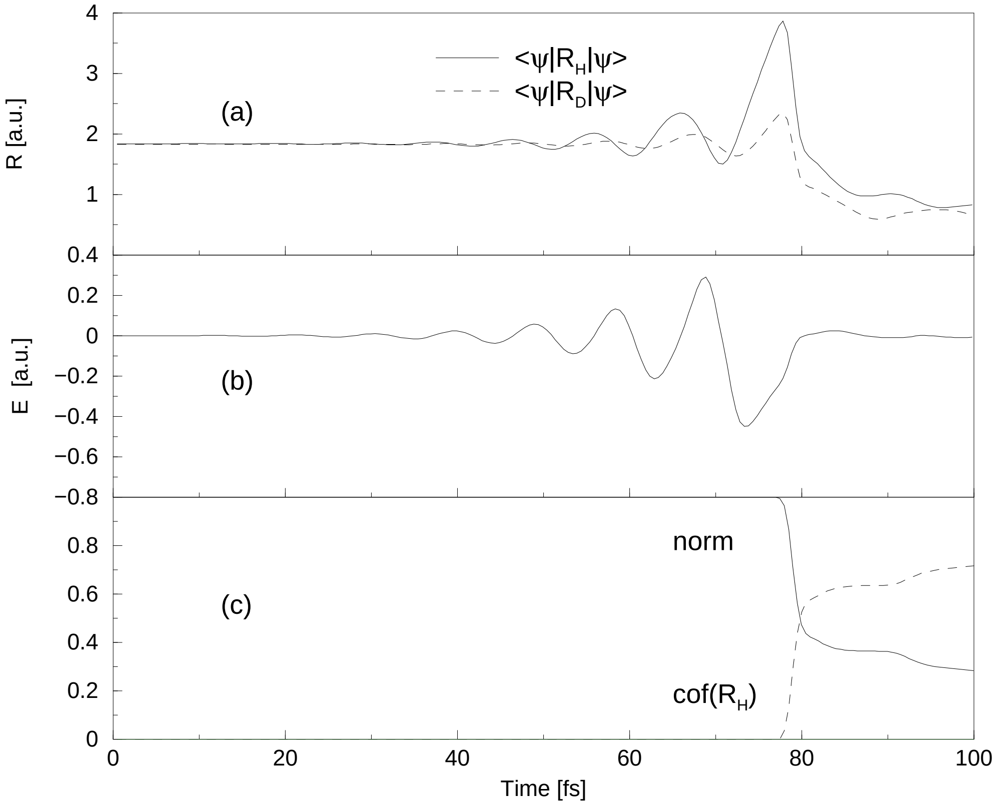

Figure 5.4: *HOD dynamics for a z-polarized field derived with the heating condition. Panel (a): expectation values of bondlengths. Panel (b): constructed electric field driving the instantaneous dynamics. Panel (c): temporal development of the norm and the dissociated part of the system.*

R_H degree of freedom, as discussed in chapter 4. The norm of the wave packets moving into the two reaction channels is also displayed in fig. 5.4. Starting at 65 fs, a first fraction of H+OD reaction products are built and a second burst of products occurs one OH-vibrational period later. For the chosen E_0 parameter of $1.3 \cdot 10^{-2}$ a.u., an overall dissociation probability of 90 % is found as on the calculated time scale the H+OD dissociation channel is not populated.

Next, the influence of the polarization of the electric field is examined. Employing the same E_0 as in the z-polarized case a similar behaviour is obtained. This case is illustrated in fig. 5.5. Here, dissociation occurs with a higher proba-

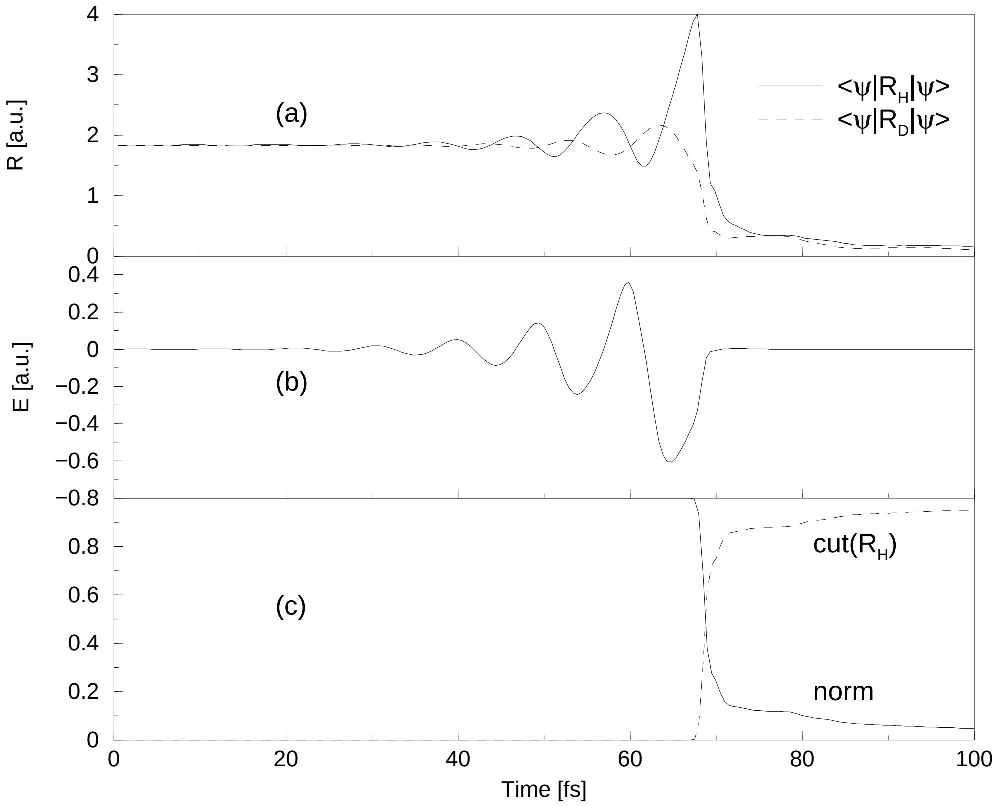

Figure 5.5: *HOD dynamics for a x-polarized field derived with the heating condition. Panel (a): expectation values of bondlengths. Panel (b): constructed electric field driving the instantaneous dynamics. Panel (c): temporal development of the norm and the dissociated part of the system.*

bility. As the field intensities are very strong the HOD molecule can be seen as a prototype system. In the next chapters the instantaneous dynamics approach is applied to heavier molecules controlling the population ratios of excited electronic states.

Chapter 6

Controlling Resonant vs. Non-Resonant Transitions

The control theories introduced in chapter 3 concerning electronic transitions of molecules are based on resonant transitions. In order to compare resonant to non-resonant excitation processes, methyl iodide being a well-known model example is regarded. The structureless absorption band, the so called A-band region centered around a wavelength of 266 nm, indicating a fast and direct dissociation process, has been studied experimentally [80,81], as well as theoretically [82], for reviews see e.g. Refs. [83, 84]. The absorption spectrum in the range of 210 to 350 nm does not exhibit a vibrational finestructure indicating only small contributions of the H-atoms to the approximately pure C – I vibrational motion [83]. At least five electronic states are accessible in the A-band, three of them being dipole-allowed. But the main contribution to the dissociation products is given by the repulsive $^3Q_0$ state leading to a methyl radical $[x^2A_2'']$ and a spin-orbit excited iodide radical $[I(^2P_{1/2})]$ [80]. A conical intersection with the $^1Q_1$ state is likewise leading to the same dissociation products. The third accessible, also repulsive electronic state, the $^3Q_1$ state, leading to ground state iodide radicals

$[I(^2P_{3/2})]$ carries a small oscillator strength and can be neglected in describing the photodissociation dynamics [80]. Time-dependent calculations have been performed implementing model systems in two [85–87], three [88], four [89], five [84], and also nine [90] dimensions. In this work, a one-dimensional, pseudo-diatomic model including one and two dissociative potential curves in the A-band, respectively is assumed in order to actively control dissociationratios.

Experiments by Gedanken et.al. investigated multi-photon transitions in methyl iodide with a wavelength of 798 nm [91]. While the A-band is accesible by a three-photon process, a corresponding four-photon process gave evidence of a Rydberg $5p\pi \rightarrow 6s$ excitation. The aim of the calculations of this work was the question whether it is possible to modify a laser pulse such that the ratio of the dissociation products of the particular states can be controlled. In order to do so, the one-dimensional model system is extended by adding a generic dissociative potential being likewise accessible by a four-photon process from the electronic ground state. The model system, consisting of three and four one-dimensional potential curves, respectively, serves as a base for a comparison of different control theories. Thereby, the possibility to restrict the algorithms to perform a non-resonant three-photon process is taken into account.

6.1 Description of the 3-Level Model System

The time-dependent Schrödinger-equation for the simplified one-dimensional model system with three electronic states ($|X\rangle, |1\rangle, |2\rangle$) is of the form

$$i\hbar\frac{\partial}{\partial t}\begin{pmatrix}\psi_X\\ \psi_1\\ \psi_2\end{pmatrix}=\mathcal{H}\begin{pmatrix}\psi_X\\ \psi_1\\ \psi_2\end{pmatrix}, \tag{6.1}$$

with the Hamiltonian $\mathcal{H}$:

$$\mathcal{H}=\begin{pmatrix}\mathcal{H}_X & w_{X1}(t,R) & w_{X2}(t,R)\\ w_{1X}(t,R) & \mathcal{H}_1 & w_{12}(t,R)\\ w_{2X}(t,R) & w_{21}(t,R) & \mathcal{H}_2\end{pmatrix}. \tag{6.2}$$

Besides the Hamiltonians $\mathcal{H}_n$ describing the nuclear motion in state $|n\rangle$, the field-molecule interaction is of the form

$$w_{nm}(t,R) = -\mu_{nm}(R)E(t), \tag{6.3}$$

with the electric field $E(t)$ and the dipole matrix elements $\mu_{nm}(R)$. For simplicity, the Condon-appoximation is applied ($\mu(R) = \mu = 1$), so that the molecule-field coupling is taken to be equal in and between all electronic states. Below, several coupling schemes are investigated, which will be specified later.

With $\mathcal{H}_n = T + V_n$ and T being the kinetic energy operator $p^2/2m$ and m the reduced mass of the $\mathrm{X-I}$ ($\mathrm{X = CH_3}$) pseudo molecule the Hamiltonian $\mathcal{H}$ can be devided into a coordinate- and momentum part, and another term depending explicitly on time. For simplification, the numerous potential surfaces of the A-band region are reduced within the model system to the one single potential

Table 6.1: *Parameters for potential energy functions in [a.u.]*

a_{11}	51.53	β_{11}	1.64	k_f	0.036225	g_1	0.0874
a_{12}	25.15	β_{12}	1.3	ϵ_0	0.034642	g_2	0.87094
a_{21}	0.71398	β_{13}	1.4	x_0	0.619702	g_3	4.04326
a_{22}	0.82978	β_{21}	0.38597	R_0	4.16799	g_4	0.036225
a_{23}	0.048149	β_{22}	1.5	R_{02}	4.5	g_5	0.15581
		β_{23}	1.5	r_x	R-0.20218x	g_6	0.4914
		β_{24}	0.5	x	0.1	g_7	0.619702
				ϵ_2	0.0615	g_8	0.034642

curve ${}^3Q_0$ $|1\rangle$ (which dominates the A-band absorption spectrum). The form of the potential is taken from Refs. [86, 87] and reduced into one dimension by fixing one parameter of the two-dimensional potential surface given there. The Rydberg state ($|2\rangle$) is described by a potential having the form of the ${}^1Q_1$ state shifted by an additional parameter ϵ_2:

$$\begin{aligned}
V_X(R) &= g_1(e^{-g_2(R-g_3)}-1)^2 - g_1 + 0.5(g_4 + (g_5 - g_4)e^{(-g_6(R-g_3))}) \\
&\cdot \quad (x - g_7 e^{-g6\cdot(R-g_3)})^2 - g_8 \\
V_1(R) &= a_{11}\cdot e^{-\beta_{11}\cdot R} + 0.5\cdot(k_f + a_{12}\cdot e^{-\beta_{12}\cdot R})(x - x_0\cdot e^{-\beta_{13}(R-R0)})^2 \\
V_2(R) &= \epsilon_2 + (a_{21}e^{-\beta_{21}\cdot R}/\{1+e^{\beta_{22}(R-R_{02})}\} + a_{22}e^{-\beta_{23}r_x} \\
&+ \quad a_{23}e^{-\beta_{24}r_x} + 0.5\cdot k_f x^2 - \epsilon_0) \qquad (6.4)
\end{aligned}$$

The potentials are displayed in fig. 6.1, which also indicates the multiphoton excitation scheme to be discussed in what follows. Their colors black (ground state $|X\rangle$), red (state $|1\rangle$) and green (state $|2\rangle$) are retained throughout this chapter encoding populations and dissociation ratios of the various states.

Because of the dissociative character of the two upper potential surfaces, it is necessary to apply a mask function (cof) removing the outgoing parts of the

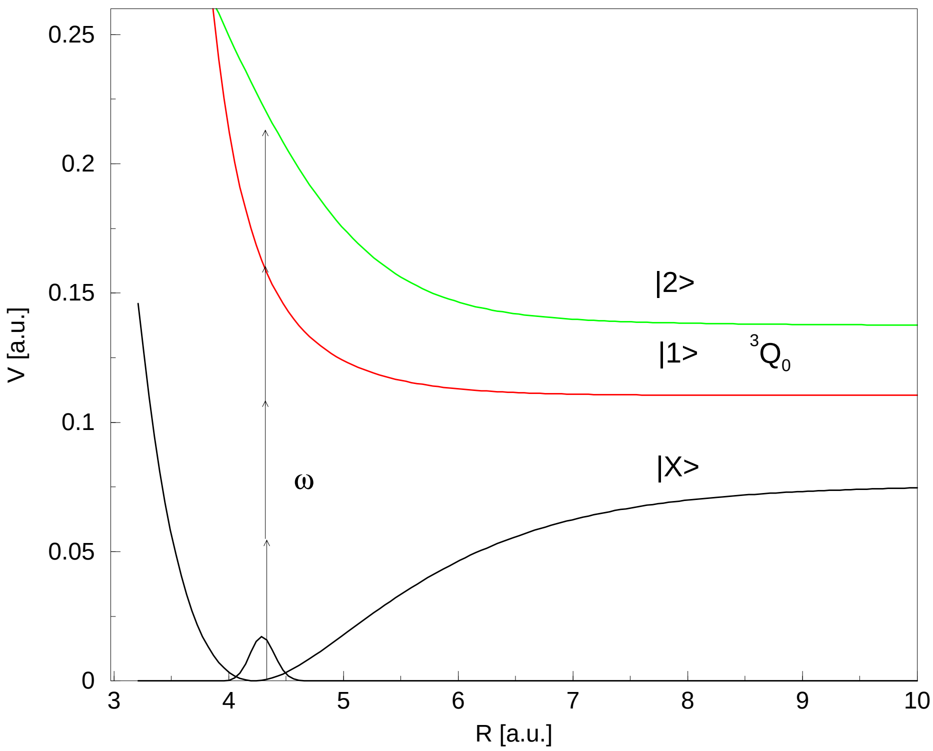

Figure 6.1: *Potential energy sufaces in methyl iodide in one dimension, assuming a reaction coordinate describing the* $X - I$ *(*$X = CH_3$*) separation. The form of the potentials for* $|X\rangle$ *and* $|1\rangle$ *are taken from [86,87]. State* $|2\rangle$ *is a model potential parameterized as described in the text. The arrows indicate three-photon non-resonant plus an additional one-photon resonant transition at a wavelength of* $5.71{\cdot}10^{-2}$ *a.u. [798 nm]. The colors black, red and green are used throughout this chapter to denote populations and dissociation yields in the* $|X\rangle, |1\rangle$ *and* $|2\rangle$ *electronic states, respectively.*

wave packets:

$$cof(R) = \begin{cases} 1 & : \quad R < 13\,\text{a.u.} \\ cos^2(0.5\pi(13\,\text{a.u.} - R)) & : \quad R \geq 13\,\text{a.u.} \end{cases} \tag{6.5}$$

The parts of the wavepacket being removed as a function of time are collected and are taken to measure the population in the respective electronic state.

6.2 Control of Photodissociation Dynamics

Applying a Fourier-transform limited Gaussian laser pulse with a carrier wavelength of 798 nm [$5.71{\cdot}10^{-2}$ a.u.], a field strength of 0.15 a.u. and a spectral width of $\beta = 1000$ cm^{-1} yields a temporal evolution of populations and dissociation yields as is shown in fig. 6.2.

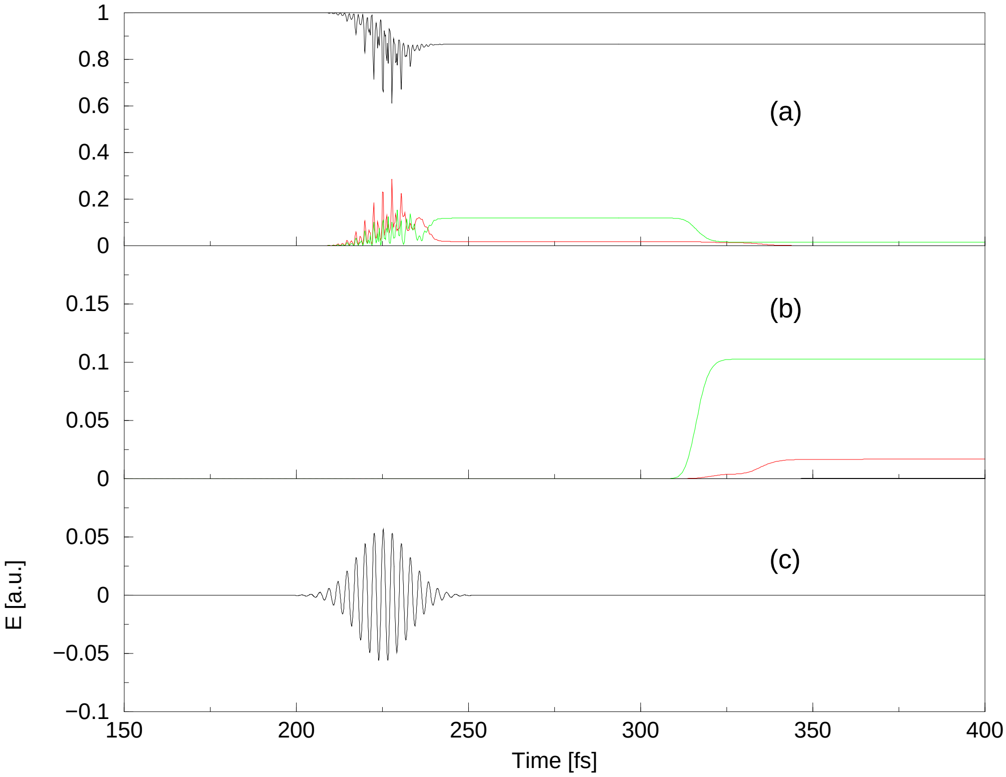

Figure 6.2: *Panel (a) displays the temporal evolution of population; (b): dissociated part of the wave packets, the main dissociation product results from state* $|2\rangle$*, but small contributions from state* $|1\rangle$ *are also obtained. Panel (c): The Gaussian pulse, E = 0.15 a.u.,* $\lambda = 798$ *nm,* $\beta = 1000$ *cm*$^{-1}$*. The colors of (a) and (b) are chosen according to the corresponding potential curves.*

Within the calculation, the coupling in eq. (6.2) is set to $w(t) = -E(t)$. Regarding the behavior of the population, oscillations in the three states can be observed. As can be taken from the figure, the main dissociation channel corresponds to the electronic state $|2\rangle$. Thereby, the fragment distribution depends on the spectral width β and strongly on the pulse intensity.

6.2.1 Genetic Algorithm

In order to maximize the population of state $|1\rangle$ a genetic algorithm was applied. Starting with a population of 10 individuals, a cross-over probability of 50% and a mutation probability of 30%, four chirp-parameters and the field strength were refined. Thereby, the evolutionary parameters are to be deliberated: a huge population dimension may lead to faster convergence but inflates the calculation time, while a very small dimension may never find a minimum. Similarly, the probability of modification has to be estimated, influencing the convergence behavior, likewise. An adequate large mutation or cross-over probability arranges for a sufficient number of new coincidental numbers in a gene's parameters. As a modified parameter set need not to be better than the "parental" unmodified parameter set, an undersized modification probability could cause to be trapped in a local minimum. In contrary, an oversized evolutionary modification probability may eliminate good parameters from the gene-pool too early. The convergence behavior for the chosen evolutionary parameters was checked upon the basis of a simple minimization problem.

Several calculations have been made, varying the laser field strength and spectral width β in the frequency domain. A small spectral width β leads to longer pulses in the time domain. For numerical reasons the step-size, both in frequency- $d\omega$ as well as in time-domain dt, are confined to very small numbers. The reciprocal relation between these two incrementals

$$dt = \frac{2\pi}{d\omega N}, \tag{6.6}$$

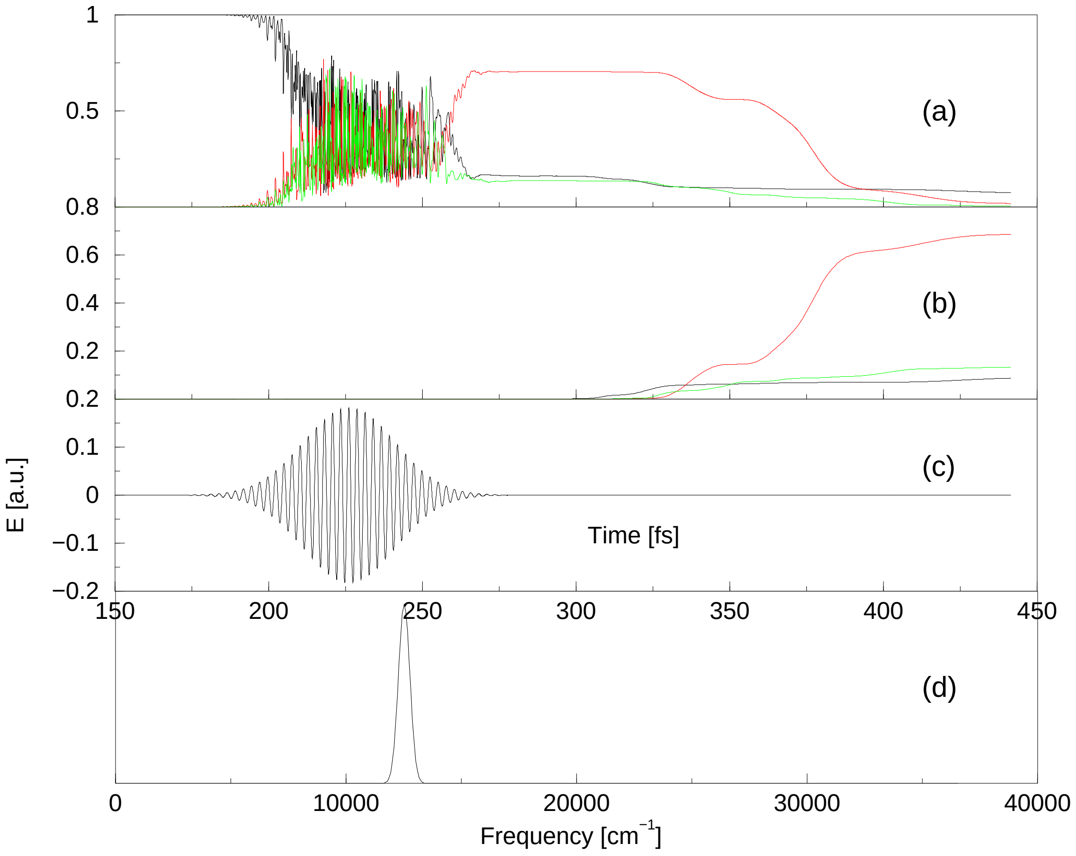

Figure 6.3: *Pulse design using genetic algorithms. Panel (a): temporal development of population and (b) dissociation yields for a pulse (c) with* β *= 500 cm*$^{-1}$, $a_1 = -2.24 \cdot 10^3$, $a_2 = 1.01 \cdot 10^6$, $a_3 = -2.27 \cdot 10^6$, $a_4 = 3.46 \cdot 10^6$ *and an field strength of E = 0.965 a.u. in time domain and (d) the absolut square in frequency domain.*

with N being the number of grid points requires a relatively huge grid (Nyquist-frequency: 2.733 a.u. [600000 cm^{-1}]) size. From $N = 2^{14}$ a step-size of $dt = 1.17$ a.u. [0.028 fs] and $d\omega = 3.37 \cdot 10^{-4}$ [73.25 cm^{-1}] arises. Fig. 6.3 and 6.4 display the temporal development of the norm in the various electronic states and the respective dissociation yields, as well as the parameterized pulses for two spectral widths, $\beta = 500$ and 1000 cm^{-1}.

Both pulses are ultra-intense. Noticeably, the first (linear) chirp parameters α_1 take in both cases negative values, while the second ones α_2, a quadratic shift

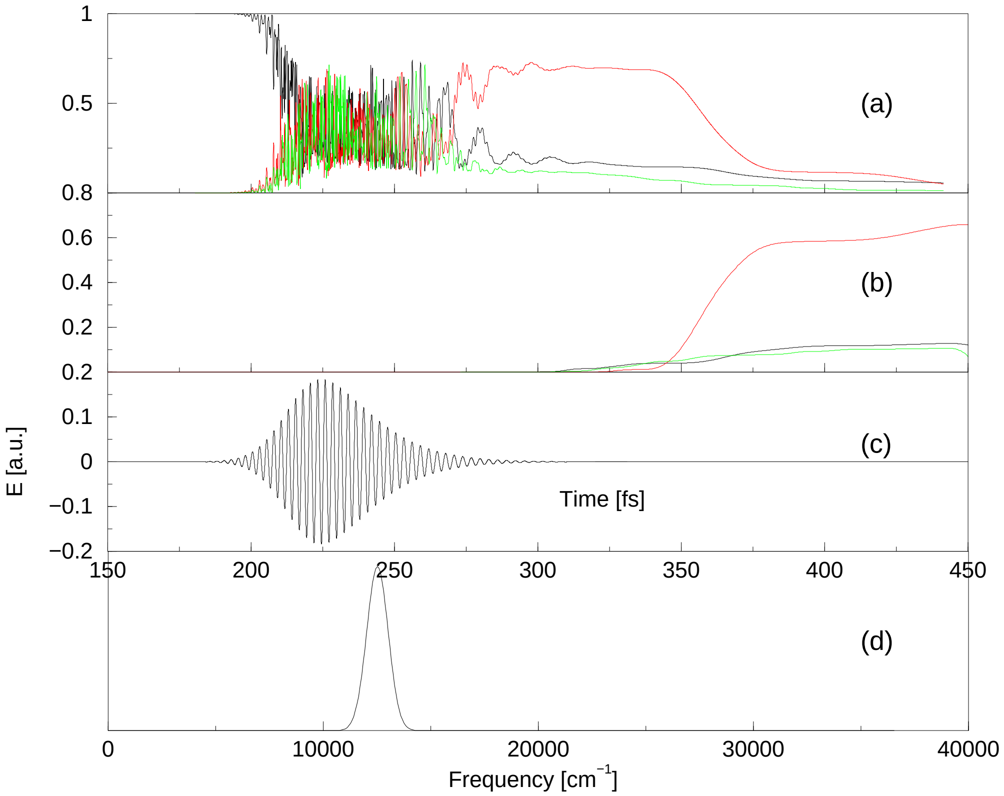

Figure 6.4: *Pulse design using genetic algorihms, see fig. 6.3 for a pulse (c) with* $\beta = 1000\,cm^{-1}$, $a_1 = -8.72 \cdot 10^4$, $a_2 = 4.51 \cdot 10^6$, $a_3 = 3.12 \cdot 10^6$, $a_4 = 1.91 \cdot 10^6$ *and an field strength of E = 0.677* a.u. *in time domain and (d) in frequency domain.*

of ω_0, are positive. [The lower-order parameters (phase factor, group delay) are not considered here.]

The negative value of α_1 can be estimated by displaying the difference potentials:

$$\begin{aligned} V_2(R) - V_X(R) &= D_{2X} \\ V_1(R) - V_X(R) &= D_{1X} \qquad (6.7) \\ V_2(R) - V_1(R) &= D_{21} \end{aligned}$$

It can be seen from fig. 6.5 that the differences between the potential energy

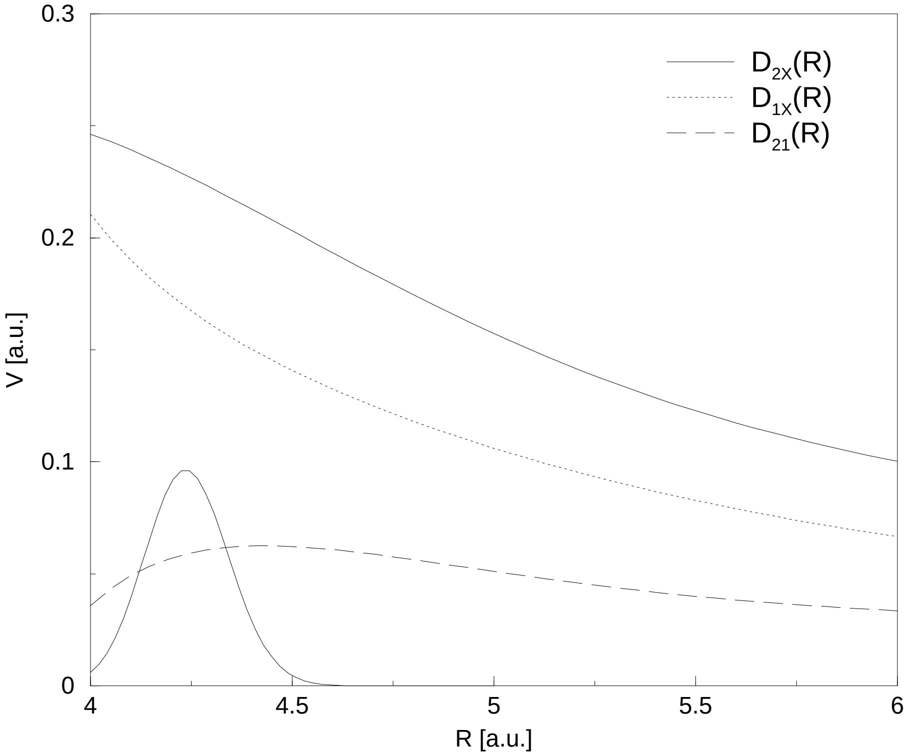

Figure 6.5: *Difference potentials of MeI, as indicated. The position of the ground-state wave-function is also displayed.*

surfaces diminish with increasing bond-lengths. Considering the temporal development of the population it is assumed that its dynamical behaviour occurs at small distances (around the ground-state wave-function's position) only. At the end of the pulse duration the generated excited-state wave packets are moving outward into the region of decreasing difference potential. The negative sign of the linear chirp parameter α_1, denoting a red-shift (i.e. the smaller frequencies arise in a temporal picture at later times) causes a population-transfer into the first excited state avoiding a population transfer into the second excited state. It can be read off the figure that the energy difference between states $|1\rangle$ and $|X\rangle$ decreases more rapidly than the difference potential between states $|2\rangle$ and $|1\rangle$. At the trailing edge of the pulses where the smaller frequencies emerge, a transition $|1\rangle \leftarrow |X\rangle$ is favored as the other transition's energies are not diminished to the same degree.

The positive sign of α_2, a quadratic shift elicits a shape deforming of the laser pulse. The symmetric Gaussian pulse envelope deforms to an asymmetric function, where the raising edge is shorter than the falling edge of the pulse. Therfore, the lower frequencies, arising mainly in the falling edge, act with a higher intensity.

These simple considerations are presented in order to estimate the dynamical processes induced by the chirped pulse. For a more accurate description a Fourier analysis of the pulse is to be performed. The parametrical defined pulses obtained in terms of chirp parameters are efficient in driving the dissociation yield. Dissociation deriving from target state $|1\rangle$ occurs with a 4.5 times higher probability namely about 70 %. It is therefore possible to reverse the ratio of dissociation products. While a rough estimation of the chirp parameter's sign can be explained in a physical picture, the exact numbers resulting from the performed genetic algorithm are very difficult to interpret in terms of a physical meaning.

6.2.2 Optimal Control Theory (OCT)

Within Optimal Control Theory the final time t_f and the position of a pre-defined wavefunction at final time $\varphi_f(t_f)$ serve as a parameter. In our calculations the initial wave function $\varphi_i(t=0)$ is the groundstate wave function. The target wave function in state $|1\rangle$ was chosen according to eq. (3.9), centered around 11.4 a.u. and slightly broadended compared to the ground state wavefunction [92]. As an initial guess a Gaussian pulse with the central wavelength of $\lambda = 798$ nm and a FWHM = 100 fs was assumed. The overlap-function $O(t)$ for the coupling scheme given in eq. (6.2) is given by

$$\begin{aligned} O(t) &= \Im\langle\psi|\mu|\chi\rangle = \Im\left\{\langle\psi_X(t)|\chi_1(t)\rangle + \langle\psi_X(t)|\chi_2(t)\rangle\right. \\ &+ \left.\langle\psi_1(t)|\chi_X(t)\rangle + \langle\psi_1(t)|\chi_2(t)\rangle + \langle\psi_2(t)|\chi_X(t)\rangle + \langle\psi_2(t)|\chi_1(t)\rangle\right\} \end{aligned} \quad (6.8)$$

where the $\chi_n(t)$ and $\psi_m(t)$ are the backward and forward-propagated wave packets, respectively. Calculating the time-dependend overlap, the electric field can be determined according to eq. (3.13). Since the backward propagated functions $\chi_n(t)$ are constructed by projection of $\psi_1(t_f)$ onto the target state $\varphi_f(t_f)$, the form of the optimal pulse depends strongly on the final time t_f as can be taken from fig. 6.6 and fig. 6.7.

Comparing the shaped pulses for 400 and 600 fs it can be seen that for a short final time t_f multi-photon processes are favored while longer times prefer one-photon processes, a tendency which is well known in literature [93]. Furthermore, in fig. 6.6 for short final time t_f the field interaction starts immediately, exciting the system into the upper electronic states. Since for the excited states wave packets a certain time (approx. 100 fs) is needed to reach the target state's position, a second pulse starting near 300 fs re-excites the system such that at $t_f = 400$ fs the overlap of the forward propagated wave function and φ_f is maximized.

A longer final time t_f of 600 fs lets the pulse start later (at about 450 fs) again that the wavepacket moving outwards overlaps with the target state wave function at $t_f = 600$ fs. The excitation is performed by a one-photon process. Regarding the disociation yield, very poor results at the final time (about 10 %) are achieved but the increase at later times (about 70 %), because $\psi_1(t_f)$ is

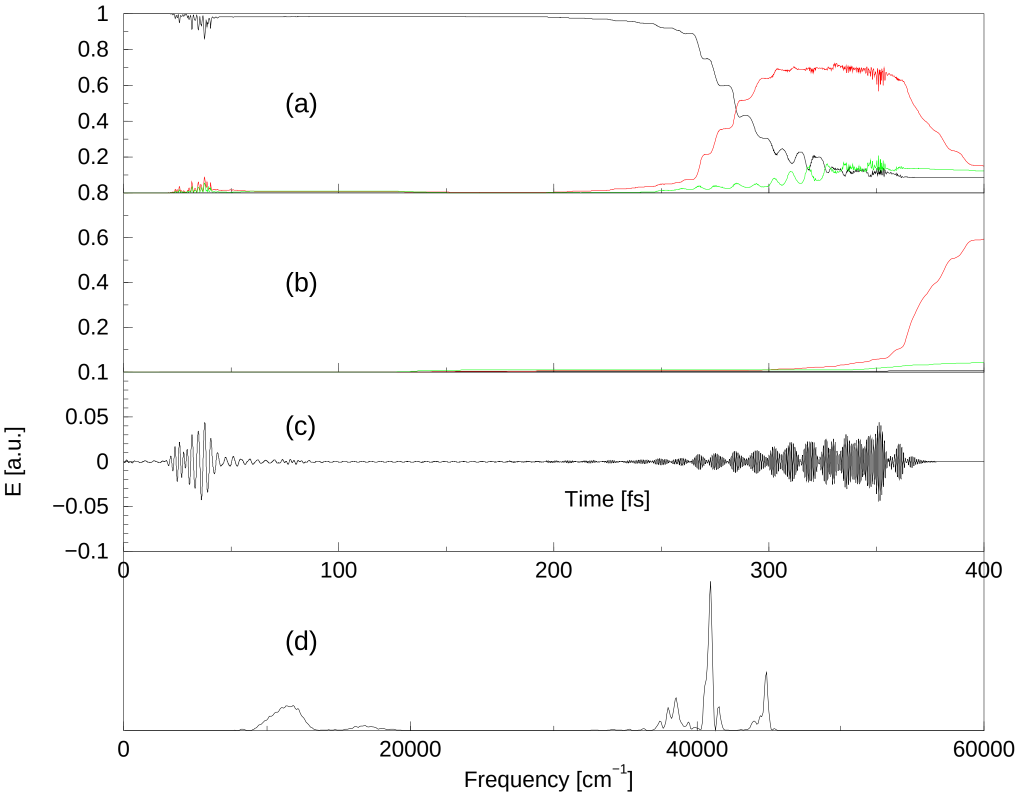

Figure 6.6: *Pulse shaping with optimal control theory. Panel (a): Temporal development of population and (b) the dissociation yields for a final time* $t_f = 400fs$*. Panel (c) shows the optimal pulse in time and (d) in frequency domain.*

centered around 11.4 a.u. and dissociation is defined to occur at $R > 13$ a.u. (see eq. (6.5)). For this case a calculation succeeding the final time is performed in oder to demonstrate the dissociation amount after the pulse derived from the optimal control theory has switched off.

The algorithm has just few possibilities to reach the target, either with a strong pulse, shaking the population via Rabi-like oscillations, remaining the bonding distance at shorter values so the wave packet moves outwards at longer times (see e.g. genetic algorithm), or with a tardy starting pulse via a one-photon process as happens here. (In principle, the tendency is influenced by the choice of the strengthning parameter α.) In fig. 6.6 (short time, $t_f = 400$ fs), parts of the

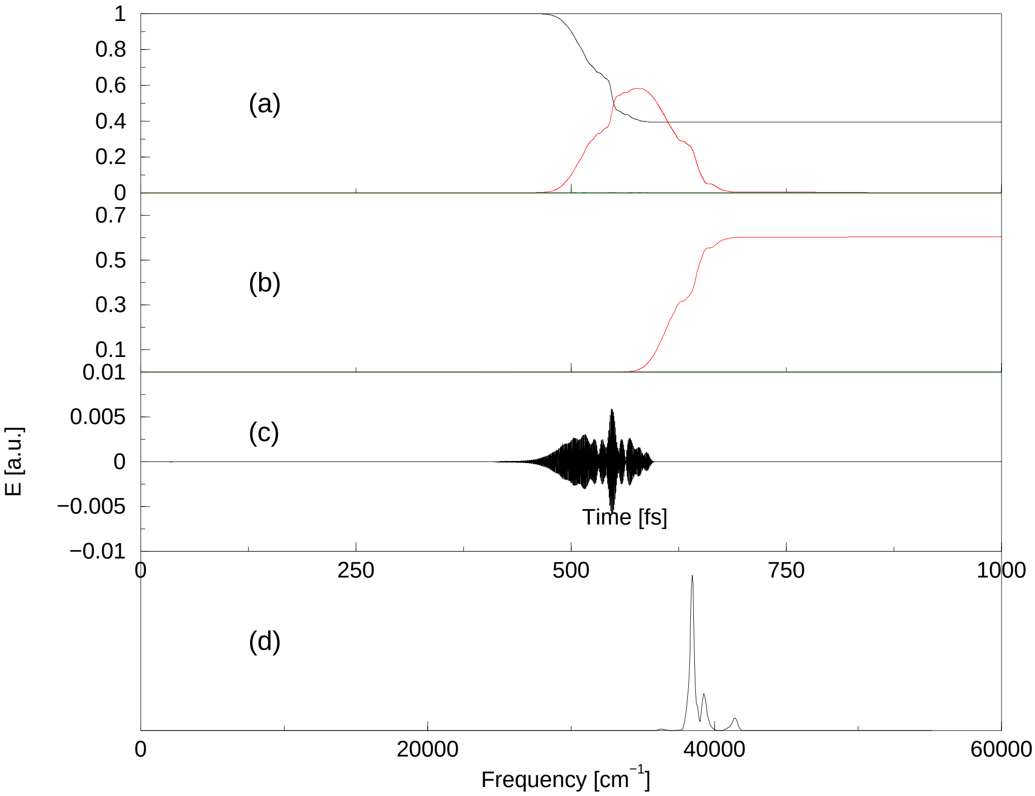

Figure 6.7: *As in fig. 6.6, pulse shaping with optimal control theory for a final time* $t_f = 600fs$. *Additionally later times, after the control pulse has switched off are shown.*

spectrum are near 12000 cm^{-1}, the corresponding 3-photon frequency, while these contributions to the spectrum are absent in the other spectrum. The 1-photon frequency at 36000 cm^{-1} can be found in both spectra.

Within optimal control theory a system starting from an initial state $|\varphi_0\rangle$ is driven into a pre-defined target state $|\varphi_f\rangle$ at a certain final time t_f by an iterative algorithm. There are only few possibilities e.g. the choice of final time t_f and position of the target state to influence the variationally obtained optimal field. The derived fields, composed of several frequency components are very efficient but perform mainly the corresponding one-photon excitation. An interpretation in terms of a physical meaning is not easy at all, as no simple considerations concerning the different temporal und frequency components can be made. In the next approach the algorithm is restricted to find an electric field transfering population with a fixed central frequency.

6.2.3 Restricted OCT

Using the restriction conditions for optimal control theory, a search in terms of chirp parameters of a field with a defined central frequency can be performed. Thus, the pulse is rewritten in terms of a Taylor series in frequency domain. With the additional condition $\delta J = 0$ for all $\delta\alpha_i$ the set of chirp parameters can be determined. For N chirp parameters N coupled integral equations are obtained. With the approximations discussed in section 3.3, the first $(F_i(\alpha_i))$ and second $(A_i(\alpha_i))$ partial derivatives of the electric field $E(\omega, \alpha_1, \alpha_2 ...)$ with respect to the chirp parameters $\alpha_1, \alpha_2 ...$ are calculated as

$$\begin{aligned}
\frac{\partial E_1(\omega)}{\partial \alpha_1} &= -i \cdot (\omega - \omega_0)^2 \cdot \exp(-((\omega - \omega_0)/\beta)^2 - i(\alpha_1 \cdot (\omega - \omega_0)^2 \\
&+ \alpha_2 \cdot (\omega - \omega_0)^3 + \alpha_3 \cdot (\omega - \omega_0)^4 + \alpha_4 \cdot (\omega - \omega_0)^5)) \\
&\vdots \\
\frac{\partial^2 E_1(\omega)}{\partial \alpha_1^2} &= -(\omega - \omega_0)^4 \cdot \exp(-((\omega - \omega_0)/\beta)^2 - i(\alpha_1 \cdot (\omega - \omega_0)^2 \\
&+ \alpha_2 \cdot (\omega - \omega_0)^3 + \alpha_3 \cdot (\omega - \omega_0)^4 + \alpha_4 \cdot (\omega - \omega_0)^5)). \\
&\vdots
\end{aligned} \tag{6.9}$$

The partial derivatives are Fourier-transformed into time domain and the $2N$ integral equations

$$\begin{aligned}
F_1(\alpha_1) &= \int_{t_0}^{t_f} dt\, (O(t) - 2\lambda E(t)) \cdot \frac{\partial E(t)_1}{\partial \alpha_1} \\
&\vdots
\end{aligned} \tag{6.10}$$

$$
\begin{aligned}
A_1(\alpha_1) &= \int_{t_0}^{t_f} dt\,(O(t) - \lambda E(t)) \cdot \frac{\partial^2 E(t)_1}{\partial \alpha_1^2} - \lambda \frac{\partial E_1}{\partial \alpha_1} \\
&\vdots
\end{aligned}
$$

are solved numerically. In the above equations, $E(t)$ is the electric field, $O(t)$ the overlap function as before (eq. (6.8)) and λ is given by the overlap function and the strength parameter α

$$
\lambda = -\sqrt{\frac{1}{\alpha} \int_{t_0}^{t_f} dt\, O(t)^2}. \tag{6.11}
$$

The new set of chirp parameters is determined with the help of eq. (3.18). Then, using these chirp parameters, the new electric field $E(\omega, \alpha_1, \alpha_2 \cdots)$ is calculated and Fourier-transformed into time-domain. Fig. 6.8 shows a such derived field and the corresponding dynamics for a set of four chirp parameters, where $\alpha_i \in [-10^6; +10^6]$.

The approach to restrict optimal control theory in terms of the chirp parameters yields only poor results concerning the dissociation yield and the ratio of dissociation products deriving from the target state $|1\rangle$. Compared to the random genetic algorithms a linear search described by a clear mathematical access is executed. The functional J differs from the one defined for the genetic algorithms as a maximal overlap of wave functions at a certain time t_f is maximized. Therefore, the system is forced to excite such that the generated wave packet in moving onward overlaps with the target wave function. Genetic algorithms possess a lower dependence concerning the time dissociation takes place, as the dissociated part in one electronic state is collected and maximized and no final time t_f influences the results.

The chirp parameters α_i differ in their absolute values compared to the ones

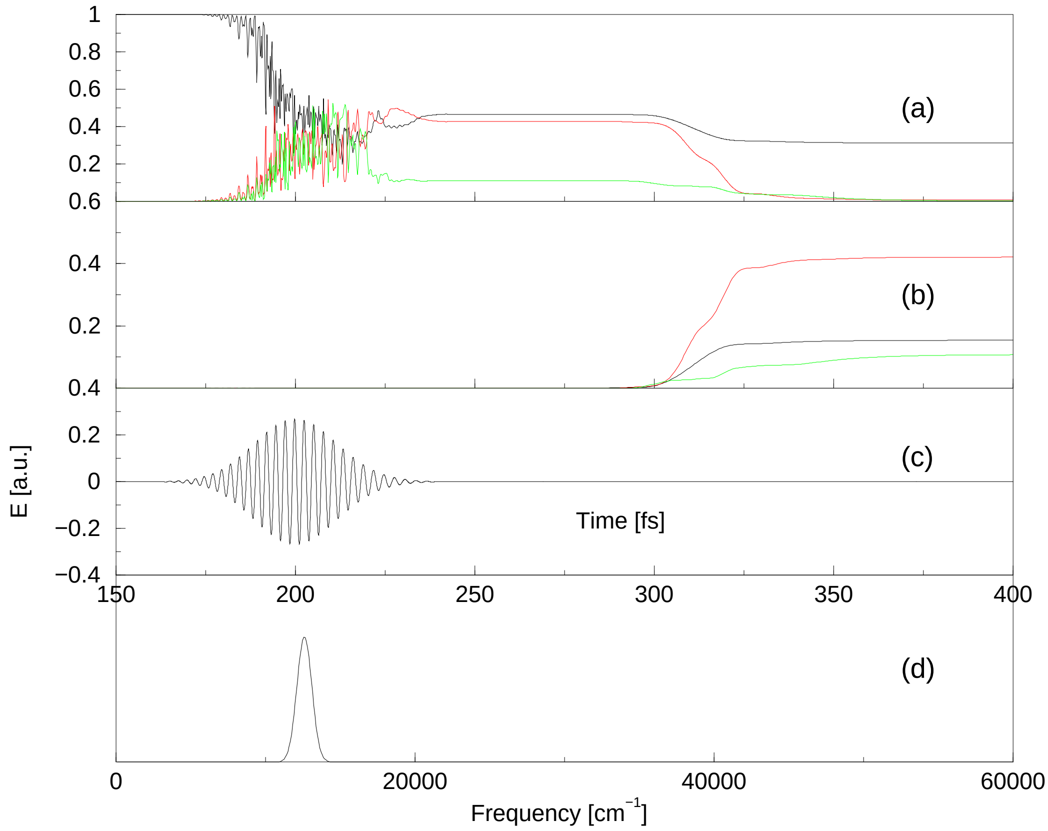

Figure 6.8: *Pulse shaping with restricted optimal control theory. Panel (a): Temporal development of population and (b) the dissociation yields for a final time* $t_f = 400 fs$. *Panel (c) shows the optimal pulse in time and (d) in frequency domain. Field strength parameter* α = *9.8e-4, E =0.35,* a_1 = *-57171.99,* a_2 = *393528.4 a.u.*

obtained from genetic algorithms, but the tendency, namely a negative sign for α_1 (-5.72·10^4) and a positive one for α_2 (+3.94·10^4), can be observed likewise. Thus, the restricted optimal control theory yields a picture consistent with the one discussed for the parameters refined with genetic algorithms.

6.2.4 Instantaneous Dynamics

Applying the instantaneous algorithm with the condition of monotonic increase of population in state $|1\rangle$ as introduced in chapter 3.4.4, a control field can be constructed in chosing

$$E(t) = -\frac{E_0}{\hbar} \sum_m \Im \langle \psi_1(t) | \mu_{1m} | \psi_m(t) \rangle, \tag{6.12}$$

where m takes the values X and 2 and the transition dipole moments μ_{1m} are constant within the Condon-approximation. In order to prepare a small amount of population in states $|1\rangle$ and $|2\rangle$ (for zero population the field is zero, see section 3.4.4) a seed pulse with a carrier wavelength $\lambda = 798$ nm, field strength $E_s = 0.05$ a.u. and a width FWHM = 20 fs is applied. After 50 fs the field is constructed via eq. (6.12) with a field strength parameter $E_0 = 1 \cdot 10^{-1}$ a.u. Fig. 6.9, panel (a) shows the population in the three electronic states, the colors according to the encoding as desribed before.

A close look at the electric field shows a strong and short pulse, centered around 55 fs. The seed-pulse does not influence the population appreciably but assures that there is a few percentage of population in the excited states. Then, the strong pulse transfers population via a 1-photon process into $|1\rangle$ state. After about 100 fs the exited state wave packet reaches the dissociation limit and the main part within the given timeframe is dissociated. Thereby a very high efficiency concerning the dissociation ratio and amount (85%) is achieved.

The derived pulse reflects the dynamical behaviour of the system, leading to a strong pulse transfering the main part of the population into the first excited state. This is due to the fact that the electric field is derived by the overlap of the excited wavepackets with the ground state wavepacket. Since the wavepackets moving outward have no significant overlap to ψ_X at later times, the main part is transfered into state $|1\rangle$ at once. Examining the spectral distribution of the pulse it can be seen that it exhibits frequency components around 36000 cm^{-1},

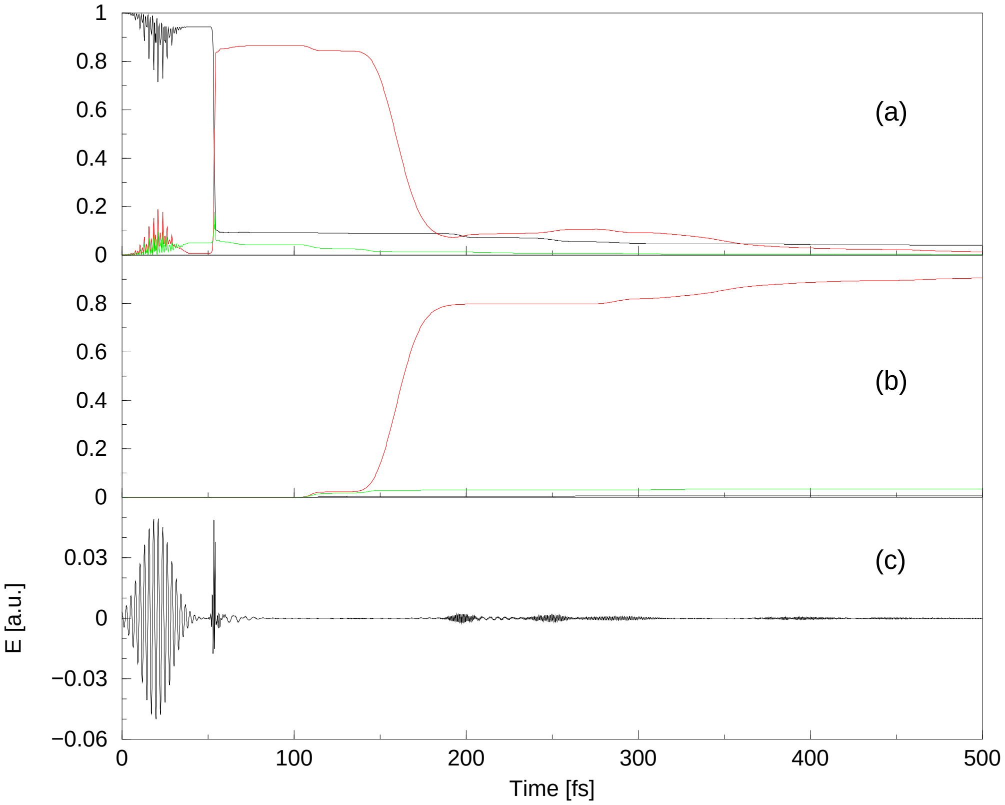

Figure 6.9: *Pulse constructed with the instantaneous dynamics algorithm. Panel (a): Temporal development of population and (b) the dissociation yield. Panel (c) shows the derived pulse in time domain obtained with a field strength parameter* $E_0 = 1 \cdot 10^{-1}$ *a.u. and a Gaussian seed pulse with field strength* E_s *= 0.05 a.u., a carrier wavelength* λ *= 798 nm and a width FWHM = 20 fs.*

describing an one-photon process. This follows from the fact that the population transfer is solely performed from the electronic ground state, being energetically seperated from the target electronic state $|1\rangle$ by about 36000 cm^{-1} – the same frequency as found here. As the algorithm describing instantaneous dynamics relies on a physical picture, only few possibilities exerting an influence on the system as well as the laser pulse are given. These effects will be discussed in the next chapter on a different model system.

6.2.5 Restricted Instantaneous Dynamics

Re-considering the excited states, it is realized that they are energetically seperated by about 12000 cm^{-1}. In order to restrict the algorithm to construct a field where the one-photon transition is eliminated and a three-photon process is enforced, the main population transfer has to originate from state $|2\rangle$. Hence, eq. (6.12) is converted to

$$E(t) = -\frac{E_0}{\hbar}\Im\langle\psi_1(t)|\psi_2(t)\rangle. \tag{6.13}$$

The algorithm can only work when there is a sufficient amount of population in state $|2\rangle$. Therefore, a much stronger seed-pulse with the same parameters as before, but an field strength of 0.1 a.u. is applied. In fig. 6.10 the obtained pulse and the driven dynamics are shown.

In comparison to the unrestricted case the seed-pulse causes not only a few percentage of population in the excited electronic states but an approximately equal distribution. Then, a very short pulse at 55 fs transfers the main part of population from $|2\rangle$ into state $|1\rangle$, exhibiting a similar dynamics as in the unrestricted case. Thereby, a dissociation yield of about 50 % is achieved. As shown in fig. 6.10, panel (d), the frequency of the pulse is – as to be expected – near 12000 cm^{-1}. Comparing the dissociation ratios to the ones obtained with the other algorithms, the field constructed by instantaneous dynamics yields a more accurate discrimination and additionally gives physical insight into the transfer processes of the system. The high field strength is within the scale of the other algorithm's intensities for a multiphoton process. In the next sections the comparison concerning the different algorithms is applied for different non-resonant transitions within this model system.

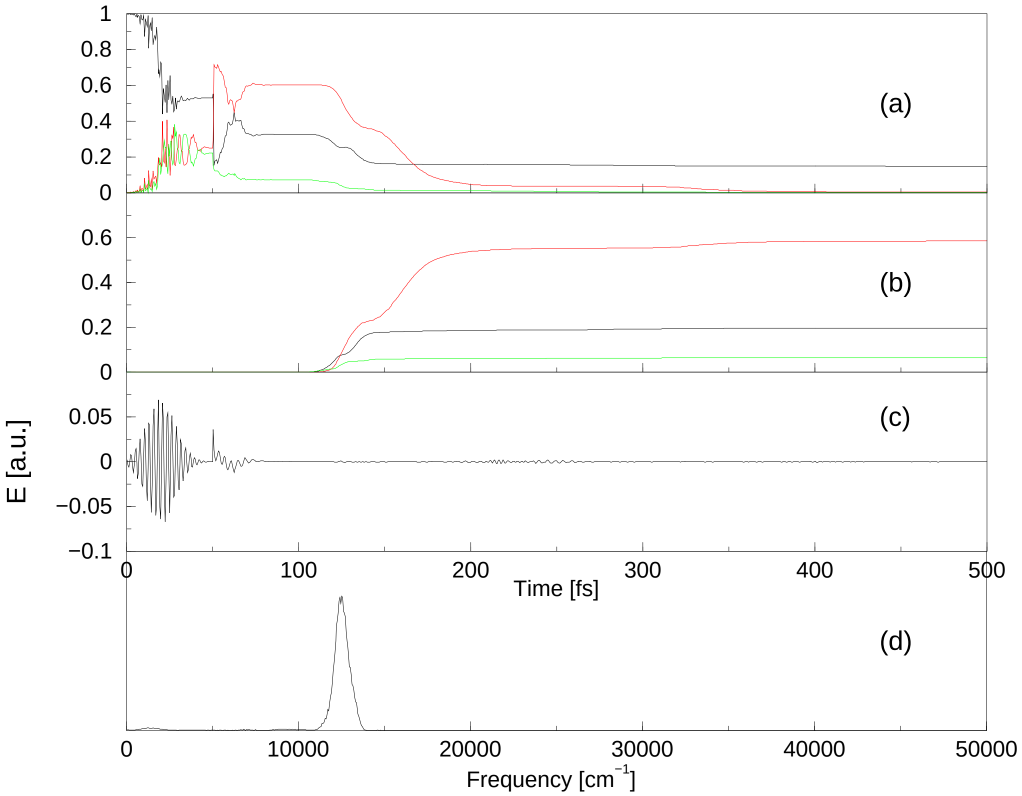

Figure 6.10: *Pulse constructed with the restricted instantaneous dynamics algorithm. Panel (a): Temporal development of population and (b) the dissociation yields. Panel (c) shows the derived pulse in time and (d) in frequency domain obtained with a field strength parameter* $E_0 = 0.9$ *a.u. and a Gaussian seed pulse with field strength* $E = 0.1$ *a.u., a carrier wavelength* $\lambda = 798$ *nm and a width FWHM = 20 fs.*

6.3 Alternative Coupling scheme

In another coupling scenario it is assumed that the Rydberg state $|2\rangle$ is not directly accessible from the electronic ground state $|X\rangle$. As before, state $|1\rangle$ is equally coupled to both other electronic states. Therefore, the coupling matrix is of the form

$$W(t) = \begin{pmatrix} 0 & w(t) & 0 \\ w(t) & 0 & w(t) \\ 0 & w(t) & 0 \end{pmatrix}, \tag{6.14}$$

where $w(t) = -E(t)$. Within this coupling scheme, the population dynamics exhibits other features. This is exemplified with an unchirped pulse (fig. 6.11), where a higher field strength is needed to transfer population into the excited state.

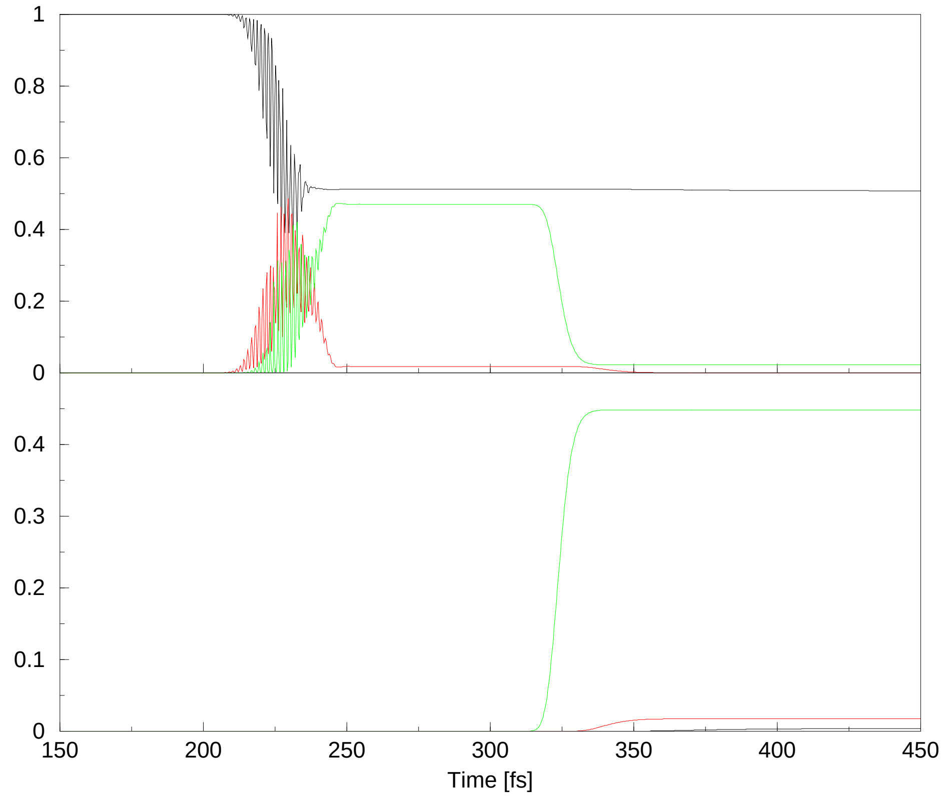

Figure 6.11: *Dynamics when applying an untaylored Gaussian laser pulse to the system in the abscence of a coupling between states $|X\rangle$ and $|2\rangle$. The upper panel displays the temporal evolution of population; lower panel: dissociated part of the wave packets, the main dissociation product results from state $|2\rangle$, but small contributions from state $|1\rangle$ are also obtained. The colors are chosen according to the corresponding potential curves. For the calculations an unchirped Gaussian with a width β = 1000 cm^{-1}, carrier wavelength λ = 798 nm, but an field strength E = 0.28 a.u. is applied.*

The instanataneous dynamics algorithms shows a similar picture as before (see fig. 6.12). We chose a seed-pulse of the form $E(t) = 5 \cdot 10^{-2} \exp(-\beta(t - t_0)^2) \cdot \cos(\omega_0 t)$ assuring a small population transfer to the excited states. Again, a low field strength is sufficient as a one-photon process occurs.

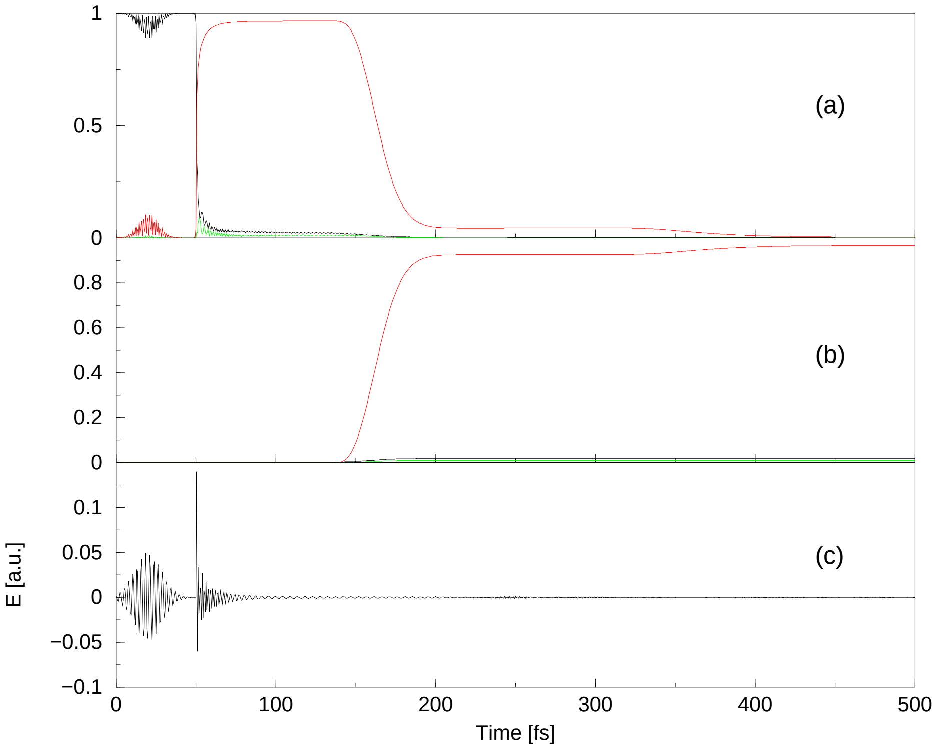

Figure 6.12: *Pulse constructed with the instantaneous dynamics algorithm without a coupling between states* $|X\rangle$ *and* $|2\rangle$*. Panel (a): Temporal development of population and (b) the cut part of the wavepackets itemized to the different dissociation channels. Panel (c) shows the derived pulse in time domain obtained with a field strength parameter* $E_0 = 9{\cdot}10^{-1}$ *a.u. and a Gaussian seed pulse with field strength E = 0.05 a.u., a carrier wavelength* λ *= 798 nm and a width FWHM = 20 fs.*

A similar scenario can be seen for a pulse optimization with a genetic algorithm. It may be surprising that the linear chirp parameter α_1 has a positive sign, but a closer look to the temporal evolution of the norm gives the explanation for this behavior. The blue shift of the pulse, that means, the increasing temporal frequency forces the system to perform the $|X\rangle$ to $|1\rangle$ transition at the end of the pulse duration. Then, as the direct four-photon transition is forbidden (coupling scheme) a high yield of population in the $|1\rangle$ state is achieved with a higher energy. This is consistent with fig. 6.5 and the resonance condition obtained from the difference potentials in eq. (6.7).

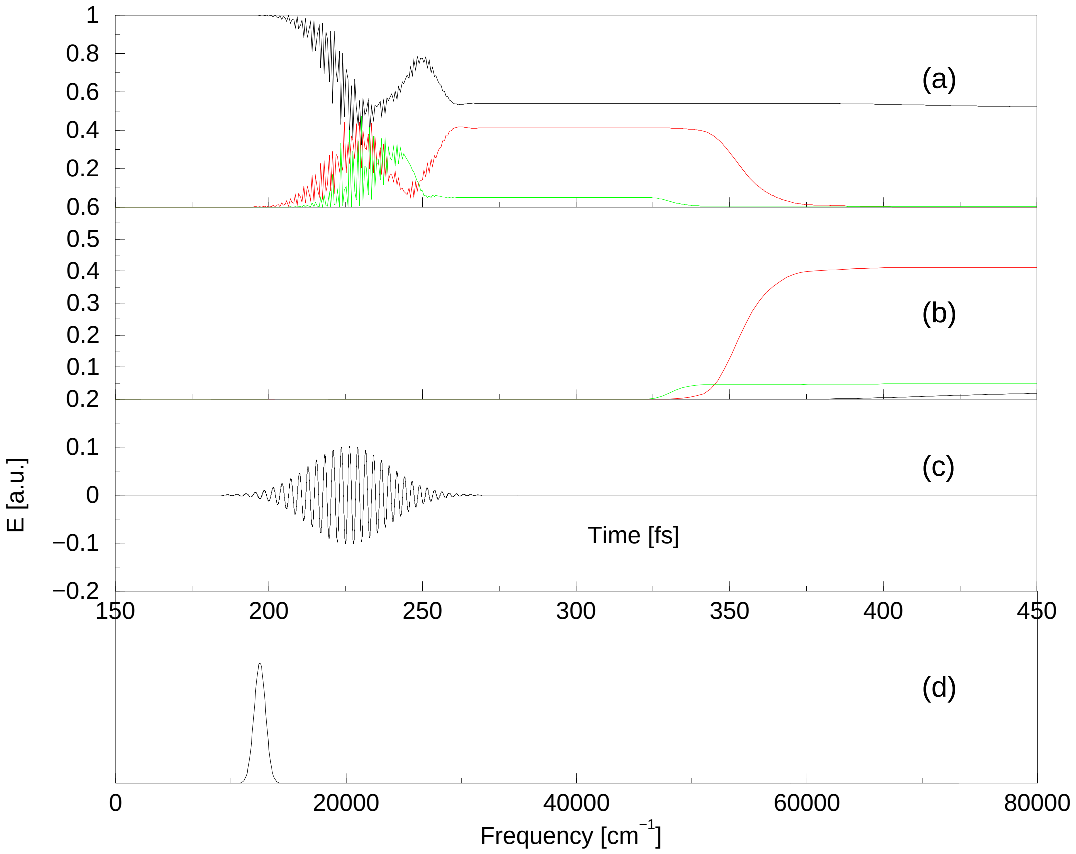

Figure 6.13: *Taylored pulse obtained by a genetic algorithm for a system without coupling between states* $|X\rangle$ *and* $|2\rangle$. *Panel (a): resulting evolution of population and dissociation amount from the both electronic excited states (panel b)). Panel (c): The pulse with* $\beta = 1000\,cm^{-1}$, $a_1 = 6.84{\cdot}10^4$, $a_2 = 2.19{\cdot}10^5$, $a_3 = -9.45{\cdot}10^6$, $a_4 = 4.50{\cdot}10^6$ *a.u. and field strength E = 0.354 a.u. in time domain and in frequency domain (panel (d)). The ordinate displays the field stength [a.u.].*

Optimal control theory gives a different picture. The objective is to maximize the overlap between a propagated wave function and a fixed target wave function at a pre-defined time t_f. Within the altered coupling scheme the time-dependent overlap $O(t)$ takes the form:

$$\begin{aligned} O(t) &= \Im\langle\psi|\mu|\chi\rangle = \Im\left(\langle\psi_X(t)|\chi_1(t)\rangle + \langle\psi_1(t)|\chi_X(t)\rangle\right. \\ &+ \left.\langle\psi_1(t)|\chi_2(t)\rangle + \langle\psi_2(t)|\chi_1(t)\rangle\right) \end{aligned} \tag{6.15}$$

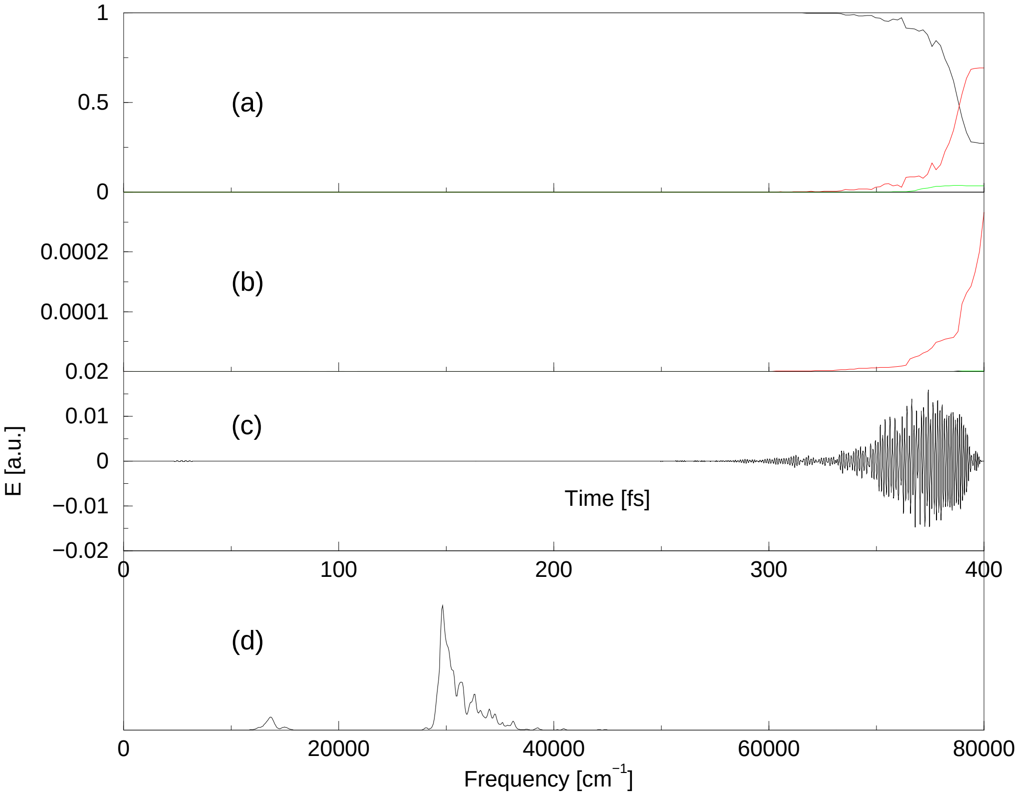

Figure 6.14: *Pulse shaping with optimal control theory for a system without coupling between states $|X\rangle$ and $|2\rangle$. Panel (a): Temporal development of population and (b) the cut part of the wavepackets itemized to the different dissociation channels for a final time $t_f = 400 fs$. Panel (c) shows the optimal pulse in time and (d) in frequency domain.*

As the target function φ_f is fixed at a certain time (t_f), the pulse sets in at later times. The resulting dissociation yield can be estimated to resulting mainly from the $|1\rangle$-state. It can be seen that a short final time of 400 fs preferes a multi-photon process. Invoking different coupling schemes results in a different fragmentation behavior. Thus, the derived control fields are quite sensitive to changes in a system's properties.

6.4 Extended Model System: 4 electronic potentials

In this section, the model system is extended to include a fourth electronic state and a non-adiabatic coupling. The corresponding potential curve represents a cut through the $^1Q_1$ potential surface in the A-band of methyl iodide. The coupling matrix is given as

$$W(R,t) = \begin{pmatrix} 0 & w(t) & w(t) & w(t) \\ w(t) & 0 & V_{12}(R) + w(t) & w(t) \\ w(t) & V_{12}(R) + w(t) & 0 & w(t) \\ w(t) & w(t) & w(t) & 0 \end{pmatrix}, \tag{6.16}$$

where the diabatic states $|1\rangle$ and $|2\rangle$ are coupled by a potential coupling term V_{12} and an external electric field $w(t) = -E(t)$ (further referred to as coupling scheme I). The analytic form of the $^1Q_1$ potential and the coupling element is taken from Ref. [87]

$$\begin{aligned} V_2(R) &= (a_{21}e^{-\beta_{21}\cdot R}/\{1 + e^{\beta_{22}(R-R_{02})}\} + a_{22}e^{-\beta_{23}r_x} \\ &+ a_{23}e^{-\beta_{24}r_x} + 0.5 \cdot k_f x^2 - \epsilon_0) \qquad (6.17) \\ V_{12}(R) &= 0.0021 \cdot e^{-(R-4.2)/2.} \qquad (6.18) \end{aligned}$$

In a second coupling scheme to be investigated, the states $|1\rangle$ and $|2\rangle$ are not coupled by the external field, i.e. the respective matrix elements contain only the potential coupling V_{12} (coupling scheme II). Fig. 6.15 shows the potential curves of the model system. States $|1\rangle$ and $|2\rangle$ are tangent to each other at a bonding distance around the equilibrium position in the electronic ground state $|X\rangle$.

The various control schemes as presented in the former sections are applied to

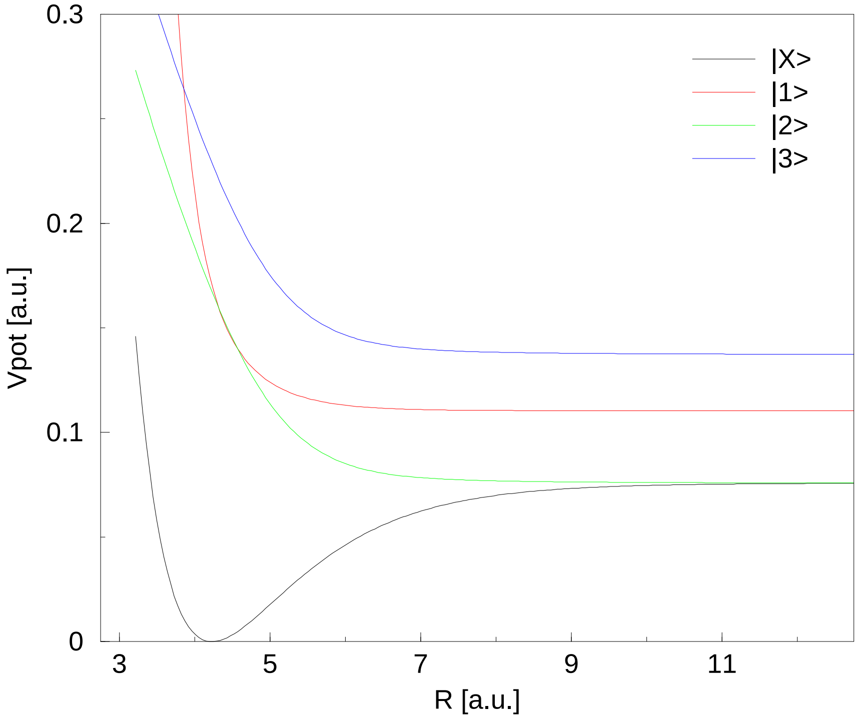

Figure 6.15: *Potential energy sufaces in methyl iodide in one dimension, assuming a single $C-I$ vibrational motion without H-atom contribution. The form of the potentials for $|X\rangle$ - $|2\rangle$ are taken from [86,87]. The exact form of the generic potential $|3\rangle$ can be found in the text. Diabatic states $|1\rangle$ and $|2\rangle$ are coupled by a potential coupling term $V_{12}(R)$ (not shown here).*

the four state system in what follows. In doing so, the objective is to selectively excite into one of the two states $|1\rangle$ and $|2\rangle$, respectively.

The two coupling schemes I and II, as mentioned above, are compared concerning the dynamical behavior of the system. Therefore, a non-taylored Gaussian laser-pulse with $\lambda = 798$ nm, a field strength of $E = 0.2$ a.u., and FWHM $= 50$ fs is applied to the system. The temporal development of the populations in the various states is shown in fig. 6.16, upper panel.

Both scenarios differ strongly in their dynamical development and therefore also in the ratio of dissociation products. For coupling case II the ratio of the main dissociation products, mainly deriving from state $|1\rangle$ and $|2\rangle$, is about 3:2;

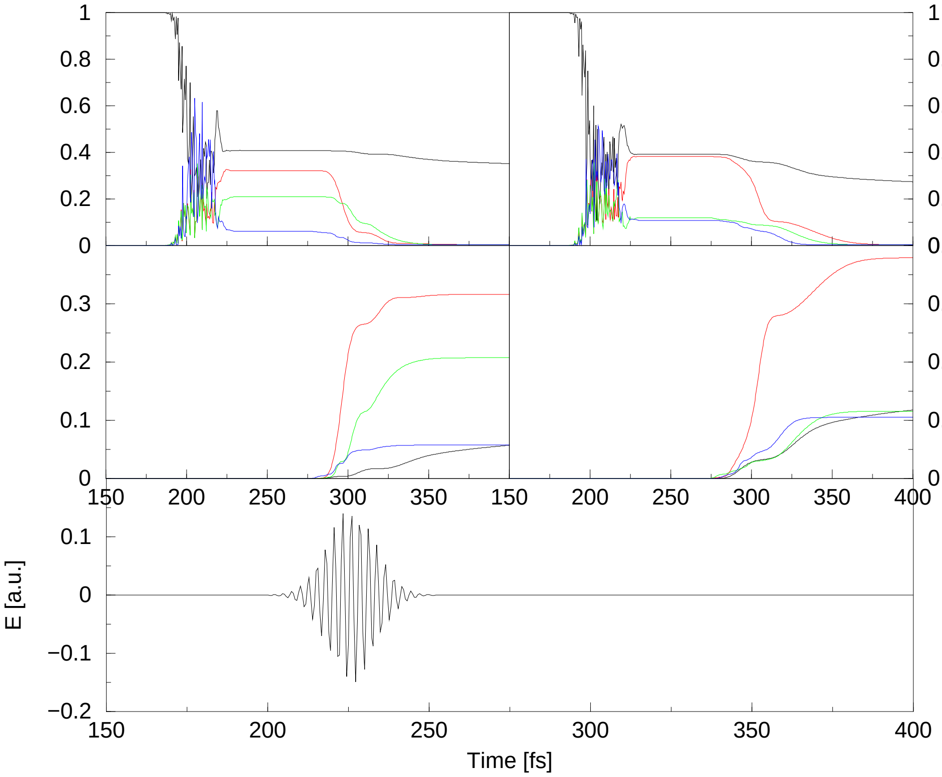

Figure 6.16: *Left panels: temporal development of the populations and the dissociation yields for coupling case II. Right panels: the same for an additional external coupling with the laser field (case I), the latter is displayed in the lowest panel. Field parameters:* λ *= 798 nm,* E *= 0.2 a.u., and FWHM = 50 fs.*

both other states are less populated. A different picture arises when the external field also couples both diabatic states. Then, state $|2\rangle$ is 3 times more populated than all the other states, which are approximately equally populated.

6.4.1 Instantaneous Dynamics

Applying the instantaneous dynamics approach in order to maximize the dissociation ratio of one particular state, either $|1\rangle$ or $|2\rangle$, the results differ strongly depending on the coupling scheme, as can be taken from fig. 6.17. First, state $|1\rangle$ is to be optimized. Choosing the same field strength parameter $E_0 = 3 \cdot 10^{-1}$

a.u. for both coupling schemes, a similar picture emerges: a short and intense pulse with the one-photon frequency follows the intitial seed pulse immediately, causing a strong increase of population in state $|1\rangle$, accompanied with a weaker increase in state $|2\rangle$, because of the potential coupling transferring population into this state. A closer look at the population in state $|1\rangle$ near 80 fs shows small oscillations according to a population transfer into state $|2\rangle$ via potential coupling. This can not be seen in coupling scheme I (Fig. 6.17, right panels), where the field is allowed to influence the coupling between the diabatic states.

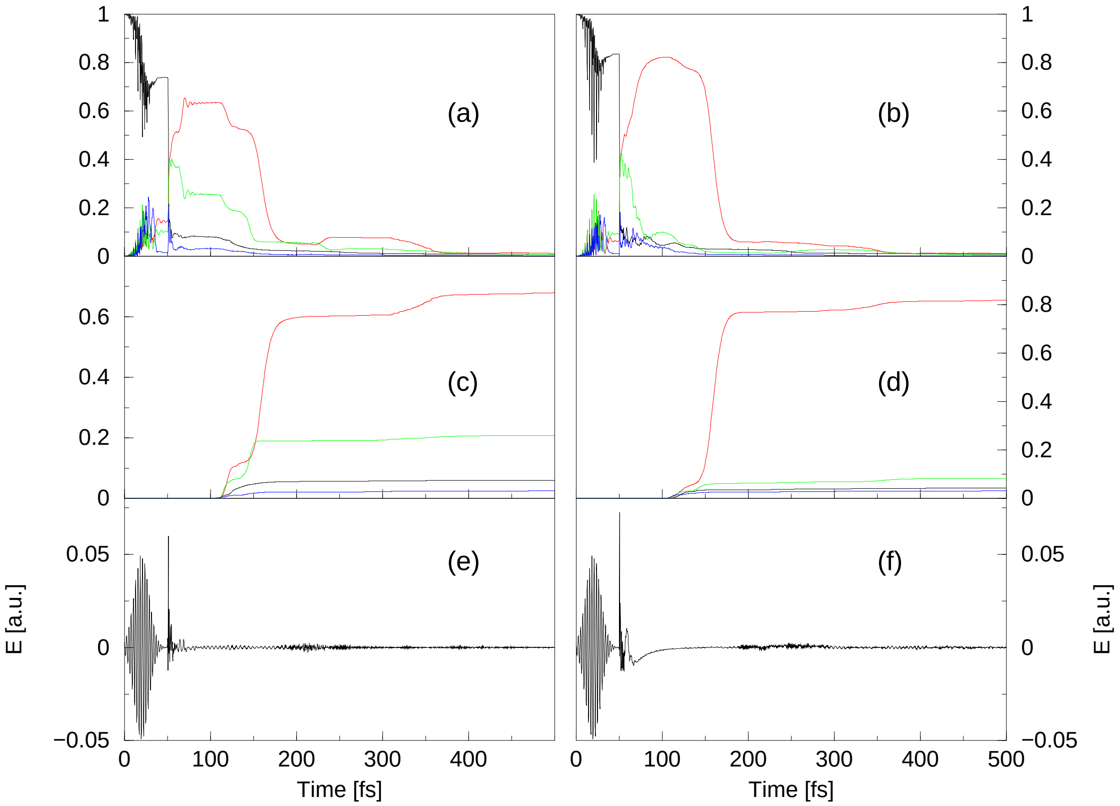

Figure 6.17: *Optimizing* $|1\rangle$ *state population employing fields from the instantaneous dynamics. Left panels: temporal development of the population (a) and the dissociation yields (c) for coupling scheme scheme II. Right panels: the same for an additional external coupling with the laser field (coupling scheme I). Field strength in both cases:* $E_0 = 3 \cdot 10^{-1}$*a.u., seed-pulse with* $E_s = 5 \cdot 10^{-2}$ *a.u..*

When both states are additionally coupled by the electric field, the dissociation yield of the target state $|1\rangle$ and also the ratio of dissociation products is higher than in the other coupling scheme. Since the diabatic potential coupling decreases for increasing bonding distances R, no significant part of population is transfered via diabatic coupling into state $|2\rangle$ at larger distances. An external coupling between states $|1\rangle$ and $|2\rangle$ reduces the part of population being transferred into the diabatic state even at smaller bondlengths.

As state $|1\rangle$ is the main dissociation channel even without a special pulse design, the more demanding objective is to maximize the dissociation products originating from state $|2\rangle$. First, coupling scheme II is assumed (fig. 6.18, left panels). The approach yields poor results concerning dissociation yield as well as the ratio of dissociation products; the temporal development of the population resembles the case where the objective was to optimize the $|1\rangle$ state population.

In the second case, where both states are additionally coupled by the external field, the system is very sensitive to an additional coupling as can be seen in the dissociation yields of state $|2\rangle$ in panels (b) and (d) of fig. 6.18. Nevertheless, the obtained pulses including and excluding external coupling look very similar but yield different populations.

All resulting fields exhibit a frequency component around 36000 cm^{-1} describing a resonant one-photon process. In order to restrict the system to perform a three-photon process, according to the preceding section, the field is constructed by excluding the electronic ground state from the calculation. Therefore, the pulse is determined by two diferent approaches depending on the coupling of

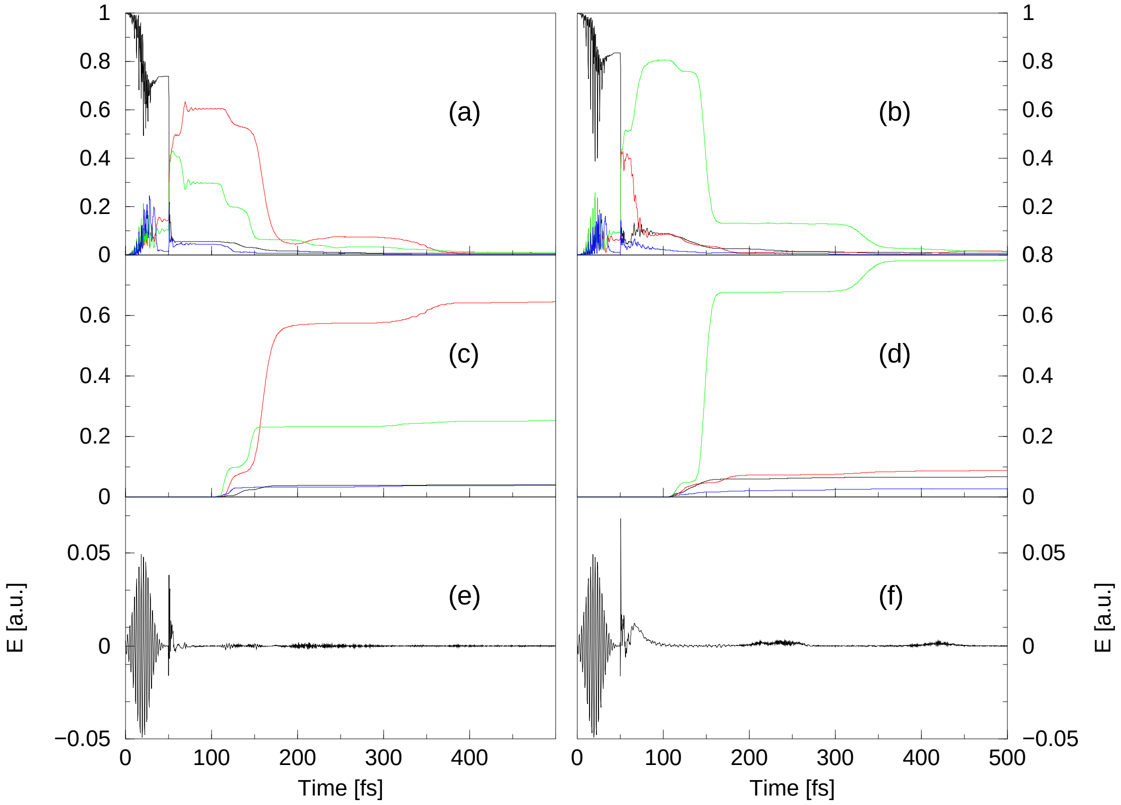

Figure 6.18: *Optimizing $|2\rangle$ state employing fields from the instantaneous dynamics. Left panels: temporal development of the population (a) and the dissociation yields (c) for coupling scheme II. Right panels: the same for an additional external coupling with the laser field. Field strength in both cases:* $E_0 = 3 \cdot 10^{-1}$*a.u., seed-pulse with* $E_s = 5 \cdot 10^{-2}$ *a.u..*

states $|1\rangle$ and $|2\rangle$:

$$\begin{aligned} (I) \qquad E(t) &= E_0 \Im\{\langle\psi_2|\psi_1\rangle + \langle\psi_2|\psi_3\rangle\} \\ (II) \qquad E(t) &= E_0 \Im\{\langle\psi_2|\psi_3\rangle\}. \end{aligned} \tag{6.19}$$

Fig. 6.19 and fig. 6.20 show the temporal developments of the population and the dissociation yields as well as the derived electric fields for a monotonic increase of population in the $|1\rangle$ (fig. 6.19) and $|2\rangle$ state (fig. 6.20), depending

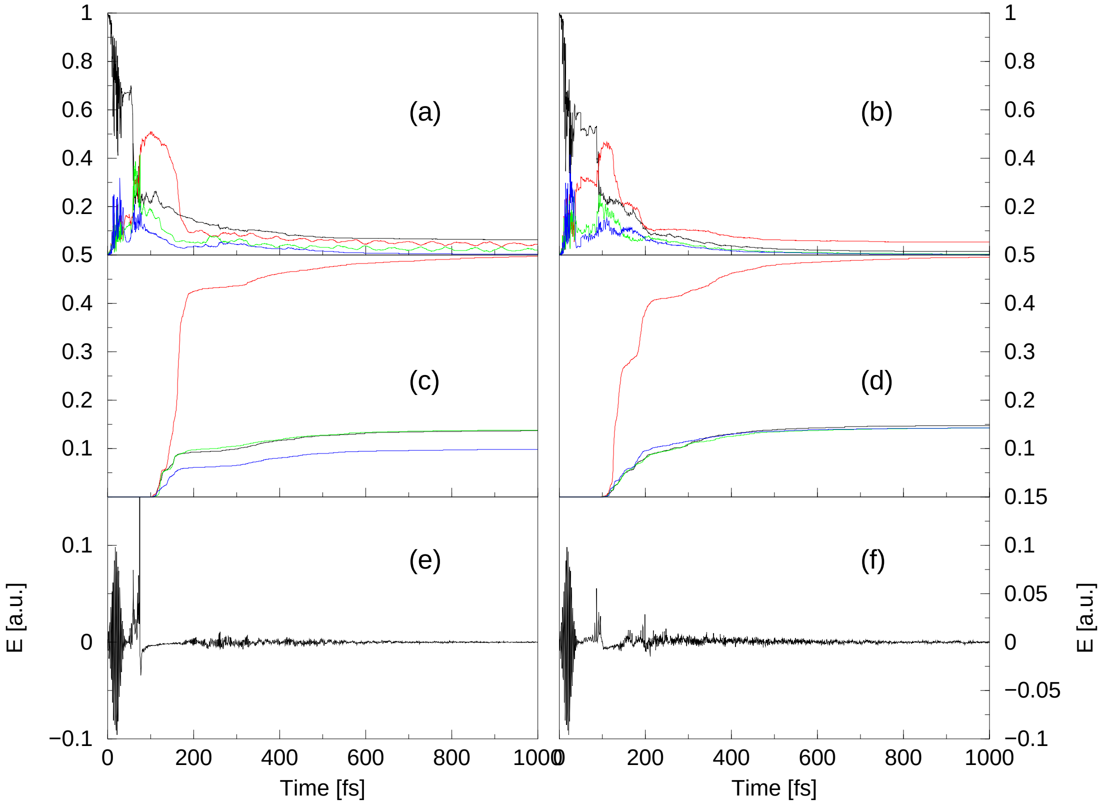

Figure 6.19: *Optimizing $|1\rangle$ state with restricted instantaneous response. Left panels: temporal development of the population (a) and the dissociation yields (b) for coupling scheme II. Right panels: the same for an additional external coupling with the laser field (scheme I). Field strength in both cases: $E_0 = 3$ a.u., seed-pulse with $E_s = 1 \cdot 10^{-1}$ a.u.*

on the coupling scheme.

As before, in the one-photon case, the dissociation amount of the $|1\rangle$ state for optimizing this state is not remarkably influenced by the additional field coupling. For both coupling schemes the resulting fields resemble each other, leading to a similar dynamical behavior. The fast dissociation process is mainly determined by pulse sequences within the first 200 fs.

A different picture arises if the objective is to optimize state $|2\rangle$. For coupling scheme II the dissociation ratio is determined by two pulse groups, the first

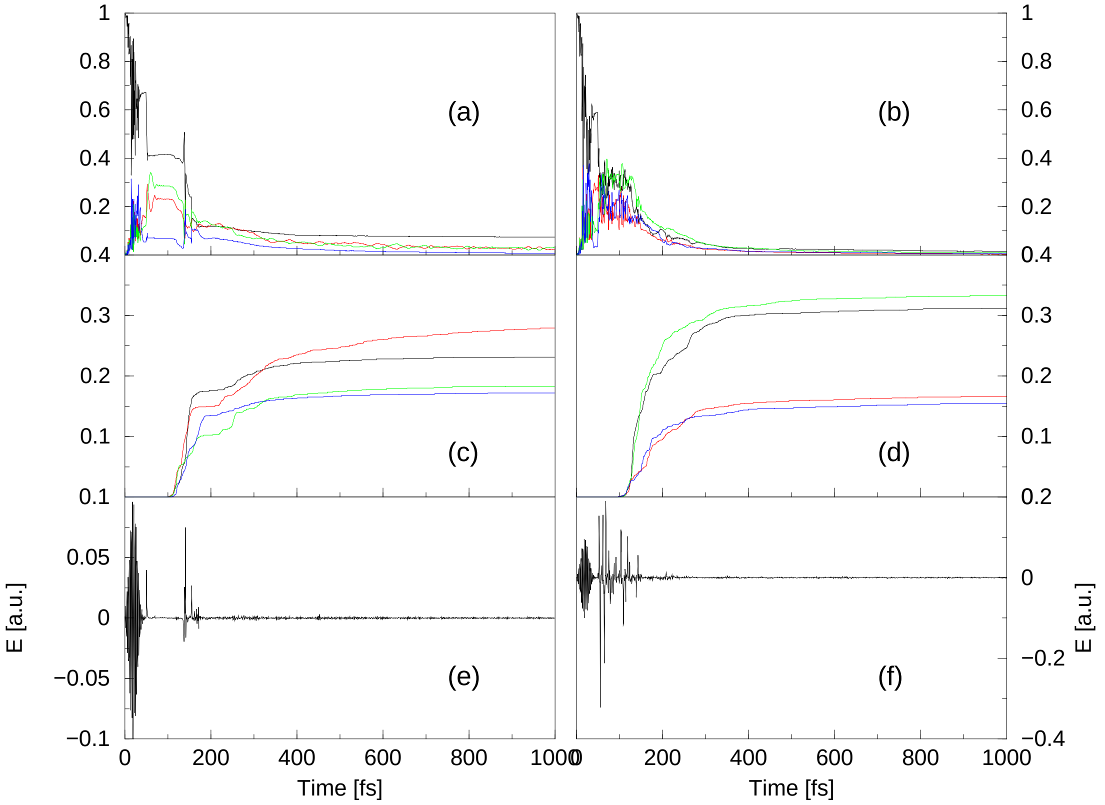

Figure 6.20: *Optimizing* $|2\rangle$ *state with restricted instantaneous response. Left panels: temporal development of the population (a) and the dissociation yields (b) for coupling scheme II. Right panels: the same for an additional external coupling with the laser field (scheme I). Field strength in both cases:* $E_0 = 3$ *a.u., seed-pulse with* $E_s = 1 \cdot 10^{-1}$ *a.u.*

located around 50 fs (shortly after the seed pulse ends), arranging a population transfer originating from state $|X\rangle$ via the (dipole allowed) $|1\rangle$ state to reach state $|2\rangle$ by potential coupling. The second pulse group is activated around 140 fs when a first part dissociates and the wave packets are located at larger bonding distances, influenced by a vanishing potential coupling. Then, by first populating state $|3\rangle$, state $|2\rangle$ is accessible directly without reaching state $|1\rangle$. Therefore, in order to achieve population tranfer into state $|2\rangle$ without a direct access by the electric field, dissociation products from all involved electronic states are obtained.

An additional field coupling between the diabatic states allows for a direct transfer into state $|2\rangle$. Thus, at larger bond distances, where the potential coupling vanishes, population from state $|1\rangle$ and $|3\rangle$ is transferred. A discrimination between state $|X\rangle$ and $|2\rangle$ leading to the same dissociation limit is more challenging to resolve. In the next subsections the objective is to maximize population in state $|2\rangle$ for coupling scheme I without additional external coupling within the afore used algorihms.

6.4.2 Optimal Control Theory

In this subsection the control fields obtained by the instantaneous dynamics algorithm are compared to the optimal control field. Optimal control theory in its unrestricted form was applied for a final time $t_f = 400$ fs and a strength parameter $\alpha = 9.8 \cdot 10^5$. The field and the dynamical behaviour of the system are shown in fig. 6.21.

A first weak pulse sequence near 40 fs excites a small part of the system. The very strong part of the field initiating at about 300 fs induces a wave packet moving outward to maximize the overlap with the target wave function at final time $t_f = 400$ fs. The derived field is stronger than the ones obtained from the instantaneous dynamics algorithm. Although the disscociation yield within the caluclated time is very poor it will increase at later times, as discussed in the last sections. The control field derived from optimal control theory transfers population effectively into state $|2\rangle$ but is difficult to interpret.

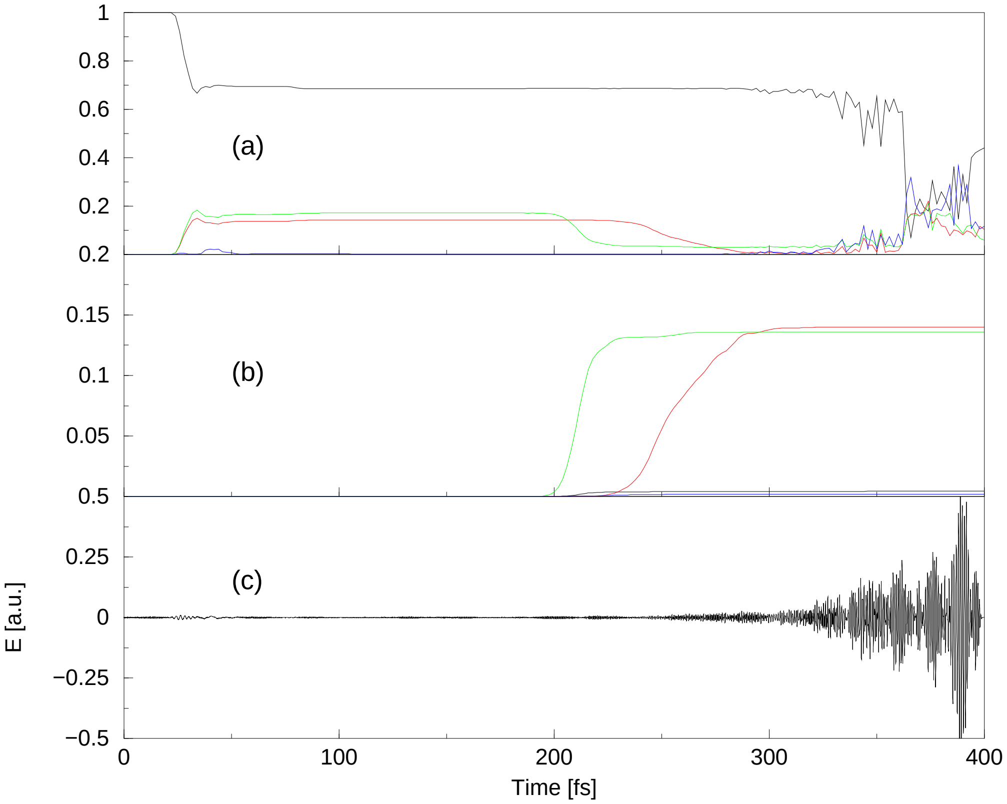

Figure 6.21: *Maximizing the overlap with a target wavefunction in state $|2\rangle$ within optimal control theory. Panel (a): temporal development of the population and the dissociation yield (middle panel) for coupling scheme II. Panel (c): Derived laser field for field strength parameter of* $\alpha = 9.8 \cdot 10^5$*a.u.*

6.4.3 Genetic Algorithm

In a last approach the dissociation amount in state $|2\rangle$ without additional coupling between the diabatic states $|1\rangle$ and $|2\rangle$ by an external electric field (coupling scheme II) was maximized using a genetic algorithm. The population size is chosen as before (10 individuals) and the evolutionary modifying parameters as cross-over and mutation probability are chosen to 60 % and 50%, respectively. In order to maximize the dissociation amount of state $|2\rangle$ the object functional is defined as

$$J = \frac{1}{|\langle \psi_2(R)|\psi_2(R)\rangle|} \tag{6.20}$$

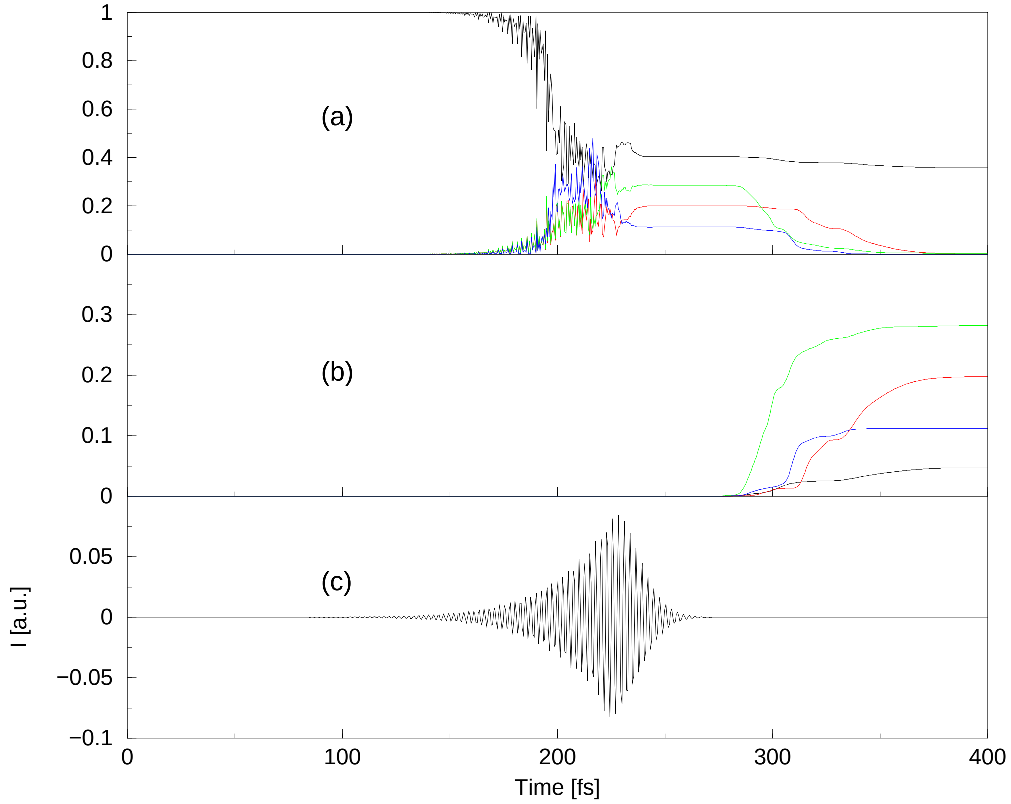

Figure 6.22: *Upper panel: Temporal development of the norm. Middle panel: The dissociation yields. Lower panel: Parameterized pulse obtained from a genetic algorithm as described in the text with* $\beta = 1000\,cm^{-1}$, $a_1 = -1.00 \cdot 10^5$, $a_2 = -1.00 \cdot 10^7$, $a_3 = 5.26 \cdot 10^6$, $a_4 = 5.95 \cdot 10^6$ a.u.. *Field strength: 0.308* a.u.

to be minimized. The resulting dynamics and dissociation yields as well as the electric field are shown in fig. 6.22.

An analysis based on difference potentials as performed in the last section is more complicated. The system is very sensitive to the present position of the wavepackets, as the various difference potentials of the energetically close lying states depending on the coordinate may change very rapidly. But similar to the behavior of the system in the last section the first two chirp parameters feature negative signs.

To conclude the comparison it can be said that the fields derived from the various control theories are effective in transfering population into the chosen target state. In the here treated case of dissociative excited states the application of optimal control theory yields control fields which are very effective in maximizing an overlap of the propagated wavepacket and the target wavefunction localized in the dissociation channel. The imposed constraints do not allow to make predictions about the overall dissociation yield or the ratio of dissociation products after excitation. The mathematically derived optimal fields consist of various frequency components but the underlying physical background is not obvious to explain. Although there are approaches in the literature to illucidate the "black box" phenomenon of optimal control theory [93], the connection between control fields and the underlying wavepacket dynamics remain unclear. The approach to restrict optimal control theory to find a field initiating a non-resonant three-photon process in varying the chirp parameters, produces poor results concerning the dissociation yield.

Feedback-control employing genetic algorithms presents a very simple method to obtain taylored fields. The parameterization of the electric field allows for a description in terms of chirp parameters around a central frequency. As this carrier frequency can be chosen at will, directing the system via a three-photon process can simply be arranged. Representing a global search method, the minimum of a constellation should easyly be found. The definition of the object functional is influencing the result and the choice of the probability of the evolutionary parameter's action is influencing the convergence behavior and has to be investigated or, at least estimated. As is the case for optimal control theory, the interpretation of the designed pulses is difficult, especially for non-resonant transitions with very intense laser fields. An advantage of the such derived field in contrast to optimal control fields for dissociative systems, is the possibility to define the object functional by the dissociation yield directly without the constraint of a final time and position. Therefore, the algorithm is not as sensitive to the overall propagation time.

The instantaneous dynamics algorithm allows to establish a direct relation between the derived fields and the underlying processes. Because no maximization or minimization search in a mathematical sense is performed, no "optimal" field is obtained. Nevertheless, the control fields are very effective. The disadvantage in dissociative systems is the condition of the wavepacket's overlap. For moving wavepackets on potentials with different gradients, the resulting difference in velocity reduces the possibility of overlaps at later times. The system is forced to perform the transition on a short time scale at once, before the outrunning wavepacktes reach larger bonding distances. A restriction to three-photon processes can also succesfully be performed. Especially for the demanding task transferring population into state $|2\rangle$ without an additional external coupling (scheme II) good performance for instantaneous response could be obtained.

The employed model of methyl iodide, although treating only a single degree of freedom, is a computational demanding task, as it combines elements of dissociative sytems, diabatic couplings and multi-photon transitions. It represents possibly the most unfavourable case. Nevertheless, the instantaneous response algorithm is comparable in quality and it is expected therefore, that bound-bound transitions can be performed more effectively. This is the objective of the next chapter.

Chapter 7

The Sodium Dimer

In this chapter the sodium dimer is investigated concerning population transfer using instantaneous dynamics. A remarkable feature of this system is the energetic difference of the two (here regarded) electronic states $|A\rangle$ and $|\Pi\rangle$. Starting from the electronic ground state $|X\rangle$, $|A\rangle$ is accessible by a pulse with a wavelength of 620 nm, whereas by a two-photon process of the same wavelength the $|\Pi\rangle$ state is populated. A direct transition $|\Pi\rangle \leftarrow |X\rangle$ is one-photon forbidden. The dynamic behaviour of the system depending on the condition which state is to be populated is reflected in the form of the pulse. Therefore, the obtained electric fields are interpreted with short-time Fourier-transforms and possibilities are presented how such derived wave packets can be re-constructed from experimental signals obtained by time-dependent pump/probe ionization experiments.

7.1 The Model System

The sodium dimer is treated here within a restricted model consisting of five electronic states. Other neutral and ionic states are decoupled. The respective potential curves for the ground state ($X^1\Sigma_g^+$), the excited states $A^1\Sigma_u^+$, $2^1\Sigma_u^+$ and

$2^1\Pi_g$ as well as the dissociative ionic state $^2\Sigma_u^+$ and the bound ionic state $^2\Sigma_g^+$ are displayed in fig. 7.1, and taken from Ref. [94–96]. Panel (a) shows the system to be discussed in connection with selective population transfer, panel (b) displays another excitation scheme regarded for the purpose of wave packet imaging.

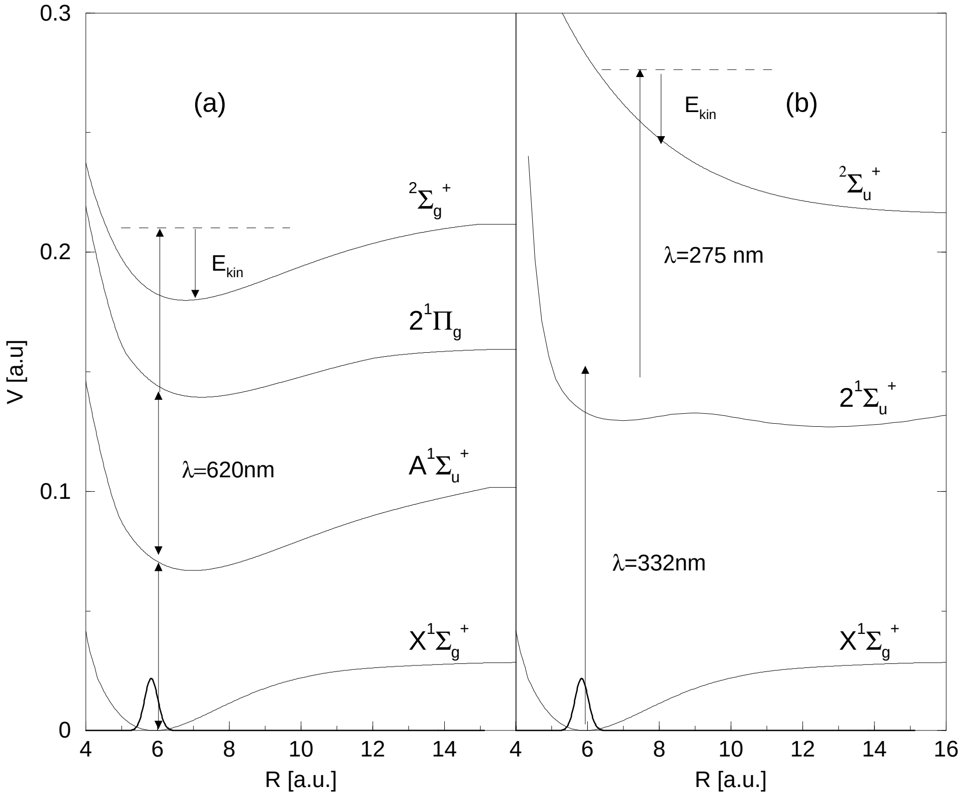

Figure 7.1: *Potential energy sufaces of the sodium dimer. (a) Potentials as used for the control algorithm: The $|\Pi\rangle$ state is not directly accessible by the electronic ground state $|X\rangle$ but via a two-photon process mediated by the $|A\rangle$ state. Furthermore, the bound ionic ground state state for the photoelectron spectra is shown. Panel (b): Potential surfaces illustrating wave packet imaging: Besides the electronic ground state the double minimum $2^1\Sigma_u^+$ and a dissociative ionic state are shown.*

As mentioned in the introduction of this chapter, the two excited states are both accessible via a pulse with the wavelength λ of 620 nm. The $|A\rangle \leftarrow |X\rangle$ transition is a parallel one while the $|\Pi\rangle \leftarrow |A\rangle$ transition is perpendicular.

7.2 Time-Frequency Analysis

Time-frequency analysis is instrumental in the interpretation of signals evolving in time in an unpredictable way. A frequency analysis that is local in time gives knowledge about the discrete changes of pulses. Mathematically this can be done by either calculating Wigner or Husimi distributions [97, 98], or by convoluting (windowing) the time-dependent signal $E(t)$. In this work the latter "short-time Fourier transform" is applied. For a fixed time τ the short-time Fourier transform of a function $E(t)$ describes the local spectral content of $E(t)$ near τ as a function of the frequency ω. It is defined as the Fourier transform of $E(t)\, g(t-\tau)$, where $g(t)$ is the window function. Moving the center of the window function g along the time axis, allows to obtain "snapshots" $S(\omega, t)$ of the time-frequency behavior of the function

$$S(\omega,\tau) = \int_{-\infty}^{\infty} E(t)\, g(t-\tau) e^{-i\omega t} dt. \tag{7.1}$$

The width of the window function $g(t)$ also scales the resolution of the short-time Fourier transforms, as the time-frequency resolution is limited by the Fourier product. A wide window yields a good frequency resolution but poor time resolution, while a small window results in the opposite behavior. Convoluting with a δ-function, however, would result in a spectrogram $|S(\omega,\tau)|^2$ completely independent of frequency, $|S(\tau)|^2$. A possible solution is using the pulse to gate itself, as a non-collinear autocorrelation function, termed FROG (frequency-resolved optical gating) [38]

$$I_{FROG}(\omega,\tau) = \left| \int_{-\infty}^{\infty} E^{+}(t) E^{+}(t-\tau)^2 e^{-i\omega t} dt \right|^2, \tag{7.2}$$

where $E^{+}(t)$ is the complex electric field, the Fourier transform of $E^{+}(\omega)$ containing solely the positive frequencies of the field (compare to eq. (1.42)). Depending on the nonlinear effect used (e.g. SHG (second harmonic generation)) different types of FROG are distinguished. Since FROG is a squared quantity, the electric field is determinable in amplitude and phase but not in the absolute phase ϕ_0. Nevertheless, short-time Fourier transform may help to interprete complex laser fields.

7.3 Instantaneous Dynamics

Regarding the excitation scheme shown in panel (a) of fig. 7.1, population transfer is controlled adapting the formalism in chapter 3. As indicated by the arrows in the figure, transitions from the ground state to the higher states as well as to the ionization continuum can be induced by photons with a wavelength of $\lambda = 620$ nm. The transition dipole-moments are taken as constant, assuming their values at the respective equilibrium position [99], such that the field-matter interaction is of the form

$$\begin{aligned} w_{XA}(t) &= -3.6\,E(t)\cos\Theta \\ w_{A\Pi}(t) &= -1.44\,E(t).\sin\Theta \end{aligned} \tag{7.3}$$

The transitions are described by matrix elements differing in their angular dependence because of the varying polarization of these transitions ($|A\rangle \leftarrow |X\rangle$ is parallel and $|\Pi\rangle \leftarrow |A\rangle$ perpendicular). Choosing the polarization vector ε of the electric field to point along the space fixed z-axis, Θ is defined as the angle between ε and the dipole-moment vector μ. Applying the instantaneous control algorithm to this excitation scheme, for an increase of population as a function of time the field can be obtained

$$E(t) = -E_0 \frac{2}{\hbar} \sum_m \Im \langle \psi_k(t) | \mu_{km} | \psi_m(t) \rangle, \tag{7.4}$$

where k is the target electronic state and m counts the other electronic states; the ionic state is not included into the instantaneous algorithm, because the dipole-coupling to the ionization continuum is much weaker than couplings between neutral molecular states. In the next subsections the electric fields obtained by dynamical response of the perturbed molecule for population transfer into different electronic states $|k\rangle$ are shown.

7.3.1 $|A\rangle$ State Population Transfer

First, the population transfer to the A-state is tmaximized. For now, exclusively molecules at an angle of 45° with respect to the field polarization are considered, orientational effects are discussed in section 7.3.3. Employing eq. (7.4), m takes the values X, Π. It is necessary to start the process by applying a seed pulse $E_s(t) = E_s f(t) \cos(\omega t)$ in order to transfer a small amount of population into the upper electronic states. The seed pulse has a Gaussian envelope with 20 fs width (FWHM) and a field strength of $E_s = 5 \cdot 10^{-5}$ a.u. The pulse is centered around $t = 20$ fs with a frequency $\omega = 0.0735$ a.u. corresponding to a wavelength of 620 nm, the resonant energy to induce transitions. Starting in the vibrational ground state $|X\rangle$, fig. 7.2 shows the population in the three electronic states and the constructed field with a parameter $E_0 = 8 \cdot 10^{-5}$ a.u.

The A-state population S_A increases in steps whereas the ground state population S_X decreases stepwise. The higher lying $|\Pi\rangle$ state is only weakly populated and a nearly 100 % population transfer into the target state $|A\rangle$ is achieved.

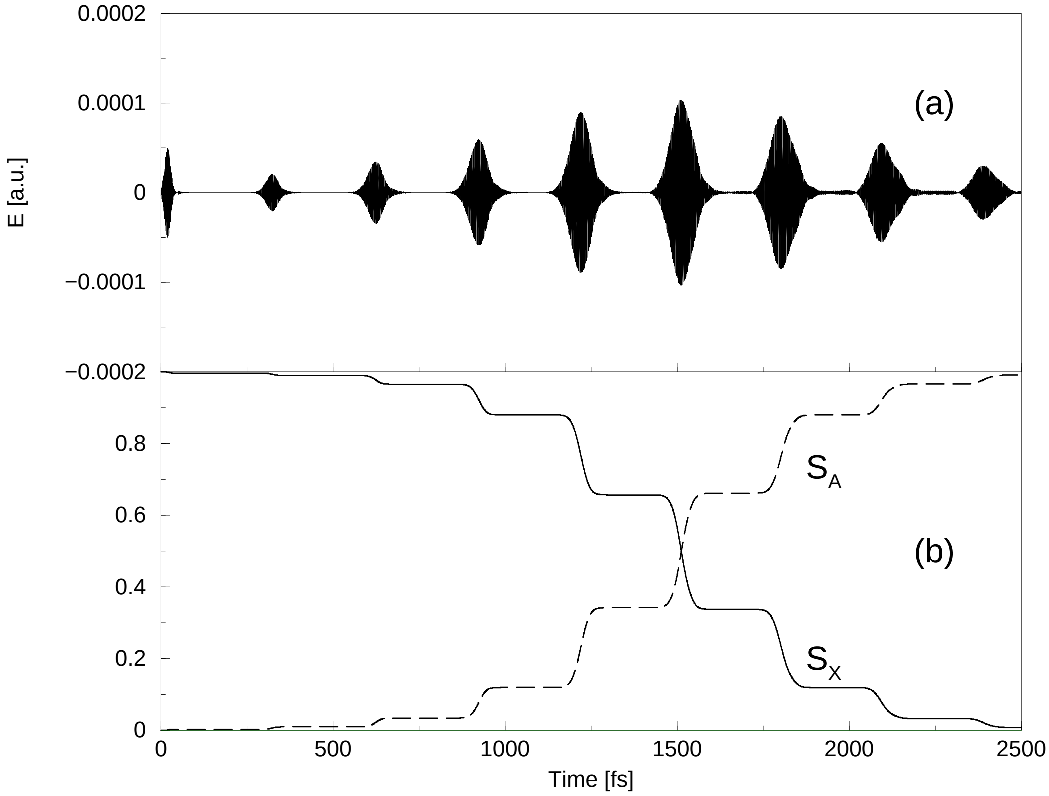

Figure 7.2: *Panel (a): Electric field $E(t)$ constructed with $E_0 = 5.6 \cdot 10^{-5}$. The first pulse is the seed pulse inducing resonant transitions between the electronic states. Panel (b): population S_n in the various electronic states, as indicated.*

Comparing the resulting dynamics for different field strength parameters, a very similar picture is obtained. Fig. 7.3 shows the constructed electric fields and the respective population. In all cases the stepwise structure can be seen, only differing in the fact that a higher field strength prepares the population inversion at earlier times.

Regarding the rather weak field (no Rabi-like oscillations in the populations), a sequence of pulses separated by the average vibrational period in the A state can be seen. Each of these sub-pulses is modulated with a faster frequency approximately proportional to the resonant electronic transition energy. The form of the field can be explained by a wave packet ψ_A, prepared in the $|A\rangle$ state

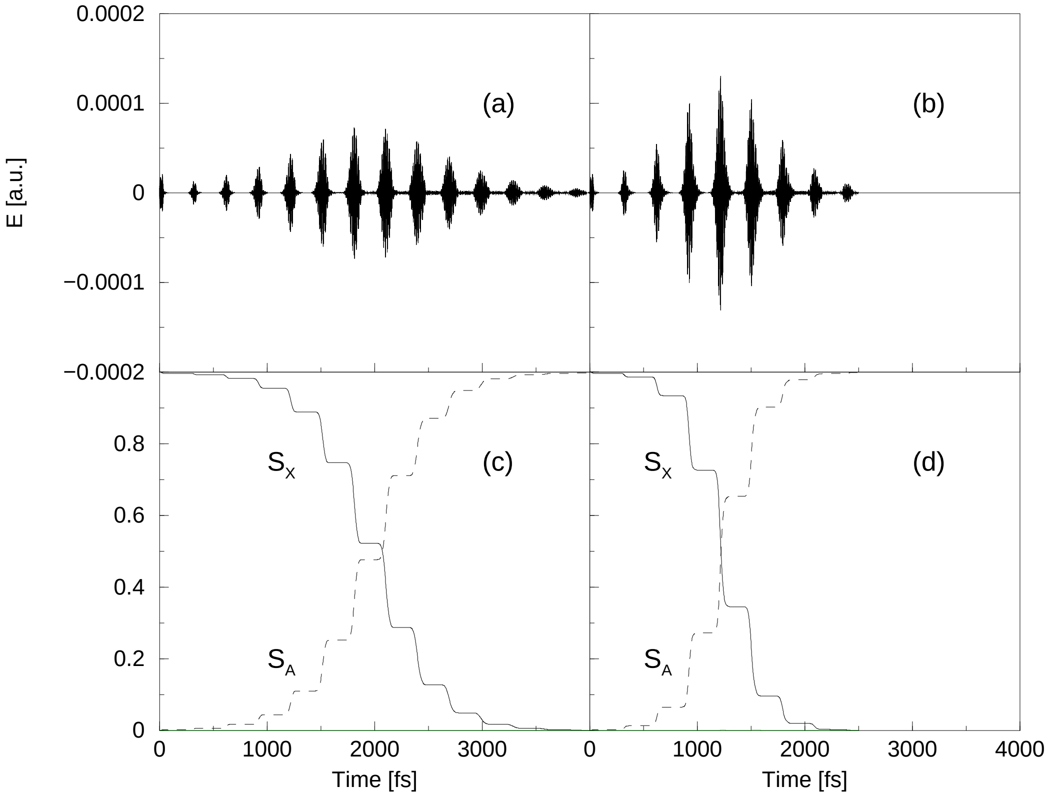

Figure 7.3: *Panel (a), (b): Electric field $E(t)$ constructed with $E_0 = 8.5 \cdot 10^{-5}$ and 1.4·10^{-5}. Lower panels (c), (d): population S in the various electronic states for the different field strengths as indicated. Population S_Π is negligible at all times.*

moving out of the Franck-Condon region for the $|A\rangle \leftarrow |X\rangle$ transition, driven by the resonant center frequency. When ψ_A is moving outward, transitions to the $|\Pi\rangle$ state become more efficient (fig. 7.4) [100]. As a consequence, a decrease in population is avoided by switching off the field to zero. After one round-trip the wave packet re-enters the Franck-Condon region and the field intensity increases again. The already existing wave packet ψ_A interfers constructively with the newly transfered part. This resembles very much the scenario where populations in excited states are influenced via sequences of phase-locked pulses [101, 102].

In order to analyze the control field, a time interval from 1300 to 1800 fs is prescinded, where only a single sub-pulse appears (panel (a) of fig. 7.4). Therefore the following difference potentials (panel (c)) are considered

$$D_{AX}(t) = V_A(\langle R_X(t)\rangle) - V_X(\langle R_X(t)\rangle) \tag{7.5}$$
$$D_{\Pi A}(t) = V_\Pi(\langle R_A(t)\rangle) - V_A(\langle R_A(t)\rangle),$$

where $\langle R_n(t)\rangle$ is the bondlength expectation value in state $|n\rangle$ at time t. Resonant transitions $|m\rangle \leftrightarrow |n\rangle$ occur for photon energies which equal the respective difference potential D_{mn} [103, 104]. The bondlength-expectation values are likewise shown in fig. 7.4, panel (b). It can be seen that $\langle R_X(t)\rangle$ assumes a nearly constant value of approx. 6 a.u., indicating that the ground state wave function is

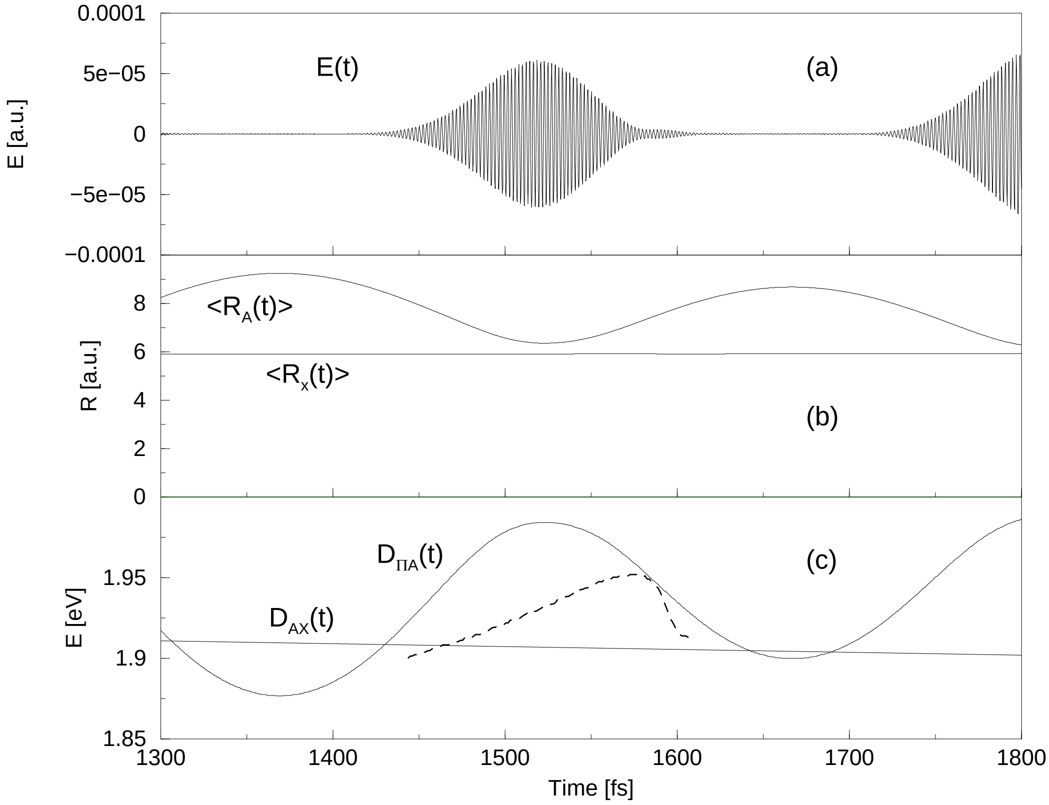

Figure 7.4: *Panel (a) shows a sub-pulse centered around 1500 fs. In panel (b) the bondlength-expectation values $R_X(t)$ and $R_A(t)$ are illustrated. The difference potentials $D_{nm}(t)$ between two states (see eq. (7.5) are displayed in panel (c). Also shown is the time-dependent frequency of the field (dashed line).*

nearly a stationary state. The time-dependence can be understood in regarding $\langle R_A(t)\rangle$. The wave packet $\psi_A(R,t)$, prepared through the interaction at earlier times moves towards smaller bondlengths and reaches its turning point at 1523 fs, which is the time the pulse envelope reaches its maximum. Afterwards, the pulse decays to zero as the wave packet moves out of the Franck-Condon region for the $|A\rangle \leftarrow |X\rangle$ transition. Since the field intensity is determined by the overlap between the ground- and excited state wave packets, it directly reflects the motion of $\psi_A(R,t)$ in and out of the Franck-Condon region. As a consequence, the sub-pulse structure is determined by the vibrational motion in state $|A\rangle$.

To identify the times when resonant transitions between the various states are possible, the average frequency $\omega(t)$ of the pulse (fig. 7.4, panel (a)) is determined for field amplitudes which differ substantially from zero. This is accomplished by calculating an average frequency of the field within a temporal window where ten field oscillations occur, shifting this window continuously over the pulse (short-time Fourier transform). The result is displayed in panel (c) of fig. 7.4 as a dashed line. A resonant transition $|A\rangle \leftarrow |X\rangle$ is effective at about 1460 fs, where the corresponding difference potential and $\omega(t)$ cross. As the field intensity increases, the frequency shifts off resonance, thus the algorithm prevents a too-strong coupling which would allow for a population transfer to states $|X\rangle$ and $|A\rangle$. At a time of 1585 fs, the transient frequency equals $D_{\Pi A}(t)$, so that resonant $|\Pi\rangle \leftarrow |A\rangle$-transitions become very probable. Obviously, the construction scheme prevents this transition by shifting $\omega(t)$ away from the transition frequency towards smaller values.

Therfore, a consistent picture of how the control field is related to the electronic and vibrational dynamics of the system is given. The analysis of other sub-pulses yields the same conclusions drawn above. The interference scheme [105] as experimentally realized [102, 106], where a pair of phase-locked pulses is able to enhance or destroy an excited state population, is naturally obtained within the here presented method to construct the control field. Taking the example of destructive interference, the replacement of the condition $dS_A(t)/dt > 0$ by $dS_A(t)/dt < 0$ yields, via eq. (7.4) to a phase shift of π in the field, as is to be expected [105].

7.3.2 $|\Pi\rangle$ State Population Transfer

The next task is a population transfer to the $|\Pi\rangle$ state. Employing the same seed pulse as before, and for $E_0 = 4.9 \cdot 10^{-2}$ a.u. we get a rather different picture. The population and the calculated pulse are depicted in fig. 7.5 and, displayed in an restricted time interval, in fig. 7.6.

At earlier times the population changes only very slightly, indicating that before any substantial transfer sets in, the $|\Pi\rangle$ state population must exceed a certain threshold value. This is verfied by calculations with a more intensive seed pulse, resulting in a similar dynamics but taking place at earlier times (fig. 7.7)

At times before a critical value, the ground state population is monotonically transferred into state $|A\rangle$, accompanied by a very small population increase in state $|\Pi\rangle$. At early times the populations behave as is expected from perturbation theory. At later times, a population inversion occurs, and perturbation theory fails. Then, Rabi-like oscillations are observed which take place under the constraint that the upper state population increases monotonically. The population

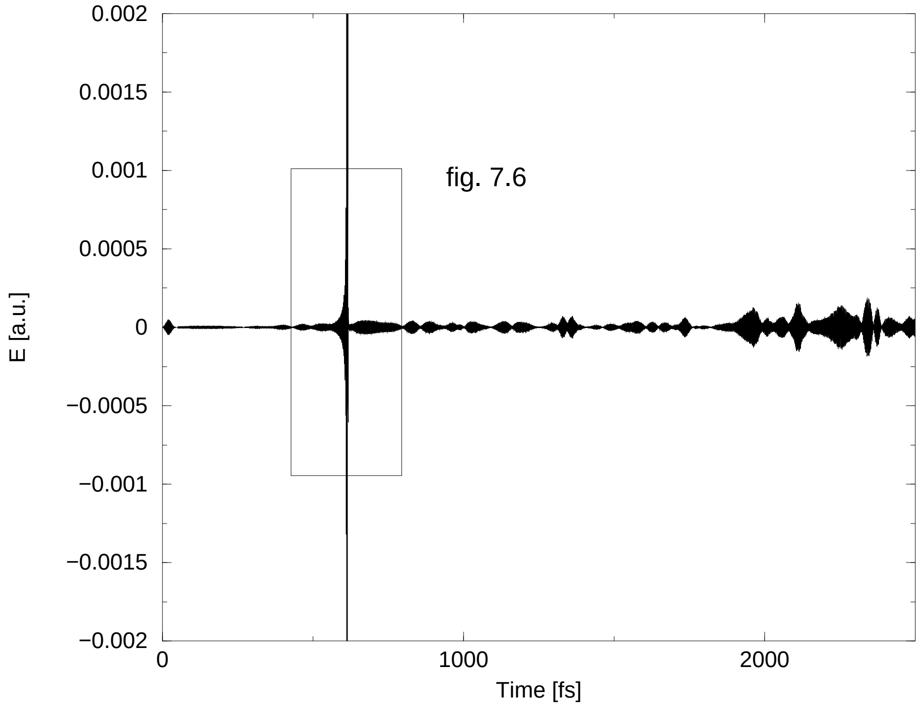

Figure 7.5: *Electric field $E(t)$ constructed with $E_0 = 7 \cdot 10^{-2}$ a.u. The same pulse is depicted within a restricted time-interval in fig. 7.6.*

flux is not exclusively directed to the target state but also, the ground state is repopulated significantly. This is not unlikely, since the dipole-coupling to the ground state is much stronger (about a factor of 2.3) than the one to the $|\Pi\rangle$ state. The same scenario repeats itself afterwards, yielding an efficiency of nearly 90 %. At later times, no substantial increase in the target state is observed.

The time-interval where the population dynamics takes place (fig. 7.7) is in the order of 10 fs, being much smaller than any vibrational periods present in the Na_2 molecule. Thus, here it is solely the electronic transition frequency determining the form of the control field, the field does not exhibit signatures of a vibrational motion. In fact, a calculation where the kinetic energy operator for the vibrational motion is ignored leads almost to identical results as compared to the numerically exact solution, confirming that the system can safely be described

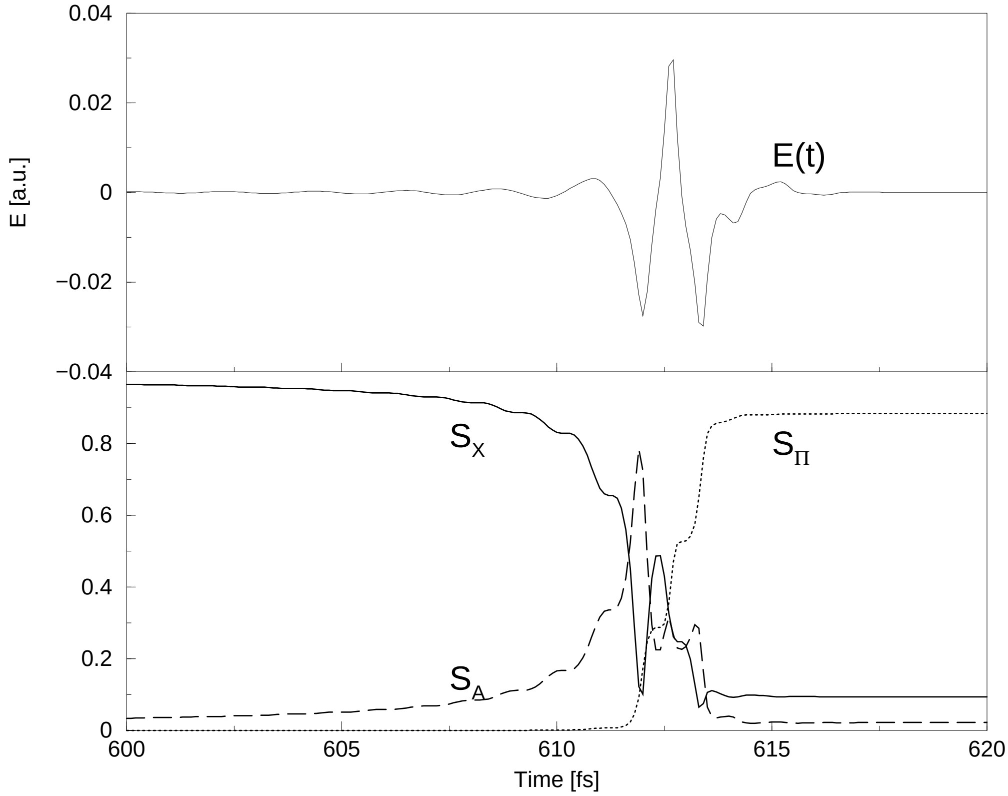

Figure 7.6: *Upper panel: Electric field $E(t)$ constructed with $E_0 = 7 \cdot 10^{-2}$ a.u. The first pulse is the seed pulse inducing resonant transitions between the electronic states. Lower panel: population S_n in the various electronic states, as indicated.*

as a three-level system where the energy separation corresponds to the difference between the potential curves taken at the ground-state equilibrium distance.

Another possibility to transfer population into the $|\Pi\rangle$ state is to first populate the $|A\rangle$ state and then change the target state and subsequently to the $|\Pi\rangle$ state. This can be thought of as a two-step process and the result is shown in fig. 7.8 using $E_{XA} = 1.1 \cdot 10^{-4}$ a.u. and $E_{A\Pi} = 3.5 \cdot 10^{-4}$ a.u.

Thereby, a first sequence of pulses (ending at 2 ps) prepares a vibrational wavepacket in state $|A\rangle$, as described before. Not surprisingly, this vibrational motion introduces a vibrational structure in the control field triggering the second step. Nevertheless, at longer times, when another wave-packet is created in the

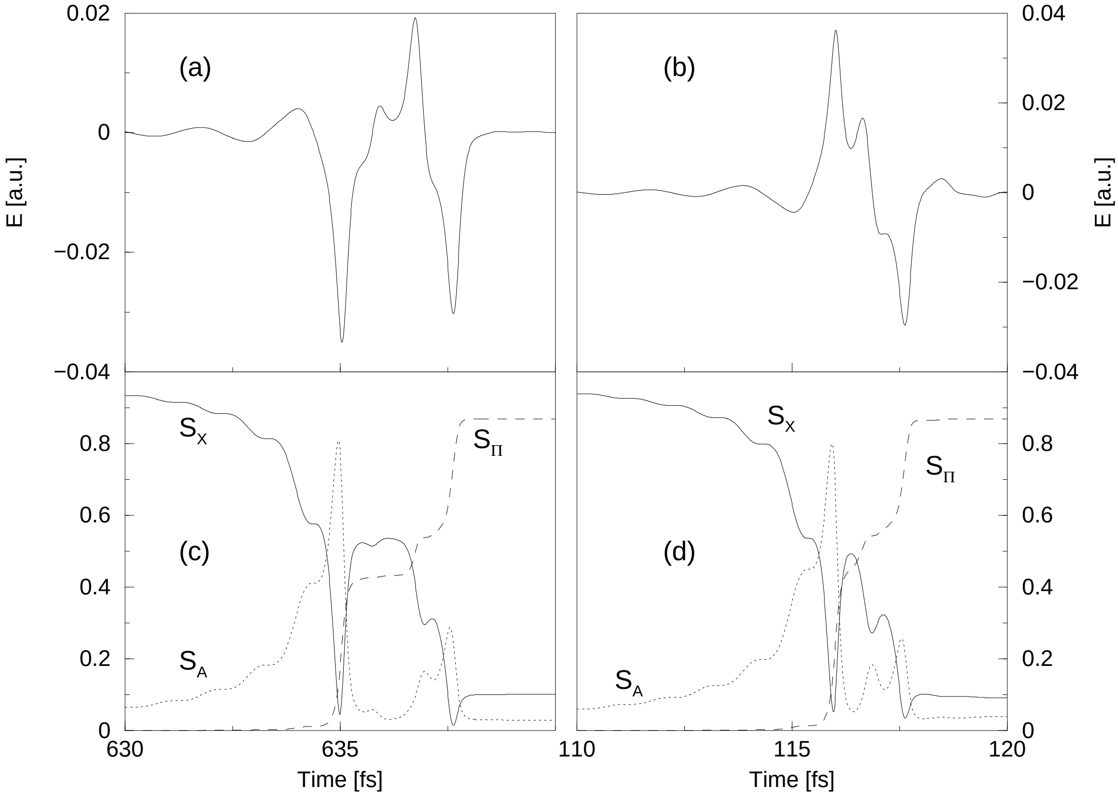

Figure 7.7: *Selective excitation of the* $|\Pi\rangle$ *state. Panels (a) and (b) show the derived control fields* $E(t)$ *constructed with two different seed pulses but the same field strengh parameter* $E_0 = 7 \cdot 10^{-2}$ *a.u. Intensity of the seed pulse: (a)* $E_s = 7.1 \cdot 10^{-5}$ *a.u., (b)* $E_s = 11.3 \cdot 10^{-5}$ *a.u. The respective population in the three electronic states are shown in panels (c) and (d).*

$|\Pi\rangle$ state, the nuclear motion in that state as well influences the field giving rise to the structure as seen in the figure. The final target state ($|\Pi\rangle$ state) is populated to nearly 100%.

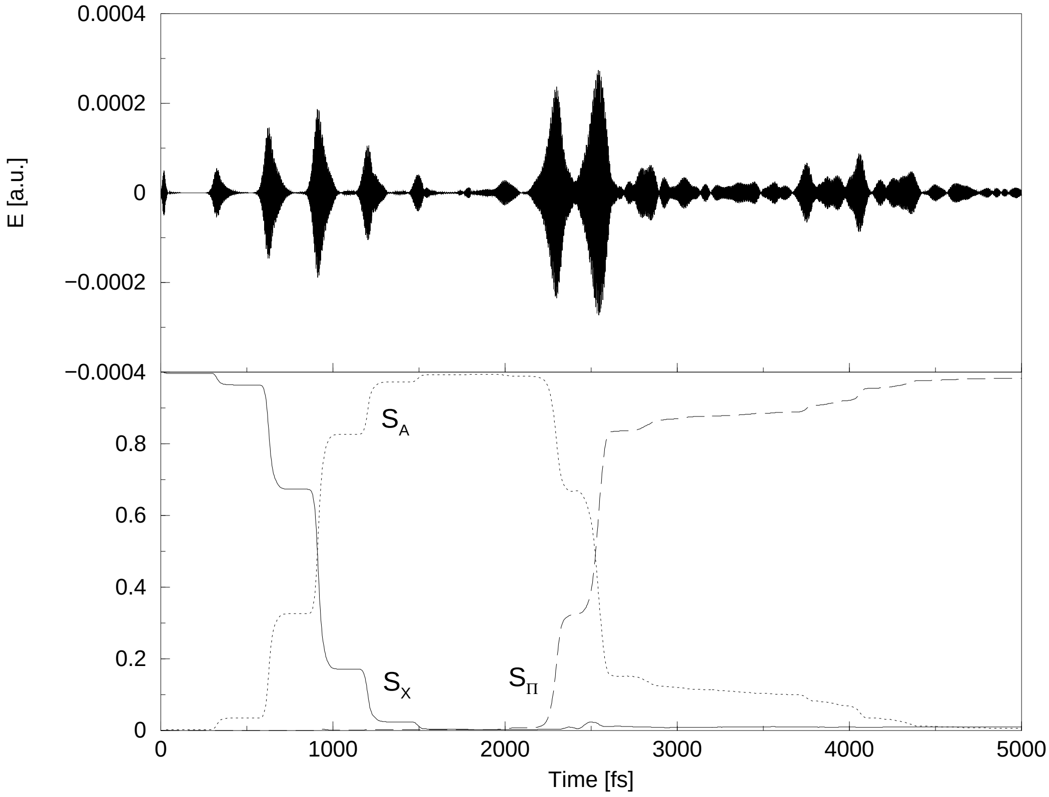

Figure 7.8: *Lower panel: Electric field* $E(t)$ *constructed with* $E_{XA} = 1.1 \cdot 10^{-4}$ *a.u. and* $E_{A\Pi} = 3.5 \cdot 10^{-4}$ *a.u. The first pulse is the seed pulse inducing resonant transitions between the electronic states with* $E_s = 3.5 \cdot 10^{-5}$ *a.u. Lower panel: population* S_n *in the various electronic states as indicated. Population is first transferred into the* $|A\rangle$ *state and in what follows into the* $|\Pi\rangle$ *state.*

7.3.3 Orientational Effects

In the last subsections control fields were constructed for the case of a fixed orientation (45°) of the molecular axis with respect to the field vector. To investigate the orientational effect, the vectorial properties are included within the rotational sudden approximation where the kinetic energy operator for the angular motion is neglected and the angular dependence enters only via the anisotropy of the field-matter interaction

$$W(t) = \begin{pmatrix} 0 & -3.6E(t)\cdot\cos\Theta & 0 \\ -3.6E(t)\cdot\cos\Theta & 0 & -1.44E(t)\cdot\sin\Theta \\ 0 & -1.44E(t)\cdot\sin\Theta & 0 \end{pmatrix}. \quad (7.6)$$

The orientation and therefore the angle Θ directly influences the coupling elements and the construction of the field. As the transitions $|A\rangle \leftarrow |X\rangle$ and $|\Pi\rangle \leftarrow |A\rangle$ are perpendicular, the dependency on the orientation implicates a favor of one transition. For an angle of $\Theta = 0$ the molecule is parallel to the electric field and the coupling into the higher $|\Pi\rangle$ state equals zero. The opposite case appears for $\Theta = 90°$ where the molecule is perpendicular to the field, the coupling $X \leftrightarrow A$ equals zero and the $|\Pi\rangle \leftarrow |A\rangle$ transistion is strongly favoured. In fig. 7.9 the electric fields and the corresponding dynamics for three values of Θ are shown. The fields are relatively similar, exhibiting the pulse-train structure, where the sub-pulses are seperated by the vibrational period in the intermediate state. As can be taken from the figures, the derived fields just differ in intensity. With increasing angle, the time when the population transfer is finished is shifted to longer times. This can be understood in terms of the coupling matrix in eq. (7.6). For an orientation of 30°, the coupling w_{XA} is strongest, so that the population inversion is achieved within 1.5 ps. On the other hand, w_{XA} is about a factor of 1.7 smaller at an orientation of 60° so that, effectively, the inversion is completed at a later time of 2 ps. In this sense, the orientation angle of 45° represents an intermediate situation.

Therefore, the question arises what happens if a field derived for an angle of 45° is used to drive the dynamics of molecules with a different orientation. Or, more commmon: is it possible to control molecules with differently distributed

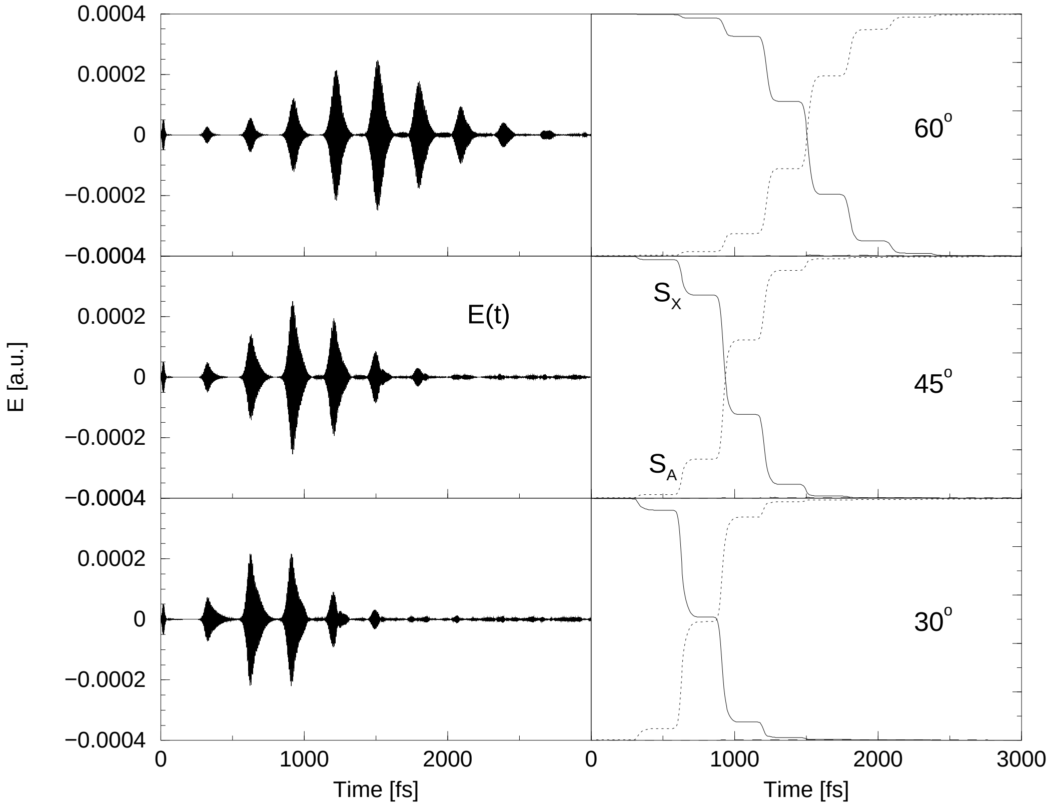

Figure 7.9: *Control fields $E(t)$ constructed with $E_0 = 1 \cdot 10^{-4}$ a.u. obtained for different fixed orientations of the molecule relative to the polarization vector, as indicated. The seed pulse has an intensity of $3.5 \cdot 10^{-5}$ a.u., the field strength parameter is chosen to be $2 \cdot 10^{-4}$ a.u. On the right hand side the particular population S_n in the various electronic states is shown.*

orientation with one single derived control field? Therefore, a calulation is performed where first, the field derived for an angle of 45° is determined and then this field is applied to molecules oriented at angles of $\Theta = 30°$ and 60°, respectively. The results are displayed in fig. 7.10, together with the 45° case which is included for comparison.

It can be seen that for the strongest coupling w_{XA} (at 30°) nearly 100% inversion is reached at 1.5 ps but the field then induces a depletion of the intermediate state, as the excited state wave-packet re-enters the Franck-Condon region for a transition into the ground state. On the other hand, in the case of the weakest

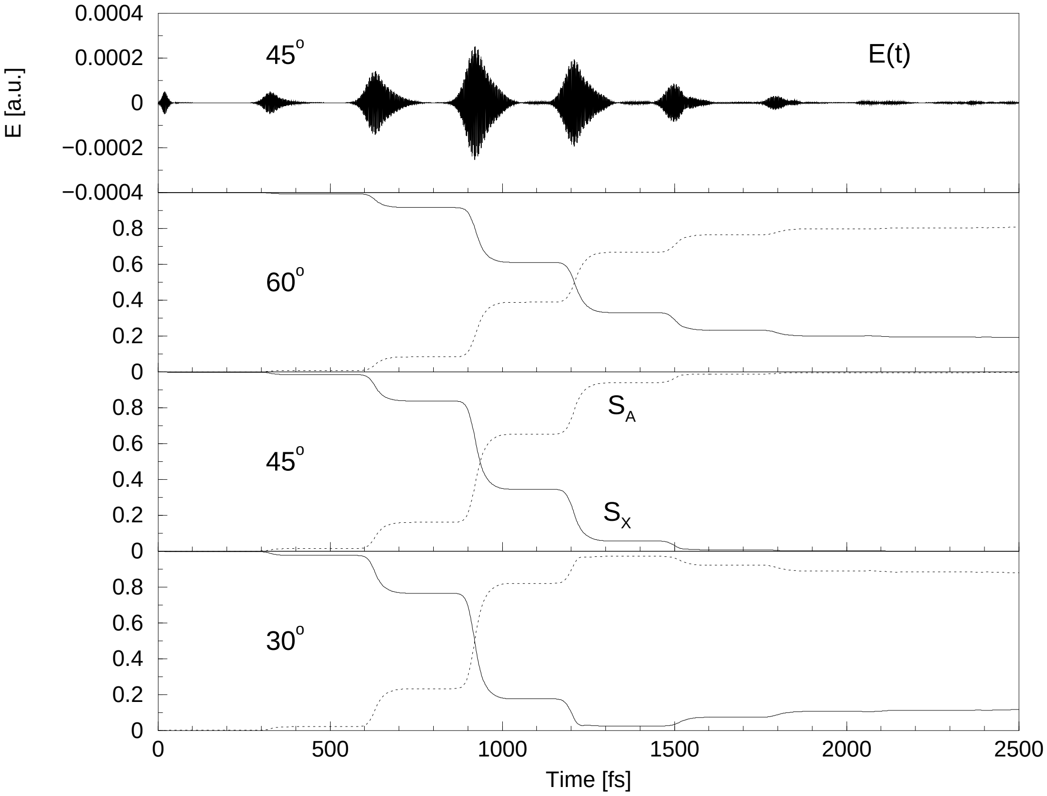

Figure 7.10: *Upper panel: control field constructed for an orientation of* $\Theta = 45°$. *The same field is applied to molecules at different oreientation leads to a different population* S *in the various electronic states as is shown in the lower panels of the figure.*

coupling (60°), not all of the ground state population is transferred to the target state, amounting a final population S_A of nearly 80%. From the presented cases it is concluded that the effect of orientation is not dramatic in the sense that only a few molecules are optimally driven to the intermediate state. Rather, the overall control yield is expected to be in the order of 70% or more.

To gain experimental information on the efficiency of control processes, femtosecond spectroscopic methods have been analyzed concerning their significance. Three of them are introduced in the next subsection and compared with respect to their accuracy.

7.4 Approaches to Wave Packet Imaging Using Femtosecond Ionization Spectroscopy

In this section different methods to obtain information about the probability density of vibrational wave packets are compared [27]. Considering time-resolved spectroscopy the derived signals directly reflect the time behaviour of the system. Here, three pump/probe ionization processes are compared with respect to the quality of their predictions . In a typical experiment, a first laser pulse $W_1(t) = 1/2\mu_{1X} g_1(t) \exp(-i\omega_1 t)$ (pump pulse) interacts with the system, producing a linear combination of eigenstates, a wave packet. The interaction W is defined by the term leading to absorption with frequency ω and pulse envelope $g(t)$. μ_{X1} is the projection of the transition dipole moment on the field polarization vector. At a variable delay-time T a second pulse $W_2(t) = 1/2\mu_{I1} g_2(t-T) \exp(-i\omega_2(t-T))$ (probe pulse) causes another transition in the system, e.g. into an ionic state $|I\rangle$. Within this section, the final ionic state is a dissociative one, see fig. 7.1, panel (b). A signal is recorded as a function of this delay-time. In the case of ionization spectroscopy the transient signal consists of ion yields or photoelectron distributions. Below, transient signals of photoelectron spectra, total ion yields, and fragment momentum distributions are calculated and the such constructed densities are compared to the numerically obtained ones.

7.4.1 Pump/Probe Ionization Signals

The photoelectron spectrum $P(R,T)$ is determined from the probability of finding electrons with a certain kinetic energy E, depending on the delaytime T. Seel and Domcke showed that $P(E,T)$ directly reflects the wave packet dynamic in molecules [107, 108]. For diatomic molecules the assignment is unique [109].

The spectrum is calculated from the norm of the ionic states, obtained by time-dependent perturbation-theory

$$P(E,T) = \langle \psi_E(T) | \psi_E(T) \rangle. \tag{7.7}$$

As the population in the ionic state remains constant after the ionizing pulse switches off, the states $|\psi_E\rangle$ at time $t = T$ enter in the expression.

The total ion yield $P_{tot}(T)$ is likewise a function of the pulse delay T and is calculated from the photoelectron spectrum by integration

$$P_{tot}(T) = \int dE \; P(E,T). \tag{7.8}$$

The momentum (p) distribution of the ionic fragments $F(p,T)$, as a third measurable quantity, is calculated from the momentum-space wave functions of the states $|\psi_E\rangle$ as

$$\begin{aligned} F(p,T) &= \lim_{t\to\infty} \int dE \, |\langle p | U_E(t-T) | \psi_E(T) \rangle|^2 \\ &= \int dE \, |\langle p - | \psi_E(T) \rangle|^2 . \end{aligned} \tag{7.9}$$

The kets $|p-\rangle$ are the eigenstates of the full nuclear Hamiltonian and $|p\rangle$ are plane waves. As the time-limit enters into the calculation a wave packet has to move into the asymptotic region. This is necessary since a constant momentum distribution must be ensured for the projection onto the plane waves.

7.4.2 Photoelectron Spectra

Concerning the re-construction of wave packets from photoelectron spectra some approximations are employed. Besides the Born-Oppenheimer approximation it is assumed that the ejected photoelectron decouples from the nuclei and the other electrons. Furthermore, the ionic states $|\psi_E(R,T)\rangle$ are calculated by neglecting the commutators between kinetic energy and the R-dependent operators (potential energy, dipole moment) [110–116]

$$\psi_E(R,T) = \mu_{I1}(R)\,\psi_1(R,T)\,I(R,E), \tag{7.10}$$

where the integral

$$I(R,E) = \frac{i}{2}\int_{-\infty}^{\infty} dt\, e^{i(V_I(R)-V_1(R)-(\omega_2-E))t} g_2(t). \tag{7.11}$$

In above equation $V_n(R)$ denotes the potential energy in state $|n\rangle$. The photoelectron-spectrum now takes the form

$$P(E,T) = \int dR\,\rho(R,T)\,|I(R,E)|^2. \tag{7.12}$$

The density to be re-constructed is defined as

$$\rho(R,T) = \left|\mu_{I1}(R)\psi_1(R,T)\right|^2. \tag{7.13}$$

To calculate the density from the spectrum $P(E)$ it is clear from eq. (7.12) that the integral $I(R,E)$ is necessary. The product between the transition dipole moment and the vibrational wave function can not be disentangled. Evaluating the time-integral employing a Gaussian envelope function $g_2(t) = \exp(-(\beta\, t/2)^2)$ leads to the expression

$$I(R,E) = \frac{i}{2}\sqrt{4\pi/\beta^2}e^{-(D(R)-(\omega_2-E))^2/\beta^2}, \tag{7.14}$$

where the difference potential $D(R) = V_I(R) - V_1(R)$ was introduced. The time-integral $I(R,E)$ represents a window function peaked around distances R_i which are roots of the equation

$$D(R) - (\omega_2 - E) = 0. \tag{7.15}$$

For a monotonic difference potential as is assumed here, eq. (7.15) establishes a connection between the bond length and the photoelectron energy. In the limit of long pulses (for $\beta \rightarrow 0$) the window function becomes a representation of the δ-function. Thus, the function $I(R, E)$ can be written as

$$I(R, E) = i\pi\{\delta(D(R) - (\omega_2 - E)) + c(R, E)\}, \tag{7.16}$$

where the additional term $c(R, E)$ compensates the error made by replacing the window function by a δ-function. Neglecting this term the spectrum is reduced to the simple form

$$P(E, T) \propto \frac{\rho(R_i, T)}{|dD(R)/dR|^2_{R_i}}. \tag{7.17}$$

Here, we used the properties of the δ-function: $\delta(f(x)) = \delta(x)/|df/dx|_{x_i}$. Eq. (7.15) and eq. (7.17) relate the radial probability density $\rho(R)$ and the photoelectron spectrum $P(E)$ for a fixed delay-time T. The quality of the two approximations, namely (a) the neglect of commutators and (b) the replacement of the window function by a δ-function are discussed in detail in Refs. [112, 117]. For a constant difference potential, approximation (a) becomes exact, but then, the spectrum $P(E, T)$ is independent of the actual position of the wave function $\psi_1(R, T)$ (and consequently of time). Also, for a δ-pulse excitation, the spectrum becomes energy- and R-independent and no information can be gathered from the signal. On the other hand, for very long pulses, the correction term $c(R, E)$ in eq. (7.16) vanishes, but then, approximation (a) is invalid. The connection in eq. (7.17) is reasonable for substantially R-dependent difference potentials $D(R)$ and for pulses that are short compared to the vibrational periods but long enough to guarantee that the window function $I(E, R)$ is strongly peaked around the root of eq. (7.15).

7.4.3 Transient Ion Yields

In the ionization scheme the photon energy ω_2 is chosen such that for small bond lengths R ionization is not possible, but for a certain bond length $R = a$ the photon energy matches the difference potential $\omega_2 = D(R = a)$, see Fig. 7.1, panel (b). The ion yield is zero if the wave packet is located at distances smaller than a and increases when the wave packet moves into regions with $R \geq a$. If the transition dipole moment μ_{1I} can be approximated by a constant and the laser frequency is large enough the ion yield will settle to a constant value [107,118,119]. For later times, when the wave packet passes the distance $R = a$ on its way back, the signal decreases to zero.

Applying a Gaussian probe-pulse as in the last subsection the total ion yield can be calculated with

$$P_{tot}(T) = \frac{\pi}{\beta^2} \int dR\, \rho(R,T) \int_0^\infty dE e^{-2\,[E-(\omega_2 - D(R))/\beta]^2}. \tag{7.18}$$

Performing the integration over energy and employing properties of the error function erf(x) [120] yields

$$P_{tot}(T) = \frac{(\pi/2)^{3/2}}{\beta} \int dR\, \rho(R,T) \left\{ 1 + erf\left[\frac{\sqrt{2}(\omega_2 - D(R))}{\beta} \right] \right\}. \tag{7.19}$$

Above equation demonstrates once again that if the density $\rho(R, T)$ is located in a region where the argument of the error function is substantially negative, the signal is zero. For larger bond lengths $R \geq a$ the signal levels off to a constant proportional to the area under the density [120, 121].

To establish the relation between the total ion yield at a fixed delay-time T and the radial density, the expression $(1 + erf(x))/2$ in eq. (7.19) is replaced by a step function $\Theta(R - a)$. It can be shown that [122]

$$\frac{dP_{tot}(T)}{dT} = j(a, T), \tag{7.20}$$

with $j(a, T)$ being the probability flux through the point $R = a$ at time T. Employing the definition

$$\mu_{I1}(R)\psi_1(R, T) = \sqrt{\rho(R, T)}e^{iS(R,T)}, \tag{7.21}$$

where $S(R, T)$ is a real function, assumed to depend only weakly on delay time, eq. (7.20) can be written as

$$\frac{dP_{tot}(T)}{dT} = \frac{1}{m}\left\{\frac{dS(R, T)}{dR}\right\}_a \rho(a, T). \tag{7.22}$$

The latter equation, where m is the reduced mass, relates the time-derivative of the total ion signal to the density at the resonance point $R = a$ at time T. The density is calculated from

$$\rho(R = a + v_0 t, T) \propto \left\{\frac{dP(\lambda)}{d\lambda}\right\}_{\lambda=T-t}. \tag{7.23}$$

Here enters the average velocity of the wavepacket in state $|1\rangle$ which can be estimated classically as $v_0 = \sqrt{2(\omega_1 - V_1(a))/m}$.

7.4.4 Transient Fragment Distributions

A third method for wave packet imaging was used in connection with the Coulomb explosion of small molecules [123–125]. For discussions see the paper of Chelkowski and Bandrauck [125]. The main idea here is to relate the asymptotic momentum distribution of the charged atoms to the density $\rho(R,T)$ at the time T of the ionization. The fragment distribution is given by eq. (7.9)

$$F(p,T) = \int dE \left| \int dR \langle p - |R\rangle\langle R| \int dt e^{i(p^2/2m+V_I(\infty)+E-\omega_2-V_1)t} \frac{i}{2} g_2(t)\mu_{1I}\psi_1(T)\rangle \right|^2 \tag{7.24}$$

In the derivation of this equation the fact that $|p-\rangle$ is an eigenstate of the Hamiltonian in the ionic state, and a neglection of the kinetic energy operator in state $|1\rangle$ was used. Employing a Gaussian envelope (as before) the time-integral can be evaluated as

$$\begin{aligned} I_p(R,E) &= \frac{i}{2}\int dt e^{i(p^2/2m+V_I(\infty)-V_1(R)+E-\omega_2)t} g_2(t) \\ &= \frac{i}{2}\sqrt{4\pi/\beta^2} e^{-(p^2/2m+V_I(\infty)-V_1(R)-(\omega_2-E)/\beta^2}. \end{aligned} \tag{7.25}$$

Employing the same arguments as given above concerning the window function, the time-integral is written as

$$\begin{aligned} I_p(R,E) &= i\pi\left\{\delta(p^2/2m + V_I(\infty) - V_1(R) - (\omega_2 - E)) + c_p(R,E)\right\} \\ &= i\pi\frac{\delta(R-R_i)}{|dV_I(R)/dR|^2_{R_i}}. \end{aligned} \tag{7.26}$$

The values R_i are defined as roots of the equation

$$\frac{p^2}{2m} + V_I(\infty) - V_1(R) - (\omega_2 - E) = 0 \tag{7.27}$$

As a projection onto the eigenstate $|p-\rangle$ was performed to calculate the fragment distribution, the value of the momentum p is fixed so that R depends only parametrically upon p. Evaluating the integral over R leads to the fragment distribution

$$F(p,T) \propto \int dE \, \frac{|\langle p- |R_i(E)\rangle|^2 \, \rho(R_i(E),T)}{dV_I(R)/dR|_{R_i(E)}}. \tag{7.28}$$

The energy integral is eliminated by an additional approximation. Employing the limit of energy conservation, saying that at a given value of R

$$V_1(R) + \omega_2 = V_1(R) + E, \tag{7.29}$$

although the probe pulse is spectrally broad, eq. (7.27) reduces to

$$\frac{p^2}{2m} + V_I(\infty) - V_1(R) = 0. \tag{7.30}$$

Since the roots from this equations are independent of E, the momentum distribution now reads

$$F(p,T) \propto \frac{|\langle p- |R_i\rangle|^2 \, \rho(R_i,T)}{|dV_I(R)/dR|^2_{R_i}}. \tag{7.31}$$

In principle, for a given potential $V_I(R)$, the stationary scattering states $\langle p - |R\rangle$ can be calculated by solving

$$\Big(p^2/2m + V_I(R)\Big) \, |p-\rangle = \Big(p^2/2m + V_I(\infty)\Big) \, |p-\rangle, \tag{7.32}$$

taking the proper boundary conditions into account. Within a linear approximation to the potential around the point R_i, the solution of the time-independent Schrödinger equation is an Airy function $Ai(R = R_i) = Ai(0)$, thus is independent of R_i [126] and may be omitted in evaluating the fragment distribution. The final expression then is

$$F(p,T) \propto \frac{\rho(R_i,T)}{|dV_I(R)/dR|^2_{R_i}}. \tag{7.33}$$

The expressions for the photofragment (eq. (7.33)) and photoelectron spectrum (eq. (7.17)) are very similar and are identical if the denominators (containing the derivative of $V_1(R)$ and $D(R)$ at the same resonance distance) are set to the same constant. It is noted that they are, nevertheless, based on different kind of approximations.

In practice, the momentum distributions are calculated from eq. (7.9): for a fixed value of E the ionic wave functions $|\psi_E(R,T)\rangle$ are propagated until they are completely localized in the asymptotic region. Then a Fourier transform into momentum space is performed. After repeating this for a discrete set of energies E the energy integral is calculated.

7.4.5 Numerical Results

First, the construction of radial densities from photoelectron spectra will be treated. In what follows, results are discussed for photon energies of 332 nm (pump-pulse into the double minimum potential) and 275 nm (probe-pulse into the dissociative ionic state), see Fig. 7.1, panel (b). The Gaussian pump-pulse has a duration of 50 fs (full width at half maximum), and a shorter (Gaussian) probe-pulse of 20 fs is employed. Figure 7.11 compares the numerically exact density $\rho(R,T)$ with the constructed density $\rho_c(R,T)$ obtained from eq. (7.17) for different delay times T, as indicated.

In this system, the difference potential between the double minimum state $|1\rangle$ and the repulsive ionic state $|I\rangle$ is a monotonically decreasing function of R (in the region, the wave packet dynamics takes place), so that there is a one-to-one correspondence between the points R_i and the photoelectron energy, as defined in eq. (7.15). The figure documents that the prescription for the construction of

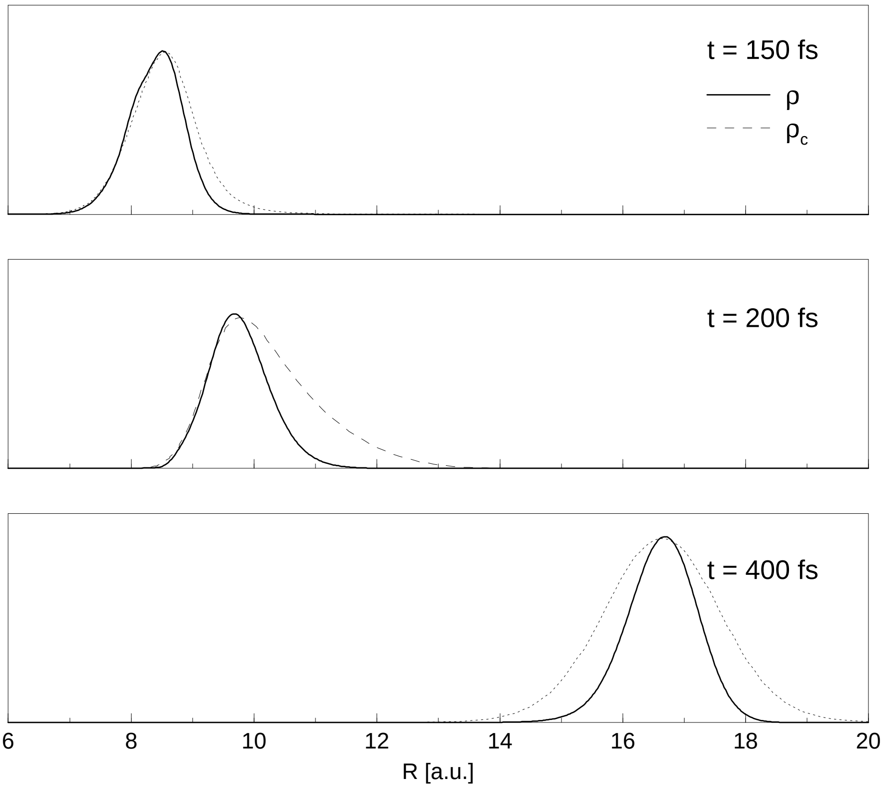

Figure 7.11: *Constructed ρ_c vs. numerically exact density ρ for different pump-probe delays. The densities are derived from the photoelectron spectra.*

the density is excellent, as was demonstrated theoretically before [127, 128]. For all three delay-times, the position of the maximum of $\rho_c(R)$ coincides with that of $\rho(R)$. Also, the widths of the density agree well so that here we may say that wave packet imaging trough time-resolved photoelectron spectroscopy works very well.

Next, the densitities as obtained from the total ion yield using eq. (7.23) are compared. The same pulse parameters as specified above were employed except that the probe photon-energy was varied for different delay times, as resonant ionization with pulses of different photon energies ω_2 selects different bond lengths $R = a$, at which the vibrational wave packet can be monitored. Figure 7.12 containes the calculated densities. The energy ω_2 was chosen to assume values of 400 nm (upper panel), 420 nm (middel panel), and 450 nm (lower panel), corresponding to bond lengths of $a = 8.1$, 8.3 and 9.4 a.u., respectively.

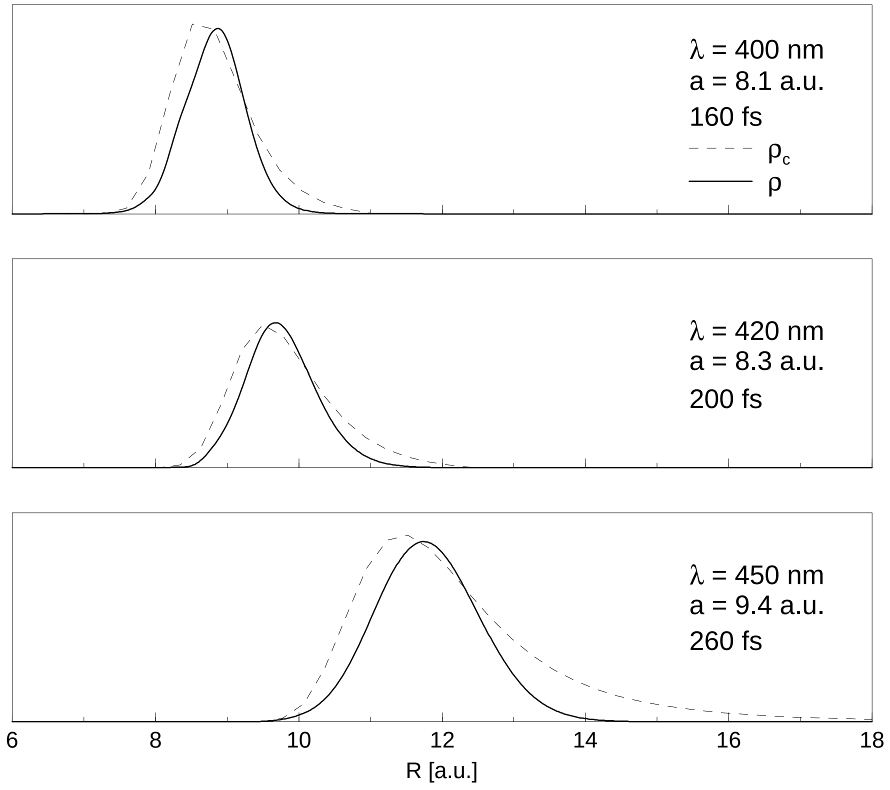

Figure 7.12: *Constructed ρ_c vs. numerically exact density ρ for different pump-probe delays. Here the wave packet imaging is performed using the time-derivative of the transient ion yield. The choice of the probe photon-energies allows for the mapping at different bond lengths. The numbers given in the different panels indicate the times when the wave packet has completely entered the excitation window so that the ionization signal has leveled to a constant.*

For the choice of the first two parameters, the constructed and numerically exact densities agree perfectly. A larger discrepancy occurs in the $a = 9.4$ a.u. case, mainly at longer bond lengths. This results from the fact that here the wave packet passes the barrier of the double minimum state and thus the approximation of a constant velocity v_0 within this state is not valid. It has to be noted that a wave packet being localized in the regions of the classical turning points in the excited state cannot be monitored using the flux method as described above, since the transient ion yield will not level to a constant value as a function of delay-time.

Finally, wave packet imaging by inversion of the fragment distribution is discussed. As in the case of the photoelectron spectra pulses with $\lambda_1 = 332$ nm, 50 fs width (pump) and $\lambda_2 = 275$ nm, 20 fs width (probe) are employed. The upper panel of fig. 7.13 compares the densities at a delay-time of $T = 100$ fs. Here, the vibrational wave packet in the intermediate state is localized at a bond length between 5.7 and 7.6 a.u. The constructed density is shifted slightly towards smaller distances as compared to the numerically exact one. At a later time of 150 fs, the fact that ρ_c peaks at smaller distances is as well observed. This trend continues and is most pronounced at $T = 250$ fs (lower panel of fig. 7.13).

The reason for the discrepancy in the location of the two densities can be rationalized in the following way: the basic idea of the construction method is that the initial wave packet, produced within the ionization step, carries a momentum distribution which is dominated by components with zero momentum, and thus the energy at early times is almost exclusively potential energy. The latter is then transformed into kinetic energy of the fragments. The assumption of a mean zero momentum is not necessarily valid: since the wave packet $\psi_1(R, T)$ is moving outward in the double minimum state, its kinetic energy is transferred into the ionic state (see, e.g. eq. (7.10)). Thus, the fragment distribution peaks at higher momentum which, in turn, yields a constructed density at shorter distances. This reasoning explains why the mismatch in the peak position increases in going from 100 to 250 fs, since for the longer time, the lower state wave packet has picked up more speed.

As a second observation, the deviation in the width of the two densities is

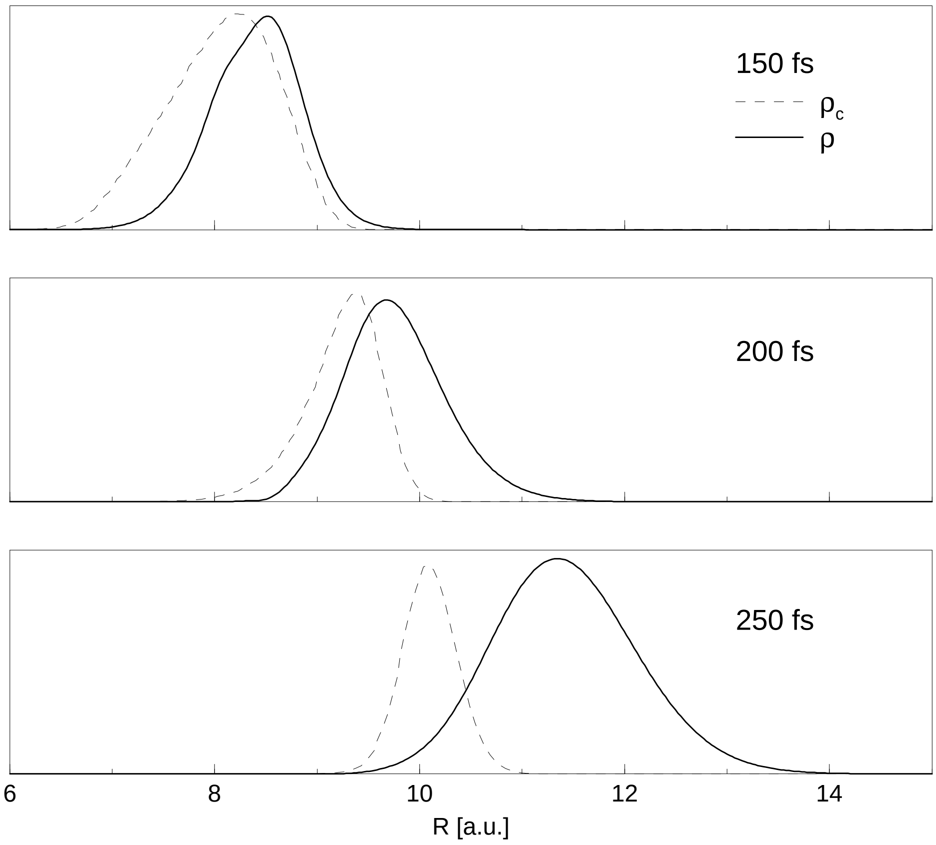

Figure 7.13: *Constructed ρ_c vs. numerically exact density ρ for different pump-probe delays. The momentum distribution of the fragments was used for the construction.*

much more pronounced in the 250 fs case than at earlier times. Because of large positive momentum from the intermediate state dynamics, the fragment momentum distribution yields a constructed density at too small distances where the potential energy is rather steep and thus the width becomes too small as well. For the example regarded here, the use of the fragment distribution is good as long as the vibrational wave packet in state $|1\rangle$ has not developed a momentum distribution far away from zero momentum which, in this example, is the case at small delay-times.

7.5 Simultaneous Monitoring of the Control Process by Time-Dependent Photoelectron Spectra

In order to obtain information about the temporal behaviour of control processes time-dependent photoelectron spectra have been calculated. As shown in the last section, it is possible to construct the nuclear density in excited electronic states from photoelectron spectra. For the discussed control scheme $|X\rangle \rightarrow |A\rangle$ or $|X\rangle \rightarrow |\Pi\rangle$ (see fig. 7.1, panel (a)) resulting from transitions into the bound ionic state have been determined. While the ground state $|\psi_X\rangle$ and the excited electronic state wave packets $|\psi_A\rangle$ and $|\psi_\Pi\rangle$ are propagated with an exact coupling of the states to the field, the ionic wave packets $|\psi_E(t)\rangle$ have been calculated by time-dependent perturbation theory. It is assumed that the probe laser with a wavelength of 620 nm ionizes the $|A\rangle$ state by a two-photon process and the $|\Pi\rangle$ state via a one-photon process. The temporal change of the kinetic energy distribution of the photoelectrons directly reflects the vibrational dynamics of the state where ionization derives from. Therefore, oberserving photoelectron spectra provides information on the excited state.

First, the amount of population in the $|A\rangle$ state while maximizing population in $|A\rangle$ state is observed. The time-dependent photoelectron spectrum is shown in fig. 7.14. Then, the $|\Pi\rangle$ state population is maximized, monitored by the corresponding photoelectron spectrum (fig. 7.15). In both cases, the spectra are modulated by the vibrational motion in the respective state. The corresponding excited state wave packets in the $|A\rangle$ and $|\Pi\rangle$ state are shown in fig. 7.16, 7.17, respectively. It can be seen that the kinetic energy distribution of the photoelectrons exhibits a maximum at the time when the coordinate expectation value is

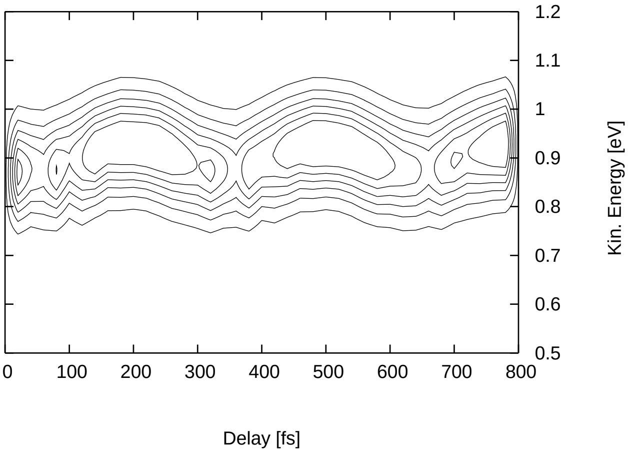

Figure 7.14: *Time-dependent photoelectron spectrum with a probe laser with wavelength of 620 nm after optimizing the $|A\rangle$ state population.*

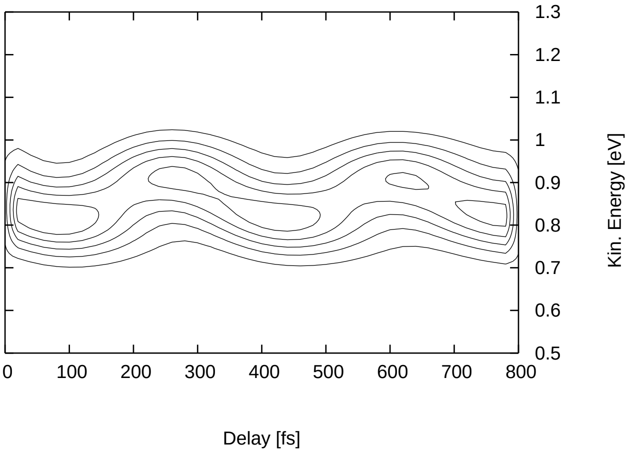

Figure 7.15: *Time-dependent photoelectron spectrum with the same probe wavelength as before after optimizing the $|\Pi\rangle$ state population.*

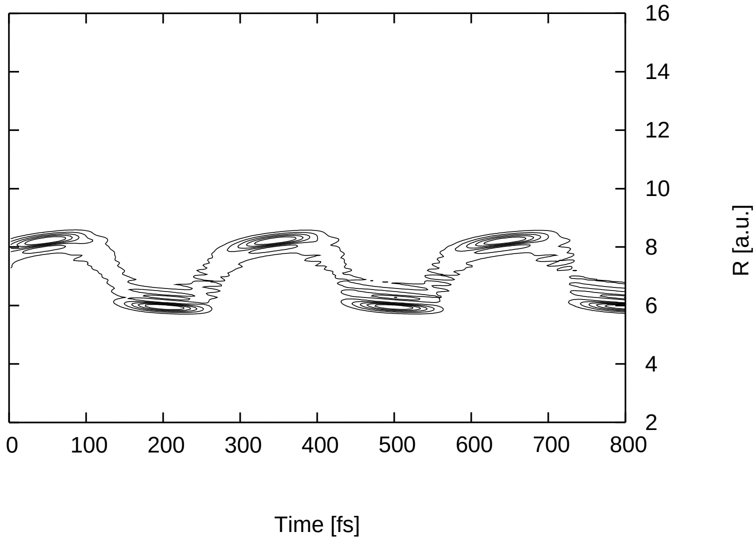

Figure 7.16: *Absolute square of the $|A\rangle$ state wavefunction $\psi_A(R,t)$, exhibiting a vibrational motion.*

largest. This can be explained in regarding the difference potential, expressed by the condition in eq. (7.15). In order to clarify the assignment to the particular electronic state, cuts through the time-dependent photoelectron distributions for selected kinetic energies are shown in fig. 7.18.

The photoelectron spectra differ in the temporal separation of their maxima. Panel (a) shows a cut at a kinetic energy of 0.976 eV after populating the $|A\rangle$ state, featuring a separation of succesive extrema of $\approx$ 300 fs, according to the average vibrational period in this state. A population of the $|\Pi\rangle$-state leads to a kinetic energy distribution of photoelectrons exhibiting a longer periodicity of $\approx$ 356 fs, which is the time-scale of vibrations taking place in the $|\Pi\rangle$ state. If both elelctronic states are populated significantly, the photoelectron spectra

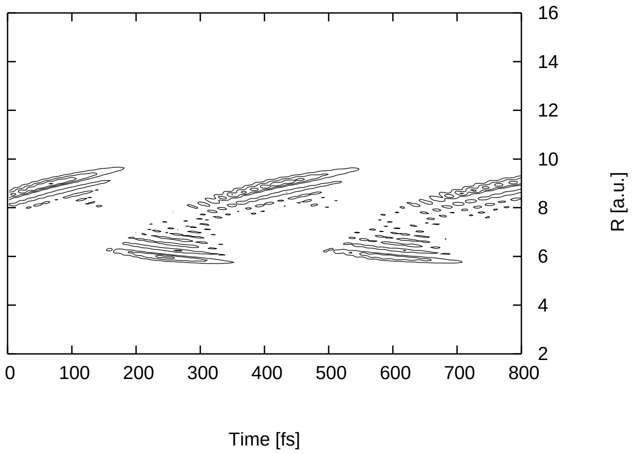

Figure 7.17: *Absolute square of the $|\Pi\rangle$ state wavefunction $\psi_\Pi(R, t)$, exhibiting a vibrational motion.*

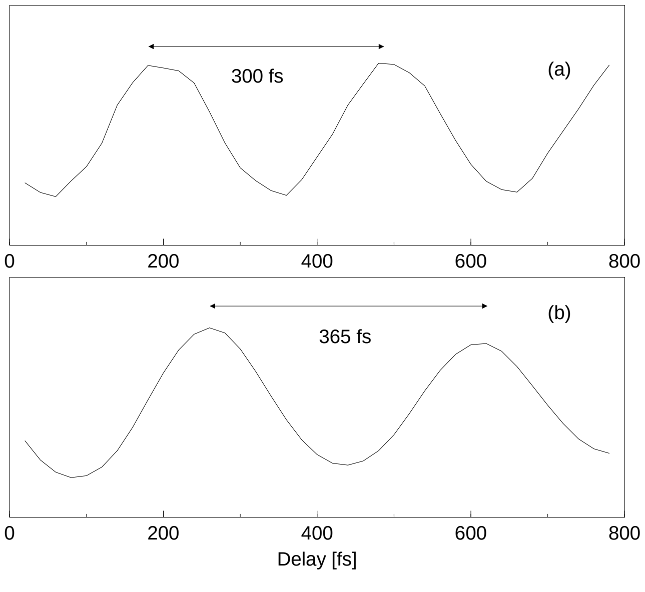

Figure 7.18: *Panel (a): Cut of the photoelectron spectrum of fig. 7.14 at 0.976 eV after populating the $|A\rangle$ state; panel (b): Cut of the time-dependent photoelectron spectrum of fig. 7.15 at 0.954 eV after transferring population into the $|\Pi\rangle$ state.*

reveal characteristics of nuclear motion in both states, as was found before for the sodium dimer [109,129]. Maximization of population in a target state $|n\rangle$ results in photoelectron spectra modulated by the characteristic vibrational period T_n. It is then possible to deduct the degree of excitation from the transient spectrum.

Chapter 8

Iodine Dimer

In this chapter a different approach to control molecules is given by investigating molecular iodine with a setup similar to the STIRAP (Stimulated Raman Adiabatic Passage) technique. Until now, this technique has been incorporated using ns laser pulses. Here, the possibility to extent it towards the fs-regime is investigated, a problem which has not been addresses so far. Within the STIRAP technique developed by Bergmann [14] two time-delayed pulses in a defined geometric arrangement interact with the molecular sample. Compared to a CARS (Coherent Anti-Stokes Raman-Spectroscopy) process the pulse sequence is counterintuitive. In a femtosecond CARS experiment a first laser pulse (pump-pulse) with frequency ω_P propagating in direction k_1, prepares a coherent superposition of molecular eigenstates. The system then interacts with the Stokes-pulse of frequency ω_S and direction k_2, and population is dumped into excited states within the electronic ground state vibrational manifold. A time-delayed probe-pulse having the same frequency as the pump-pulse and propagating in direction k_3 again excites the molecule and the CARS signal is obtained in direction $k_4 = k_1 - k_2 + k_3$.

The STIRAP technique now modifies the CARS experiment by choosing a counterintuitive pulse sequence: the Stokes-pulse acts before the pump-pulse. In this work, the conditions of generating highly excited vibrational states by a STIRAP-like scenario in the fs regime are established employing the I_2 molecule as a prototype example. The temporal behavior of the population transfer is investigated as a function of photon energy, intensity and delay-time. The present studies are motivated by experiments, performed most recently in the Kiefer group in Würzburg.

8.1 Model System

Spectroscopic transitions in the iodine molecule have been investigated extensively, both experimentally and theoretically. In particular, the $|B\rangle \leftarrow |X\rangle$ transition [130–133] was extremely well characterized by Raman spectroscopy [134], time-resolved spectroscopy [135, 136] and time-dependent CARS experiments [137–140].

In what follows, the molecule is described within an artificial system of three electronic states, where $|1\rangle$ denotes the electronic ground state ($|X\rangle$) which is coupled via the pump-pulse to the excited electronic state $|2\rangle$ (the $|B\rangle$ state). The model incorporates an initially not populated third state $|3\rangle$ which is the electronic ground state coupled only to $|2\rangle$ via the Stokes-pulse interaction. A direct transition from the vibrational ground state $|1\rangle$ to the vibrational excited state $|3\rangle$ is excluded so that the coupling matrix reads

$$W(t) = \begin{pmatrix} 0 & w_1(t) & 0 \\ w_1(t) & 0 & w_2(t) \\ 0 & w_2(t) & 0 \end{pmatrix}, \tag{8.1}$$

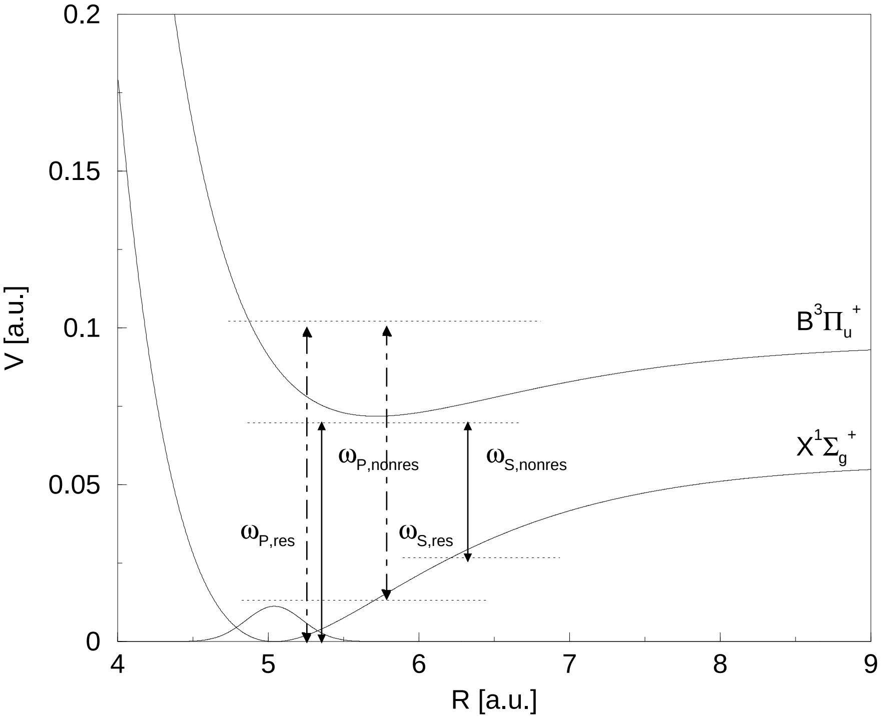

Figure 8.1: *Potential energy curves of molecular iodine. The examined* $|X\rangle \leftrightarrow |B\rangle$ *transitions for resonant and off-resonant excitation are indicated by the arrows. The solid arrows display the non-resonant transitions, while the resonant transitions are represented by the dot-dashed arrows*

where $w_1(t)$ and $w_2(t)$ contain the interaction with the electric fields. The matrix describes the so-called Λ-configuration as shown in fig. 8.2.

Within a numerically exact coupling scheme, the field coupling of the three states is given by the sum of the pump- and Stokes-pulse $w_1(t) = w_2(t) = w_P(t) + w_S(t)$, where

$$\begin{aligned} w_P(t) &= -\mu \cdot E_P(t) = -E_P \cdot e^{-(t-t_P)^2 * \gamma_P} \cos \omega_P(t-t_P) \\ w_S(t) &= -\mu \cdot E_S(t) = -E_S \cdot e^{-(t-t_S)^2 * \gamma_S} \cos \omega_S(t-t_S), \end{aligned} \quad (8.2)$$

with E_n being the field strength, $\gamma_n = 2 \ln 2/\beta^2$ related to the the pulse width β_n, ω_n the frequency and t_n (n = P,S) the time where the Gaussian pulses exhibit

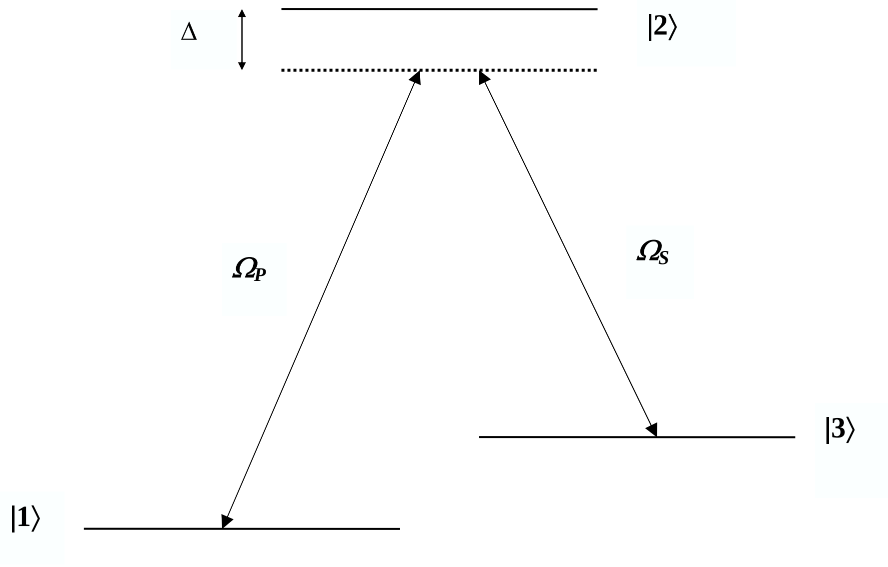

Figure 8.2: *Three level system in the Λ-configuration [141]. A direct transition between states $|1\rangle$ and $|3\rangle$ is forbidden. The two pulses (pump and Stokes) couple the three states, as indicated, where Δ characterizes a possible detuning.*

their maxima. The transition dipole momenent μ is constant within the Condon-approximation ($\mu = 1$).

Another coupling scheme is regarded where $w_1(t) = w_P(t)$ and $w_2(t) = w_S(t)$. This scheme will be called "adiabatic", because possible $|2\rangle \leftrightarrow |1\rangle$ transitions induced by the Stokes pulses, and also transitions $|3\rangle \leftrightarrow |2\rangle$ caused by the pump pulse are neglected. The adiabatic approach allows a description within the picture of dressed states. In the next section the adiabtic description of dressed states in a three level system is presented.

8.2 Adiabatic Limit - STIRAP

The coupling matrix in eq. (8.1) can be adapted to describe an adiabatic population transfer within the STIRAP mechanism [6,142]. For a system including three potential curves in the Λ-configuration illustrated in fig. 8.2, the Schrödinger equation reads as [143]

$$i\hbar\frac{\partial}{\partial t}\begin{pmatrix}\psi_1(x,t)\\ \psi_2(x,t)\\ \psi_3(x,t)\end{pmatrix} = \Bigg[-\frac{\hbar^2}{2m}\frac{\partial^2}{\partial x^2}\mathcal{I}+ \tag{8.3}$$

$$\begin{pmatrix}V_1(x) & -\mu E_P(t) & 0\\ -\mu E_p(t) & V_2(x) & -\mu E_S(t)\\ 0 & -\mu E_S(t) & V_3(x)\end{pmatrix}\Bigg]\begin{pmatrix}\psi_1(x,t)\\ \psi_2(x,t)\\ \psi_3(x,t)\end{pmatrix},$$

where $\mathcal{I}$ is the unitary matrix, $V_n(x)$ are the potential energy curves (where $V_1(x) = V_3(x)$), μ is the transition dipole moment ($\mu = 1$ within the Condon-approximation) and $E_P(t)$, and $E_S(t)$ are pump and Stokes pulse, respectively. As the laser frequency ω is close to the transition energy between states $|1\rangle, |2\rangle$ $\omega_0 = (E_2 - E_1)/\hbar$, the off-diagonal elements of the Hamiltonian can be represented by a sum of two terms. One term oscillates rapidly near $(\omega_0 + \omega)$, (twice the transition frequency) and the second term slowly at $\Delta = \omega_0 - \omega$ where Δ is the detuning. Following the rotating wave approximation (RWA) the rapidly oscillating term is neglected. The Rabi frequencies (compare to section 1.4) are the field amplitudes in frequency units $\Omega_P(t) = E_P(t)/\hbar$ and $\Omega_S(t) = E_S(t)/\hbar$, represented by the pulse envelopes (compare to eq. (1.74)). Thus, separating the time-dependent part, $\mathcal{H}(t) = \mathcal{H}_{mol} + \mathcal{H}(t)_{STIRAP}$, the Hamiltonian describing the field interaction is of the form

$$\mathcal{H}_{STIRAP} = \frac{\hbar}{2} \begin{pmatrix} 0 & -\Omega_P(t) & 0 \\ -\Omega_p(t) & \Delta & -\Omega_S(t) \\ 0 & -\Omega_S(t) & 0 \end{pmatrix}. \tag{8.4}$$

The state vector $|\Psi\rangle$ can be written as

$$|\Psi\rangle = c_1|1\rangle + c_2|2\rangle + c_3|3\rangle. \tag{8.5}$$

The system is initially in state $|1\rangle$, $|c_1(t_0)|^2 = 1$; for a complete population transfer $|c_3(t)|^2 = 1$. Explaining the dynamics results from an adiabatic representation being obtained via an unitary transformation [144]

$$|\Psi\rangle = A|\Phi\rangle, \tag{8.6}$$

diagonalizing the Hamiltonian

$$A^\dagger \mathcal{H}_{STIRAP} A = D, \tag{8.7}$$

where D is the diagonal form of $\mathcal{H}_{STIRAP}$, and A is the rotation matrix

$$A = \begin{pmatrix} \sin\gamma\sin\Theta & \cos\Theta & \cos\gamma\sin\Theta \\ \cos\gamma & 0 & -\sin\gamma \\ \sin\gamma\cos\Theta & \sin\Theta & \cos\gamma\cos\Theta \end{pmatrix}, \tag{8.8}$$

where the angle Θ is specified below. The transformed Schrödinger equation

$$i\hbar\frac{\partial}{\partial t}|\Phi\rangle = \left(D - i\hbar A^\dagger \frac{\partial}{\partial t} A\right)|\Phi\rangle \tag{8.9}$$

yields, together with the unitary matrix A, the adiabatic form of the Hamiltonian

$$\begin{aligned}\mathcal{H}_{ad} &\equiv \left(D - i\hbar A^{\dagger}\frac{\partial}{\partial t}A\right) \\ &= \begin{pmatrix} \Omega_T \cot\gamma & i\dot{\Theta}\sin\gamma & i\dot{\gamma} \\ -i\dot{\Theta}\sin\gamma & 0 & -i\dot{\Theta}\cos\gamma \\ -i\dot{\gamma} & i\dot{\Theta}\cos\gamma & -\Omega_T\tan\gamma \end{pmatrix}. \end{aligned} \tag{8.10}$$

The new basis vectors $\{|\phi_+\rangle, |\phi_0\rangle, |\phi_-\rangle\}$ for state $|\Phi\rangle$ with eigenvalues $\{\epsilon_+, \epsilon_0, \epsilon_-\}$, are obtained according to the procedure described in chapter 1.4

$$|\phi_+(t)\rangle = \frac{1}{\sqrt{2}}\left[\sin\Theta(t)\sin\gamma(t)|1\rangle + |2\rangle + \cos\Theta(t)\sin\gamma(t)|3\rangle\right] \tag{8.11}$$

$$|\phi_0(t)\rangle = \cos\Theta(t)|1\rangle - \sin\Theta(t)|3\rangle \tag{8.12}$$

$$|\phi_-(t)\rangle = \frac{1}{\sqrt{2}}\left[\sin\Theta(t)\cos\gamma(t)|1\rangle - |2\rangle + \cos\Theta(t)\cos\gamma(t)|3\rangle\right] \tag{8.13}$$

with the eigenvalues ϵ

$$\begin{aligned}\epsilon_+(t) &= 1/2\left[\Delta(t) + \sqrt{\Delta^2(t) + 4\Omega_T^2(t)}\right] = \Omega_T(t)\cot\gamma(t) \\ \epsilon_0(t) &= 0 \\ \epsilon_-(t) &= 1/2\left[\Delta(t) - \sqrt{\Delta^2(t) + 4\Omega_T^2(t)}\right] = -\Omega_T(t)\tan\gamma(t).\end{aligned} \tag{8.14}$$

The eigenenergy ϵ_0 does not depend on the laser parameters while both other eigenenergies are expressed in terms of $\Omega_T(t)$, the mean square Rabi frequency

$$\Omega_T(t) = \sqrt{\Omega_P^2(t) + \Omega_S^2(t)}. \tag{8.15}$$

The time-dependend Euler's angles $\Theta(t)$ and $\gamma(t)$ appearing in the rotation matrix A in eq. (8.8) are defined by

$$\tan\Theta(t) = \frac{\Omega_P(t)}{\Omega_S(t)},$$

$$\tan 2\gamma(t) \quad = \quad \frac{2\Omega_T(t)}{\Delta}. \tag{8.16}$$

Population transfer with the counterintuitive pulse sequence, for the Stokes pulse $\Omega_S(t)$ preceeding the pump pulse $\Omega_P(t)$, implies the condition of a sufficient overlap of both pulses. The two-photon resonance of this counterintuitive pulse sequence is termed STIRAP. It relies on the compositon of eigenstate $|\phi_0\rangle$ as a coherent superposition of the initial state $|1\rangle$ and the final state $|3\rangle$ only. As the complete state vector can be expressed by a linear combination of the three dressed states at any time, the aim is to perform a complete population inversion by restricting the system into the dark state $|\phi_0\rangle$ at all times. Figure 8.3 shows the temporal behavior of the system for a population inversion.

For $t \to -\infty$ the fraction Ω_P/Ω_S vanishes as the pump pulse is very weak, therefore $\cos\Theta = 1, \sin\Theta = 0$, and ϕ_0 coincides with the initial state $|1\rangle$. Likewise, for $t \to \infty$, when $(\Omega_P/\Omega_S)^{-1}$ vanishes and ϕ_0 assumes the form of the target state $|3\rangle$. At resonance, $\Delta = 0$, and therefore, with eq. (8.16), $\gamma = \pi/4$. In the adiabatic limit, as the mixing angle $\Theta(t)$ rises from 0 to $\pi/2$, the adiabatic state $|\phi_0\rangle$ evolves from the pure initial state $|1\rangle$ to a superposition of states $|1\rangle$ and $|3\rangle$ at intermediate times, and finally to the target state $|3\rangle$. Therefore, for a high efficiency of population transfer, non-adiabatic transitions are to be reduced. The requirement for adiabatic conditions can be expressed as

$$\hbar \left| \frac{d\Theta}{dt} \right| \ll |\epsilon_0 - \epsilon_\pm| = \hbar |\Omega_T(t)|. \tag{8.17}$$

That means, for adiabaticity a large pulse area is obligatory. Thus, in the counterintuitive pulse sequence, the pump laser should start only after the Stokes pulse provided a sufficiently large separation of the dressed eigenstates. For the most efficient population transfer the delay time of both pulses corresponds to ap-

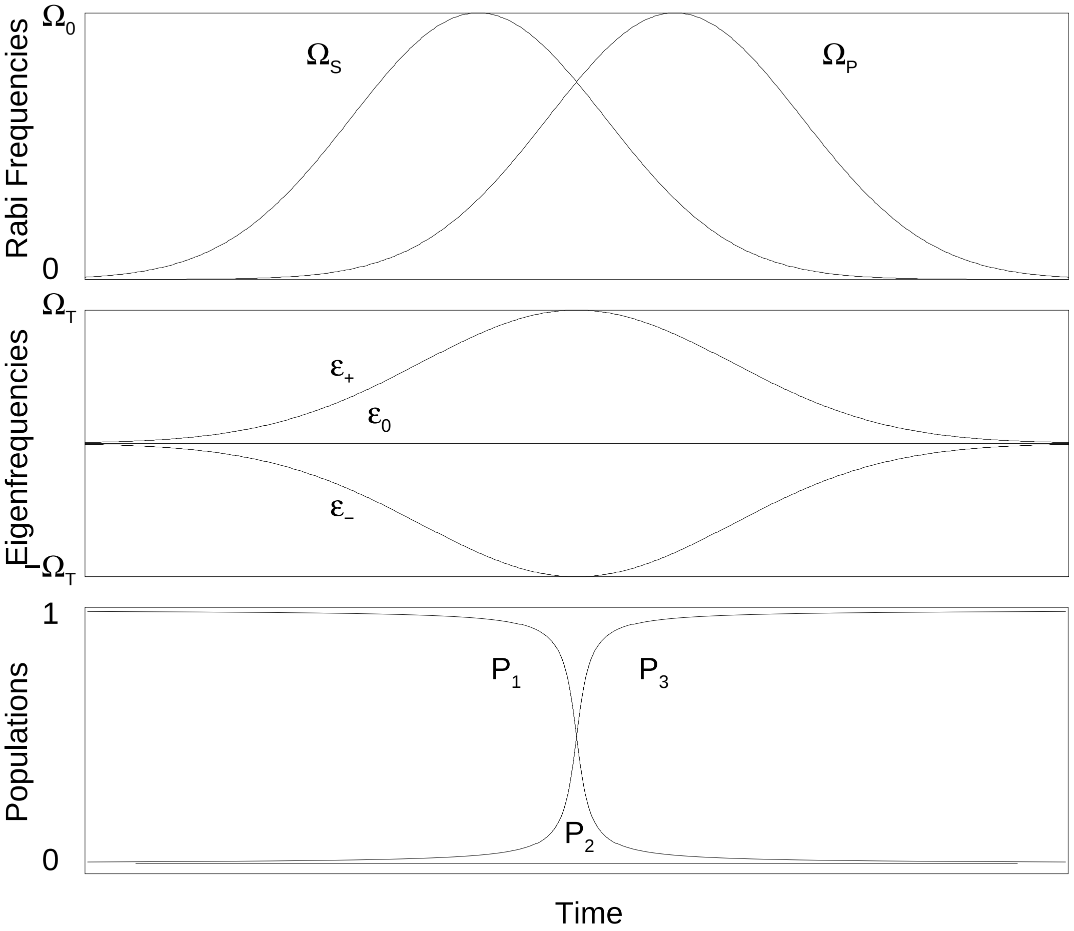

Figure 8.3: *Temporal behavior (schematic) of pump and Stokes Rabi frequencies (top), the eigenenergies (middle) and the populations (bottom) for a three-state STIRAP process.*

proximately the half of the pulse width. The delay time influences the population transfer the more sensitively with increasing Rabi frequency. Non-adiabatic effects can be corrected by summing perturbation series in the adiabatic basis [145].

In order to prepare a large pulse area a similar process related to STIRAP, called fractional STIRAP (f-STIRAP), where the Stokes pulses still preceeds the pump pulse but both pulses vanish simultaneously,

$$\lim_{t\to-\infty}\frac{\Omega_P(t)}{\Omega_S(t)}=0, \qquad \lim_{t\to+\infty}\frac{\Omega_P(t)}{\Omega_S(t)}=\tan\Theta, \tag{8.18}$$

can be applied. This scenario causes a sufficient separation of the dressed eigenstates by the preceeding Stokes pulse and a fast population transfer by the pump pulse, where the limits are [146]

$$\begin{aligned} |\phi_0(-\infty)\rangle &= |1\rangle, \\ |\phi_0(+\infty)\rangle &= \cos\Theta|1\rangle - \sin\Theta|3\rangle. \end{aligned} \tag{8.19}$$

For $\lim_{t\to+\infty}\Omega_P(t)/\Omega_S(t) = 1$, $\Theta = \pi/4$ and $\phi_0(+\infty) = 1/\sqrt{2}(|1\rangle - |3\rangle)$. The eigenstate $|\phi_0\rangle$ represents, within the f-STIRAP approach, a coherent superpostition of eigenstates $|1\rangle$ and $|3\rangle$, in which the ratio of the probability amplitudes of these states is proportional to the ratio of pump and Stokes pulse. Adiabatic behavior in this case will not yield complete population transfer. In contrast to the standard STIRAP, f-STIRAP is more robust concerning variations in pulse parameters.

Comparing the possible pulse sequences, the physical processes in the strong field regime are very different. While within the STIRAP picture population transfer from $|1\rangle$ to $|3\rangle$ is performed adiabatically without populating state $|2\rangle$, the intuitive pulse order (pump pulse preceeds the Stokes pulse) describes a pump/dump process and therefore state $|2\rangle$ is populated. For completely overlapping pulses with the same time dependence, the mixing angle $\Theta(t)$ is constant and therefore $\dot{\Theta} = 0$. As the $|\phi_0\rangle$ decouples (compare to eq. (8.10)), the system is reduced to an effective two-level system with the adiabatic states $|\phi_+\rangle$ and $|\phi_-\rangle$. This can be demonstrated analytically assuming pulses of the form [141]

$$\Omega_P(t) = \frac{\alpha}{T} f\left(\frac{t}{T}\right), \qquad \Omega_S(t) = \frac{\beta}{T} f\left(\frac{t}{T}\right), \tag{8.20}$$

where the parameters are real and positive. Both fields may have different strenghts α and β but the same pulse width T. The envelope function $f(x)$ is assumed to be a Gaussian. In the adiabatic equation of motion

$$i\hbar\frac{d}{dt}\begin{pmatrix}\phi_+(t)\\ \phi_-(t)\end{pmatrix} = \begin{pmatrix}\Omega_T\cot\gamma & i\dot{\gamma}\\ -i\dot{\gamma} & -\Omega_T\tan\gamma\end{pmatrix}\begin{pmatrix}\phi_+(t)\\ \phi_-(t)\end{pmatrix}, \tag{8.21}$$

the coupling between states $|\phi_+\rangle$ and $|\phi_-\rangle$ vanishes on resonance, when $\Delta = 0$, $\gamma = \pi/4$ and, $\dot{\gamma} = 0$. The exact solution

$$P_3 = \left(\frac{2\alpha\beta}{\alpha^2+\beta^2}\right)^2 \sin^4\left(1/2\sqrt{\alpha^2+\beta^2}\right) \tag{8.22}$$

is an analytic expression for the Rabi-like oscillations describing the population transfer into state $|3\rangle$ as a function of the field strengths α and β. For $\alpha = \beta$ the amplitude is largest.

8.3 CARS-Signals

In this section an expression for resonant CARS signals within a perturbative description of the wave functions is given [138,139,147]. The wave function picture shows a simple connection between the wave functions and the transitions contributing to the signal. Regarding the response of a molecule with two electronic states, $|X\rangle$ and $|B\rangle$ (here the notation is changed as state $|3\rangle$ is a virtual state and does not contribute to the signal), to an electric field consisting of a sequence of three laser pulses, the Hamiltonian is given as

$$\mathcal{H} = \mathcal{H}_{mol} + \mathcal{H}_{int}. \tag{8.23}$$

The molecular Hamiltonian $\mathcal{H}_{mol}$ including the kinetic energy operator as well as the potential energy operators is represented in the basis of vibronic states

$\{|Xn\rangle, |Bm\rangle\}$ with eigenenergies $\{E_{Xn}, E_{Bm}\}$ as

$$\mathcal{H}_{mol} = \sum_n |Xn\rangle\langle Xn|\, E_{Xn} + \sum_m |Bm\rangle\langle Bm|\, E_{Bm}. \tag{8.24}$$

The time-dependent pulses are of the form

$$E(x,t) = \sum_{j=1}^{3} E_j(x,t) = \sum_{j=1}^{3} \frac{1}{2} E_{0,j} f_j(t-\tau_i) \left[e^{i\omega_j(t-\tau_i)-ik_jx} + e^{-i\omega_j(t-\tau_i)+ik_jx} \right], \tag{8.25}$$

where $f_j(t-\tau_j)$ are the pulse envelopes centered at time τ_j, ω_j are frequencies, k_j wave vectors and x the spatial coordinate, see chapter 1, eq. (1.38). Within the dipole approximation the radiation-matter interaction is written without the position dependency, assuming a dipole operator of the form [148]

$$\begin{aligned} \mathcal{H}_{int} &= -\mu^+ \cdot E(t) - \mu^- \cdot E^*(t), \\ \mu^+ &= \sum_{nm} |Bm\rangle \mu_{mn} \langle Xn|, \\ \mu^- &= (\mu^+)^\dagger = \sum_{mn} |Xn\rangle \mu_{mn} \langle Bm|. \end{aligned} \tag{8.26}$$

The μ_{mn} are matrix elements of the dipole moment operator, $\mu_{mn} = \langle Bm|\mu|Xn\rangle$. Here, the dipole operators are defined such that $\mu^+ \cdot E_i(t)$, defining absorption, couples a ket in the ground state to the excited state and, in contrast, $\mu^- \cdot E_i^*(t)$ corresponds to stimulated emission, coupling an excited ket-state into the ground state. Entering in the experimental signal is the polarization, defined as

$$P(t) \equiv \langle \psi(t)|\mu|\psi(t)\rangle, \tag{8.27}$$

where $|\psi(t)\rangle$ is the total nuclear and electronic wave function, being iteratively determined by time-dependent perturbation theory (compare to chapter 1.3)

$$|\psi^{(n)}\rangle = (i\hbar)^{-1} \int_{-\infty}^{t} dt'\, e^{-i\mathcal{H}_{mol}(t-t')/\hbar} \mathcal{H}_{int}(t') |\psi^{(n-1)}(t')\rangle. \tag{8.28}$$

The states $|\psi^{(n)}\rangle$ carry a spatial dependence, according to the wave vector of the particular pulse. The signal S is detected in direction $k_1 - k_2 + k_3$ as (dependence on τ being supressed)

$$S(\tau) = \int_{-\infty}^{T_E} dt \left| P^{(3)}(t) \right|^2, \tag{8.29}$$

where T_E is the detection time, τ the delay time and $P^{(3)}(t)$, the third order polarization, given by

$$P^{(3)}(t) = \sum_{n=0}^{3} \langle \psi^{(n)}(t) | \mu | \psi^{(3-n)}(t) \rangle. \tag{8.30}$$

The polarization including the geometric configurational constraint into direction $k_1 - k_2 + k_3$ can be written as

$$\begin{aligned} P^{(3)}(t, k_1 - k_2 + k_3) = \Big\{ & \langle \psi^{(0)}(t) | \mu | \psi^{(3)}_{k_1-k_2+k_3}(t) \rangle + \langle \psi^{(0)}(t) | \mu | \psi^{(3)}_{k_3-k_2+k_1}(t) \rangle \\ & + \langle \psi^{(2)}_{k_2-k_1}(t) | \mu | \psi^{(1)}_{k_3}(t) \rangle + \langle \psi^{(2)}_{k_2-k_3}(t) | \mu | \psi^{(1)}_{k_1}(t) \rangle \Big\} + c.c. \end{aligned} \tag{8.31}$$

including all possible time orderings of the three interactions. In the latter equation $\langle \psi^{(0)}(t)|$ is the unperturbed initial state, $|\psi^{(3)}_{k_1-k_2+k_3}(t)\rangle$ is created by a successive absorption in direction k_1, emission in k_2 and absorption in k_3. The other wave functions can be explained likewise by absorption (positive sign) and emission (negative sign of the k-vectors). In many CARS experiments the signal is dominated by the first term in eq. (8.31)

$$P^{(3)}(t) \approx P^{CARS}(t) = \langle \psi^{(0)}(t) | \mu | \psi^{(3)}_{k_1-k_2+k_3}(t) \rangle + c.c. \tag{8.32}$$

Applying third order perturbation theory, the CARS signal (eq. 8.29) can be evaluated from

$$P^{CARS}(t) = -\frac{i}{\hbar^3} \sum_{n,n',m,m'} p_n \mu_{nm'} \int_{-\infty}^{t} dt_3 \int_{-\infty}^{t_3} dt_2 \int_{-\infty}^{t_2} dt_1 \, e^{-i\omega_{nm'}(t-t_3)/\hbar}$$

$$(\mu_{nm'} E_3(t_3))\, e^{-i\omega_{nn'}(t_3-t_2)/\hbar}\, (\mu_{n'm} E_2^*(t_2))\, e^{-i\omega_{nm}(t_2-t_1)/\hbar}\, (\mu_{nm} E_1(t_1)) + c.c., \quad (8.33)$$

where the indices n, n' and m, m' correspond to ground and excited state vibrations, respectively, and the ω are the transition frequencies, see fig. 8.4. Weighting the paths with Boltzmann factors p_n of the initial states, the terms in eq. (8.33) represent an amplitude for creating polarization along the direction $k_1 - k_2 + k_3$. With respect to the frequency difference between the currently occupied level and the inital level a phase is attained to the amplitude, given by $E_{m'n} = E_{Bm'} - E_{Xn}, E_{n'n} = E_{Xn'} - E_{Xn}$ etc. The oscillations in the CARS signal in varying the delay times are caused by these phases, connecting initial and final states.

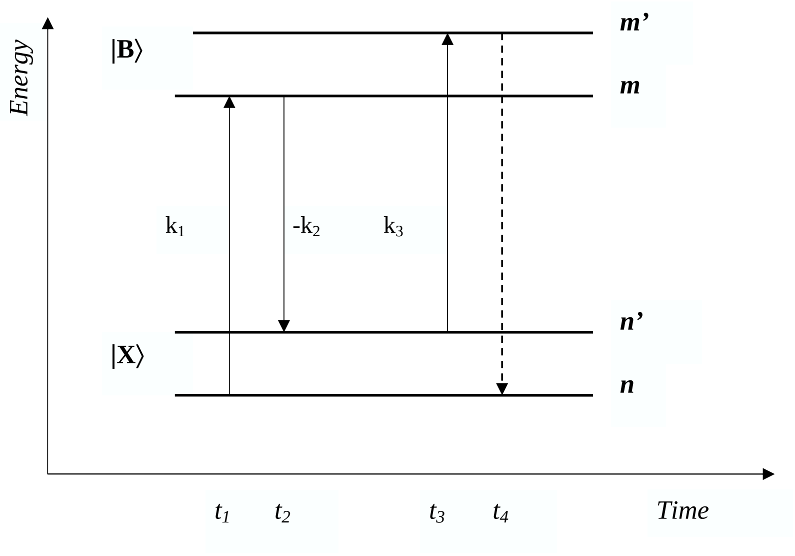

Figure 8.4: *CARS scheme for transitions beteween ground $|X\rangle$ and excited state $|B\rangle$ energy levels. The up-arrows indicate absorption from, and the down-arrow emission processes into the vibrational levels n, n', m, m'. The dashed arrow illustrates the CARS signal being obtained.*

Within this work no CARS signals are calculated: Rather, the wave packet motion in the ground and excited states $|X\rangle$ and $|B\rangle$ are related to experimentally derived CARS signals.

8.4 Numerical Results

In this section numerical results on the population transfer are presented for various pulse sequences differing in the pulse order, wavelengths and intensities. A comparison of results from the numerically exact coupling scheme to those derived from the adiabatic approximation (as discussed in section 8.1 and 8.2) provides evidence for the existance of STIRAP in the fs-regime. The efficiency of population transfer is embodied by the norm in the particular states after the time when both pulses, the pump and the Stokes pulse, are switched off. Then, in absence of both pulses, the population ratio does not change any more.

8.4.1 Pump/ Stokes Resonant Excitation

Here, the case of resonant excitation with wavelengths of $\lambda_S = 545$ nm and $\lambda_P = 525$ nm is treated. Both pulses have a FWHM of 150 fs and an intensity of $8 \cdot 10^{-3}$ a.u., being resonant with the excited $|B\rangle$-state, as indicated by the dot-dashed arrows in fig. 8.1. The wavelengths are adjusted to the $v'' = 5$ vibrational state of the electronic ground state. The parameters for the calculations are chosen according to the experimental values.

The experimental CARS signals in fig. 8.5 show a sequence of at least two vibrational periods depending on the delay time of both pulses. First, a fast decaying signal with a peak separation of about 160 fs (fig. 8.5, panel (a)),

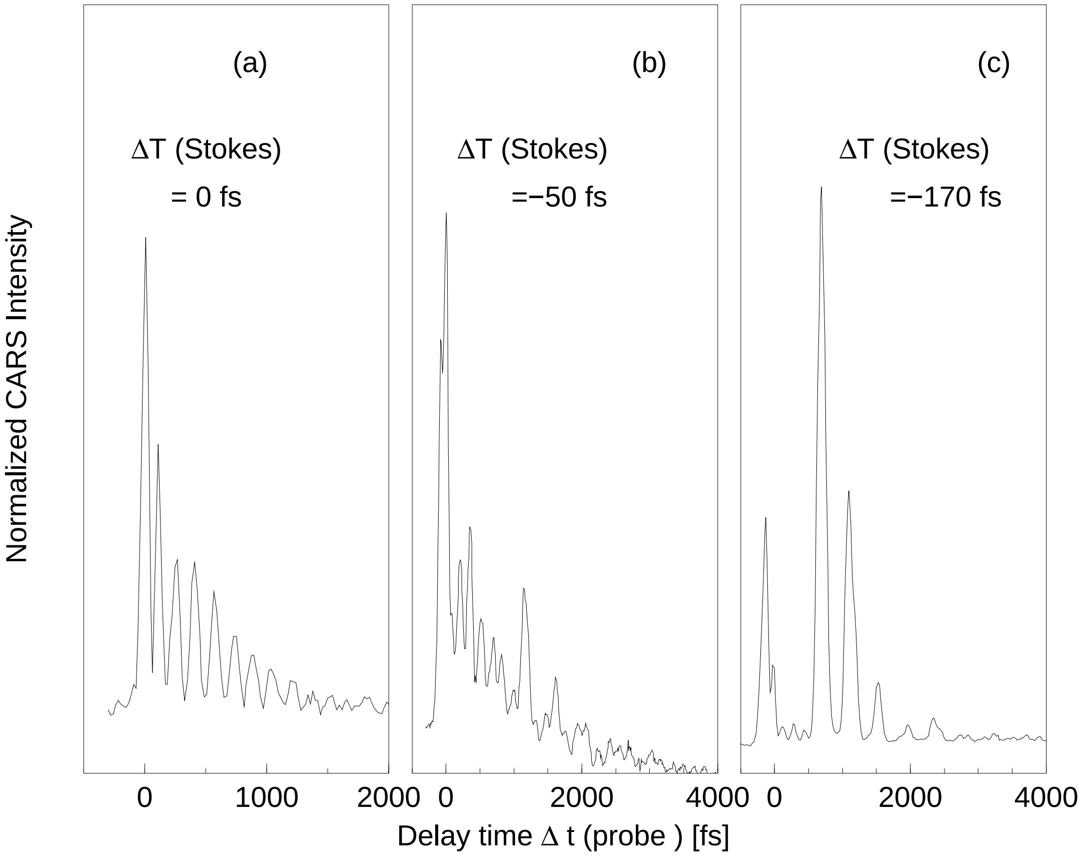

Figure 8.5: *Experimental CARS signals with wavelengths 525/545/554 nm for pump, Stokes, and the probe pulse. The signals are obtained for different delay times ΔT of the Stokes pulse, as indicated. Panel (a) features a short vibrational period estimated to be about 160 fs, according to energy separations around the $v'' = 5$ vibrational state. Panel (c) exhibits a long oscillatory period deriving from the excited electronic state. In panel (b) contributions of both, the electronic ground and excited states can be seen.*

second, a longer oscillation period of about 400 fs (panel (c)), and an intermediate situation (panel (b)), where a superposition of the two sequences occurs, can be seen. The separation of the peaks reflects the vibrational dynamics in different electronic states. The pronounced peaks with the short separation, corresponding to an energy of 213 cm^{-1}, originate from the electronic ground state signal being superposed by the contribution of the excited electronic state's nuclear motion.

As the signals reflect the vibrational wave packet motion, calculations have been performed describing the dynamics starting from a fixed vibrational state $v'' = 0$, and neglecting rotations. The different dynamical behavior for the adiabatic and the numerically exact coupling schemes are shown in fig. 8.6. Comparing the results from an adiabatic description (fig. 8.6, lower panel) with the case of numerically exact coupling (fig. 8.6, upper panel) it is obvious that the adiabatic picture for the chosen case of resonant excitation does not describe a STIRAP-process, as the main part remains in the excited state. A second feature is the asymmetric behavior of the norm for the counterintuitive pulse sequence (Stokes pulse preceeds the pump pulse) as compared to the intuitive one (Stokes pulse succeds the pump pulse). Regarding the wave packet motion in the particular states gives an explanation for the described features. Since both laser pulses are resonant with the excited state, both prepare interfering excited state wave packets in the $|B\rangle$ electronic state, see fig. 8.7.

Figure 8.6, upper panel, also explains why the experimental CARS signals feature the ground and excited electronic state dynamics: Since a substantial part remains in the excited state and a small part is dumped into the electronic ground state, both state's vibrational periods contribute to the signal. The separation of the peaks reflecting the electronic ground state contribution can be assigned

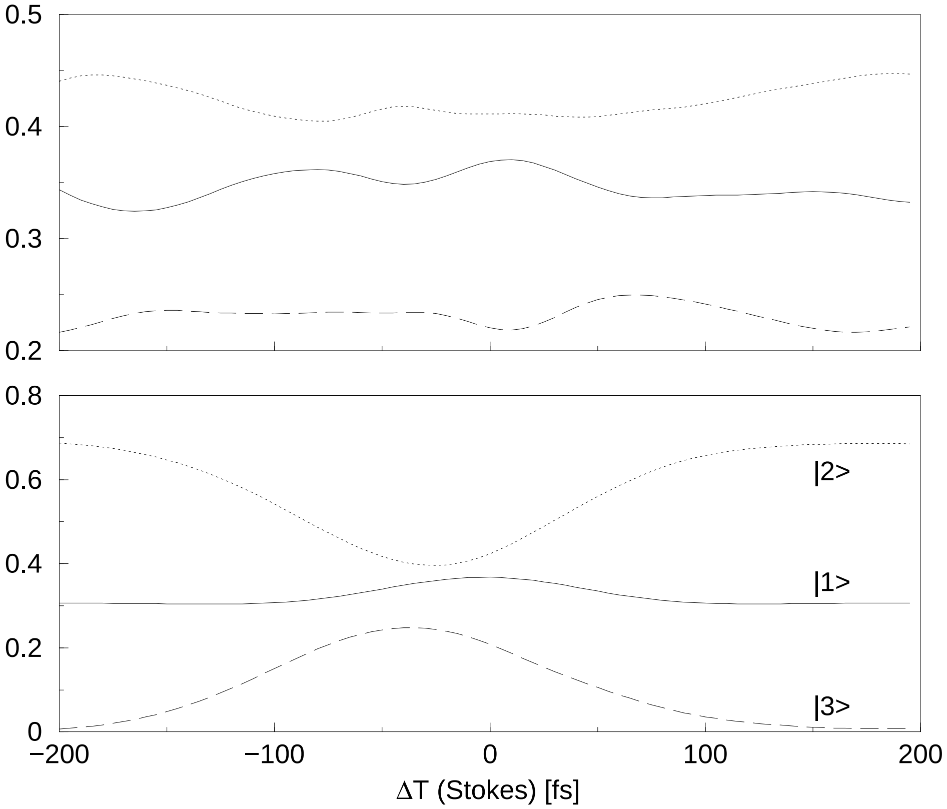

Figure 8.6: *Temporal development of the norm in the different states, where the solid line describes the* $|1\rangle$*, the dotted line the* $|2\rangle$ *and the dashed line the* $|3\rangle$ *state. The norm is calculated after 1000 fs for one pulse sequence. The abscissae display the temporal delay of the Stokes pulse relative to the pump pulse located at* $\Delta T = 0$ *fs; negative delay times mean a preceeding Stokes pulse. Upper panel: Norm for an exact coupling case, lower panel: adiabatic description. Field strength of both pulses* $E = 3 \cdot 10^{-3}$ *a.u.(*$3 \cdot 10^{11}\, W/cm^2$*).*

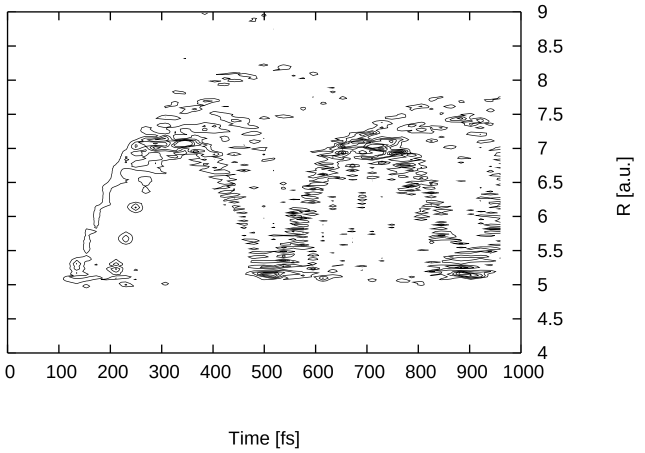

Figure 8.7: *Probability density of the excited state wave packet for a fixed delay-time* ΔT = *-200 fs of pump and Stokes pulse .*

to the period ($\approx$ 160 fs) of the vibrational excited ground state wave packet displayed in fig. 8.8.

The experimental as well as the theoretical results show that a counterintuitive pulse sequence comparable to a STIRAP scheme does not represent a STIRAP but a simple pump/dump process with two interfering excited states wave packets. Therefore, to increase the adiabaticity, the most important condition for a STIRAP process to take place, the detuning Δ and the pulse intensity Ω^0_{max}, or, alternatively, the pulse width have to be increased [141]. Therefore, the case of an increased detuning achieved in choosing larger wavelengths λ_S and λ_P is investigated in the next subsection.

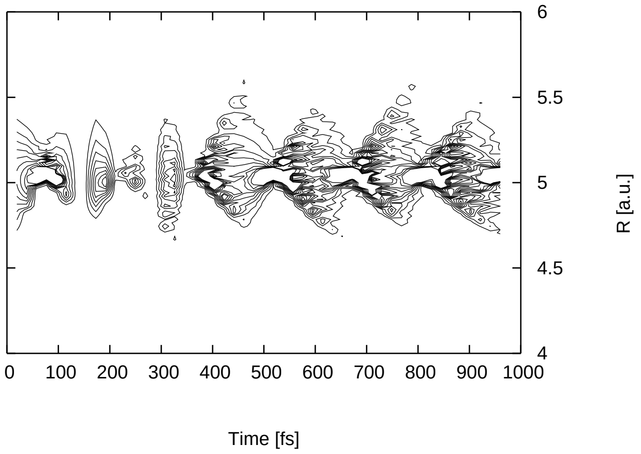

Figure 8.8: *Probability density of the ground state wave packet for a delay time ΔT = -200 fs of the pulses. The maxima exhibit a period of about 160 fs.*

8.4.2 Pump/Stokes Off-Resonant Excitation

In order to avoid the preparation of excited state wave packets and to increase adiabaticity, next the wavelenghts are chosen as $\lambda_S = 795$ nm and $\lambda_P = 645$ nm. Using the same pulse widths as in the resonant case but higher intensities ($8 \cdot 10^{-3}$ a.u.), leads to the experimental signals in fig. 8.9.

A very broad and intense signal centered around 0 fs is accompanied by a sequence of small peaks reflecting a vibrational structure. In a three-dimensional representation (fig. 8.10) the weak vibrational structure can be seen. The calculations performed to compare the adiabatic (lower panel) to the exact coupling case (upper panel) yield the picture shown in fig. 8.11

The adiabatic picture fails in describing the temporal changes of the population exactly but gives a qualitatively correct description of the population

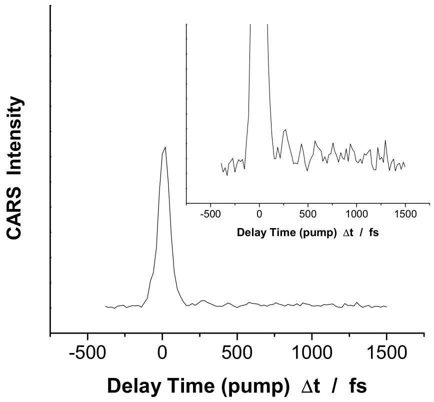

Figure 8.9: *Experimental CARS signals with wavelengths 634/795/554 nm for pump, Stokes, and the probe pulse. The vibrational period is estimated to be 180 fs, according to energy separations around the* $v'' = 15$ *vibrational state.*

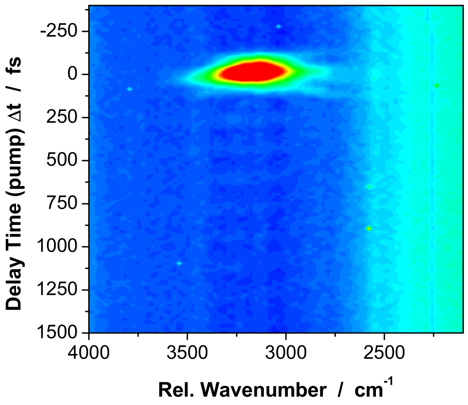

Figure 8.10: *Experimental CARS signals with wavelengths 634/795/554 nm for pump, Stokes, and the probe pulse. A three-dimensional representation is shown.*

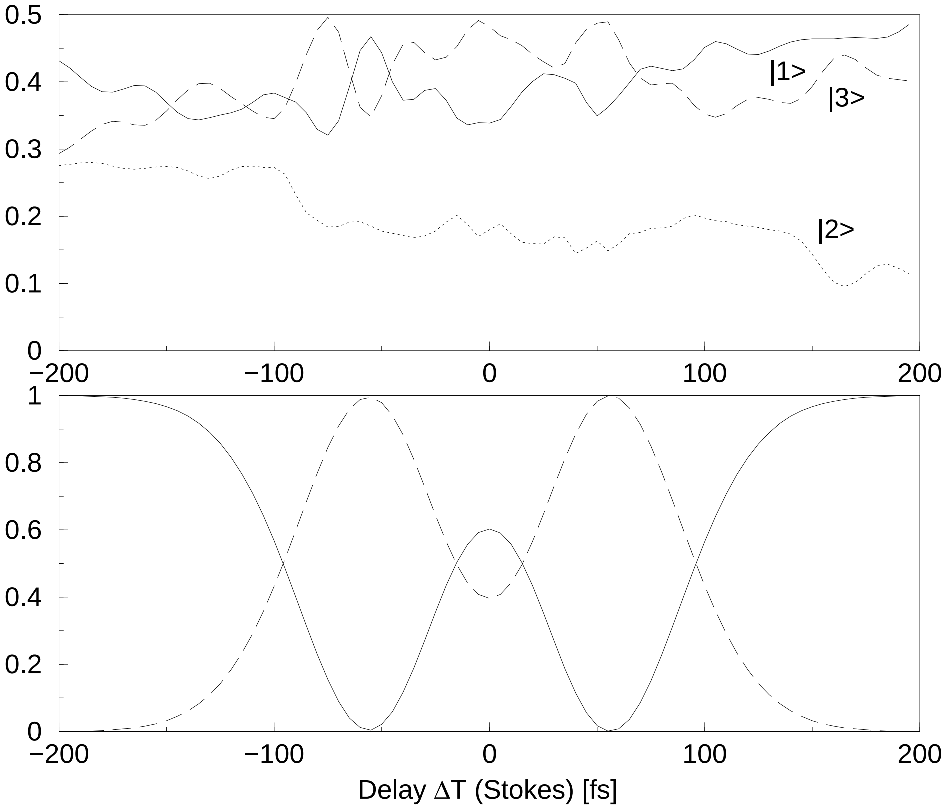

Figure 8.11: *Temporal development of the norm in the different states, as indicated. Upper panel: Norm for an exact coupling case, lower panel: adiabatic description. Intensity of both pulses* $I = 8 \cdot 10^{-3}$ *a.u..*

maxima. As its accuracy is correlated to the effect of the adiabaticity criterion of eq. (8.17), depending on the pulse area, an increase of intensity should give a better description within this picture. Additionally, the temporal separation of the two pulses (delay) influences the validity of the adiabatic picture: when both pulses act at shortly successive times the shared pulse area is relatively high and the Rabi frequency Ω_T is large. At the same time, the temporal change of the mixing angle Θ is largest. For larger pulse delays Ω_T decreases and the adiabaticity is not assured any more. At a delaytime corresponding to the width at half maximum (FWHM) the transfer efficiency is the optimal one [141]. In the case of vanishing detuning Δ, the three-level problem can be reduced to an effective two-level problem. Then, depending on the adiabaticity parameter $\alpha = \Omega^0/T$, where T is the pulse width and Ω^0 the pulse intensity, the inital state population for both pulse orders is the same while the final state popualation oscillates. Therefore, the temporal behavior of the states, and also the final population of state $|3\rangle$ is very sensitive towards changes in the pulse width and intensity, since it influences the adiabaticity of the process [141]. Figure 8.12 and 8.13 compare two cases where the counterintuitive pulses are separated by the same delay time $\Delta\tau$ but differ in the width of the Stokes pulse.

For the case where the Stokes pulse preceeds the pump pulse for about the width at half maximum of the pulses, the population tranfer into state $|3\rangle$ is very effective (nearly complete within the adaibatic calculation). Regarding the dressed state picture in panels (f), the dressed state $|\phi^0(t)\rangle$, the one without contribution of state $|2\rangle$, is mainly populated. According to a constant small value of the mixing angle Θ the population of state $|\phi^0(t)\rangle$ originates from initial state $|1\rangle$. At times, when the overlap of both pulses is very large, the other dressed states $|\phi^+\rangle$ and $|\phi^-\rangle$ contribute. At later times when the pulse interaction

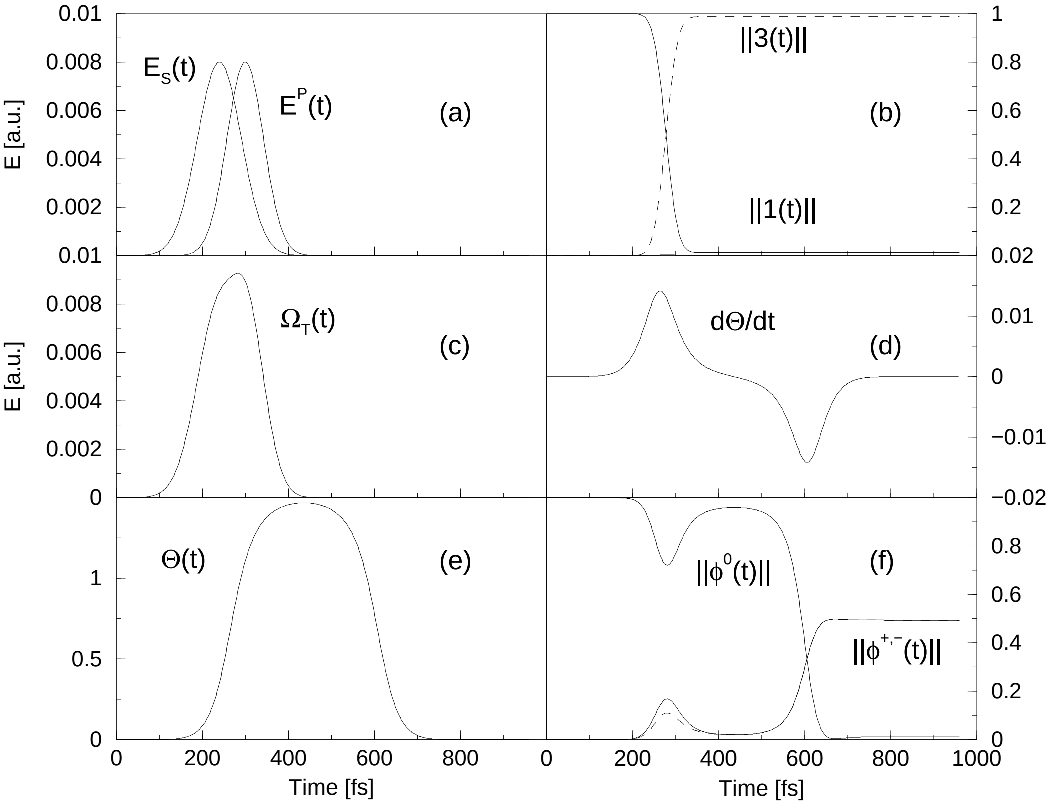

Figure 8.12: *Temporal development of the norm in the different states for a counterintuitive pulse sequence. Panel (a): Pulse envelopes of the pump ($E_P(t)$) and the Stokes pulse ($E_S(t)$), as indicated. Pulse parameters are $I = 4 \cdot 10^{-2}$ a.u. for both pulses, pump pulse: λ_P = 645 nm, $FWHM_P$ = 120 fs and Stokes pulse λ_S = 795 nm, $FWHM_S$ = 100 fs preceeding the pump pulse with $\Delta\tau$ = 60 fs. Panel (c) shows the mean-square Rabi frequency calculated within the rotating wave approximation (RWA). The mixing angle $\Theta(t)$ is displayed in panel (e) and its time derivative in panel (d). Panel (b) shows the norm in the various states and (f) the norm in the dressed states.*

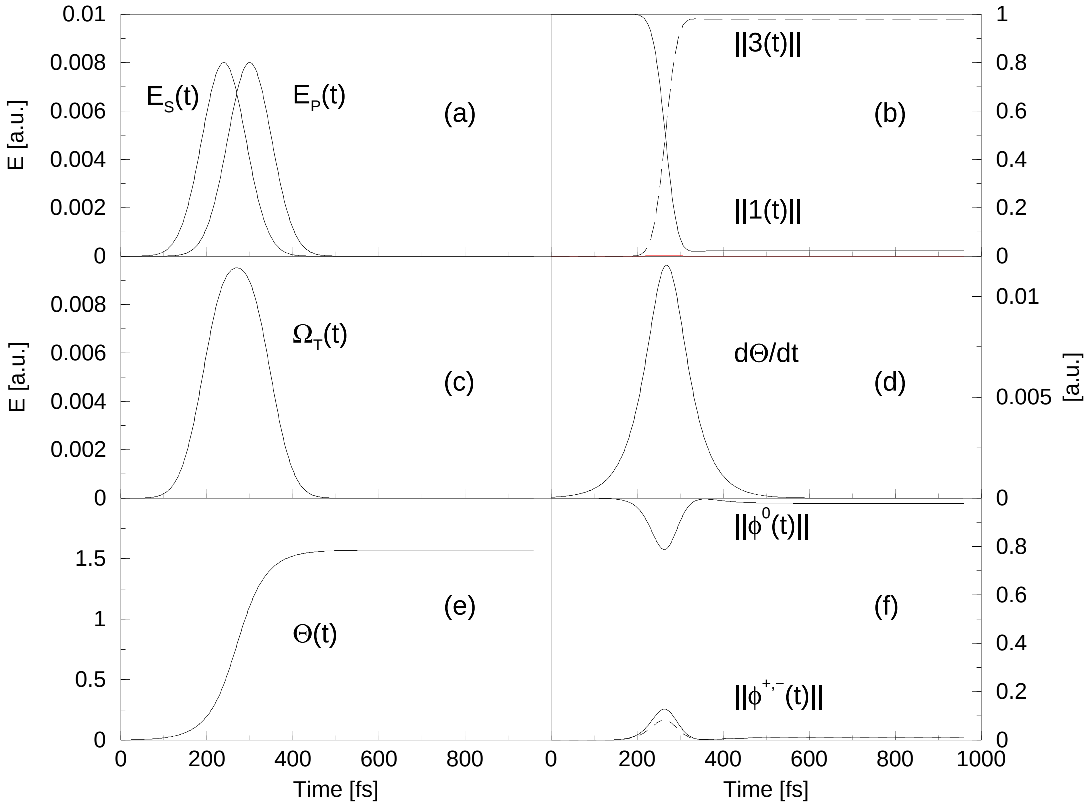

Figure 8.13: *As before, but with the same pulse width of both pulse parameters, FWHM = 120 fs.*

vanishes and Θ levels to the constant value $\pi/2$, the dressed state $|\phi^0\rangle$ corresponds to state $|3\rangle$.

The dynamics of the dressed states depends sensitively on the adiabaticity. For very small or very large times the adiabatic approximation is not valid because of the vanishing pulse area. Then, when adiabaticity can be assumed and the system is locked onto the dressed states, the most critical time concerning the validity of the adiabaticity arises when both pulses overlap and $d\Theta/dt$ is largest. For each time the condition $d\Theta/dt \ll \Omega_T$ must be guaranteed. The maximal change $d\Theta/dt$ in both cases reaches a similar value where adiabaticity breaks down (compare $d\Theta/dt \approx 0.012 \not\ll \Omega_T \approx 0.008$). This can be observed in the temporal development of the dressed states in this time interval, since under validity of the adiabaticity criterion state $|\phi^0\rangle$ should be solely populated for all times. In the case of equal pulse widths the derivative takes values different from zero for a longer time. Thus, the adiabatic locking onto state $|\phi^0\rangle$ cannot be ensured. Therefore, in order to reduce the time derivative of the mixing angle, the pulse ratio is changed.

8.4.3 Intensity Effects

Experimentally, the intensity of the Stokes pulse was chosen to be about a factor of four higher than the pump pulse's intensity. The wavelengths and widths for pump and Stokes pulse were set to $\lambda_P = 645$ nm, $\lambda_S = 805$ nm, $\text{FWHM}_P = 80$ fs, and $\text{FWHM}_S = 70$ fs. In fig. 8.14 the obtained CARS signals are shown. The pulse arrangement gives a similar picture as shown above for fractional-STIRAP.

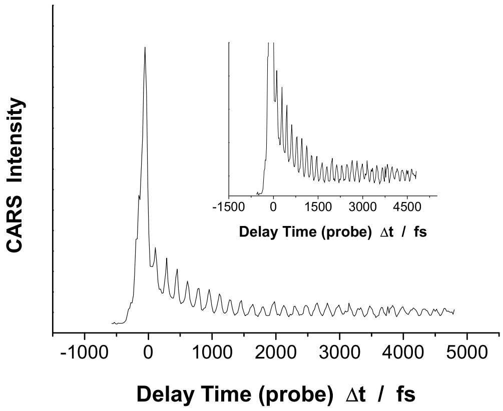

Figure 8.14: *Experimental CARS signals with wavelengths 654/805/554 nm for pump, Stokes, and the probe pulse, where the Stokes pulse has a four times higher intensity than the pump pulse.*

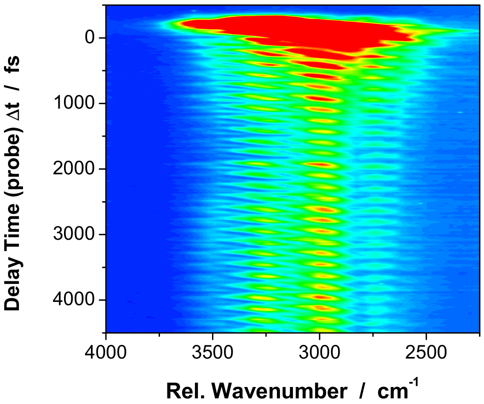

Figure 8.15: *Experimental CARS signals with wavelengths 654/805/554 nm for pump, Stokes, and the probe pulse, where the Stokes pulse has a four times higher intensity than the pump pulse. Three-dimensional representation.*

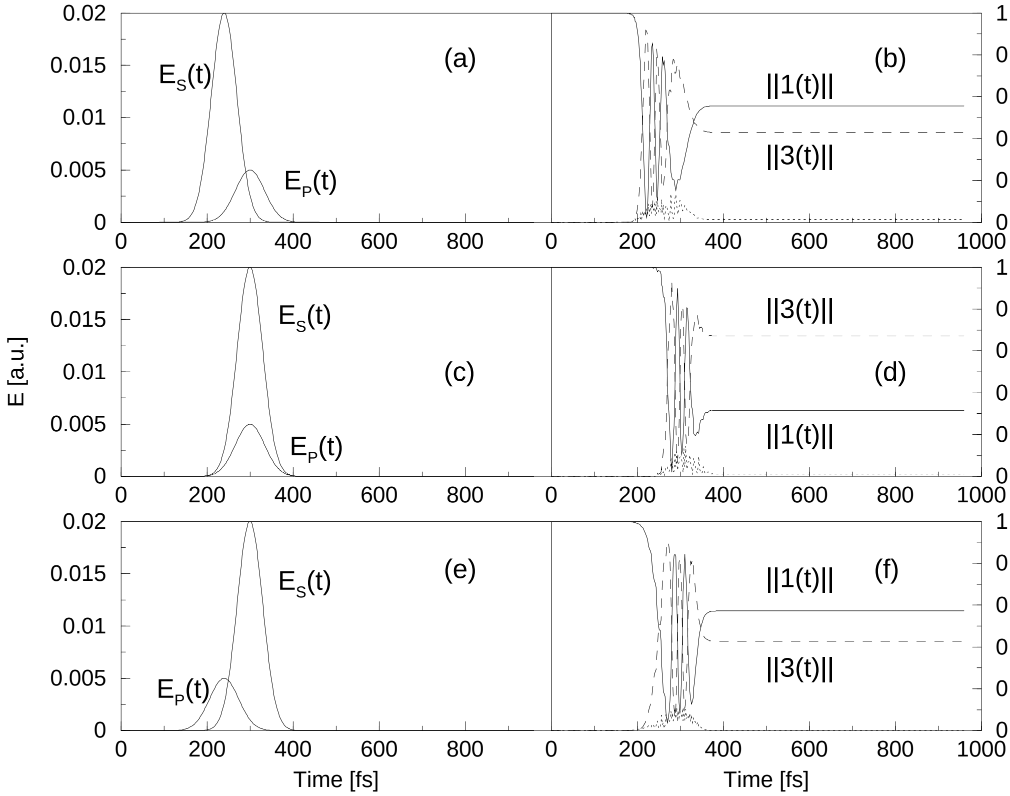

Figure 8.16: *Pulses and populations for the exact couplig case. Right panels: Temporal development of the norm in the various states for three different pulse pulse orders illustrated in the left panels. Panel (a) Stokes pulses preceeds the pump pulse; panel (c): both pulses centered around the same time, panel (e): pump pulse preceeds the Stokes pulse. Field strength of the pulses is* $E_S = 2 \cdot 10^{-2}$ *a.u.,* $E_S = 2.5 \cdot 10^{-3}$ *a.u.*

In order to understand the dynamics of the system, three cases are considered where the delay time between pump and Stokes pulse is varied. Fig. 8.16 illustrates three different pulse orders for the exact coupling case. It can be seen that, depending on the pulse sequence, states $|3\rangle$ and $|1\rangle$ are mainly populated and state $|2\rangle$ does not contribute remarakbly. Therefore, the the dyncamics is calculated within the adiabatic picture. Although the population ratio of the three situations yields similar values, the temporal behavior described by the dressed states differs very much.

First, the case where the Stokes pulse preceeds the pump pulse is discussed (fig. 8.17). As to be expected, the system initially in state $|1\rangle$ can be described in the dressed state formalism by state $|\phi^0\rangle$. The short pulses cause a rapid change of the mixing angle (panel (d)), violating the adiabaticity. The mixing angle's time derivative $\dot{\Theta}$ is now smaller than the Rabi frequency Ω_T but only to a small extent. One can say to be in the "vicinity" of adiabatic behavior. Panel (f) shows how during the non-adiabatic conditions a population transfer from dressed state $|\phi^0\rangle$ into the other dressed states occurs. Afterwards, when the interaction stops, the system is fixed in the actual state.

For the case of both pulses being centered around the same time $t = 300$ fs a different picture arises, as displayed in fig. 8.18. The population is transferred effectively into state $|3\rangle$. In the dressed state picture the system is originally in states $|\phi^+\rangle$ and $|\phi^-\rangle$. Since both pulses exhibit the same pulse envelopes, the mixing angle is constant and therefore, the differential change of Θ equals zero. As a consequence, state $|\phi^0\rangle$ decouples and the system can be described by an effective two-level system.

A similar case emerges for the intuitive pulse sequence describing a pump/

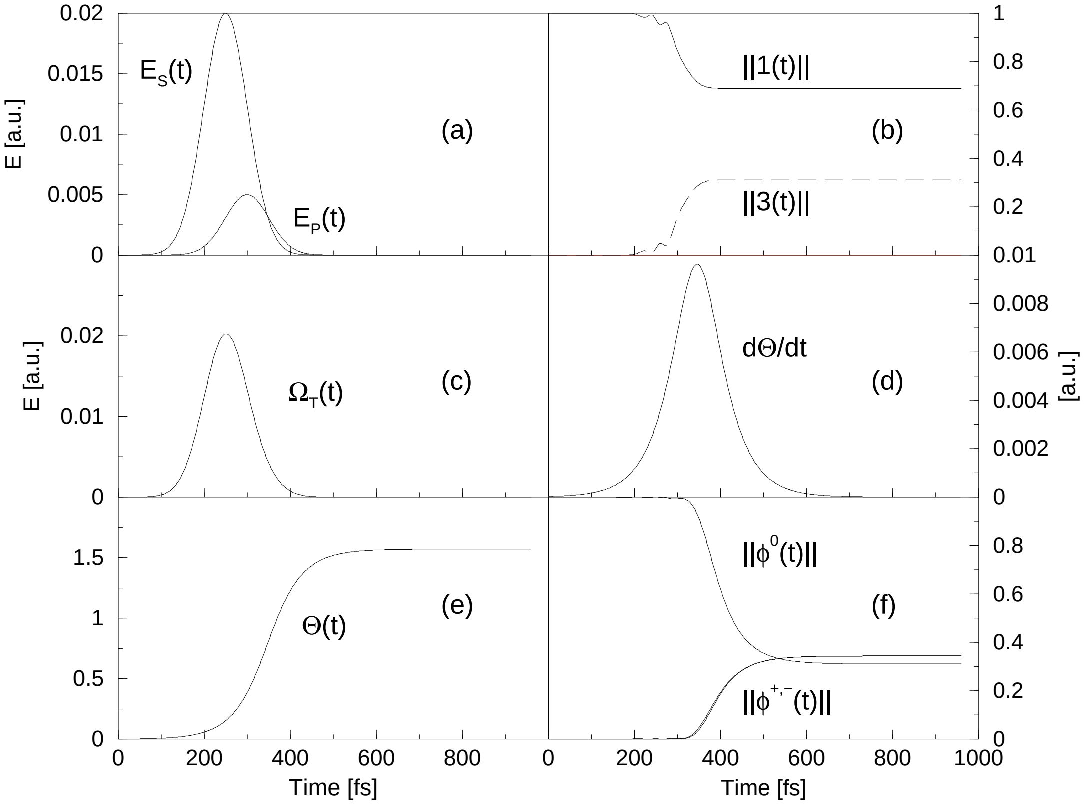

Figure 8.17: *Temporal development of the norm in the particular states for a counter-intuitive pulse sequence. Panel (a): Pulse envelopes of the pump ($E_P(t)$) and the Stokes pulse ($E_S(t)$), as indicated. Pulse parameters are for the pump pulse: $I = 1.2 \cdot 10^{-3}$ a.u., λ_P = 645 nm, FWHM$_P$ = 120 fs and Stokes pulse $I = 5.5 \cdot 10^{-3}$ a.u., λ_S = 795 nm, FWHM$_S$ = 100 fs preceeding the pump pulse with $\Delta\tau$ = 40 fs. Panel (c) shows the mean-square Rabi frequency within RWA. The mixing angle $\Theta(t)$ is displayed in panel (e) and its time derivative in panel (d). Panel (b) shows the norm in the molecular and (f) the norm in the dressed states.*

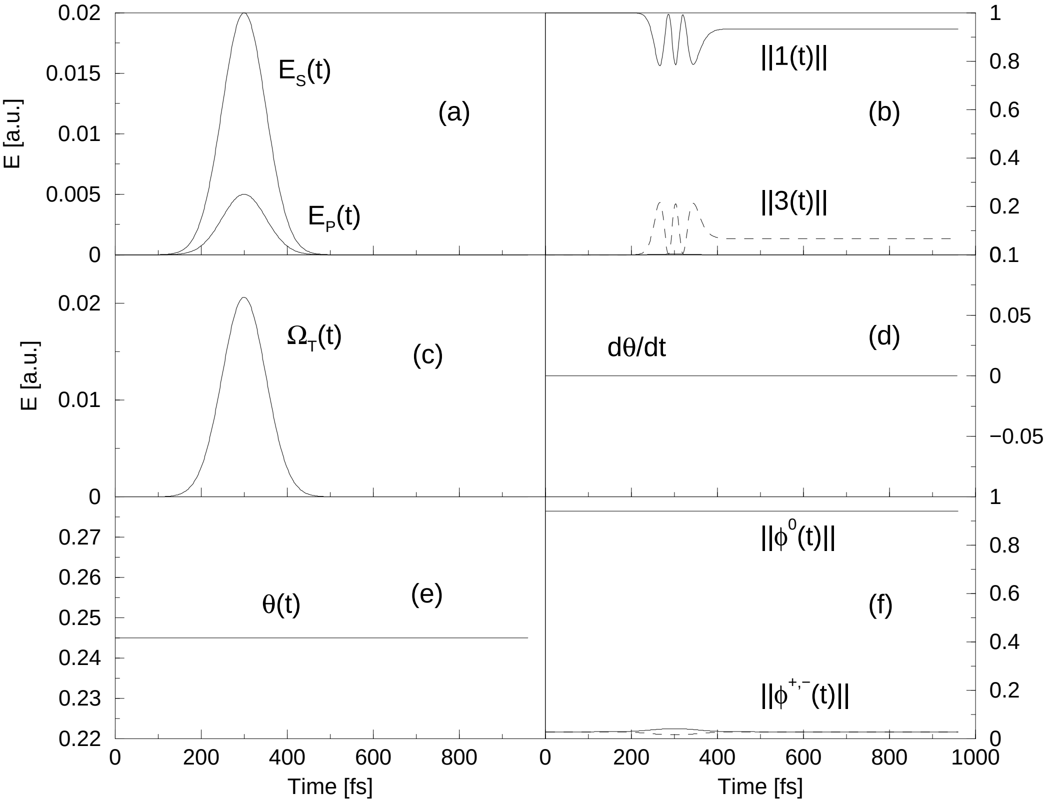

Figure 8.18: *Temporal development of the norm in the various states for pulses centered around 0 fs. Panel (a): Pulse envelopes of the pump ($E_P(t)$) and the Stokes pulse ($E_S(t)$), as indicated. Pulse parameters are for the pump pulse: $I = 1.2 \cdot 10^{-3}$ a.u., λ_P = 645 nm, FWHM$_P$ = 120 fs and Stokes pulse $I = 5.5 \cdot 10^{-3}$ a.u., λ_S = 795 nm, FWHM$_S$ = 100 fs, both centered around $\Delta\tau$ = 0 fs. Panel (c) shows the mean-square Rabi frequency within RWA. The mixing angle $\Theta(t)$ is displayed in panel (e) and its time derivative in panel (d). Panel (b) shows the norm in the molecular and (f) the norm in the dressed states.*

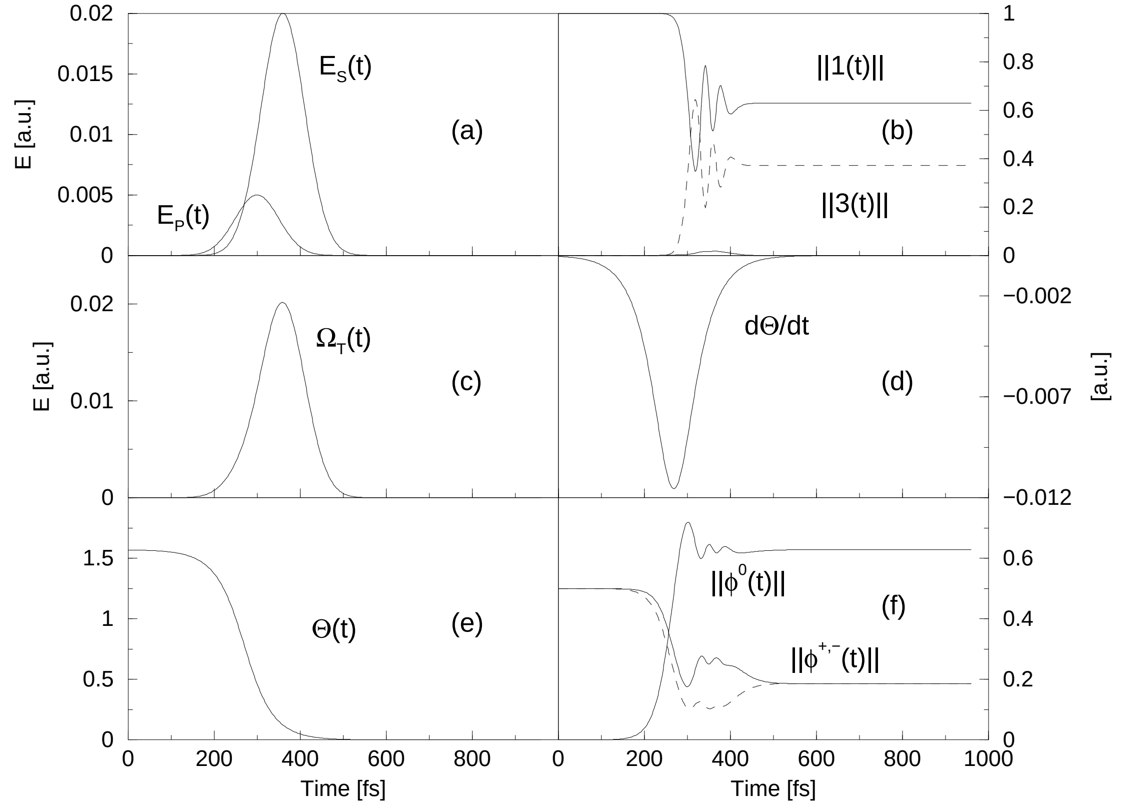

Figure 8.19: *Temporal development of the norm in the different states for an intuitive pulse sequence. Panel (a): Pulse envelopes of the pump ($E_P(t)$) and the Stokes pulse ($E_S(t)$), as indicated. Pulse parameters are for the pump pulse: $I = 1.2 \cdot 10^{-3}$ a.u., λ_P = 645 nm, FWHM$_P$ = 120 fs and Stokes pulse $I = 5.5 \cdot 10^{-3}$ a.u., λ_S = 795 nm, FWHM$_S$ = 100 fs succeeding the pump pulse with $\Delta\tau$ = 40 fs. Panel (c) shows the mean-square Rabi frequency within RWA. The mixing angle $\Theta(t)$ is displayed in panel (e) and its time derivative in panel (d). Panel (b) shows the norm in the molecular and (f) the norm in the dressed states.*

dump like scenario (fig. 8.19). In contrast to the counterintuitive pulse sequence, Θ starts at the value $\pi/2$ and decreases. Except from the sign, $d\Theta/dt$ features the same gradient as in the counterintuitive pulse sequence. Starting from dressed states $|\phi^+\rangle$ and $|\phi^-\rangle$ with non-adiabtic perturbation by state $|\phi^0\rangle$ finally the system ends in both initially occupied dressed states mainly consisting of state $|3\rangle$.

As a conclusion, it can be said that neither the f-STIRAP like pulse sequence nor the STIRAP-like pulse sequence are describable solely by adiabatic processes. Regarding the rate of the adiabatic mixing angle Θ, its change is largest for the case when both pulses, the pump- and Stokes-pulse, overlap. Then, the adiabatic picture is violated, as the rate $\dot{\Theta}$ is not very much smaller than the mean square Rabi frequency, Ω_T. Nevertheless, the analysis of the dressed states formalism helps to understand the concurrent processes in the system. It is shown that the f-STIRAP-like pulse sequence is suited to prepare ground state wavepackets of highly excited vibrational states and monitor it using femtosecond spectroscopy.

Summary

In this work a new algorithm to determine quantum control fields from the instantaneous response of systems has been developed. The derived fields allow to establish a direct connection between the applied perturbation and the molecular dynamics. The principle is most easily illustrated in regarding a classical forced oscillator. A particle moving inside the respective potential is accelerated if an external field is applied acting in the same direction as its momentum (heating). In contrary, a deceleration is achieved by a field acting in the opposite direction as the momentum (cooling). Furthermore, when the particle reaches a classical turning point and then changes its direction, the sign of the field has to be changed to further drive the system in the desired way. The frequency of the field therefore is in resonance with the oscillator. This intuitively clear picture of a driven classical oscillator can be used for directing (or controlling) quantum mechanical wave packet motion.

The efficiency of the instantaneous dynamics algorithm was demonstrated in treating various model problems, the population transfer in double well potentials, excitation and dissociation of selective modes, and also the population transfer between molecular electronic states. Although it was not tried to optimize the fields to gain higher yields, the control was found to be very efficient. Driving population transfer in a double well potential could be shown to take

place with nearly 100 % efficiency. Furthermore, it was shown that selective dissociation within the electronic ground state of HOD can be performed by either maximizing a selected coordinate's differential momentum change or the energy absorption.

Concerning the population transfer into excited electronic states, a direct comparison with common control algorithms as optimal control theory and genetic algorithms was accomplished using a one-dimensional representation of methyl iodide. The fields derived from the various control theories were effective in transferring population into the chosen target state but the underlying physical background of the derived optimal fields was not obvious to explain.

The instantaneous dynamics algorithm allowed to establish a direct relation between the derived fields and the underlying molecular dynamics. Naturally, because no variational principle was employed, no "optimal" field was obtained. Nevertheless, the constructed fields were found to be very effective. The disadvantage in dissociative systems is the condition of the wavepacket's overlap which directly determines the electric fields. For wavepackets moving on potentials with different gradients, the resulting difference in velocity reduced the possibility of overlaps at later times. Thus, the system is forced to perform the transition suddenly on a short time scale. A restriction to three-photon processes could also succesfully be performed. Especially, for the difficult task to transfer population selectively into a single of two diabatically coupled states without an additional external coupling, good performance for instantaneous response could be obtained.

Whereas the control of dynamics in dissociative systems represents a very demanding task, as is to be expected, bound-to-bound transitions could be handled more effectively. This was demonstrated on the sodium dimer in a representation of three electronic states being initially in its vibronic ground state. The objective was to transfer population into a predefined excited state. Choosing the first or the second state as a target, the control fields exhibited quite different features. In the case of selective excitation of the first excited electronic state, a π-pulse was obtained consisting of a sequence of pulses. The separation of the subpulses is determined by the vibrational motion. The carrier-frequency, on the other hand, is related to the energy gap between the curves. A time-frequency analysis utilizing the difference potentials dependend on the time-varying coordinate expectation values, was employed to relate the pulse-structure to the excited state wave packet, moving in, and out of the Franck-Condon region. Changing the control objective, the derived control field did not feature a vibrational structure any more. The electronic transition was performed on a fast time-scale via a two-step transition.

Regarding the sodium dimer, orientational effects have been investigated. The question of an overall-efficiency of the population transfer for differently oriented molecules was answered to be about 70 % or more if applying a control field derived for an 45° orientation. Furthermore, spectroscopic methods to gain information about the outcome of the control process have been investigated. Therefore the exact nuclear probability density and the density construced from spectroscopic data were contrasted. It was shown that pump/probe femtosecond ionization spectroscopy is suited to monitor time-dependend molecular probability distributions. In particular, it was shown that time-dependend photoelectron spectra are able to monitore the population in the various electronic states after applying the control field.

In the last chapter a completely different possibility of controlling molecules was regarded by investigating molecular iodine with a setup similar to the STIRAP ("Stimulated Raman Adiabatic passage") scenario. The possibility to extend this technique to a fs-time scale was examined in theory as well as in experiments, the latter being performed by Dr. Torsten Siebert in the Kiefer group, University of Würzburg. It was shown that resonant excitation with a STIRAP-like pulse sequence caused two interfering excited state wave packets contributing to the CARS signals. For off-resonant excitation completely different pictures emerged depending on the relative intensity of the two pulses. Implementation of the pulses with a higher intensity of the Stokes pulse as compared to the pump pulse – describing a so-called f-STIRAP like configuration – was shown to effectively transfer population into excited ground-state vibrational levels. This was theoretically underlined by comparing the numerically exact coupling case with the adiabatic picture. The process was described to run in the vicinity of adibaticity.

Recent experiments and calculations have given additional insight into the dynamical processes for the counterintuitive pulse sequence in the f-STIRAP like setup. Experimental results in varying pulse intensities gave new information about the composition of the CARS signals. A new model explaining the CARS signals by a rotating dressed state vector will be adopted in future calculations to expand the picture of a near-adiabatic behavior of the system in the femtosecond regime.

Concerning the instantaneous response algorithms, manifold applications can be thought of. The principle works for selective population transfer in double well systems and will be expanded to treat quantum well structures, where an electron is transferable from one into a neighboring quantum dot. In principle, for a semiconductor energy band consisting of a series of adjoint quantum dots a selective transfer of one or more electrons should be possible.

Another application concerning population transfer may be expanded to molecular bridges mediating electron-transfer or linking vibrational modes between molecular entities. In the context of quantum information the objective is to transport information deriving from an initial state and a spaitally separated final state being connected by linkers. This should be feasable to accomplish employing the instantaneous response algorithm.

Furthermore, the latter algorithm can be modified to selectively transfer population into excited vibrational eigenstates of molecules. This may represent an alternative to the STIRAP process.

Altogether, a new promising algorithm to control dynamical processes based on the instantaneous response has been developed. Because the derived control fields have been shown to be very efficient in selectively influencing molecules, it is to be expected that farther reaching applications can be realized in future investigations.

Zusammenfassung

In dieser Arbeit wurde ein neuer Algorithmus zur Bestimmung von Kontrollfeldern aus der instantanen Respons von Systemen auf die Wirkung von Laserfeldern entwickelt. Die damit berechneten Felder ermöglichen es, eine Verbindung zwischen der durch das Laserfeld applizierten Störung und der molekularen Dynamik herzustellen. Das Prinzip lässt sich am einfachsten anhand eines klassischen Oszillators veranschaulichen. Ein sich innerhalb dieses Oszillatorpotenzials bewegendes Teilchen wird durch ein extern angelegtes Feld beschleunigt, wenn dieses und der Impuls des Teilchens in die gleiche Richtung weisen („Heizen“). Im Gegensatz dazu wird ein Abbremsen des Teilchens durch ein Feld erzielt, welches dem Impuls des Teilchens entgegengerichtet ist („Kühlen“). Wenn nun das Teilchen in diesem Oszillator einen klassischen Umkehrpunkt erreicht und dort seine Richtung ändert, muss das Vorzeichen des Feldes der neuen Richtung entsprechend angepasst werden, damit das Feld das System weiterhin steuern kann. Die Frequenz des Feldes befindet sich demnach in Resonanz mit der Oszillatorfreuqenz. Dieses intuitive, klassische Bild einer erzwungenen Schwingung eines Oszillators kann für die Steuerung (oder Kontrolle) einer quantenmechanischen Wellenpaketbewegung angewendet werden.

Die Effizienz des Algorithmus' wurde innerhalb dieser Arbeit an verschiedenen, grundlegenden Problemen, wie dem Populationstransfer in Doppelminimum-

Potenzialen, Anregung und Dissoziation selektiver Moden und den Populationstransfer zwischen unterschiedlichen elektronischen Zuständen aufgezeigt. Obwohl eine Optimierung der Kontrollfelder bezüglich höherer Ausbeuten nicht durchgeführt wurde, konnte dennoch eine hohe Effizienz der Kontrollprozesse nachgewiesen werden. Ein Populationstransfer in Doppelminimum-Potentialen wurde nahezu vollständig erreicht. Des weiteren wurde selektive Dissoziation innerhalb des elektronischen Grundzustandes des HOD-Moleküls unter Verwendung zweier unterschiedlicher Methoden, der Maximierung der zeitlichen Änderung des Impulses oder der Energieabsorption einer Koordinate, erzielt.

Bezüglich des Populationstransfers in elektronisch angeregte Zustände wurden bekannte Kontrollalgorithmen wie der Theorie der optimalen Kontrolle und genetischer Algorithmen mit dem in dieser Arbeit entwickelten Prinzip der instantanen Respons anhand einer eindimensionalen Darstellung des Methyliodids verglichen. Die mit Hilfe der verschiedenen Kontrolltheorien konstruierten Felder erzielten einen effektiven Populationstransfer in einen zuvor definierten Zielzustand, jedoch ist der dem zu Grunde liegende, physikalische Hintergrund nicht einfach zu beschreiben.

Mit Hilfe des Instantanen-Dynamik-Algorithmus' konnte eine direkte Relation zwischen den Kontrollfeldern und der molekularen Dynamik hergestellt werden. Nachdem kein Variationsprinzip im Sinne einer mathematischen Minimierung angewandt wurde, konnte kein ,,optimales" Feld erhalten werden; die berechneten Kontrollfelder sind dennoch sehr effektiv. Ein Nachteil der Methode ist die Bedingung überlappender Wellenpakete, aus der die elektrischen Felder berechnet werden: da sich die Wellenpakete auf Potenzialen mit unterschiedlichen Steigungen bewegen, sinkt mit fortlaufender Zeit die Wahrscheinlichkeit eines großen

Überlapps. Daher ist das System zu einem plötzlichen Übergang auf einer sehr kurzen Zeitskala gezwungen. Auch die Einschränkung auf einen nicht-resonanten drei-Photonen Prozess konnte erfolgreich implementiert werden. Besonders das schwierige Problem eines selektiven Populationstransfers in eines von zwei diabatisch gekoppelten Zuständen zeigte erfreuliche Ergebnisse.

Da die Kontrolle von Dynamiken in einem dissoziativen System eine besondere Herausforderung darstellt, konnten Übergange in gebundene Zustände erwartungsgemäß besser behandelt werden. Dies wurde für den Fall des Natrium-Dimers in einer Darstellung von drei elektronischen Zuständen gezeigt. Ausgehend von einer Besetzung des vibronischen Grundzustandes sollte nur ein Zustand selektiv angeregt werden. Je nach Wahl des Zielzustandes zeigten sich in der Form des Kontrollfeldes deutliche Unterschiede. Selektive Anregung des ersten Zustandes erzeugte ein Kontrollfeld bestehend aus einer Pulsfolge. Dabei wird der zeitliche Abstand dieser Pulse durch die Schwingungsbewegung festgelegt, während die Trägerfrequenz durch die Energiedifferenz zwischen den Potentialkurven festgelgt wird. Eine Zeit-Frequenz-Analyse anhand dieser Differenzpotentiale in Abhängigkeit vom Ortserwartungswert konnte die Pulse der zuvor beschriebenen Pulsfolge mit einem Wellenpaket im angeregten Zustand, welches sich in und aus dem Franck-Condon Fenster wieder heraus bewegt, in Beziehung setzen. Eine Änderung des zu populierenden Zustandes führte zu einem Kontrollfeld, welches nun keinerlei Vibrationsstruktur mehr zeigt. Die elektronische Anregung fand in einem zwei-Schritte-Prozess auf einer sehr kurzen Zeitkskala statt.

Anhand dieses Moleküls wurden zusätzlich Orientierungseffekte untersucht. Die Frage nach einer Gesamteffizienz des Populationstransfers für alle Orientierungen konnte mit einem Kontrollfeld, welches aus einer mittleren Orientierung bestimmt wurde, beantwortet und auf ca. 70 % abgeschätzt werden. Des weiteren wurden spektroskopische Methoden untersucht, die in der Lage sind, Informationen über die Effizienz von Kontrollprozessen zu liefern. Dabei konnte in einem Vergleich exakter Kernwahrscheinlichkeitsdichten und aus spektroskopischen Daten konstruierten Dichten gezeigt werden, dass Pump-Probe Ionisationsspektroskopie im Femtosekundenbereich sehr gut dazu geeignet ist, detaillierte Abbilder molekularer Wahrscheinlichkeitsverteilungen zu konstruieren. Im Speziellen konnte mit zeitabhängigen Photoelektronenspektren die Populationen in den verschiedenen elektronischen Zuständen nach Anlegen des jeweiligen Kontrollfeldes ,,beobachtet“ werden.

Im letzten Kapitel wurde eine komplett andere Methode der Kontrolle von Molekülen in Anlehnung an einen STIRAP (,,Stimulated Raman Adiabatic Passage“) Prozess am Beispiel molekularen Iods vorgstellt. Dabei wurde die Möglichkeit, diese Technik auf die Femtosekunden-Zeitskala auszudehnen, in Theorie und Experiment untersucht, wobei die Messungen von Dr. Torsten Siebert (Universität Würzburg, Arbeitskreis Prof. Kiefer) durchgeführt worden sind. Es konnte gezeigt werden, dass resonante Anregung mit einer STIRAP-ähnlichen Pulssequenz zwei interferierende Wellenpakete im angeregten Zustand erzeugt, die zu den CARS-Signalen beitragen. Bei nicht-resonanter Anregung hingegen konnten zwei verschiedene Szenarien beobachtet werden, welche von dem Intensitätsverhältnis der beiden Pulse zueinander abhängen. Eine Abfolge der Pulse, so dass der Stokes-Puls mit der höheren Intensität im Vergleich zum Pump-Puls in einer f-STIRAP-artigen Anordnung dem Pump-Puls vorausgeht, führte dabei zu einem effizienten Populationstransfer in einen schwingungsangeregten Zustand im elektronischen Grundzustand. Dies konnte durch einen Vergleich des numerisch exakten Falls mit einer adiabatischen Behandlung theoretisch untermauert werden. Dabei wurde festgestellt, dass die zu Grunde liegenden Prozesse näherungsweise durch adiabatisches Verhalten charakterisiert sind.

Neuere Experimente und Rechnungen haben zusätzliche Informationen über die ablaufenden dynamischen Prozesse bei einer umgekehrten Pulsfolge geliefert. Über die Variation der Pulsintensitäten konnte zusätzlich Einblick über die Zusammensetzung der CARS-Signale erhalten werden. Dazu wird gerade ein neues Modell entwickelt, welches die CARS-Signale mit einem rotierenden dressed-state-Vektor erklärt und als als Grundlage für weitere Rechnungen dient, die das Bild eines nahezu-adiabatischen Verhaltens des Systems in der Femtosekunden-zeitskala erklären sollen.

Bezüglich des Instantanen-Dynamik-Algorithmus' bestehen noch vielfältige Anwendungsmöglichen. Aufgrund des effektiven Populationstransfers in den Doppelminimum-Potentialen können auf der gleichen Grundlage ,,Quanten-Well"-Strukturen behandelt werden, wobei ein Elektron von einem in einen benachbarten Quanten-Dot übertragen werden kann. Im Prinzip sollte demnach in den Energieband-Strukturen von Halbleitern, die aus einer großen Anzahl solcher miteinander verknüpfter Quanten-Dots bestehen, ein selektiver Transfer von einem oder mehreren Elektronen möglich sein.

Weitere Anwendungsmöglichkeiten bezüglich eines Populationstransfers können auf sogenannte ,,Molekulare Brücken" ausgedehnt werden, welche Elektronen-Transfer übermmitteln oder Schwingungsmoden zwischen verschiedenen molekularen Einheiten miteinander verknüpfen. Im Kontext von Quanteninformation übernehmen diese Brücken die Aufgabe, Information von einem Ausgangspunkt zu einem räumlich getrennten Endpunkt weiterzuleiten. Dieses sollte auch durch Anwendung instantaner Resonanz möglich sein.

Des weiteren kann der entwickelte Algorithmus auch dementsprechend verändert werden, dass Population in einen bestimmten, schwingungsangeregten Eigenzustand übertragen wird. Dies mag eine Alternative zum STIRAP-Prozess darstellen.

Zusammenfassend wurde in dieser Arbeit ein vielversprechender Algorithmus zur Kontrolle von Moleküldynamik entwickelt, der auf der instantanen Antwort eines Systems bei Wechselwirkung mit einem elektrischen Feld beruht. Es konnte gezeigt werden, dass die daraus berechneten Kontrollfelder sehr effizient bezüglich einer selektiven Kontrolle von Molekülen sind und noch viele zukünftige Anwendungsmöglichkeiten versprechen.

Bibliography

[1] A. M. Weiner, Rev. Sci. Instrum. **71**, 1929 (2000).

[2] S. A. Rice and M. Zhao, *Optical Control of Molecular Dynamics* (Wiley, New York, 2000).

[3] M. Shapiro and P. Brumer, *Principles of Quantum Control of Molecular Processes* (Wiley, New York, 2003).

[4] S. A. Rice, Adv. Chem. Phys. **101**, 213 (1997).

[5] R. J. Gordon and S. A. Rice, Ann. Rev. Phys. Chem. **48**, 601 (1997).

[6] N. Vitanov, T. Halfmann, B. W. Shore, and K. Bergmann, Ann. Rev. Phys. Chem. **52**, 763 (2001).

[7] T. Brixner, N. H. Damrauer, and G. Gerber, Adv. At. Molec. Opt. Phys. **46**, 1 (2001).

[8] M. Shapiro and P. Brumer, Rep. Prog. Phys. **66**, 859 (2003).

[9] A. Assion *et al.*, Science **282**, 919 (1998).

[10] D. Zeidler *et al.*, J. Chem. Phys. **116**, 5231 (2002).

[11] D. Zeidler *et al.*, in *Mode-selective excitation of polydiacetylene by feedback-controlled pulse shaping in Femtochemistry and Femtobiology*, edited by A. Douhal and J. Santamaria (World Scientific Publishing Co., Singapore, 2002), p. 531.

[12] D. Tannor and S. A. Rice, J. Chem. Phys. **83**, 5013 (1985).

[13] D. Tannor, R. Kosloff, and S. A. Rice, J. Chem. Phys. **85**, 5805 (1986).

[14] U. Gaubatz, P. Rudecki, S. Schiemann, and K. Bergmann, J. Chem. Phys. **92**, 5363 (1990).

[15] P. Brumer and M. Shapiro, Chem. Phys. Lett. **126**, 541 (1986).

[16] P. Brumer and M. Shapiro, Ann. Rev. Phys. Chem. **43**, 257 (1992).

[17] A. P. Peirce, M. A. Dahleh, and H. Rabitz, Phys. Rev. A **37**, 4950 (1988).

[18] R. Kosloff *et al.*, Chem. Phys. **139**, 201 (1989).

[19] R. S. Judson and H. Rabitz, Phys. Rev. Lett. **68**, 1500 (1992).

[20] V. Malinovsky, C. Meier, and D. J. Tannor, Chem. Phys. **221**, 67 (1997).

[21] D. J. Tannor, R. Kosloff, and A. Bartana, Adv. Chem. Phys. **101**, 301 (1997).

[22] D. Tannor, in *in: Molecules in Laser Fields*, edited by A. D. Bandrauk (Marcel Dekker, New York, 1994).

[23] P. Gross, H. Singh, and H. Rabitz, Phys. Rev. A **47**, 4593 (1993).

[24] S. Gräfe *et al.*, Chem. Phys. Lett. **398**, 180 (2004).

[25] S. Gräfe, C. Meier, and V. Engel, J. Chem. Phys. **122**, accepted (2005).

[26] S. Gräfe, M. Erdmann, and V. Engel, Phys. Rev. A (submitted).

[27] S. Gräfe *et al.*, J. Phys. Chem. A **108**, 8954 (2004).

[28] D. T. Greenwood, *Principles of Dynamics*, 2nd ed. (Prentice Hall, Inc., Englewood Cliffs, New Jersey, 1988).

[29] J. V. José and E. J. Saletan, *Classical Dynamics* (Cambridge University Press, Cambridge, UK, 1998).

[30] E. J. Heller, J. Chem. Phys. **65**, 1289 (1976).

[31] G. Esposito, G. Marmo, and G. Sudarshan, *From Classical to Quantum Mechanics* (Cambridge University Press, Cambridge, UK, 2004).

[32] S. Mukamel, *Principles of Nonlinear Optical Spectroscopy* (Oxford University Press Inc., New York, 1995).

[33] F. Jensen, *Introduction to Computational Chemistry* (John Wiley & Sons, New York, 1999).

[34] M. Born and R. Oppenheimer, Ann. Phys. **84**, 457 (1927).

[35] W. P. Schleich, *Quantum Optics in Phase Space* (Wiley-VCH, Berlin, 2001).

[36] M. O. Scully and M. S. Zubairy, *Quantum optics* (Cambridge University Press, Cambridge, UK, 1997).

[37] I. N. Bronstein, K. A. Smendjajew, G. Musiol, and M. Mühlig, *Taschenbuch der Mathematik*, 5. ed. (Verlag Harri Deutsch, Frankfurt, Germany, 2001).

[38] M. Wollenhaupt, A. Assion, and T. Baumert, *Springer Handbook of Optics* (Springer, Heidelberg, 2004).

[39] J. D. McMullen, J. Opt. Soc. Am. **67**, 698 (1977).

[40] W. Vogel, D.-G. Welsch, and S. Wallentowitz, *Quantum Optics An Introduction*, second revised ed. (Wiley-VCH, Berlin, 2001).

[41] M. P. Allen and D. J. Tildesley, *Computer Simulation of Liquids* (Oxford University Press Inc., Oxford, 1987).

[42] M. D. Feit, J. A. Fleck, and A. Steiger, J. Comput. Phys. **47**, 412 (1982).

[43] M. Frigo and S. G. Johnson, ICASSP conference proceedings **3**, 1381 (1998).

[44] R. Kosloff and H. Tal-Ezer, Chem. Phys. Lett. **127**, 223 (1986).

[45] W. Zhu and H. Rabitz, Int. J. Quant. Chem. **93**, 50 (2003).

[46] W. Zhu, J. Botina, and H. Rabitz, J. Chem. Phys. **108**, 1953 (1998).

[47] V. D. Kleiman, L. Zhu, J. Allen, and R. J. Gordon, J. Chem. Phys. **103**, 10800 (1995).

[48] T. Hornung, R. Meier, and M. Motzkus, Chem. Phys. Lett. **326**, 445 (2000).

[49] C. Lupulescu *et al.*, Chem. Phys. **296**, 63 (2004).

[50] B. Amstrup, G. J. Tóth, H. Rabitz, and A. L. orincz, Chem. Phys. **201**, 95 (1995).

[51] H. Tang, R. Kosloff, and S. A. Rice, J. Chem. Phys. **104**, 5457 (1996).

[52] R. Storn and K. Price, *Minimizing the real functions of the ICEC'96 contest by Differential Evolution. IEEE International Conference on Evolutionary Computation, Nagoya, May 1996* (IEEE, New York, USA, 1996), pp. 842 – 844.

[53] B. Amstrup, R. J. Carlson, A. Matro, and S. A. Rice, J. Phys. Chem. **95**, 8019 (1991).

[54] T. Hornung, M. Motzkus, and R. de Vivie-Riedle, J. Chem. Phys. **115**, 3105 (2001).

[55] T. Hornung, M. Motzkus, and R. de Vivie-Riedle, Phys. Rev. A **65**, 021403(R) (2002).

[56] R. Loudon, *The Quantum Theory of Light*, 2nd ed. (Clarendon Press, Oxford, 1983).

[57] D. Geppert, L. Seyfarth, and R. de Vivie-Riedle, Appl. Phys. B **79**, 987 (2004).

[58] M. V. Basilevsky, A. V. Soudackov, and M. V. Vener, Chem. Phys. **200**, 87 (1995).

[59] H. Naundorf, K. Sundermann, and O. Kühn, Chem. Phys. **240**, 163 (1999).

[60] Y. Ohta *et al.*, J. Phys. Chem. A **105**, 8031 (2001).

[61] X.-F. He *et al.*, Appl. Phys. Lett. **70**, 214 (1997).

[62] A. E. Botha and M. R. Singh, Phys. Rev. B **67**, 195334 (2003).

[63] P. F. Barbara, T. J. Meyer, and M. A. Ratner, J. Phys. Chem. **100**, 13148 (1996).

[64] C. Cohen-Tannoudji, B. Diu, and F. Laloë, *Quantum Mechanics Vol. I* (J. Wiley & Sons, Paris, France, 1977).

[65] N. Došlić, O. Kühn, J. Manz, and K. Sundermann, J. Phys. Chem. A **102**, 9645 (1998).

[66] O. Kühn, Euro. Phys. J. D **6**, 49 (1999).

[67] R. de Vivie-Riedle, V. D. Waele, L. Kurtz, and E. Riedle, J. Phys. Chem. A **107**, 10591 (2003).

[68] B. Armstrup and N. E. Henriksen, J. Chem. Phys. **97**, 8285 (1992).

[69] S. Meyer and V. Engel, J. Phys. Chem. **101**, 7749 (1997).

[70] N. Elgobashi, P. Krause, J. Manz, and M. Oppel, Phys. Chem. Chem. Phys. **5**, 4806 (2003).

[71] R. L. V. Wal and F. F. Crim, J. Phys. Chem. **93**, 5331 (1989).

[72] M. Shapiro and P. Brumer, J. Chem. Phys. **98**, 201 (1993).

[73] K. Nagaya, Y. Teranishi, and H. Nakamura, J. Chem. Phys. **113**, 6197 (2000).

[74] W. Jakubetz, J. Manz, and V. Mohan, J. Chem. Phys. **90**, 3686 (1989).

[75] M. V. Korolkov, J. Manz, and G. K. Paramonov, J. Phys. Chem. **100**, 13927 (1996).

[76] W. Jakubetz, E. Kades, and J. Manz, J. Phys. Chem. **97**, 12609 (1989).

[77] M. V. Korolkov, J. Manz, and G. K. Paramonov, Chem. Phys. **217**, 341 (1997).

[78] J. R. Reimers and R. O. Watts, Mol. Phys. **52**, 357 (1984).

[79] R. T. Lawton and M. S. Child, Mol. Phys. **40**, 773 (1980).

[80] A. T. J. B. Eppink and D. H. Parker, J. Chem. Phys. **110**, 832 (1999).

[81] P. C. Samartzis, B. L. G. Bakker, D. H. Parker, and T. N. Kitsopoulos, J. Phys. Chem. A **103**, 6106 (1999).

[82] M. Shapiro, J. Phys. Chem. **97**, 12473 (1993).

[83] B. R. Johnson, C. Kittrell, P. B. Kelly, and J. L. Kinsey, J. Phys. Chem. **100**, 7743 (1996).

[84] A. D. Hammerich *et al.*, J. Chem. Phys. **101**, 5623 (1994).

[85] M. Shapiro and R. Behrson, J. Chem. Phys. **73**, 3810 (1980).

[86] M. Shapiro, J. Phys. Chem. **90**, 3644 (1986).

[87] H. Guo and G. C. Schatz, J. Chem. Phys. **93**, 393 (1990).

[88] H. Guo, J. Chem. Phys. **96**, 6629 (1992).

[89] T. Gerdts and U. Manthe, J. Chem. Phys. **107**, 6584 (1997).

[90] Y. Amatatsu, S. Yabushita, and K. Morokuma, J. Chem. Phys. **104**, 9783 (1996).

[91] A. Gedanken, M. B. Robin, and Y. Yafet, J. Chem. Phys. **76**, 4798 (1982).

[92] S. Shi and H. Rabitz, J. Chem. Phys. **92**, 364 (1990).

[93] I. R. Sola, J. Santamaria, and D. J. Tannor, J. Phys. Chem. A **102**, 4301 (1998).

[94] P. Kusch and M. M. Hesse, J. Chem. Phys. **68**, 2591 (1978).

[95] G. Gerber and R. Möller, Chem. Phys. Lett. **113**, 546 (1985).

[96] A. J. Taylor, K. M. Jones, and A. L. Schawlow, J. Opt. Soc. Am. B **73**, 994 (1983).

[97] M. Hug, C. Menke, and W. P. Schleich, J. Phys. A: Math. Gen. **31**, L217 (1998).

[98] H.-W. Lee, Phys. Rev. A **50**, 2746 (1994).

[99] D. D. Konowalow, M. E. Rosenkranz, and D. S. Hochhauser, J. Mol. Spectrosc. **99**, 321 (1983).

[100] A. Assion *et al.*, Chem. Phys. Lett. **259**, 488 (1996).

[101] N. F. Scherer, A. J. Ruggiero, M. Du, and G. R. Fleming, J. Chem. Phys. **93**, 856 (1990).

[102] N. F. Scherer *et al.*, J. Chem. Phys. **95**, 1487 (1991).

[103] R. S. Mullikan, J. Chem. Phys. **55**, 309 (1971).

[104] T. Baumert and G. Gerber, Adv. At. Molec. Opt. Phys. **35**, 163 (1995).

[105] H. Metiu and V. Engel, J. Opt. Soc. Am. **7**, 1709 (1990).

[106] V. Blanchet, C. Nicole, M. Bouchene, and B. Girard, Phys. Rev. Lett. **78**, 2716 (1997).

[107] M. Seel and W. Domcke, Chem. Phys. **151**, 59 (1991).

[108] M. Seel and W. Domcke, J. Chem. Phys. **95**, 7806 (1991).

[109] C. Meier and V. Engel, Chem. Phys. Lett. **212**, 691 (1993).

[110] M. Lax, J. Chem. Phys. **20**, 1752 (1952).

[111] S.-Y. Lee, W. T. Pollard, and R. A. Mathies, Chem. Phys. Lett. **163**, 11 (1989).

[112] M. Braun, C. Meier, and V. Engel, J. Chem. Phys. **103**, 7907 (1995).

[113] Z. Li, J.-Y. Fang, and C. C. Martens, J. Chem. Phys. **104**, 6919 (1996).

[114] E. M. Hiller and J. A. Cina, J. Chem. Phys. **105**, 3419 (1996).

[115] J. Cao and K. R. Wilson, J. Chem. Phys. **106**, 5062 (1997).

[116] S. Dilthey, S. Hahn, and G. Stock, J. Chem. Phys. **112**, 4910 (2000).

[117] V. A. Ermoshin and V. Engel, Euro. Phys. J. D **15**, 413 (2001).

[118] V. Engel, Chem. Phys. Lett. **178**, 130 (1991).

[119] T. Lohmüller, M. Erdmann, and V. Engel, Chem. Phys. Lett. **373**, 319 (2003).

[120] N. E. Henriksen, Adv. Chem. Phys. **91**, 433 (1995).

[121] N. E. Henriksen and V. Engel, Int. Rev. Phys. Chem. **20**, 93 (2001).

[122] V. Engel and N. E. Henriksen, J. Chem. Phys. **112**, 106 (2000).

[123] H. Stapelfeldt, E. Constant, H. Sakai, and P. B. Corkum, Phys. Rev. A **58**, 426 (1998).

[124] A. D. Bandrauk and S. Chelkowski, Phys. Rev. Lett. **87**, 273004 (2001).

[125] S. Chelkowski and A. D. Bandrauk, Phys. Rev. A **65**, 023403 (2002).

[126] R. Schinke, *Photodissociation Dynamics* (Cambridge University Press, Cambridge, 1993).

[127] Z. Shen, I. Boustani, M. Erdmann, and V. Engel, Chem. Phys. Lett. **339**, 362 (2001).

[128] Z. Shen and V. Engel, Chem. Phys. Lett. **358**, 344 (2002).

[129] A. Assion *et al.*, Phys. Rev. A **54**, R4605 (1996).

[130] S. Gerstenkorn and P. Luc, *Atlas du Spectre d'Absoption de la Molecule d'Iode* (CNRS II, Paris, 1978).

[131] J. Tellinghuisen, J. Chem. Phys. **76**, 4736 (1982).

[132] M. Lamrini *et al.*, J. Chem. Phys. **100**, 8780 (1994).

[133] J. Tellinghuisen, J. Chem. Phys. **106**, 1305 (1997).

[134] M. Ganz and M. Kiefer, J. Raman Spectrosc. **24**, 463 (1993).

[135] R. M. Bowman, M. Dantus, and A. H. Zewail, Chem. Phys. Lett. **161**, 297 (1989).

[136] R. M. Bowman, M. Dantus, and A. H. Zewail, Chem. Phys. Lett. **174**, 546 (1990).

[137] M. Schmitt, G. Knopp, A. Materny, and W. Kiefer, Chem. Phys. Lett. **270**, 9 (1997).

[138] S. Meyer *et al.*, Chem. Phys. Lett. **281**, 332 (1997).

[139] S. Meyer *et al.*, Chem. Phys. Lett. **301**, 248 (1999).

[140] A. Materny *et al.*, Appl. Phys. B **71**, 299 (2000).

[141] N. V. Vitanov and S. Stenholm, Phys. Rev. A **55**, 648 (1997).

[142] K. Bergmann, *Coherent Population Transfer* (World Scientific, Singapore, 1995).

[143] V. S. Malinovsky, J. Santamaría, and I. R. Solá, J. Phys. Chem. A **107**, 8259 (2003).

[144] T. A. Laine and S. Stenholm, Phys. Rev. A **53**, 2501 (1996).

[145] K. Drese and M. Holthaus, Euro. Phys. J. D **3**, 73 (1998).

[146] N. V. Vitanov, K.-A. Suominen, and B. W. Shore, J. Phys. B: At. Mol. Phys. **32**, 4535 (1999).

[147] S. Meyer and V. Engel, J. Raman Spectrosc. **31**, 33 (2000).

[148] J. Faeder *et al.*, J. Chem. Phys. **115**, 8440 (2001).

Danksagung

An dieser Stelle möchte ich allen danken, die zum Gelingen dieser Arbeit beigetragen haben. In erster Linie ist dies mein Betreuer Prof. Dr. Volker Engel, der mir eine faszinierende Themenstellung bot und mir viele Freiheiten bei der Themenerarbeitung ließ. Dabei konnte ich immer auf sein fachliches Feedback zurückgreifen, welches er gerne weitergab. Oft haben sich daraus völlig neue Lösungsansätze entwickelt. Ferner möchte ich ihm für die Möglichkeit danken, an nationalen und internationalen Fachtagungen teilzunehmen. Dabei kam der Spaß an der Arbeit auf keinen Fall zu kurz.

Des weiteren möchte ich allen jetzigen und ehemaligen Mitarbeitern des Arbeitskreises danken, das ist zum einen Dr. Marco Erdmann, der schon seit meines F–Prakitkums mir die Welt der Computer versucht hat nahezubringen. Diese Geduld hat er auch in vielen fachlichen, aber auch nicht–fachlichen Gesprächen beibehalten und gegen Ende immer neuen Versionen meines ,,Telefonbuchs“ geduldig und gewissenhaft gelesen. Zum anderen danke ich Philipp Marquetand, der freundlicherweise alle administrativen und verwaltenden Aufgaben übernommen hat und mit viel Humor und der Wahl adäquater Hotels den Alltag erheitert hat. Danke auch Theo Lohmüller und Jochen Beck für eine einmalige Zeit während der Diplomarbeit und Daniel Scheidel für abwechslungsreiche sechs Wochen während seines Praktikums.

Zu einer guten Stimmung hat das ganze zweite Stockwerk der PC beigetragen (Horia-Sorin Andrei, Stefan “Woodie“ Dümmler, Thomas Schüßler, Dr. Nicola Solca, Dr. Matthias Zierhut und Prof. Dr. Ingo Fischer) es war eine witzige Zeit mit einem bunt gemischten Haufen. Der obligatorische Nachmittags-Kaffeeklatsch oder die bitter nötigen, regelmäßigen Fußball-Trainingseinheiten mit den Jungs waren immer eine besondere Herausforderung für die Lachmuskeln. PD Dr. Otto Dopfer danke ich für die vielen erfrischenden Diskussionen über die verschiedenen Teilbereiche der Physik, insbesondere der Quantenchromodynamik und die Welt des Standard-Modells, aber auch über das Leben außerhalb der Uni.

Mit Dr. Torsten Siebert zusammen habe ich ein neues, interessantes Arbeitsgebiet kennengelernt und gleichzeitig einen Einblick in die Welt eines Nachwuchs-Wissenschaftlers zu erhalten. Ihm danke ich auch für ein paar witzige Tage in Salt Lake City und immer neue Messdaten.

Am Schluss möchte ich mich besonders bei meiner Familie für die fortwährende Unterstützung während des Studiums bedanken.

Lebenslauf

Persönliche Daten:

Name: Stefanie Gräfe

Geburtsdatum: 27.08.1979

Geburtsort: Düsseldorf

Staatsangehörigkeit: deutsch

Schulbildung:

1985–1989	Grundschule Florensstraße Düsseldorf
1989–1998	Städt. Görres Gymnasium Düsseldorf
1998	Abschluss Allgemeine Hochschulreife

Studium

1998 – 2003	Studium der Chemie an der Bayerischen Julius – Maximilians Universität Würzburg
07/2002	Diplomprüfung in Chemie
07/2002 – 01/2003	Diplomarbeit im Arbeitskreis von Prof. V. Engel, Institut für Physikalische Chemie
01/2003	Abschluss als Diplom-Chemiker Univ.
04/2003 – 03/2005	Promotion im Arbeitskreis von Prof. V. Engel.